frontiers | Research Topics

Geomechanics and induced seismicity for underground energy and resources exploitation

Edited by
Longjun Dong, Wenzhuo Cao and Thomas Hermans

Published in
Frontiers in Earth Science

ISSN 1664-8714
ISBN 978-2-83251-562-4
DOI 10.3389/978-2-83251-562-4

About Frontiers

Frontiers is more than just an open access publisher of scholarly articles: it is a pioneering approach to the world of academia, radically improving the way scholarly research is managed. The grand vision of Frontiers is a world where all people have an equal opportunity to seek, share and generate knowledge. Frontiers provides immediate and permanent online open access to all its publications, but this alone is not enough to realize our grand goals.

Frontiers journal series

The Frontiers journal series is a multi-tier and interdisciplinary set of open-access, online journals, promising a paradigm shift from the current review, selection and dissemination processes in academic publishing. All Frontiers journals are driven by researchers for researchers; therefore, they constitute a service to the scholarly community. At the same time, the *Frontiers journal series* operates on a revolutionary invention, the tiered publishing system, initially addressing specific communities of scholars, and gradually climbing up to broader public understanding, thus serving the interests of the lay society, too.

Dedication to quality

Each Frontiers article is a landmark of the highest quality, thanks to genuinely collaborative interactions between authors and review editors, who include some of the world's best academicians. Research must be certified by peers before entering a stream of knowledge that may eventually reach the public - and shape society; therefore, Frontiers only applies the most rigorous and unbiased reviews. Frontiers revolutionizes research publishing by freely delivering the most outstanding research, evaluated with no bias from both the academic and social point of view. By applying the most advanced information technologies, Frontiers is catapulting scholarly publishing into a new generation.

What are Frontiers Research Topics?

Frontiers Research Topics are very popular trademarks of the *Frontiers journals series*: they are collections of at least ten articles, all centered on a particular subject. With their unique mix of varied contributions from Original Research to Review Articles, Frontiers Research Topics unify the most influential researchers, the latest key findings and historical advances in a hot research area.

Find out more on how to host your own Frontiers Research Topic or contribute to one as an author by contacting the Frontiers editorial office: frontiersin.org/about/contact

Geomechanics and induced seismicity for underground energy and resources exploitation

Topic editors

Longjun Dong — Central South University, China

Wenzhuo Cao — Imperial College London, United Kingdom

Thomas Hermans — Ghent University, Belgium

Citation

Dong, L., Cao, W., Hermans, T., eds. (2023). *Geomechanics and induced seismicity for underground energy and resources exploitation*. Lausanne: Frontiers Media SA. doi: 10.3389/978-2-83251-562-4

Table of contents

frontiers | Frontiers in Earth Science

TYPE Editorial
PUBLISHED 17 January 2023
DOI 10.3389/feart.2023.1135659

OPEN ACCESS

EDITED AND REVIEWED BY
Derek Keir,
University of Southampton,
United Kingdom

*CORRESPONDENCE
Longjun Dong,
lj.dong@csu.edu.cn

SPECIALTY SECTION
This article was submitted to Structural Geology and Tectonics, a section of the journal Frontiers in Earth Science

RECEIVED 01 January 2023
ACCEPTED 10 January 2023
PUBLISHED 17 January 2023

CITATION
Dong L, Cao W and Hermas T (2023), Editorial: Geomechanics and induced seismicity for underground energy and resources exploitation.
Front. Earth Sci. 11:1135659.
doi: 10.3389/feart.2023.1135659

Editorial: Geomechanics and induced seismicity for underground energy and resources exploitation

Longjun Dong[1]*, Wenzhuo Cao[2] and Thomas Hermas[3]

[1]School of Resources and Safety Engineering, Central South University, Changsha, China, [2]Department of Earth Science and Engineering, Royal School of Mines, Imperial College London, London, United Kingdom, [3]Department of Geology, Ghent University, Ghent, Belgium

KEYWORDS

geomechanics, microseismic monitoring, underground engineering, induced seismicity geo-energy, mineral resources

Editorial on the Research Topic
Geomechanics and induced seismicity for underground energy and resources exploitation

1 Introduction

Exploiting energy and resources from the Earth subsurface is a development trend all over the world. These anthropogenic activities lead to underground stress perturbations, which may trigger hazardous events. Deep mining and tunneling may induce dynamic disasters such as fault slippage and rock burst, leading to serious casualties and economic losses. Engineering applications such as well drilling, fluid injection into the subsurface, and the creation of deep underground space provide direct sources to seismic activities. It is imperative to minimize the risk of these disasters and even prevent their occurrences, which is crucial for a safe and efficient energy and resources exploitation. However, the physical mechanism of induced hazardous events is not well understood. Through innovative theoretical analysis and techniques (Ma et al., 2018; Ma et al., 2019a; Ma et al., 2019b; Ma et al., 2019; Dong et al., 2022a; Dong and Luo, 2022; Li et al.; Meng et al.; Sun et al., 2022), experimental techniques (Dong et al., 2021a; Dong et al.; Chen et al.; Dong et al. 2020a; Hermans et al. 2018; Dong et al. 2022b; Dong et al., 2023), data mining (Dong et al., 2022c; Qian et al.; Yu et al.), and simulation methods (Dong and Luo, 2020; Cao et al., 2020; Dong et al. 2021b; Lei; Xu et al.), researchers conducted in-depth research on these key problems. Efforts in integrating these technological means will help advance geomechanics and induced seismicity-related research that contributes to resolving challenging Research Topic in the exploitation of underground energy and resources. This Research Topic aims to focus on the most recent theoretical, experimental, and technological advances in Geomechanics and Induced Seismicity for Underground Energy and Resources Exploitation. This editorial presents a brief summary of the articles published under this Research Topic.

2 Theoretical analysis and techniques

Meng et al. presented a non-parametric simultaneous reconstruction and denoising of seismic data *via* sparse and low-rank regularization, efficiently and automatically dealing with the prestack gathers. The effectiveness of this method is verified through practical applications. Beside the hypothesis that the seismic signal is compressible, the proposed method makes no additional prior assumptions on the original data. First, the solution matrix is extracted from the Fourier dictionary. Then the reconstruction and denoising are performed successively in the sparse domain. The key parameters are estimated in a data-driven framework. The method can reduce the computational complexity of sparse representation. It can be effectively applied to data reconstruction and denoising.

Li et al. established a tunnel excavation model test based on a true triaxial stress loading system, combined with three-dimensional scanning technology for a superimposed sandy soil. Based on this model, the vector displacement response range and three-dimensional deformation characteristics of the excavation face were studied in the main displacement affected area around the excavation face. Meanwhile, the deformation characteristics, such as vertical settlement and horizontal displacement of the stratum in the main influence affected area were analyzed. The results show that the model can provide some references for the excavation engineering of superimposed sand-soil tunnels.

3 Progress in experimental research

Chen et al. studied the deterioration characteristics of the tunnel surrounding rock under the scouring of flowing groundwater. Experiments were carried out with acidic solutions representative of the groundwater composition. The microstructure of granite samples cored on site, deformation features, and evolution characteristics of mechanical parameters under saturations with different flow rates and various pH values were analyzed using scanning electron microscopy (SEM), energy dispersive spectroscopy (EDS), nuclear magnetic resonance (NMR), and X-ray diffraction (XRD). The experimental results can bring inspiration to the research in this field.

Dong et al. proposed a comprehensive abnormal area detection method, which is based on transient electromagnetic detection and supplemented *via* drilling detection. It was used to determine the spatial position and location of heterogeneous rock mass in the goaf underlying the subway station. The detection results provide a basis for the safety and stability of the proposed substation foundation. This method provides a reference for the detection of the stability of non-homogeneous rock masses in the extraction area, and helps to take effective management measures for heterogeneous rock masses.

4 Data mining and simulation methods

Yu et al. proposed a method for simultaneously imaging multi-fracture networks using microseismic monitoring data. The algorithms commonly used in multi-model fitting were integrated to produce an upgraded method that accommodates geophysical data for faster and more accurate simultaneous multi-fracture model imaging within a point cloud. The accuracy of the method was improved using circular calculation and density-based spatial clustering of applications with noise, such that the estimated fracture orientations correspond well to those at the actual locations. The proposed algorithm was applied to synthetic data to assess the impact of considering orientation and outlier data on the model results. Field microseismic data were also used to depict fractures representing the dominant orientation, and the errors of the strike and dip angle estimates were 2.89% and 2.83%, respectively. Results demonstrate the suitability of the algorithm for fast and accurate field data modeling.

Qian et al. observed paired signals that are induced by cavern roof instability for the first time with the aid of a microseismic monitoring system. By studying the two events of the paired signals, the whole process of rock debris rupture development at the cave roof, the time of rock debris crossing the brine and the collision process of rock debris at the cave floor were analyzed. It was found that by locating the first event of the paired signals, the spatial distribution of the roof can be outlined. Using the delay time between the two events of the paired signals, the height of the cave chamber can be estimated qualitatively. By observing the collision signal, the size of the rock debris can be further analyzed. The derived information could be combined to assess the cavern collapse hazard through some rock mechanics analysis.

Xu et al. analyzed the equivalent elastic modulus and occurrence effect of rockmass with orthogonal random joints. Firstly, the eigenvalue distribution function of joints is obtained through statistically analyzing a large number of joints in the field. Secondly, the orthogonal random joint model is constructed using Monte Carlo method based on UDEC software platform. Then, a large number of numerical experiments of discrete elements are carried out. The results showed that the equivalent elastic modulus of rockmass with orthogonal random joints has an obvious scale effect. The relationship between the average equivalent elastic modulus and the representative basic volume (REV) size of rockmass follows a negative power function distribution. Under different joint angles, the standard deviation and variation coefficient of the equivalent elastic modulus of rockmass are distributed discretely. When the model size reaches REV size, the occurrence effect of equivalent elastic modulus of rockmass is not significant.

Lei analyzed the relationship between the 2018 Hokkaido East Ibri earthquake and carbon dioxide (CO_2) injection through a geomechanical model. The results show that even under extreme conditions, CO_2 is injected at the rate of 180,000 tons/year for 10 consecutive years, the impact of CO_2 injection on the Yibuli seismic fault is far lower than that caused by the Earth tide. There is no convincing mechanism to allow fluid channels to heal and block the natural fluid flow along the fault in a short time. CO_2 injection is therefore unlikely to be a trigger for the East Ibri earthquake. The geological storage of CO_2 is very important for slowing down the trend of global warming. For fault reactivation and earthquake caused by risk related injection, it is necessary to avoid too large and too small assessment.

5 Conclusion

The study of geomechanics and induced earthquake of underground energy and resource development is of great significance to study, understand and predict subsurface systems affected by the exploitation of natural resources. In particular, the prediction of disasters caused by human activities is still a very

important research topic. We sincerely thank all the authors for their outstanding and meaningful contributions to this Research Topic. It is hoped that there will be more relevant research in the field of geomechanics and geophysics in the future to bring further breakthroughs in theory, field observation, laboratory experiments, numerical simulation, and the development of geophysical monitoring equipment and technology towards a safe underground energy and resources exploitation.

Author contributions

LD and WC drafted the first version of the editorial. LD, WC, and TH revised the first draft and made contributions about papers they edited.

Conflict of interest

The authors declare that the research was conducted in the absence of any commercial or financial relationships that could be construed as a potential conflict of interest.

Publisher's note

References

Cao, W., Shi, J. Q., Durucan, S., Si, G., and Korre, A. (2020). Gas-driven rapid fracture propagation under unloading conditions in coal and gas outbursts. *International Journal of Rock Mechanics and Mining Sciences* 130, 104325. doi:10.1016/j.ijrmms.2020.104325

Dong, L., and Luo, Q. (2020a). Stress heterogeneity and slip weakening of faults under various stress and slip. *Geofluids* 2020, 1–12. doi:10.1155/2020/8860026

Dong, L. J., Hu, Q. C., and Tong, X. J. (2020b). Velocity-Free MS/AE Source Location Method for Three-Dimensional Hole-Containing Structures. *Engineering* 6, 827–834. doi:10.1016/j.eng.2019.12.016

Dong, L., Chen, Y., Sun, D., and Zhang, Y. (2021a). Implications for rock instability precursors and principal stress direction from rock acoustic experiments. *Int. J. Min. Sci. Technol.* 31, 789–798. doi:10.1016/j.ijmst.2021.06.006

Dong, L. J., Tong, X. J., and Ma, F. (2021b). Quantitative Investigation of Tomographic Effects in Abnormal Regions of Complex Structures. *Engineering* 7, 1011–1022. doi:10.1016/j.eng.2020.06.021

Dong, L., and Luo, Q. (2022). Investigations and new insights on earthquake mechanics from fault slip experiments. *Earth-Sci Rev.* 228, 104019. doi:10.1016/j.earscirev.2022.104019

Dong, L., Tao, Q., Hu, Q., Deng, S., Chen, Y., Luo, Q., et al. (2022a). Acoustic emission source location method and experimental verification for structures containing unknown empty areas. *Int. J. Min. Sci. Technol.* 32, 487–497. doi:10.1016/j.ijmst.2022.01.002

Dong, L., Chen, Y., Sun, D., Zhang, Y., and Deng, S. (2022b). Implications for identification of principal stress directions from acoustic emission characteristics of granite under biaxial compression experiments. *J. Rock Mech. Geotechnical Eng.* doi:10.1016/j.jrmge.2022.06.003

Dong, L. J., Pei, Z. W., and Xie, X. (2022c). Early identification of abnormal regions in rock-mass using traveltime tomography. *Engineering*. doi:10.1016/j.eng.2022.05.016

Dong, L., Zhang, Y., Bi, S., Ma, J., Yan, Y., and Cao, H. (2023). Uncertainty investigation for the classification of rock micro-fracture types using acoustic emission parameters. *Int. J. Rock Mech. Min.* 162, 105292. doi:10.1016/j.ijrmms.2022.105292

Hermans, T., Nguyen, F., and Klepikova, M. (2018). Uncertainty Quantification of Medium-Term Heat Storage From Short-Term Geophysical Experiments Using Bayesian Evidential Learning. *Water Resources Research* 54 (4), 2931–2948. doi:10.1002/2017WR022135

Ma, J., Dong, L., Zhao, G., and Li, X. (2018). Discrimination of seismic sources in an underground mine using full waveform inversion. *Int. J. Rock Mech. Min. Sci.* 106, 213–222. doi:10.1016/j.ijrmms.2018.04.032

Ma, J., Dong, L., Zhao, G., and Li, X. (2019a). Focal mechanism of mining-induced seismicity in fault zones: A case study of yongshaba mine in China. *Rock Mech. Rock Eng.* 52, 3341–3352. doi:10.1007/s00603-019-01761-4

Ma, J., Dong, L., Zhao, G., and Li, X. (2019b). Ground motions induced by mining seismic events with different focal mechanisms. *Int. J. Rock Mech. Min. Sci.* 116, 99–110. doi:10.1016/j.ijrmms.2019.03.009

Ma, J., Dong, L., Zhao, G., and Li, X. (2019). Qualitative method and case study for ground vibration of tunnels induced by fault-slip in underground mine. *Rock Mech. Rock Eng.* 52, 1887–1901. doi:10.1007/s00603-018-1631-x

Sun, D., Wu, Y., Dong, L., and Luo, Q. (2022). Closed-form solutions for locating heat-concentrated sources using temperature difference. *Mathematics* 10 (16), 2843. doi:10.3390/math10162843

frontiers | Frontiers in Earth Science

ORIGINAL RESEARCH
published: 30 May 2022
doi: 10.3389/feart.2022.873645

Was the 2018 Hokkaido Eastern Iburi Earthquake in Japan Related to Carbon Capture and Storage (CCS)-CO_2 Injection? Insights From Geomechanical Analysis

Xinglin Lei *

Geological Survey of Japan, AIST, Ibaraki, Japan

In a recent paper ["Groundwater anomaly related to CCS-CO_2 injection and the 2018 Hokkaido Eastern Iburi earthquake in Japan" by Sano et al. (Front. Earth Sci., 2020, 8)], the authors claimed that CO_2-enriched fluid may have initially migrated through permeable channels, blocking the fluid flow from the source region, increasing pore pressure in the focal region and triggering a natural earthquake where the brittle crust was already critically stressed. The proposed model is very interesting, but the authors have not shown any quantitative evaluation supporting their conclusion. Here, through geomechanics model analysis, even under extreme conditions, which overestimate the impact of the injection, the impact of the CO_2 injection on the Iburi earthquake fault, whether the deep section or shallow part of the fault, is much lower than that caused by Earth tides. In addition, no convincing mechanism exists that would allow fluid channels to heal within a short period of time and block the natural fluid flow along the fault. Therefore, the occurrence of earthquakes was not related to CO_2 injection. Geological storage of CO_2 is expected to become an effective option for global warming countermeasures, and the assessment of its environmental impact must be carefully conducted.

Keywords: hokkaido earthquake, geological CO_2 storage, geomechanics, coupled thermal-hydraulic-mechanical simulation, earthquake triggering

OPEN ACCESS

Edited by:
Longjun Dong,
Central South University, China

Reviewed by:
Mikhail Rodkin,
Institute of Earthquake Prediction Theory and Mathematical Geophysics (RAS), Russia
Xueyi Shang,
Chongqing University, China

***Correspondence:**
Xinglin Lei
xinglin-lei@aist.go.jp

Specialty section:
This article was submitted to Structural Geology and Tectonics, a section of the journal Frontiers in Earth Science

Received: *11 February 2022*
Accepted: *04 May 2022*
Published: *30 May 2022*

Citation:
Lei X (2022) Was the 2018 Hokkaido Eastern Iburi Earthquake in Japan Related to Carbon Capture and Storage (CCS)-CO_2 Injection? Insights From Geomechanical Analysis. Front. Earth Sci. 10:873645. doi: 10.3389/feart.2022.873645

INTRODUCTION

As one effective option for mitigating global warming, the geological storage of carbon dioxide (CO_2) appears promising. Injecting a large amount of CO_2 fluid into an underground aquifer will inevitably cause certain formation deformation and increase fluid pressure. There is therefore a risk of accelerating the activation of pre-existing faults nearby and inducing/triggering earthquakes. In several industrial applications that require the injection of fluids into the Earth's crust, including disposal of wastewater, development of unconventional oil and gas resources, enhanced geothermal development, and well salt production, injection-induced seismicity, including destructive earthquakes with a sizable magnitude ($M > 5$), has been observed and has attracted widespread attention (e.g., Ellsworth et al., 2019; Atkinson et al., 2020; Lei et al., 2020). At the same time, it also poses challenges for effective operation. At present, some demonstration projects of CO_2 geological storage have been carried out around the world, but there are no reports of important induced earthquakes related to these projects.

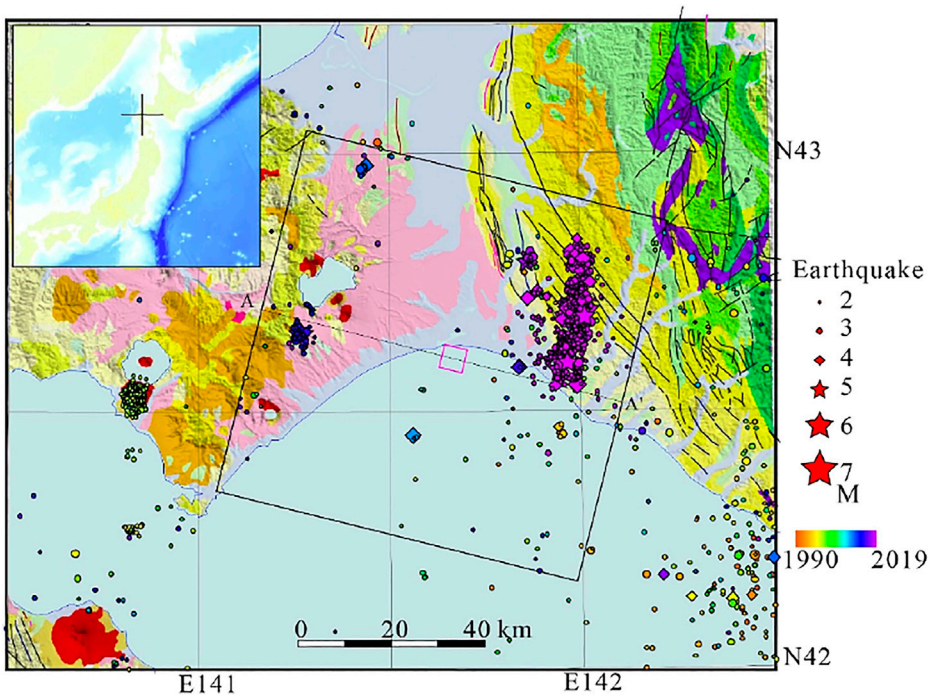

FIGURE 1 | Map view of the Tomakomai carbon capture and storage (CCS)-CO_2 injection site and earthquake epicenters observed from 1990 through 2019 (from the Japan Meteorological Agency (JMA) earthquake catalog) overlaid on geological map (from (Japan, 1995)). The pink square indicates the injection site. Line A-A′ masks the profile in **Figure 2**.

The carbon capture and storage (CCS) demonstration project in Tomakomai, Hokkaido, Japan, is a medium-scale CO_2 offshore storage and has injected approximately 300,000 tons of CO_2 into a porous sandstone aquifer at a depth of approx. 1,000 m from April 2016 to November 2019. During this period, on September 5, 2018, at 18:08 (UTC), a JMA (the Japan Meteorological Agency) magnitude 6.7 earthquake occurred in the eastern Iburi region in Hokkaido. The focal depth of the earthquake is 37 km, and the epicenter is approx. 20 km east from the injection location (**Figure 1**). Joint inversion of strong motion and geodetic data shows that a large slip occurred at a depth of approx. 22 km, which is shallower than the hypocenter (initial rupture) depth. This indicates that the main seismogenic fault is an east-dipping high-angle reverse fault, which is consistent with the Ishikari-Teichi-Toen fault zone (ITTFZ) (Kobayashi et al., 2019). Based on detailed 3D injection simulation, the predicted pressure buildup at the end of the injection is limited within a few kilometers from the injection well (Kano et al., 2014). By considering that the stress disturbance caused by CO_2 injection cannot reach the ITTFZ, it is generally believed that the earthquake is not directly or indirectly related to CO_2 injection. However, recently, a previous study (Sano et al., 2020) determined isotopes of commercially available mineral water produced from a depth of approx. 100 m in a well located 13 km from the injection site, showing dissolved components of injected CO_2. Furthermore, the steady flow of deep celestial fluid along the ITTFZ is speculated to be blocked, which increased the fluid pressure in the deep part of the fault and triggered the earthquake. The model proposed in the paper is very interesting, but making such an assumption without any geomechanical analysis may not be valid.

The purpose of the present brief study is to investigate the validity of the above assumption. First, the theoretical solution of a simple two-dimensional radial flow model is used to analyze the decay of fluid pressure with distance. Then, a simplified three-dimensional (3D) and coupled thermal-hydraulic-mechanical (THM) model is constructed to quantitatively analyze the influence range and degree of actual CO_2 injection under some extreme conditions.

ANALYSIS BASED ON GEOMECHANICS

Geological Environment of the Tomakomai Carbon Capture and Storage-Injection Site

Figure 2 shows a simplified 3D geological model of the Tomakomai CCS-CO_2 injection site and distribution of earthquakes from the JMA catalog. The geological model is modified from the summary of time report of the Tomakomai CCS large-scale demonstration test 300,000 tons injection (METI, NEDO, and JCCS, 2020) METI, NEDO, and JCCS. There are two potential reservoirs, Moebetsu formation and Takinoue formation, for CO_2 storage. The Moebetsu formation is located at a depth of approx. 870 to 1,200 m. The upper part of the formation, which is dominated by silt/mudstone, acts as a cap layer. The lower part of the formation (below 1,070 m),

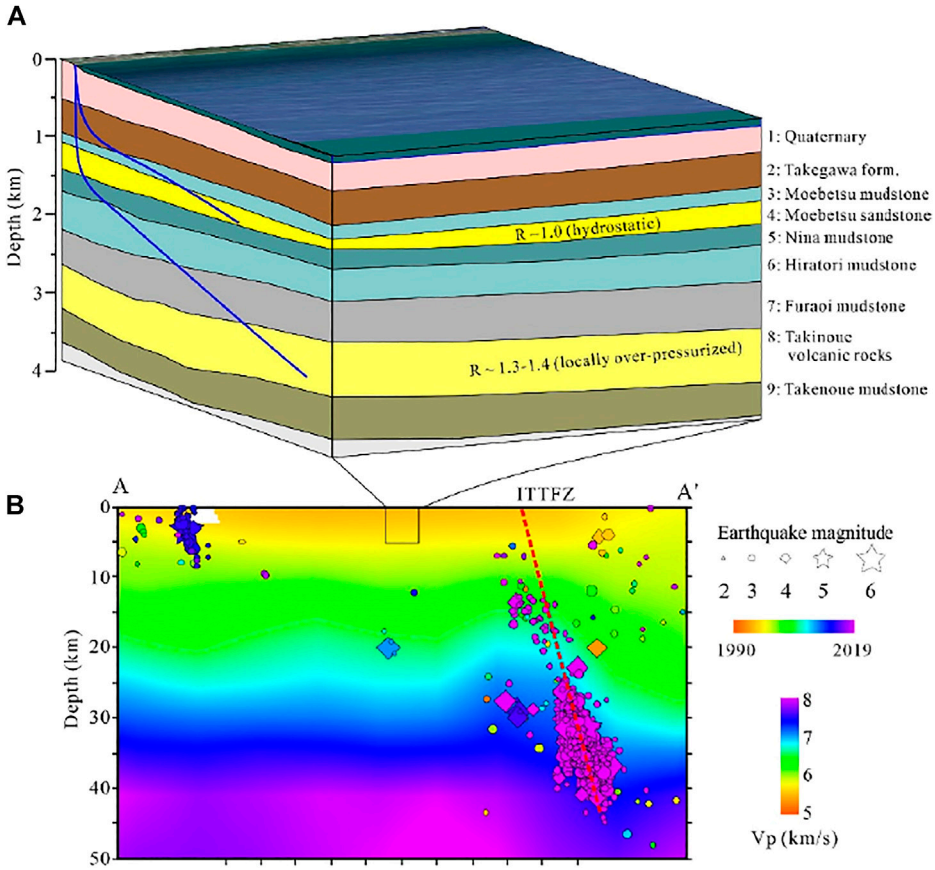

FIGURE 2 | (A) A simplified 3D geological model of the Tomakomai CCS-CO_2 injection site (modified from (METI, NEDO, and JCCS, 2020)). **(B)** Vertical section showing the P velocity (from (Matsubara et al., 2017)) and the earthquake (from JMA catalog) distribution. Ishikari-Teichi-Toen fault zone (ITTFZ).

dominated by sandstone, is a potential CO_2 reservoir. Another potential reservoir is the Takinoue formation at a depth of approx. 2,400 to 3,000 m, which is a volcanic formation composed of Neogene lava and tuff. Although the reservoir pressure is hydrostatic in the Moebetsu formation, the Takinoue formation is characterized by heterogeneously distributed overpressure zones. The temperature gradient is 3.7–4.4 ˚C/100 m (Kano et al., 2014).

The injection was started in April 2016 and ended in Oct. 2019, achieving a cumulative injection of 300,012 tons in the Moebetsu reservoir. The maximum injection rate was approx. 18,000 tons/month, and the maximum pressure increase was 12.6 MPa. Only 98 tons was injected into the Takinoue reservoir by two short tests (METI, NEDO, and JCCS, 2020). Thus, we only focus on the injection in the Moebetsu formation in this study.

Two-Dimensional Radial Flowing Model

As shown in **Figure 2**, the Moebetsu sandstone aquifer in the CCS site is quite stable and relatively flat over a few tens of kilometers. Thus, it is valuable to make a rough estimate of some key parameters using simple models for which theoretical solutions are available. To this end, a two-dimensional (2D) radial flowing model of an infinite and isotropic horizontal layer was tested. Under the assumption that Darcy's law holds, the theoretical solution of the pore pressure change is given as (Barker, 1988):

$$\Delta P(t,r) = Q\frac{\eta}{4\pi kH}\Gamma\left(0,\frac{r^2}{4Dt}\right) \tag{1}$$

$$D = \frac{k}{\eta S_a}, S_a = \phi\left(\beta_{fl}+\beta_{pv}\right) \tag{2}$$

where Γ represents the Gamma function, t (s) is the time since the start of injection, r (m) is the distance from the injection well, Q (m^3/s) is the pumping/injection rate, H (m) and k (m^2) are the thickness and permeability of the layer, D (m^2/s) is the hydraulic diffusivity, η (Pa·s) is the dynamic viscosity of water, ϕ is the porosity, S_a (Pa^{-1}) is the unconstrained specific storage coefficient, and β_{fl} (Pa^{-1}) and β_{pv} (Pa^{-1}) are the compressibility of the fluid and pores, respectively. This kind of model has been successfully applied to represent fluid pressure and strain observed during pumping tests in soft sedimentary formations (Lei et al., 2019).

The thickness of the Moebetsu formation surrounding the injection well is greater than 100 m, and the permeability and porosity are 50 mD and 0.15, respectively (Kano et al., 2014). We

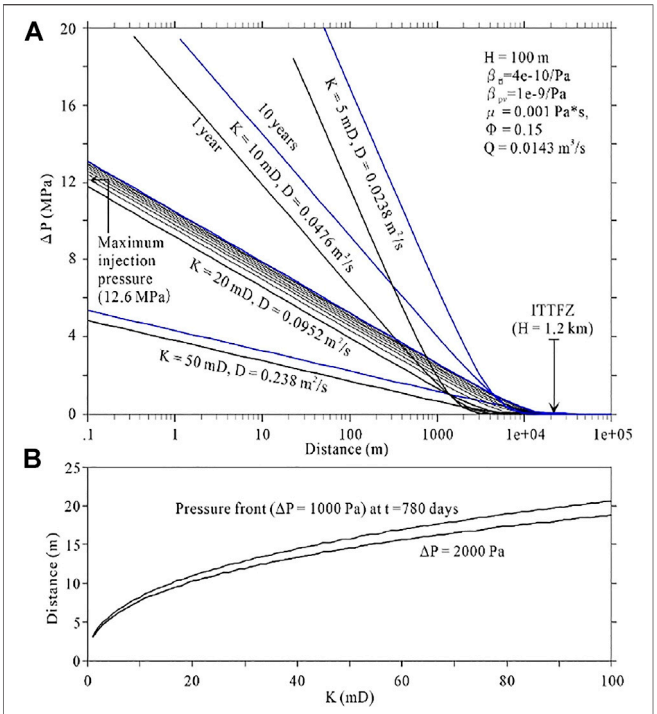

FIGURE 3 | (A) Increase in fluid pressure as a function of distance from the injection well as estimated from two-dimensional radial flowing model. **(B)** Pressure fronts after 780 days of continuous water injection.

assume that H = 100 m, ϕ = 0.15, and k from 1 to 100 mD. In order to perform an overestimation, the injection rate of water is assumed to be $Q = 0.0143\ m^3/s$, approx. 270,000 tons/year, which is greater than the actual mean injection rate of CO_2 (less than 100,000 tons/year). For the case of K = 10 mD, the predicated pressure buildup surrounding the injection well falls in the range from 22 to 25 MPa after one to 10 years of injection, which is greater than the actual maximum injection pressure (12.6 MPa). Even so, the fluid pressure front (pressure increased by 0.01 MPa) is far from the ITTFZ, even at the end point of the 10-years injection (**Figure 3A**). As shown in **Figure 3B**, the pressure front increases with increasing K. Even for the worst case of K = 100 mD, the front did not reach the fault at 780 days after injection started.

Three-Dimensional Thermal-Hydraulic-Mechanical-Coupled Simulation

The coupled THM simulation was used to predict injection-induced changes in rock properties, formation deformation, stress redistribution, and fracture/fault stability. In the present study, Tough2 and Flac3D were selected for the coupled THM simulation. Tough2 is a multiphase reservoir simulation program developed by the U.S. Lawrence Berkeley National Laboratory (LBNL). Flac3D is commercially available software for stress analysis (Itasca, 2000). As a promising combination, the "Tough-Flac3D″ approach with couplers and post-processing tools has proven useful in the analysis of deformation accompanied with fluid flow within reservoirs of hard and soft rocks (Itasca, 2000; Todesco et al., 2004; Rutqvist et al., 2008; Rutqvist et al., 2015; Sorai et al., 2015; Lei et al., 2017).

In the coupled simulation, permeability is revised within every time step by built-in functions. Following previous works, permeability has been expressed as a function of volumetric strain (ε_v) (Chin et al., 2000; Cappa and Rutqvist, 2011) as.

$$k = k_0\left(\frac{\phi}{\phi_i}\right)^n, \phi = 1 - (1 - \phi_i)e^{-\varepsilon_v} \quad (3)$$

Where ϕ and k are porosity and permeability, respectively, with ϕ_i and k_i being the initial values. A n of ~20 results in a 2-order-of-magnitude permeability increase for a fully reactivated fault, as estimated by *in situ* testing (Ohtake, 1974) and laboratory experiments (Alam et al., 2014).

A numerical model covering an area of 80 km × 80 km centered at the Tomakomai CCS injection site was constructed. The ITTFZ is taken as the thin fault zone. Since the upper limitation of temperature of Tough2 is 300°C, we only focus on the uppermost 6 km (**Figure 4**). The model is divided into grids by steps so that the volumes of the fault and injection well are split into small parts while the surrounding matrix becomes coarser as the distance from the fault increases. The total number of grids and elements are 18,954 and 16,796, respectively. The hydraulic and mechanic properties for all nine formations and the fault zone are listed in **Table 1**. The hydraulic properties are similar to that used in previous studies (e.g., Kano et al., 2014). The upscaled mechanical properties are based on laboratory tests on core samples from the site at 10 MPa confining pressure. The most sensitive parameters are the permeability of porosity of the Moebetsu formation, which were firstly determined based on the permeability profile estimated from injection tests using salt water and logging data (METI, NEDO, and JCCS, 2020) and then optimized by tuning simulation. Aided by the 2D radial flow analysis results, the determination of the optimal parameters required only a few tuning steps. At the same time, we also performed calculations for different permeability (10, 20, 50, 100 mD) and porosity (0.1, 0.15) to examine the influence of the uncertainty of these sensitive parameters on the results. Due to the lack of monitoring data on rock mechanical responses, in-depth studies on the uncertainty of mechanical parameters cannot be carried out. The only water injection pressure data can be well fitted by modifying the reservoir hydraulic parameters (METI, NEDO, and JCCS, 2020).

First, simulation was carried out without any injection in order to obtain a hydraulic and thermal steady state. The top layer (air) has a constant pressure (0.1 MPa) and temperature (10°C), and the temperature gradient is assumed to be 4°C/100 m. Roller boundary conditions were imposed on the four sides and bottom of the model. The fluid pressure at the four sides was assumed to be hydrostatic and was kept constant during injection simulation. Both the flow rate and heat flux were fixed at the lower boundary. The in-site stress values are installed in all zones, and also applied as loads acting on the far-field boundaries. The vertical stress σ_V

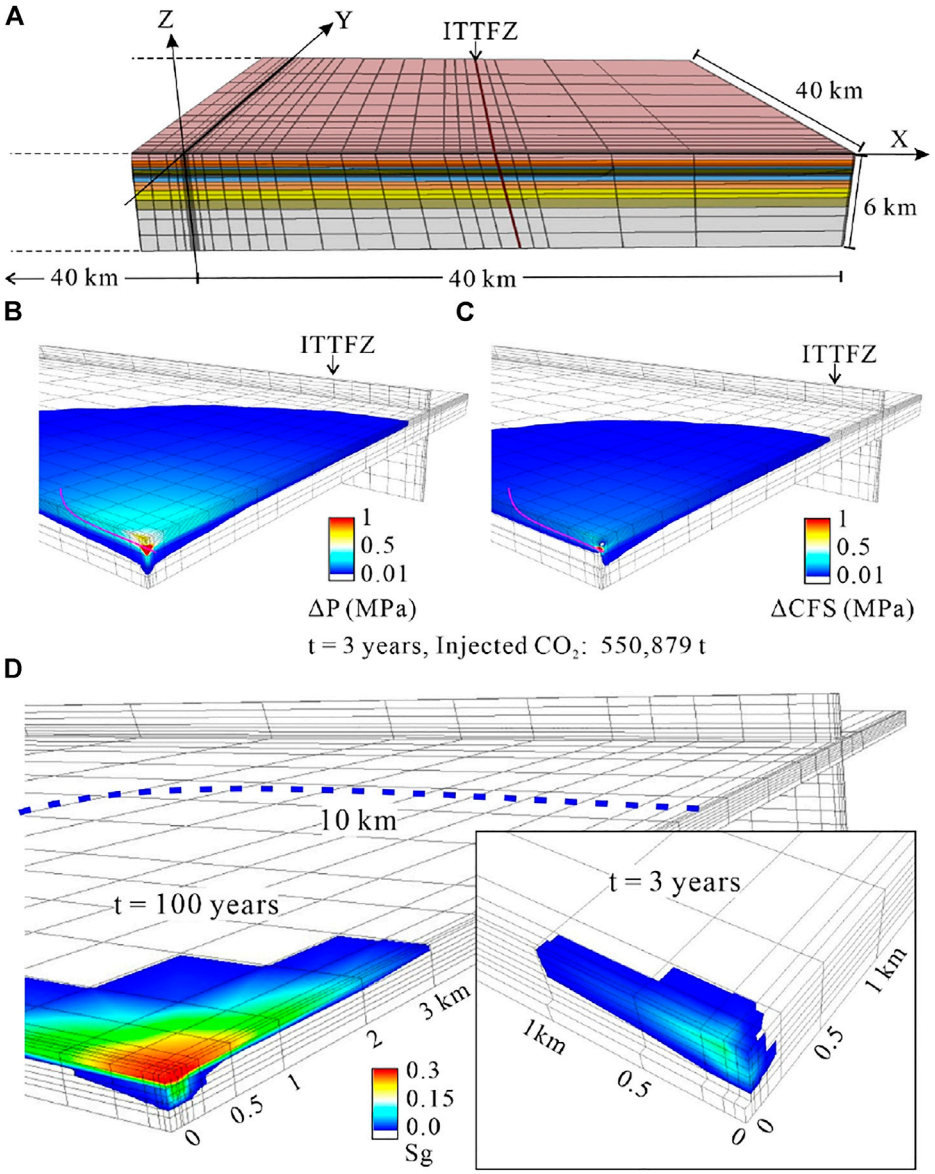

FIGURE 4 | Three-dimensional numerical model **(A)**, pressure/CFS increase after injection for three years **(B,C)**, and distribution of CO_2 saturation after injection for three and 100 years **(D)**. Permeability of 50 mD and porosity of 0.15 were assumed for the injection layer.

TABLE 1 | Mechanical properties.

Property\Formation #	**1**	**2**	**3**	**4**	**5**	**6**	**7**	**8**	**9**	**Fault**
Bulk modulus (GPa)	3.6	5.7	5.7	5.7	5.7	5.7	3.6	3.6	7.8	6.0
Shear modulus (GPa)	3.3	5.2	5.2	5.2	5.2	5.2	3.3	3.3	6.2	4.0
Ini. Perm. (k_O) (mD)	100	10	3.5E-5	10, **20**,50,100	3.5E-5	.1	3.5E-5	3.5E-5	.002	1
Perm. (k) (m^2)					**Equation 3** , n = 20					
Porosity	.25	.15	.05	.1, **0.15**	.05	.15	.01	.01	.02	0.05

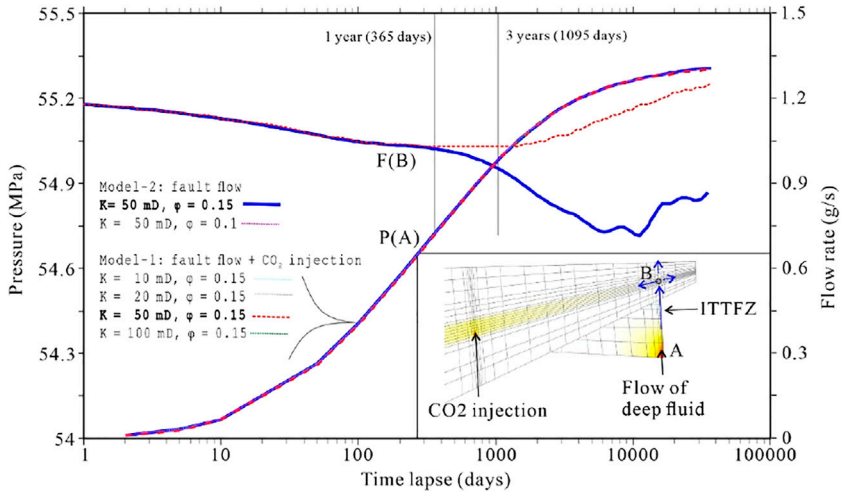

FIGURE 5 | Pressure and flow rate at key points. A: Injection point within the fault at a depth of 6 km. B: Intersection of the fault and the Moebetsu injection layer. The results of different permeability and porosity for the Moebetsu formation consistently show that CO_2 injection has no effect on fluid pressure at the deep part of the fault event after 100 consecutive years of injection.

was calculated from assumed density values. Because the main rock of the model is soft rock, the maximum and minimum horizontal stress values were assumed as $\sigma_H = 1.3\ \sigma_V$, and $\sigma_h = 1.2\ \sigma_V$, respectively. Since the main purpose of the present study is to assess the impact of water injection activities on faults, the background tectonic stress itself is not important. During the coupled simulation, the permeability increases with increasing volumetric strain. The peak well head pressure during injection is 12.6 MPa (METI, NEDO, and JCCS, 2020) and decreases rapidly with increasing distance from the injection zone. Thus, we only consider the elastic behaviors.

In addition to the injection of CO_2 in the Moebetsu formation, a water source was added at the bottom of the fault to simulate natural flow along the ITTFZ. First, fluid flow along the fault zone was carried out at an injection rate of 10,000 tons/year for 1,000 years to reach a relatively stable state of fluid flow and heat flux. The CO_2 injection was then started at an injection rate of ~183,600 tons/year for 100 years. This is the base model (Model-1). For comparison, a simulation was also carried out without CO_2 (Model-2) to verify whether CO_2 injection alters deep fluid flow along the fault.

The simulation results show that after three years of injection, by which point more than 550,000 tons of supercritical CO_2 were injected into to the Moebetsu formation, the injected CO_2 is distributed within a few hundred meters around the injection well (**Figure 4D**), which is slightly larger than that revealed by the 3D seismic exploration implemented in 2019 (METI, NEDO, and JCCS, 2020). This result is expected since larger injection rate was assumed in the simulation. The pressure buildup is still beyond the fault for both models (**Figures 4B,C**). As compared with Model-1, the pressure front of Model-2 is farther from the fault zone due to the background flow from deep in the fault. The change of the Coulomb Failure Stress (CFS) acting on the fault planes, which have the same strike, dip, and rake with the seismogenic fault of the 2018 Hokkaido Eastern Iburi earthquake, is governed by fluid pressure. Although there is a redistribution of flow velocity at the intersection of the fault and the reservoir, the resulted fluid pressure (P(A) in **Figure 5**) by Model-1 of different permeability and porosity for the Moebetsu formation is exactly the same as Model-1, consistently show that CO_2 injection has no effect on fluid pressure at the deep part of the fault event after 100 consecutive years of injection (**Figure 5**).

DISCUSSION AND CONCLUSION

The results of the present study show that, even under extreme conditions, when CO_2 is injected at a rate of ~180,000 tons/year (actually less than 100,000 tons/year) for 10 consecutive years (actually less than three years), the 0.01-MPa front of the fluid pressure increment is far from the hypocenter of the Iburi Earthquake. After three years injection, the injected CO_2 is distributed within a few hundred meters around the injection well, which is slightly larger than that revealed by the 3D seismic exploration implemented in 2019 (METI, NEDO, and JCCS, 2020) after injection 207,208.9t CO_2. If the injected CO_2, including dissolved CO_2, could rapidly migrate beyond 10 km as claimed in Sano et al. (2020), 3D seismic exploration would either see nothing or show anomalies on a large area, but this is not the case. Detailed discussion on geochemical issues is interesting but beyond the scope of this study. In the absence of wide-area groundwater flow, the distribution of gaseous and dissolved CO_2 is also limited within a small zone of only a few kilometers at most. Even if there is a wide area of groundwater flow, the distribution range of CO_2 has expanded, compared with

the stable fluid pressure before water injection, the range where the fluid pressure has increased still does not change significantly. The changes in fluid pressure and pore-elastic effects at the intersection of the ITTFZ and the Moebetsu layer 20 km away are much smaller than the changes caused by daily tidal action, not to mention the 37-km depth of the fault, where the 2018 Hokkaido Eastern Iburi Earthquake initiated. For reference, tidal stress amplitude thresholds required to trigger earthquakes, for static and dynamic triggering, have been estimated to range from 0.01 to 0.03 MPa (pore pressure: 0.015–0.05 MPa) (King et al., 1994; Cochran et al., 2004). Therefore, the implementation of the Tomakomai CO_2 geological storage demonstration project is unlikely to be the triggering factor of the earthquake.

In our simulation, the dissolution of injected CO_2 into the groundwater of the aquifer was counted but other chemical processes, such as mineralization were ignored. In general, minerals, such as silica in the deep source hydrothermal fluid, precipitated to the pressure drop caused by earthquake to heal the fault reduce the permeability of the fault (Saishu et al., 2017). However, no convincing mechanism exists that would allow fluid channels to be healed within a short period of time and block the natural fluid flow along the fault during CO_2 injection, which increases the fluid pressure.

As mentioned above, the geological sequestration of CO_2 is important in mitigating the global warming trend. Demonstration projects of various scales are for the development of technology and the verification of the safety and effectiveness of the corresponding technology. With regard to risk-related injection-induced fault reactivation and earthquakes, both oversized and undersized assessments must be avoided.

The model proposed by Sano et al., (2020) is worth investigating for commercial applications of large-scale and long-term CO_2 storage. Thermally, hydraulically, mechanically, and chemically coupled geomechanics modeling will be a key technology.

DATA AVAILABILITY STATEMENT

The original contributions presented in the study are included in the article/Supplementary Material, further inquiries can be directed to the corresponding author.

AUTHOR CONTRIBUTIONS

The author confirms being the sole contributor of this work and has approved it for publication.

ACKNOWLEDGMENTS

The author would like to thank two reviewers for their helpful comments during the review process.

REFERENCES

Alam, A. K. M. B., Niioka, M., Fujii, Y., Fukuda, D., and Kodama, J.-i. (2014). Effects of Confining Pressure on the Permeability of Three Rock Types under Compression. *Int. J. Rock Mech. Min. Sci.* 65, 49–61. doi:10.1016/j.ijrmms.2013.11.006

Atkinson, G. M., Eaton, D. W., and Igonin, N. (2020). Developments in Understanding Seismicity Triggered by Hydraulic Fracturing. *Nat. Rev. Earth Environ.* 1, 264–277. doi:10.1038/s43017-020-0049-7

Barker, J. A. (1988). A Generalized Radial Flow Model for Hydraulic Tests in Fractured Rock. *Water Resour. Res.* 24 (10), 1796–1804. doi:10.1029/wr024i010p01796

Cappa, F., and Rutqvist, J. (2011). Modeling of Coupled Deformation and Permeability Evolution during Fault Reactivation Induced by Deep Underground Injection of CO2. *Int. J. Greenh. Gas Control* 5 (2), 336–346. doi:10.1016/j.ijggc.2010.08.005

Chin, L. Y., Raghavan, R., and Thomas, L. K. (2000). Fully Coupled Geomechanics and Fluid-Flow Analysis of Wells with Stress-dependent Permeability. *Spe J.* 5 (01), 32–45. doi:10.2118/58968-pa

Cochran, E. S., Vidale, J. E., and Tanaka, S. (2004). Earth Tides can Trigger Shallow Thrust Fault Earthquakes. *Science* 306, 1164–1166. doi:10.1126/science.1103961

Ellsworth, W. L., Giardini, D., Townend, J., Ge, S., and Shimamoto, T. (2019). Triggering of the Pohang, Korea, Earthquake (Mw 5.5) by Enhanced Geothermal System Stimulation. *Seismol. Res. Lett.* 90 1844–1858. doi:10.1785/0220190102

Itasca, F. (2000). *Fast Lagrangian Analysis of Continua*. Minneapolis: Itasca Consulting Group Inc.

Japan, G. S. o. (1995). *1/1,000,000 Japanese Geological Map CD-ROM Version* Digital Geological Map G-1.

Kano, Y., Funatsu, T., Nakao, S., Kusunose, K., Ishido, T., Lei, X., et al. (2014). Analysis of Changes in Stress State and Fault Stability Related to Planned CO2 Injection at the Tomakomai Offshore Site. *Energy Procedia* 63, 2870–2878. doi:10.1016/j.egypro.2014.11.310

King, G. C., Stein, R. S., and Lin, J. (1994). Static Stress Changes and the Triggering of Earthquakes. *Bull. Seismol. Soc. Am.* 84, 935–953. doi:10.1186/s40623-019-1041-7

Kobayashi, H., Koketsu, K., and Miyake, H. (2019). Rupture Process of the 2018 Hokkaido Eastern Iburi Earthquake Derived from Strong Motion and Geodetic Data. *Earth, Planets Space* 71 (1), 1–9. doi:10.1186/s40623-019-1041-7

Lei, X., Huang, D., Su, J., Jiang, G., Wang, X., Wang, H., et al. (2017). Fault Reactivation and Earthquakes with Magnitudes of up to Mw4.7 Induced by Shale-Gas Hydraulic Fracturing in Sichuan Basin, China. *Sci. Rep.* 7 (1), 79717971. doi:10.1038/s41598-017-08557-y

Lei, X., Su, J., and Wang, Z. (2020). Growing Seismicity in the Sichuan Basin and its Association with Industrial Activities. *Sci. China Earth Sci.* 63 (11), 1633–1660. doi:10.1007/s11430-020-9646-x

Lei, X., Xue, Z., and Hashimoto, T. (2019). Fiber Optic Sensing for Geomechanical Monitoring: (2)- Distributed Strain Measurements at a Pumping Test and Geomechanical Modeling of Deformation of Reservoir Rocks. *Appl. Sci.* 9 (3), 417. doi:10.3390/app9030417

Matsubara, M., Sato, H., Uehira, K., Mochizuki, M., and Kanazawa, T. (2017). Three-Dimensional Seismic Velocity Structure beneath Japanese Islands and Surroundings Based on NIED Seismic Networks Using Both Inland and Offshore Events. *J. Disaster Res.* 12 (5), 844–857. doi:10.20965/jdr.2017.p0844

METI, NEDO, and JCCS (2020). Summary of Time Report of the Tomakomai CCS Large-Scale Demonstration Test 300,000 Tons Injection. Available at: https://www.meti.go.jp/press/2020/05/20200515002/20200515002.html.

Ohtake, M. (1974). Seismic Activity Induced by Water Injection at Matsushiro, Japan. *J. Phys. Earth.* 22, 163–176. doi:10.20965/jdr.2017.p0844

Rutqvist, J., Birkholzer, J. T., and Tsang, C.-F. (2008). Coupled Reservoir-Geomechanical Analysis of the Potential for Tensile and Shear Failure Associated with CO2 Injection in Multilayered Reservoir-Caprock Systems. *Int. J. Rock Mech. Min. Sci.* 45 (2), 132–143. doi:10.1016/j.ijrmms.2007.04.006

Rutqvist, J., Rinaldi, A. P., Cappa, F., and Moridis, G. J. (2015). Modeling of Fault Activation and Seismicity by Injection Directly into a Fault Zone Associated with Hydraulic Fracturing of Shale-Gas Reservoirs. *J. Petroleum Sci. Eng.* 127, 377–386. doi:10.1016/j.petrol.2015.01.019

Saishu, H., Okamoto, A., and Otsubo, M. (2017). Silica Precipitation Potentially Controls Earthquake Recurrence in Seismogenic Zones. *Sci. Rep.* 7 (1), 13337. doi:10.1038/s41598-017-13597-5

Sano, Y., Kagoshima, T., Takahata, N., Shirai, K., Park, J.-O., Snyder, G. T., et al. (2020). Groundwater Anomaly Related to CCS-CO2 Injection and the 2018 Hokkaido Eastern Iburi Earthquake in Japan. *Front. Earth Sci.* 8. doi:10.3389/feart.2020.611010

Sorai, M., Lei, X., Nishi, Y., Ishido, T., and Nakao, S. (2015). *CO2 Geological Storage*. New York: Springer.

Todesco, M., Rutqvist, J., Chiodini, G., Pruess, K., and Oldenburg, C. M. (2004). Modeling of Recent Volcanic Episodes at Phlegrean Fields (Italy): Geochemical Variations and Ground Deformation. *Geothermics* 33 (4), 531–547. doi:10.1016/j.geothermics.2003.08.014

Conflict of Interest: The author declares that the research was conducted in the absence of any commercial or financial relationships that could be construed as a potential conflict of interest.

Publisher's Note: All claims expressed in this article are solely those of the authors and do not necessarily represent those of their affiliated organizations, or those of the publisher, the editors and the reviewers. Any product that may be evaluated in this article, or claim that may be made by its manufacturer, is not guaranteed or endorsed by the publisher.

frontiers | Frontiers in Earth Science

TECHNOLOGY AND CODE
published: 30 May 2022
doi: 10.3389/feart.2022.888551

Study on the Size and Occurrence Effects of Equivalent Elasticity Modulus of Orthogonal Random Jointed Rock Masses

Xu Naizhong[1], *Liu Changqing*[2]*, *Su Chang*[1] *and Zhou Tian*[1]

[1]Anhui University of Science & Technology, School of Mining Engineering, Huainan, China, [2]Anhui Academy of Emergency Management Science, Hefei, China

Under the engineering background of a + 144-m mining platform on an open pit slope of Xinqiao Mining Corporation, the eigenvalue distribution function of joints was acquired based on the massive statistics of field joints. Next, an orthogonal random joint model was constructed using the Monte Carlo method based on the UDEC software platform. Subsequently, the representative elementary volume (REV) size and occurrence effects of the equivalent elasticity modulus of the orthogonal random jointed rock mass were explored through numerical experiments with lots of discrete elements. The results showed that the equivalent elasticity modulus of the orthogonal random jointed rock mass was of evident size effect, and the relationship between the mean equivalent elasticity modulus E_{eq} and the REV size of the rock mass followed the negative power function distribution. Before the model size reached the REV size, its E_{eq} was greatly discrete. Under different joint angles, both the standard deviation σ_f and coefficient of variation δ of the equivalent elasticity modulus of this model presented discrete distribution. As the model size reached the REV size, the mean equivalent elasticity modulus E_{eq} showed "two-high and one-low" morphological distribution. E_{eq} was small when the main joint angle was $\alpha \in [30^{\circ}, 40^{\circ}]$, but it was large when $\alpha = 0^{\circ}$ or 90°. δ was taken as 10%, so the REV size of the corresponding E_{eq} was 10 m × 20 m. When the model size reaches the REV size, the occurrence effect of its equivalent elasticity modulus was no longer significant.

Keywords: random jointed rock mass, numerical simulation, rock mass parameter, size effect, occurrence effect, equivalent elastic modulus

OPEN ACCESS

Edited by:
Wenzhuo Cao,
Imperial College London,
United Kingdom

Reviewed by:
Fuqiong Huang,
China Earthquake Networks Center,
China
Fei Wang,
Colorado School of Mines,
United States

***Correspondence:**
Liu Changqing
chqliu8118@126.com

Specialty section:
This article was submitted to Structural Geology and Tectonics, a section of the journal Frontiers in Earth Science

Received: *03 March 2022*
Accepted: *07 April 2022*
Published: *30 May 2022*

Citation:
Naizhong X, Changqing L, Chang S and Tian Z (2022) Study on the Size and Occurrence Effects of Equivalent Elasticity Modulus of Orthogonal Random Jointed Rock Masses. Front. Earth Sci. 10:888551. doi: 10.3389/feart.2022.888551

INTRODUCTION

Studies and engineering practices have shown that rock mass is a kind of complex geologic body (Sun, 1988), including slope engineering, tunneling, and deep underground chamber engineering, in which the reliability and accuracy of the mechanical parameter values of rock masses are specifically crucial for the engineering design, construction, and operation. The mechanical properties of rock masses are intricate due to the massive structural planes in them (Sun and Li, 1965; Gu, 1979). Usually constructed in jointed rock masses, rock mass engineering works are affected by the structural planes inside the rock masses of different sizes, so the mechanical parameters of engineering rock masses will unavoidably be characterized by heterogeneity or spatial variability. Representative elementary volume (REV) is the core content in the studies regarding the size effect of

mechanical properties of rock masses (Bear, 1972; Bear, 1979), that is, the values of mechanical parameters should be determined in such studies. In practical geotechnical design, the mechanical parameters of REV, but not the mechanical parameters of intact rock specimens, should be used. Hence, the key to studying the real mechanical parameters of rock masses and the reliability design of rock mass engineering lies in figuring out the size effect of mechanical parameters of rock masses and determining the REV of rock masses. At present, the REV of rock masses is determined through the experimental method, analytical method, and numerical experimental method.

As for the experimental method, Wang et al. (2002) numerically estimated the REV of the coefficient of transmissivity based on the drilling data. Aubertin et al. (2000) studied the size effect of rock strength based on the MSDPu strength criterion and put forward the change relation of rock strength with the size. According to the laboratory test results, Zhang and Qiao. (2006a), Wang and Zuo. (1998) and Wang and Li. (2008) gave the expressions to the size effects of the corresponding mechanical parameters of rock masses. Fan et al. (2018) experimentally studied the crack propagation and evolution in shales with a material testing machine considering the bedding angle, loading rate, and specimen size. Du et al. (2021) developed a combined testing system for the size effect of the shear strength of structural planes in rock masses, thus providing a basic experimental support platform for studying key scientific problems such as the size effect of the shear strength of structural planes.

When it comes to the analytical method, Zhou and Xiong. (1996a) explored the relationships between the elastic parameters of random jointed rock masses with their volumetric change and permeability tensor, according to the principle of energy superposition, and then determined the REV of mechanical parameters of jointed rock masses. Zhang and Xu. (2008) simulated the 3D fracture network of jointed rock masses using a planar quadrangle and used this fracture network to study the indexes determining the REV size of rock masses. Chen S. J. et al. (2019) applied random numbers to the projective covering method, in an effort to improve triangulation when calculating the fractal dimensions of structural planes with the projective covering method.

The analytical methods adopted in the numerical experiments mainly include the finite element method, finite difference method, natural element method, and discrete element method. Kulatilake. (1985) and Pouya and Ghoreychi. (2001) simulated the structural planes in rock masses using Goodman joint elements in the finite element model and studied the REV of mechanical parameters of rock masses. Zhang et al. (2010), Zhou et al. (2004), Yan et al. (2009), and Zhu et al. (2009) explored the size effect of mechanical parameters of rock masses *via* FLAC3D finite difference software. Bhasin and Hoeg. (1998) and Min and Jing. (2003) studied the size effect of jointed rock masses through the UDEC software model. Lu et al. (2020) and Li et al. (2019) generated the plane network diagram of jointed rock masses based on fractal theory and the Monte Carlo method. Taking the center of the rock mass network diagram as the base point, the jointed rock mass simulation specimen was selected, and the numerical experiment of the compressive strength of jointed rock masses was performed *via* discrete element software UDEC. Ning et al. (2008) and Ni et al. (2015) introduced the Voronoi method into 3DEC discrete element software to probe the size effect of the deformation parameter of columnar basalt. Esmaileli et al. (2010) and Li et al. (2021) studied the REV size of mechanical parameters of jointed rock masses *via* PFC3D software. Wang et al. (2021) determined the REV of rock masses using the heterogeneity index (HI). Zhu et al. (2019) used FLUENT software to perform a 2D numerical analysis of seepage characteristics at nine differently sized crack intersections. Wang et al. (2018) established a rough discrete fracture network (RDFN) model and studied the mechanical properties of this RDFN model under direct shear conditions based on grain flow PFC2D. Chen Q. F. et al. (2019) built a multiscale three-dimensional fracture network model of rock mass with 35 combinations of ductility and spacing of different structural planes based on general block software. Using the proposed block degree correction theory, the geometric characteristic size rev of fractured rock mass is determined. Through the docking of correlation parameters of the general block-3dec model, a multiscale discrete fracture network model of the rock mass is constructed, the calculation results of geometric rev and mechanical Rev are compared, and the correlation between the geometric size effect and mechanical size effect of the rock mass is discussed.

To summarize, domestic (Chinese) and foreign scholars have investigated the size effect of mechanical parameters of rocks or rock masses through theoretical analysis, experimental study, and numerical simulation. Given the complexity of jointed rock masses, the randomness of joint distribution, experimental limitations, and the size effect of mechanical parameters of jointed rock masses remain to be further explored. In particular, the discreteness of small-size experimental results is considerably great, the number of numerical experimental times is partially small, and the statistical results are not reliable enough, all of which, to some extent, results in inconsistent research results and conclusions. The precondition for numerically studying the size effect of mechanical parameters of rock masses is to reflect the joint distribution laws in rock masses as truly as possible. Studies have shown that the geometric parameters such as joint length, joint distribution, and joint spacing are self-similarities, which can be calculated through a small-scale fracture network so as to derive the development characteristics of a large-scale fracture network. Such self-similarity is actually a fractal character. Given this, based on the statistical data of measured joints of rock masses on an engineering slope, a random fracture network model was established in this study according to the Monte Carlo principle. Next, the size effect of the equivalent elasticity modulus of orthogonal random jointed rock masses was analyzed *via* discrete element software UDEC. Subsequently, enough numerical experiments were conducted according to different experimental sizes so that the statistical results (such as the mean value and standard deviation) of sample parameters could be accurate and reliable, expecting to provide a theoretical support for the construction and safety operation of slope rock mass engineering.

FIGURE 1 | Open-pit slope of Xinqiao Mining Corporation.

TABLE 1 | Geometric parameters of joint fractures.

Joint set	Joint density /strip·m^{-2}	Joint dip /°		Mean value of the joint trace length /m
		Mean value	Variance	
1	0.3	63.8	3.0	12.8
2	1.0	150.3	5.0	2.0

TABLE 2 | Mechanical parameters.

Rock parameter				Structural plane parameter			
E/GPa	μ	φ/°	c/MPa	J_{kn}/GPa·m^{-1}	J_{ks}/GPa·m^{-1}	J_{coh}/MPa	J_{fric}/°
43.7	0.29	42.0	4.0	20.0	20.0	1.0	30.0

INVESTIGATION AND STATISTICS OF JOINTS IN JOINTED ROCK MASSES

Engineering Background

Through decades of open-pit mining, a large-scale multi-metal sulfide ore deposit of the Xinqiao Mining Corporation is now about 148 m in the minimum elevation of the open pit and about + 320 m in the elevation of the slope crest, along with a bench slope angle of 50°, bench width of 12 m, and bench height of 25 m. With a + 144-m platform taken, for example, a group of orthogonal joints were developed on the slope through the site investigation, and it was obtained that the joint angles followed a normal distribution (**Figure 1**). The geometric parameters of the joints are listed in **Table 1** he rock mass structure of the site slope is shown in **Figures 1**. The mechanical parameters of rocks and joint planes measured after field drilling are as seen in **Table 2**.

Generation of Orthogonal Random Joints

The joint fracture generating program was compiled through the FISH language in UDEC software. The uniformly distributed random numbers of central points of joints within the interval of [0,1] were generated using the Monte Carlo method, and then, random joint fractures were formed. The generated fracture network model of the slope on the + 144-m mining platform is shown in **Figure 2**.

NUMERICAL EXPERIMENTAL SCHEME OF THE SIZE EFFECT OF ORTHOGONAL RANDOM JOINTED ROCK MASSES

Reliability Analysis of Rock Parameters Solved *via* UDEC Software

The shear strength parameters—cohesion c and internal frictional angle φ—were acquired through the uniaxial and triaxial compression tests of rocks based on the Mohr–Coulomb strength criterion. In comparison, the reliability of the parameters obtained through the UDEC-aided uniaxial and triaxial numerical compression tests of rocks was verified. With an intact rock taken as the study object, the compressive strength values under different confining pressures were solved through triaxial numerical compression tests; the c and φ values were acquired using the Mohr–Coulomb strength theory and compared with the rock strength parameters obtained through laboratory tests, and the reliability of the solved equivalent strength parameters was verified.

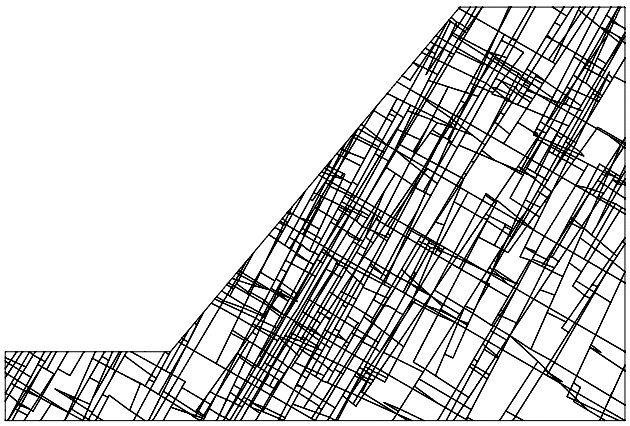

FIGURE 2 | Random fracture network model of the slope on the + 144-m platform.

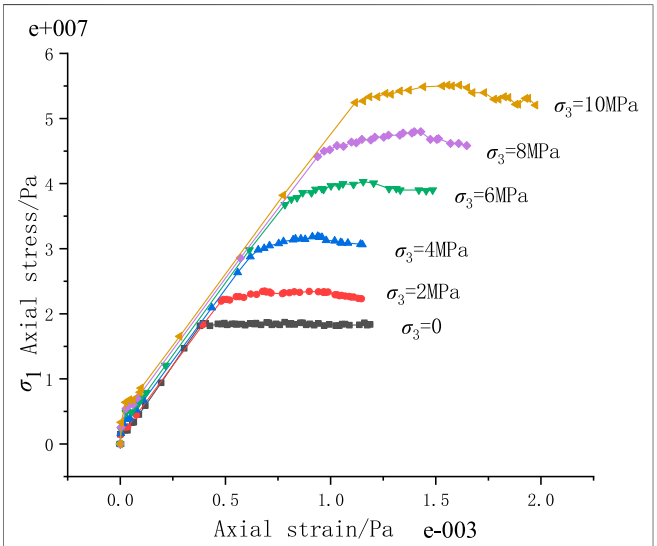

FIGURE 3 | Axial stress–strain curves of the intact rock under different confining pressures.

The dimensions of the numerical simulation test model were 1 m (width) * 2 m (height). The confining pressure was taken as 0–10 MPa at six levels with the interval of 2 MPa. The Mohr–Coulomb model was chosen as the constitutive model, and the rock parameters are listed in **Table 2**. The rock stress–strain curves under different confining pressures acquired through the numerical experiments are shown in **Figure 3**.

The numerical triaxial compression test results under different confining pressures were drawn within the σ_1-σ_3 plane. According to the Mohr–Coulomb strength failure criterion, σ_1-σ_3 followed a linear relation, so the σ_1-σ_3 data points were fitted using straight lines, as shown in **Figure 4**.

The straight slope a and intercept b showed the following relations with the shear strength parameters c and φ:

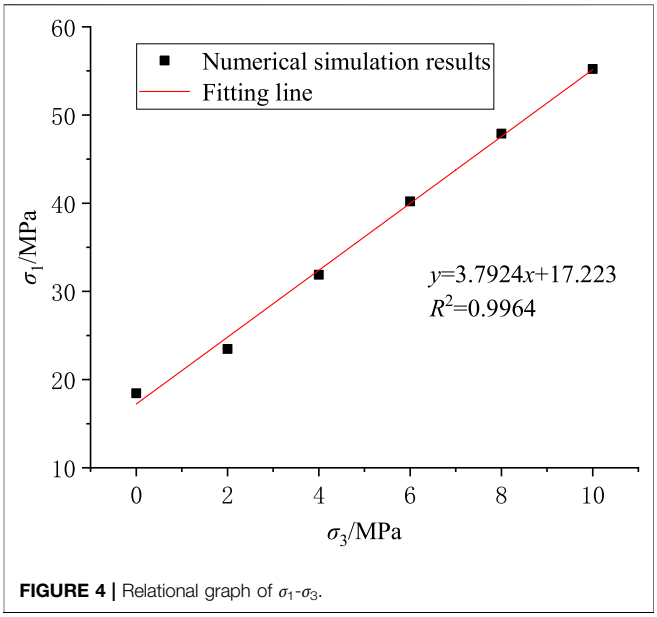

FIGURE 4 | Relational graph of σ_1-σ_3.

$$a = \frac{2c\cos\varphi}{1-\sin\varphi}, \tag{1}$$

$$b = \frac{1+\sin\varphi}{1-\sin\varphi}. \tag{2}$$

As solved through **Eqs. 1**,**2**, the internal frictional angle and cohesion of the intact rock were φ = 35.64 and c = 4.42, respectively, which were relatively approximate to the rock strength parameters acquired through the laboratory tests. Hence, it is reliable to perform the analog computation of equivalent rock strength parameters *via* UDEC software.

Numerical Experimental Scheme for the Representative Elementary Volume Size of Mechanical Parameters of Random Jointed Rock Masses

In order to determine the mechanical parameters representing the real mechanical properties of jointed rock masses, the rock structure model should accord with the physical situation as far as possible. When the structural plane network is simulated using the Monte Carlo method and since the random number generated each time is different under the same structural plane probability distribution model, the geometrical characteristics of structural planes generated each time, such as spatial position, trace length, and orientation, will be slightly different and so will the rock structure model, which is the error brought by the feature of this method. For the same structural plane probability distribution model, the mechanical parameters of different rock mass structure models generated by the Monte Carlo method may differ in the REV size. Min and Jing. (2003) generated 10 300 m × 300 m square rock mass structure models using the discrete fracture network (DFN) program and studied the REV size of equivalent deformation parameters by intercepting square rock specimens with different

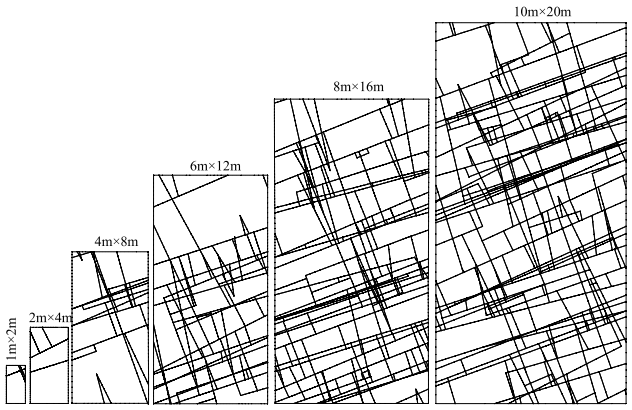

FIGURE 5 | Orthogonal random joint models with different sizes.

side lengths from the center of each model. Xiang (2005) compiled a random sampling program following probability distribution for the sake of Monte Carlo simulation, generated 8 10 m × 10 m fracture networks, and explored the REV size of rock strength parameters by intercepting squares with different side lengths from the center of each network. As deemed by Kulatilake (1985), such random errors can be eliminated only by experimenting on over ten rock specimens, so the rock mass of each size should be studied using multiple models when determining its mechanical parameters.

Therefore, a Monte Carlo method-based orthogonal random joint generation program was compiled using the FISH language of UDEC software to determine the REV size for the mechanical parameters of orthogonal random jointed rock masses. The model dimensions (width* height) were taken as 1 m × 2 m、 2 m × 4 m, 4 m × 8 m, 6 m × 12 m, 8 m × 16 m, and 10 m × 20 m. To eliminate the random errors of rock joints simulated through the Monte Carlo method, a total of 11 rock joint models were generated for each model size. Given the anisotropic characteristics of mechanical parameters of rock masses, the main joint angle changed within [0°, 90°] at an interval of 10°. Taking the main joint angle of 20°, for example, the generated orthogonal random joint models with different sizes are presented in **Figure 5**.

REPRESENTATIVE ELEMENTARY VOLUME SIZE EFFECT ANALYSIS OF THE EQUIVALENT ELASTICITY MODULUS E_{EQ} OF ORTHOGONAL RANDOM JOINTED ROCK MASSES

Multiple rock joint models with the same size could reflect the random fluctuations of mechanical properties before the rock masses reached the REV size of their mechanical parameters, indicating that the size effect of their mechanical properties was not one sidedly understood as follows: the mechanical properties of rock masses declined with the increase in the rock size. Instead, the mechanical properties fluctuated now and then. Only when the rock size reached the REV size would the fluctuation range of their mechanical parameters be greatly reduced and tend to be constant. Therefore, the rock size-dependent change line of the coefficient of variation (CV) of each parameter could be obtained by calculating the CV of each equivalent mechanical parameter of multiple rock structure models with the same size. In addition, it was feasible to determine the REV size of each mechanical parameter according to the acceptance level of CV.

Without loss of generality, the elasticity moduli solved through the numerical experiments on different models under the same confining pressure were taken to analyze the rock size effect of orthogonal random joint models. E_{eq}, σ_f, and δ of orthogonal random joint masses acquired through the numerical experiments under σ_3 = 4 MPa are listed in **Table 3**. On this basis, the relationship between the equivalent elasticity modulus of orthogonal random jointed rock masses and the model size could be analyzed.

Relationship Between the Mean Equivalent Elasticity Modulus E_{eq} of Orthogonal Random Jointed Rock Masses and the Model Size

The relational graph between E_{eq} of orthogonal random joint models and the model size was drawn, as shown in **Figure 6**.

1) Regardless of the occurrence of the main model joint, E_{eq} of the random joint model was gradually reduced with the increase in the model size.
2) Under a small model size, the reduced amplitude of E_{eq} was large. As the model size was enlarged, the reduced amplitude of E_{eq} was gradually reduced. When the model size exceeded 8 m × 16 m, E_{eq} approached a stable value.

Relationship Between the Mean Equivalent Elasticity Modulus E_{eq} of Orthogonal Random Jointed Rock Masses and Main Joint Angle α

The relational graph between E_{eq} of orthogonal random joint models and the main joint angle was drawn, as shown in **Figure 7**.

1) Under different main joint angles α and a small model size, E_{eq} was discrete, with inapparent relational characteristic with the main joint angle α.
2) After the model size was enlarged to 4 m × 8 m, E_{eq} presented a "two-high and one-low" morphological distribution with the change in the main joint angle α. E_{eq} was small under $\alpha \in [30°, 40°]$ and large when α = 0° or 90°. Moreover, it reached the maximum value under α= 90°.

Relationship Between the Standard Deviation σ_f of the Equivalent Elasticity Modulus and Main Joint Angle α

For two or more groups of data with the same mean value, the dispersion degree of each group of data is different. For the mean

TABLE 3 | Mean elasticity moduli under different model sizes and joint angles (σ_3 = 4 MPa).

Dip angle of the main joint	Model size: width × height								
	1 m × 2 m			2 m × 4 m			4 m × 8 m		
	E_{eq}	σ_f	δ	E_{eq}	σ_f	δ	E_{eq}	σ_f	Δ
0°	21.94	2.9016	0.1322	24.17	3.4147	0.1413	15.63	1.5959	0.1021
10°	22.82	5.6643	0.2482	23.96	5.0319	0.2100	16.15	2.1142	0.1310
20°	23.20	7.9011	0.3406	23.68	5.4089	0.2284	15.56	1.5318	0.0984
30°	23.35	7.0954	0.3039	20.34	4.1526	0.2042	14.45	1.9226	0.1331
40°	20.59	5.0165	0.2437	24.32	8.2700	0.3400	14.39	2.4793	0.1724
50°	20.93	6.5514	0.3130	18.75	3.3627	0.1793	15.85	2.2014	0.1389
60°	23.68	8.3934	0.3544	20.15	8.2430	0.4091	15.38	2.8334	0.1843
70°	21.23	5.2156	0.2457	20.07	6.0051	0.2992	15.98	4.0129	0.2511
80°	24.74	11.7196	0.4738	20.50	7.5295	0.3672	16.28	3.3301	0.2045
90°	22.67	8.0490	0.3551	21.26	7.2158	0.3393	16.98	3.9278	0.2313
Dip angle of the main joint	**Model size: width × height**								
	6 m × 12 m			**8 m × 16 m**			**10 × 20 m**		
	E_{eq}	σ_f	δ	E_{eq}	σ_f	δ	E_{eq}	σ_f	Δ
0°	16.45	1.1952	0.0727	10.67	0.9278	0.0869	9.16	0.7644	0.0835
10°	15.31	2.5405	0.1659	10.51	0.6671	0.0635	9.16	0.6948	0.0759
20°	14.30	1.9752	0.1381	10.07	0.9918	0.0985	9.39	1.0468	0.1115
30°	13.35	2.5477	0.1909	9.80	0.9185	0.0937	9.28	0.8940	0.0963
40°	14.50	3.7325	0.2574	9.67	0.7585	0.0785	9.32	1.0347	0.1110
50°	15.78	2.9207	0.1851	11.12	1.3684	0.1231	9.53	0.9385	0.0985
60°	15.52	3.7370	0.2408	11.82	1.2502	0.1058	10.16	0.8106	0.0798
70°	16.51	2.7138	0.1644	11.86	1.5343	0.1293	12.12	1.2332	0.1018
80°	16.68	2.6062	0.1562	13.43	1.2142	0.0904	12.81	1.7867	0.1395
90°	17.46	3.4983	0.2004	13.69	1.0677	0.0780	13.01	1.0782	0.0829

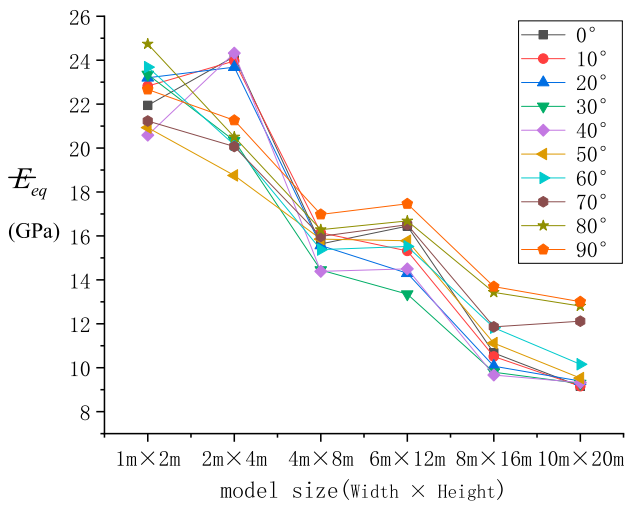

FIGURE 6 | Relationship between the equivalent elasticity modulus and model size.

value of the equivalent elastic modulus E_{eq} of the aforementioned jointed rock mass, the standard deviation can be used to reflect the difference of each group of data under the conditions of different sizes and joint dip angles.

The relational graph between σ_f of orthogonal random joint models and main joint angle α was drawn, as shown in **Figure 8**.

1) Under different main joint angles α and a small model size, σ_f of the equivalent elasticity modulus was discretely distributed without any obvious law. It shows that when the model size is small, the equivalent elastic modulus E_{eq} of each group of the jointed rock mass is greatly dispersed.
2) As the model size was enlarged, σ_f was gradually reduced. It shows that when the model size increases, the elastic modulus of any group of the randomly jointed rock mass can reflect the real value of the jointed rock mass under the strip of this size.
3) When the model size was enlarged to 8 m × 16 m, the standard deviation of the equivalent elastic modulus of different main joint dip models is very small, and the standard deviation is also very small. It shows that when the model size increases to a certain value, the difference in the elastic modulus of the jointed rock mass in the same group is very small. This size can be used as a reference for the selection of the equivalent elastic modulus REV scale of the jointed rock mass model.

Relationship Between the Sample Coefficient of Variation δ and Main Joint Angle α

The sample coefficient of variation (δ) is the ratio of the standard deviation σ_f to E_{eq}, where δ is not restricted by the sample mean or standard deviation. The relational graph between δ of the equivalent elasticity modulus of orthogonal random joint models and the main joint angle α was drawn as shown in **Figure 9**.

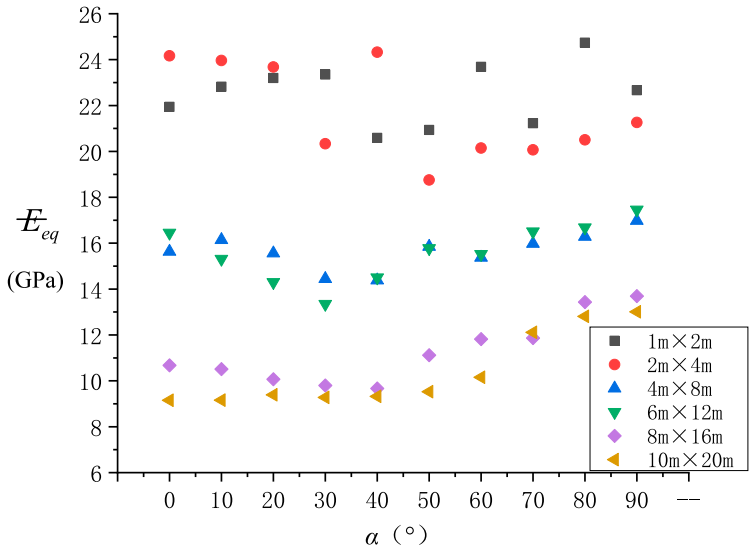

FIGURE 7 | Relationship between the equivalent elasticity modulus and main joint angle α.

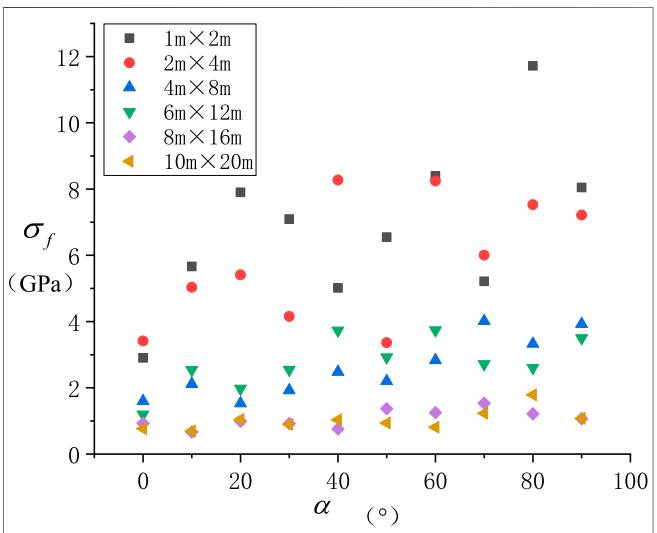

FIGURE 8 | Relationship between the standard deviation σ_f of the equivalent elasticity modulus and main joint angle α; relationship between sample δ and main joint angle α.

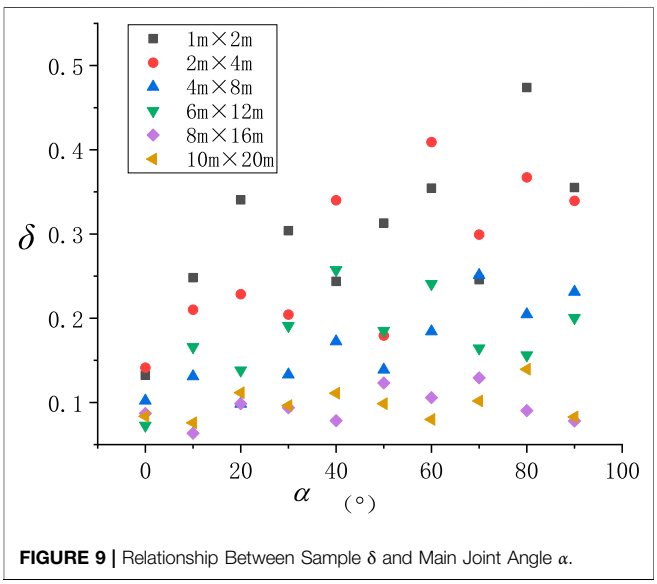

FIGURE 9 | Relationship Between Sample δ and Main Joint Angle α.

1) The sample δ was greater than 10% under a small model size. A great difference was manifested between the models with different main joint angles in δ.
2) The sample δ was significantly reduced with the increase in the model size. After the model size was enlarged to 8 m × 16 m, the sample δ was about 10%. Under this circumstance, the occurrence effect of the equivalent elasticity modulus of the model was no longer significant. It can be inferred from this that there is a certain size value. When the size of the jointed rock mass model exceeds this value, the value of the variation coefficient of the sample equivalent elastic modulus will be less than a given value (e.g., 10%), which can be used as the scale of the equivalent elastic modulus REV of the jointed rock mass.

REV Scale of the Equivalent Elastic Modulus E_{eq} of Orthogonal Random Jointed Rock Mass Under Given Variation Conditions

The δ values of the equivalent elasticity modulus obtained through experimenting on the models with different sizes and main joint attitudes were drawn into a scatter diagram (**Figure 10**). Next, they were fitted using a power function to obtain the following relationship between δ of the equivalent elasticity modulus and model size:

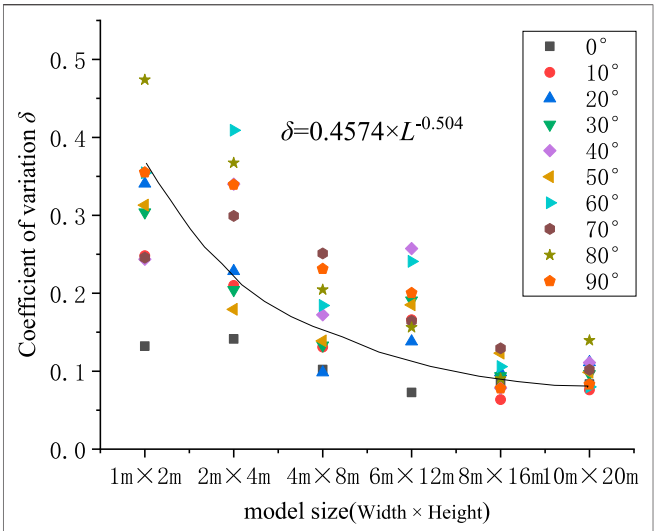

FIGURE 10 | Relationship between the sample δ and model size.

$$\delta\left(E_{eq}\right) = 0.4574 \cdot L^{-0.504}. \quad (3)$$

The model size required under the given δ could be estimated according to **Eq. 3**, thus providing a reference for selecting the minimum model size needed in the numerical model tests.

$$E_{eq} = 31.652 \cdot L^{-0.347}. \quad (4)$$

The equivalent elasticity moduli obtained by experimenting on the models with different sizes and main joint attitudes were drawn into a scatter diagram (**Figure 11**) and then fitted with a power function to acquire the relationship between the equivalent elasticity modulus and model size as follows:

Based on **Eq. 3**, the model size required under the given δ was acquired. The equivalent elasticity modulus under the corresponding model size could be solved through **Eq. 4** so as to provide a reference for selecting the elasticity modulus value in the numerical model calculation.

CONCLUSION

Under the engineering background of the + 144-m mining platform on an open pit slope of the Xinqiao Mining Corporation, an orthogonal random joint model was constructed using the Monte Carlo method based on the UDEC software platform, followed by a lot of numerical discrete element experiments. In full consideration of the random distribution characteristic of orthogonal joints in the rock mass, the REV size effect characteristics of the equivalent elasticity modulus of orthogonal random jointed rock masses under the given confining pressure were acquired as follows:

1) As the model size is enlarged, E_{eq} of the random joint model is gradually reduced.
2) Under a small model size, E_{eq} is discrete, with inapparent relational characteristics with the main joint angle α. After the model size is enlarged to 4 m × 8 m, E_{eq} presents a "two-high and one-low" morphological distribution. It is small under $\alpha \in [30^{\circ},40^{\circ}]$ and large when $\alpha = 0^{\circ}$ or 90°.

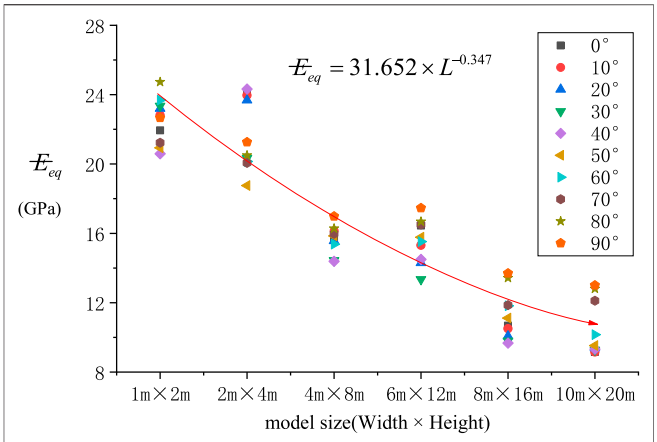

FIGURE 11 | Relationship between the equivalent elasticity modulus and model size.

3) When the model size is small, both σ_f and δ are discretely distributed. As the model size is enlarged to 8 m × 16 m, the models with different main joint angles differ little in σ_f and δ.
4) If δ is taken as 10%, the REV size of the corresponding E_{eq} is 10 m × 20 m. When the model reaches the REV size, the occurrence effect of its equivalent elasticity modulus is no longer significant.
5) The model size needed under the given δ can be solved according to the fitting formulas of δ, model size L, and E_{eq}, thus providing a reference for selecting a reasonable equivalent elasticity modulus value in the simulation analysis.

DATA AVAILABILITY STATEMENT

The original contributions presented in the study are included in the article/Supplementary Material, further inquiries can be directed to the corresponding author.

AUTHOR CONTRIBUTIONS

CL designed the tests, provided funds, and experimental apparatus. TZ performed the tests and processed the data. NX performed the tests, wrote the manuscript, and also was responsible for contacting the journal editor. CS performed the laboratory tests.

FUNDING

This study was funded by the Anhui Natural Science Research Program of Universities and Colleges (No: KJ 2018A0073) and the Science and Technology Program of Key Major Safety Production Accident Prevention and Control Technology (No: anhui-0004-2017AQ).

ACKNOWLEDGMENTS

The authors wish to acknowledge the support. The reviewers are gratefully acknowledged for their valuable comments on the manuscript.

REFERENCES

Aubertin, M., Li, L., and Simon, R. (2000). A Multiaxial Stress Criterion for Short- and Long-Term Strength of Isotropic Rock media. *Int. J. Rock Mech. Mining Sci.* 37, 1169–1193. doi:10.1016/s1365-1609(00)00047-2

Bear, J. (1972). *Dynamics of Fluids in Porous media*. New York: American Elsevier.

Bear, J. (1979). *Hydraulics of Groundwater*. New York: McGraw-Hill.

Bhasin, R., and Høeg, K. (1998). Numerical Modelling of Block Size Effects and Influence of Joint Properties in Multiply Jointed Rock. *Tunnelling Underground Space Tech.* 13 (2), 181–188. doi:10.1016/s0886-7798(98)00046-7

Chen, Q. F., Zheng, W. S., and Niu, W. J. (2019b). Correlation of the Geometrical and Mechanical Size Effects of Fractured Rock Masses. *Chin.J.Rock Mech.Eng.* 38 (Suppl. 1), 2857–2870. doi:10.13722/j.cnki.jrme.2017.0988

Chen, S. J., Yang, Z. D., and Wang, C. (2019a). Analysis of Size Effect of Structural Surface Roughness Based on Improved Projective Covering Method. *Chin.J. Eng.Geol.* 27 (6), 1244–1252. doi:10.13544./j.cnki.jeg.2018-451

Chun, Z., Yuan, C., Xuebin, C., Fuqiang, R., and Xiaohu, Z. (2019). Study on the Size Effect of Fracture Intersections Based on the Fractal Theory. *Geotech. Geol. Eng.* 37, 2999–3006. doi:10.1007/s10706-019-00818-z

Du, S. G., Lyu, Y. J., and Luo, Z. Y. (2021). Combined Test System for Size Effect of Rock Joint Shear Strength and its Primary Application Research. *Chin.J.Rock Mech.Eng.* 40 (7), 1337–1349. doi:10.13722/j.cnki.jrme.2020.1215

Esmaieli, K., Hadjigeorgiou, J., and Grenon, M. (2010). Estimating Geometrical and Mechanical REV Based on Synthetic Rock Mass Models at Brunswick Mine. *Int. J. Rock Mech. Mining Sci.* 47 (6), 915–926. doi:10.1016/j.ijrmms.2010.05.010

Fan, X. G., Guo, D. Y., and Zhang, Q. G. (2018). Experimental Study on the Crack Propagation Mechanism of Shale Considering the Effect of the Bedding Loading Rate and Sample Size. *Chin.Sci. Tech. Eng.* 18 (9), 63–71.

Gu, D. Z. (1979). *Fundamentals of Rock Engineering Geomechanics*. Beijing: Science Press.

Kulatilake, P. H. S. W. (1985). Estimating Elastic Constants and Strength of Discontinuous Rock. *J. Geotechnical Eng.* 111 (7), 847–864. doi:10.1061/(asce)0733-9410(1985)111:7(847)

Li, D. P., Li, J., and Sun, R. R. (2019). Numerical Simulation on Compressive Strength Size Effect of Rock Mass Based on UDEC. *Chin. J. Underground Space Eng.* 15 (4), 1098–1105.

Li, K. L., Song, X. K., and Zhang, C. S. (2021). Particle Flow Code Analysis Geometrical and Mechanical Representative Elementary Volumes Size of Fractured Rock Mass. *J.Shandong Univ. Sci. Tech. (Natural Science)* 40 (5), 59–68. doi:10.16452/j.cnki.sdkjzk.2021.05.007

Lu, H. Y., Li, D. P., and Zhong, J. C. (2020). Numerical Study of Joint Rock Mass Compressive Strength Based on UDEC. *J. Hebei Univ. Eng. (Nat. Sci. Edition)* 37 (3), 17–25. doi:10.3969/j.issn.1673-9469.2020.03.003

Min, K.-B., and Jing, L. (2003). Numerical Determination of the Equivalent Elastic Compliance Tensor for Fractured Rock Masses Using the Distinct Element Method. *Int. J. Rock Mech. Mining Sci.* 40 (6), 795–816. doi:10.1016/S1365-1609(03)00038-8

Ni, H. J., Xu, W. Y., Shi, A. C., Wang, W., Bo, L. U., Lifang, Z., et al. (2015). Scale Effect on Equivalent Continuum Elastic Modulus of Columnar Jointed Rock Masses by Distinct Element Method. *Chin.Engineering Mech.* 32 (3), 90–96. doi:10.6052/j.issn.1000-4750.2013.09.0849

Ning, Y., Xu, W. Y., Zheng, W. T., Meng, G., Shi, A., Wu, G., et al. (2008). Study of Random Simulation of Columnar Jointed Rock Mass and its Representative Elementary Volume Scale. *Chin.J.Rock Mech. Eng.* 27 (6), 1202–1208.

Pouya, A., and Ghoreychi, M. (2001). Determination of Rock Mass Strength Properties by Homogenization. *Int. J. Numer. Anal. Meth. Geomech.* 25 (13), 1285–1303. doi:10.1002/nag.176

Sun, G. Z. (1988). *Rock Mass Structure Mechanics*. Beijing: Science Press.

Sun, Y. K., and Li, J. G. (1965). Engineering Geological Study on Stability of Rock Slope. *Chin.Geol.Sci.* 04, 330–352.

Wang, J. L., and Zuo, H. W. (1998). Study on Size Effect of Young's Modulus for Rock. *Chin.Rock Soil Mech.* 19, 60–64.

Wang, M., Kulatilake, P. H. S. W., Um, J., and Narvaiz, J. (2002). Estimation of REV Size and Three-Dimensional Hydraulic Conductivity Tensor for a Fractured Rock Mass through a Single Well Packer Test and Discrete Fracture Fluid Flow Modeling. *Int. J. Rock Mech. Mining Sci.* 39, 887–904. doi:10.1016/s1365-1609(02)00067-9

Wang, P. T., Ren, F. H., and Cai, M. F. (2018). Mechanical Analysis and Size Effect of Rough Discrete Fractures Network Model under Direct Shear Tests Based on Particle Flow Code. *Chin.J.China Coal Soc.* 43 (4), 976–983. doi:10.13225/j.cnki.jccs.2017.1061

Wang, Q. Y., and Li, Y. (2008). Experimental Study of Scale Effects in Strength and Deformation of Fractal-Joint Rock Masses. *Chin.Rock Soil Mech.* 29, 1325–1328. doi:10.1016/0148-9062(81)90262-X

Wang, X. M., Du, Y. F., and Liang, X. L. (2021). Investigation of the Representative Elementary Volume of Fractured Rock Mass Using the Homogeneity index. *Chin.Hydrogeology Eng. Geology.* 48 (2), 55–60. doi:10.16030/j.cnki.issn.1000-3665.202007029

Xiang, W. F. (2005). *A Study on the Representative Elementary Volume of Fractured Rock Masses and the Size Effects of Mechanical Properties*. China Wuhan: Wuhan University.

Yan, C. G., Wu, F., Qi, S. W., Liu, T., and Masakasu, M. (2009). Deformation and Strength Parameters and Size Effect of Random Jointed Rock Mass by Numerical Simulation. *Chin.J.Geotech.Eng.* 31 (6), 879–885.

Zhang, G. K., and Xu, W. Y. (2008). Analysis of Joint Network Simulation Method and REV Scale. *Chin.Rock Soil Mech.* 29 (6), 1675–1680. doi:10.16285/j.rsm.2008.06.052

Zhang, Z. G., and Qiao, C. S. (2006b). Improved Empirical Determination of Strength Parameter for Jointed Rock Masses and its Application in Engineering. *J. Beijing Jiaotong Univ.* 30, 46–49.

Zhang, Z. G., and Qiao, C. S. (2006a). Improved Empirical Method for Determination of Deformation Modulus of Jointed Rock Masses and its Application Engineering. *Chia.J.Eng. Geol.* 14, 233–238.

Zhang, Z. R., Sheng, Q., Yang, Y. S., Zhu, Z. Q., Zhang, Y. M., and Wang, Z. W. (2010). Study of Size Effect of Rock Mass Deformation Modulus Based on Iin-Ssitu Test. *Chin.Rock Soil Mech.* 31 (9), 2875–2881. doi:10.16285/j.rsm.2010.09.032

Zhou, C. B., and Xiong, W. L. (1996a). On Permeability Characteristics of Rock Mass. *Chin.J. Eng. Geol.* 4 (2), 69–74.

Zhou, C. B., and Xiong, W. L. (1996b). Permeability Tensor for Jointed Rock Masses in Coupled Seepage and Stress Field. *Chin.J.Rock Mech.Eng.* 15 (4), 338–344.

Zhou, H. M., Sheng, Q., and Chen, S. W. (2004). Numerical Simulation on Size-Effect in Deformation Test of Layer Composite Rockmass. *Chin.J. Rock Mech. Eng.* 23 (2), 289–292.

Zhu, D. J., Yang, L. D., and Cai, Y. C. (2009). Research on Anisotropic Characteristics and Size Effect of Columnar Jointed Rock Mass. *Chin.J.Rock Mech. Eng.* 28 (7), 1405–1414.

Conflict of Interest: The authors declare that the research was conducted in the absence of any commercial or financial relationships that could be construed as a potential conflict of interest.

frontiers | Frontiers in Earth Science

ORIGINAL RESEARCH
published: 12 July 2022
doi: 10.3389/feart.2022.927159

Experimental Study on Damage Properties of Granites Under Flowing Acid Solution

Wei Chen[1,2], Wen Wan[2], Yanlin Zhao[2], Qiuhong Wu[2], Huan He[3], Wenqing Peng[2], Xiaofan Wu[4], Yu Zhou[2], Li Wu[5] and Senlin Xie[6]*

[1]Department of Building Engineering, Hunan Institute of Engineering, Xiangtan, China, [2]School of Resource, Environment and Safety Engineering, Hunan University of Science and Technology, Xiangtan, China, [3]Mianyang Economic-Technological Development Zone, Sichuan University of Culture and Arts, Mianyang, China, [4]School of Mathematics and Computational Science, Hunan University of Science and Technology, Xiangtan, China, [5]School of Earth Sciences and Spatial Information Engineering, Hunan University of Science and Technology, Xiangtan, China, [6]School of Energy and Mining Engineering, China University of Mining and Technology (Beijing), Beijing, China

In order to study the deterioration characteristics of the tunnel surrounding rock under the scouring of flowing groundwater, we ratioed similar acidic solutions based on groundwater composition. The microstructure of granite samples cored on site, deformation features, and evolution characteristics of mechanical parameters under saturations with different flow rates and various pH values were analyzed using scanning electron microscopy (SEM), energy dispersive spectroscopy (EDS), nuclear magnetic resonance (NMR), and X-ray diffraction (XRD). The results indicate the following: 1) compared with the static water condition, the higher flow rate produces greater relative changes in granite's microstructure, porosity, mass, and pH of the immersed solution. Moreover, the rate of change is relatively fast in the early stage and gradually slows down until it reaches a stable state. 2) Compared with the natural dry condition, the solution with a lower pH value causes the structural framework of the specimen to loosen, the mass loss degree to increase, and the porosity dispersion to intensify. 3) The dynamic water is more sensitive than the static water to the elastic vertical wave velocity of granite. Compared with the dry sample, the elastic longitudinal wave velocity of the sample in acidic solution with pH = 2 and flow rates of 0, 150, and 300 mm·s^{-1} for 49 days decreased by 8.7, 10.9, and 13.5%, respectively, which accelerates the instability and failure of the granite surroundings.

Keywords: granite surroundings, rock mechanics parameters, effect of solution velocity, hydration corrosion, damage mechanism

OPEN ACCESS

Edited by:
Thomas Hermans,
Ghent University, Belgium

Reviewed by:
Bing Bai,
Beijing Jiaotong University, China
Xiangxin Liu,
North China University of Science and Technology, China

****Correspondence:***
Wei Chen
chenweiwade@mail.hnust.edu.cn

Specialty section:
This article was submitted to Structural Geology and Tectonics, a section of the journal Frontiers in Earth Science

Received: *23 April 2022*
Accepted: *30 May 2022*
Published: *12 July 2022*

Citation:
Chen W, Wan W, Zhao Y, Wu Q, He H, Peng W, Wu X, Zhou Y, Wu L and Xie S (2022) Experimental Study on Damage Properties of Granites Under Flowing Acid Solution. Front. Earth Sci. 10:927159. doi: 10.3389/feart.2022.927159

1 INTRODUCTION

The surrounding rock in underground engineering has been longtime damaged and degraded by various physical and chemical actions (Dong et al., 2020; Liu et al., 2020; Bai et al., 2021; Zhao et al., 2021b). For instance, during groundwater flow, the rock mass will not only happen to softening, migration, argillization, and other physical effects but produce the chemical reaction such as ion exchange, dissolution, and hydrolysis, which will bring about the changes in overall structure, mineral composition, and physical properties of surrounding rock and will accordingly deteriorate its mechanical properties to cause engineering accidents (Bai et al., 2017; Liu et al., 2019; Zhao et al., 2021b).

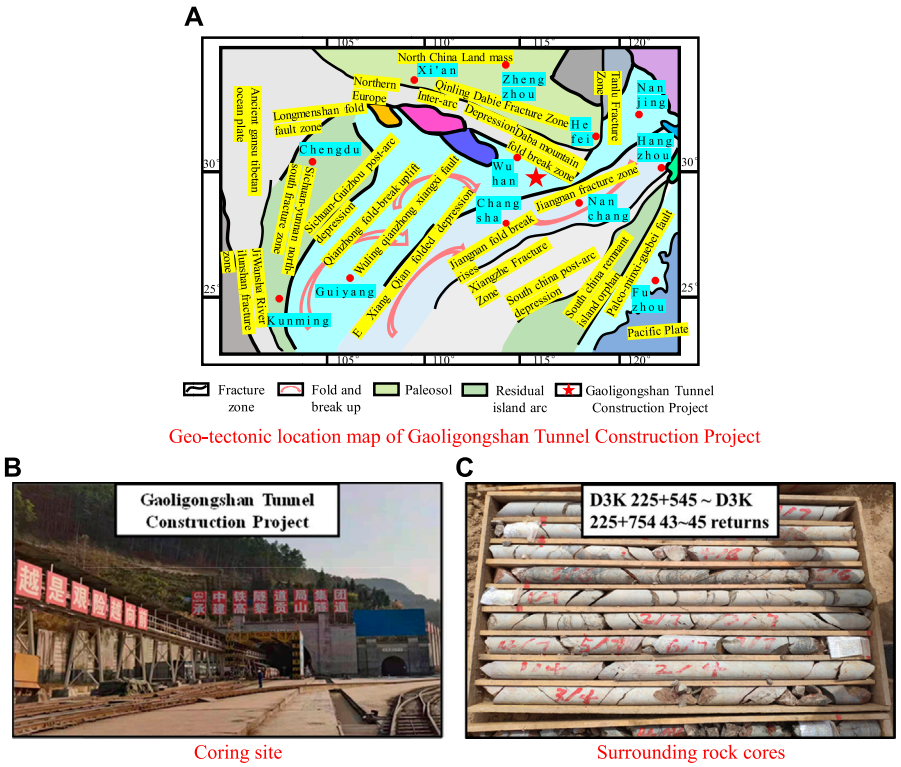

Geo-tectonic location map of Gaoligongshan Tunnel Construction Project

Coring site

Surrounding rock cores

FIGURE 1 | Preparation process of granite specimens. **(A)** Geo-tectonic location map of Gaoligongshan Tunnel Construction Project. **(B)** Coring site. **(C)** Surrounding rock cores.

Currently, rich achievements have been made for the different aqueous chemical solutions to the macro–microstructure of rocks and physical and mechanical properties of damage effects. Huang et al. (2021) studied the changes in chroma, mass, vertical wave velocity, porosity, thermal conductivity, and tensile strength of granite, sandstone, and marble induced by chemical erosion and found that rock materials exhibit varying degrees of changes in physical and mechanical properties under the action of acidic solution corrosion. Huo et al. (2018) and Li et al. (2021) discussed the physical-chemical properties and mechanical properties of sandstone after saturations in different acid solutions and established the dynamical model of acid rock reaction. Through triaxial rheological tests, Xie et al. (2011) found out that chemical corrosion greatly accelerated the instantaneous strain rate of limestone under triaxial stress. Chen et al. (2021) derived the damage evolution equation and constitutive model of acid-corroded rock under the coupling effect of freezing–thawing and confining pressure based on the theory of continuous damage mechanics and carried out triaxial compression test to further reveal the damage mechanism and failure law of acid-corroded rock under the coupling effect of freezing–thawing and confining pressure. Wang et al. (2021) soaked the granite in nitric acid with different pH values and analyzed the mechanical properties of granite under corrosion acid and freeze–thaw cycles by uniaxial compression and freeze–thaw cycles.

However, the above tests were basically carried out under static water saturations, ignoring the erosion of underground rock engineering by longstanding flowing groundwater, and lacking in-depth discussion on the chemical damage mechanism and microscopic response mechanism (Zhao et al., 2017a; Liu et al., 2021b). In this article, based on the ion content of groundwater in the field, similar solutions with different pH values (pH = 7, 4, and 2) were mixed. Considering the scouring action of different velocity environments (v = 0, 150, and 300 mm·s^{-1}), we analyzed the granite surrounding rock of the tunnel at the water-rich area and chemical damage mechanism of microstructure, deformation characteristics, and physical properties under dynamic water environment. The results from this study are practically significant, which can provide some theoretical basis for the stability control of the rock mass of the bridge pile foundation bearing layer and tunnel surrounding rock at flowing groundwater.

2 LABORATORY TEST DESIGN

2.1 Sample and Solution Preparation

Granite was selected from the surrounding rock of the Gaoligongshan Tunnel Construction Project (see **Figures 1A,B**). According to the hydrogeological survey report of this section, groundwater in this area was abundant and weakly acidic (pH = 6.24), mainly containing cations such

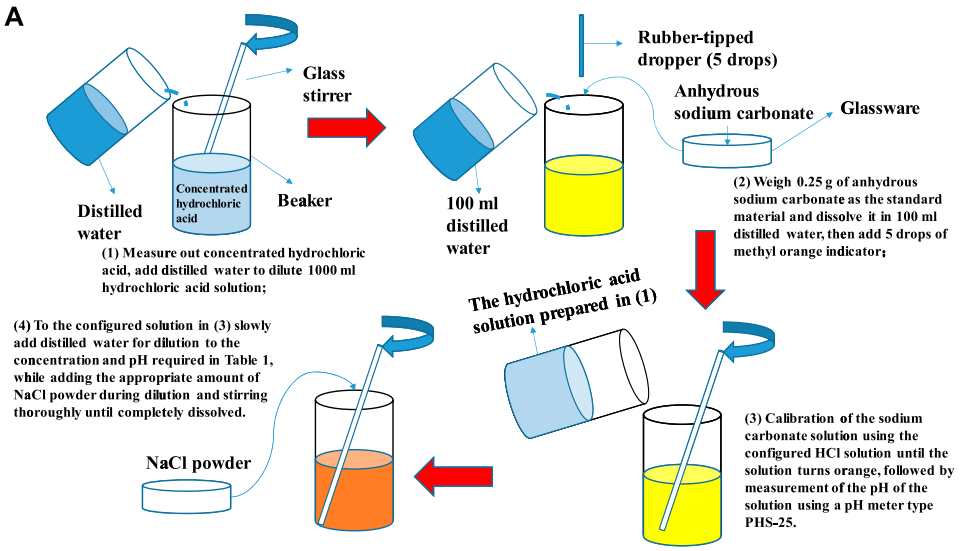

Diagram for configuration and calibration steps of acidic NaCl solution

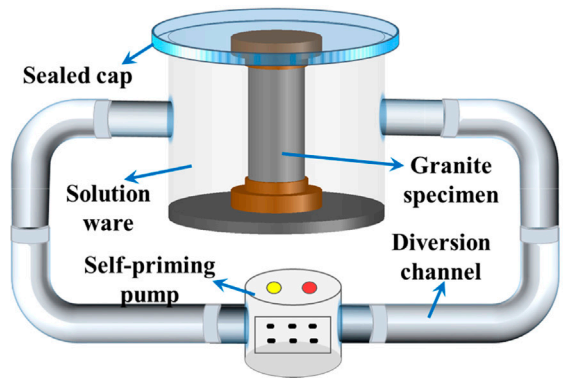

Schematic diagram of the water scouring device

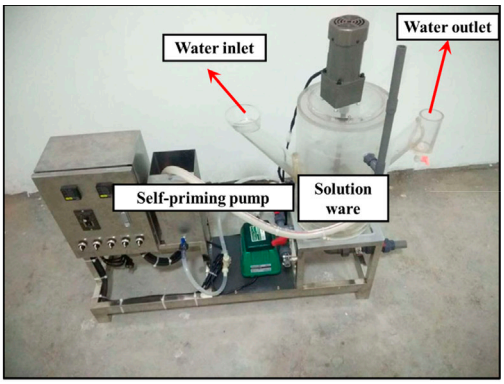

Water chemical solution scouring device

FIGURE 2 | Realization of dynamic water conditions. **(A)** Diagram for configuration and calibration steps of acidic NaCl solution. **(B)** Schematic diagram of the water scouring device. **(C)** Water chemical solution scouring device.

as Na^+, K^+, and Mg^{2+} and anions such as Cl^-, SO_4^{2-}, and HCO^{3-}. In addition, the annual average flow rate was about 150 mm·s^{-1}. Standard cylindrical samples of 50 × 100 mm (Zhao et al., 2016; Zhou et al., 2020; Dong et al., 2021) were prepared after drilling and coring of granite (see **Figure 1C**). The test synthesized the cations and anions with the largest percentage of groundwater content in the site and collocated NaCl solution with pH values of 7, 4, and 2 and a concentration of 0.01 mol·L^{-1}, respectively (see **Figure 2A**). Furthermore, three flow rate environments were simulated: v = 0, 150, and 300 mm·s^{-1}, and different immersion time nodes were set for follow-up measurements.

2.2 Dynamic Water Scouring Test Design

A hydro-chemical solution scouring device (see **Figures 2B,C**) was used to conduct scouring treatment tests on sandstone in solutions of different pH values and at different flow rates. The flushing device consists of a solution ware, a diversion channel, and a self-priming pump. The working principle is as follows: the solution ware is loaded into the solution, and the sample is placed and sealed, and the self-priming pump is operated. The solution circulates between the solution ware, the diversion channel, and the self-priming pump, and the flow rate of the solution is determined by the self-priming pump.

3 LABORATORY RESULTS AND ANALYSIS

3.1 Damage of Granite Under the Effect of Flowing Acid Solution

3.1.1 Analysis of Microstructure Changes

The macroscopic physical–mechanical state of granite is closely related to its own microstructure change (Zhao et al., 2017b;

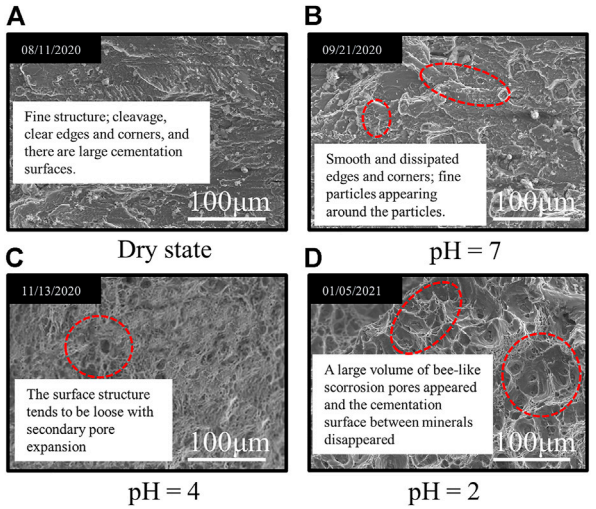

FIGURE 3 | Apparent scanning electron microscopy images of granite under different solution conditions for 49 days. **(A)** Dry state. **(B)** pH=7. **(C)** pH=4. **(D)** pH=2.

Dong et al., 2019; Zhou et al., 2019; Liu et al., 2021a). The test analyzed the differences in apparent morphological damage and pore structure of the samples before and after immersion treatment in acidic hydro-chemical solution with different flow rates and pH values through scanning with an electron microscope at a magnification of 500 times. The change in mineral composition near the pores was tracked using the electron energy spectrum analysis technology so as to explore the deterioration degree of granite microstructure under the effect of flowing acidic solution.

The surface scanning electron microscopy images of granite samples at different pH values under acidic solution environment (v = 0 mm·s^{-1}) for 49 days are shown in **Figure 3**.

After the samples were treated with hydro-chemical solution at various flow rates (pH = 6.24), the microscopic structure characterization (× 10^4 times) is shown in **Figure 4**.

As v = 150 mm·s^{-1}, the microstructure deterioration of the sample was more obvious than that in static water (see **Figure 4B**). Compared with the low velocity (v = 150 mm·s^{-1}), the micro-deterioration degree of the sample in the immersion environment with v = 300 mm·s^{-1} was stronger (see **Figure 4C**), but the deterioration degree was not as significant as the former.

Based on the groundwater flow rate of v = 150 mm·s^{-1} on site, the scanning electron microscopy at 10,000 times was observed under this flow rate with each solution rinsing for 49 days (see **Figure 5**).

Energy dispersive spectroscopy was used to measure the small area in the scanning image of electron microscope (the random three red crosses in **Figure 5**) to obtain the number of atoms and mass of the main components, and their average values are shown in **Table 1**. During saturation in NaCl acidic solution with pH = 4 and 2, a small amount of mineral composition in granite reacted with H^+ ions in the solution, causing some elements to dissolve and thereby break away from the rock, which resulted in the reduction of the content of metal elements such as Al, K, and Ca to different extents (see **Figure 5** and **Table 1**). On top of that, granite is a porous medium with certain absorbability, resulting in the increase of Na, Cl, and other elements after the effect of NaCl solution. Under the effect of NaCl solution with pH = 7 and distilled water, there was no obvious change in the content of main elements.

3.1.2 Porosity Change Analysis

Corrosion and hydrolysis will enable the active minerals to migrate with the groundwater and will increase the porosity,

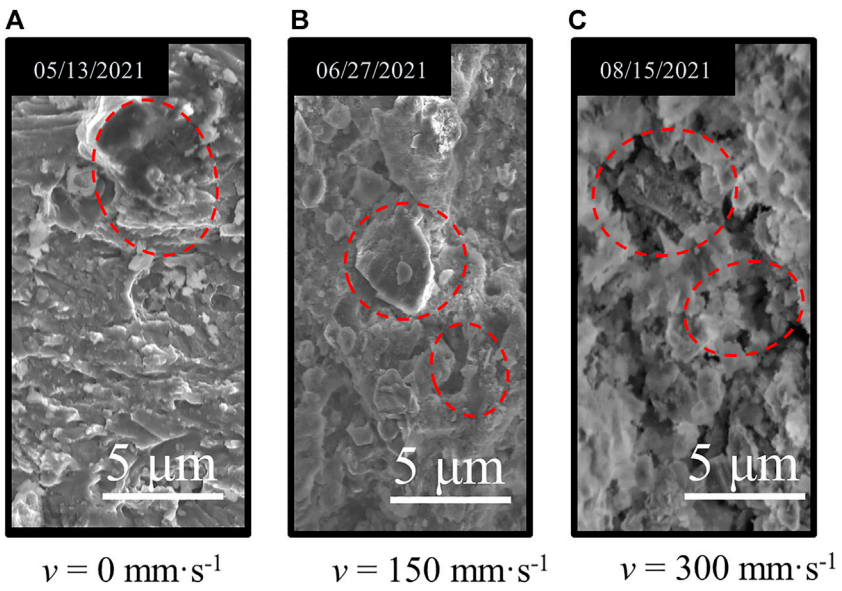

FIGURE 4 | Microstructural damage of granite immersed at different solution flow rates. **(A)** v = 0 mm·s^{-1} . **(B)** v = 150 mm·s^{-1}. **(C)** v = 300 mm·s^{-1}.

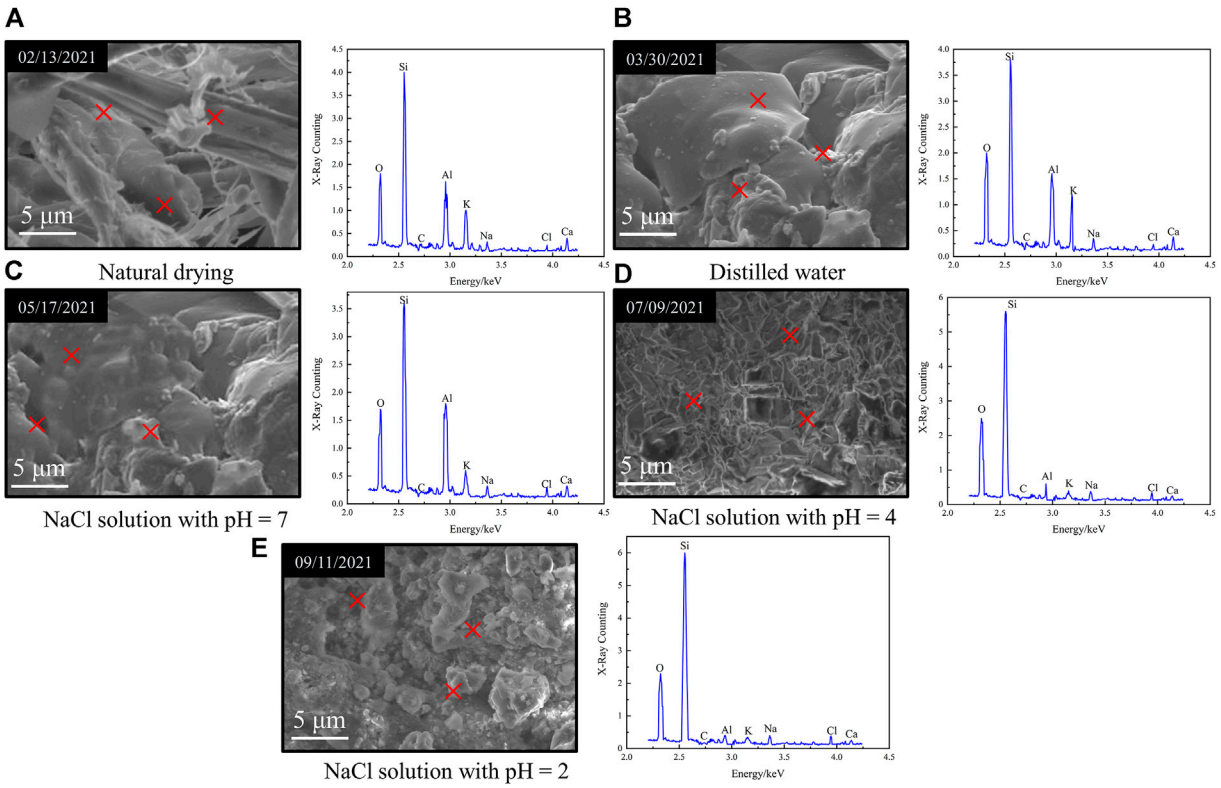

FIGURE 5 | Energy dispersive spectroscopy analysis of granite under the flow rate of v = 150 mm·s^{-1} with different aqueous chemical solutions for 49 days. **(A)** Natural drying. **(B)** Distilled water. **(C)** NaCl solution with pH=7. **(D)** NaCl solution with pH=4. **(E)** NaCl solution with pH=2

TABLE 1 | Comparison of the atomic number and mass content of the main components of granite under the flow rate of v = 150 mm·s^{-1} with different aqueous chemical solutions for 49 days.

Parameter		O	Si	C	Al	K	Na	Cl	Ca
Atom content/%	Dry	44.38	20.96	16.10	8.92	4.01	2.76	0.81	1.52
	Distilled water	41.52	15.87	19.32	6.05	5.23	4.06	1.10	2.26
	pH = 7	49.07	24.03	11.95	7.14	2.96	3.24	1.73	1.36
	pH = 4	51.05	15.31	11.01	6.40	3.33	4.56	1.99	1.00
	pH = 2	42.26	24.72	21.23	2.46	2.60	3.01	2.69	0.60
Mass content/%	Dry	34.48	29.46	9.23	11.85	7.13	3.23	1.30	3.06
	Distilled water	31.78	22.05	14.66	10.06	9.45	4.51	3.84	4.45
	pH = 7	39.06	30.43	8.06	9.30	4.98	3.72	3.40	2.75
	pH = 4	43.09	18.99	5.31	14.10	7.20	4.99	2.83	1.56
	pH = 2	32.52	33.93	15.41	3.74	3.96	2.88	5.51	1.00

which will impact on the pore pressure and permeability of the granite (Zhao et al., 2021a; Dong et al., 2022). The porosity of the sample subjected to acidic solution was determined by the pycnometer bottle test method (Grgic et al., 2022) and nuclear magnetic resonance (NMR) technique. Three samples were selected for each solution with different pH values and flow rates. **Figure 6** shows the test results. Porosity was calculated as follows (Zhao et al., 2019):

$$n = \left(\rho_g - \rho_d\right)/\rho_g \times 100\%, \quad (1)$$

where n is the porosity of the rock sample, ρ_g is the grain density of the rock sample, and ρ_d is the dry density of the sample.

Figure 6 indicates that the porosity of the sample increases exponentially with the decrease in pH of the acid solution. Compared to the dry sample, the porosity of the samples under various acidic solution saturations (pH value from high to low) with the flow rate of 0 had smaller variations, and the growth rates were 3.5, 9.4, 30.7, and 45.9%, respectively (see **Figure 6A**). The average porosity of the treated samples increased by 4.5, 10.8, 34.1, and 48.3%, respectively, under

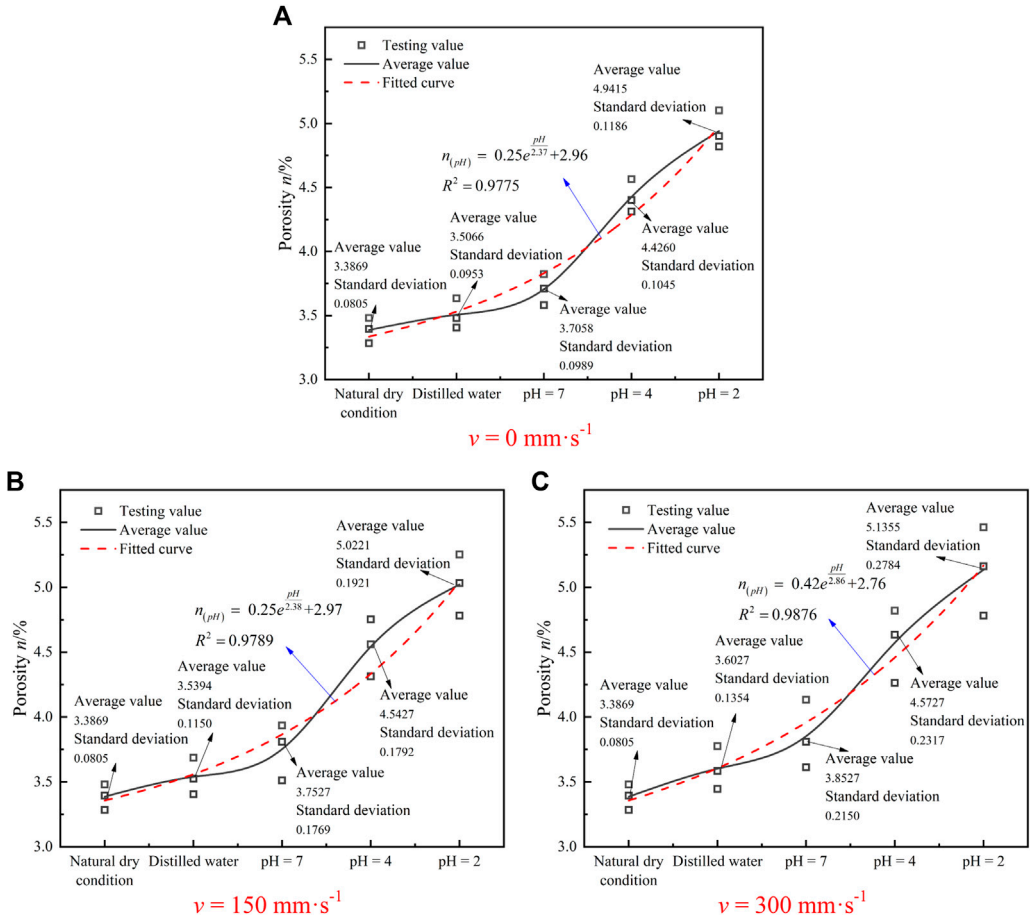

FIGURE 6 | Porosity change diagram of granite samples under different flow rates of acid solution. **(A)** v = 0 mm·s^{-1} . **(B)** v = 150 mm·s^{-1}. **(C)** v = 300 mm·s^{-1}.

different saturations with v = 150 mm·s^{-1} (see **Figure 6B**). As v = 300 mm·s^{-1}, the average porosity increases with 6.4, 13.8, 35, and 51.6%, respectively (see **Figure 6C**). In addition, compared with natural drying and distilled water, the porosity of samples measured by acidic solution had more obvious dispersion, and the porosity dispersion of v = 150 mm·s^{-1} was significantly lower than that of v = 300 mm·s^{-1}. There are two reasons: one is the heterogeneity of the rock sample, and the other is the selective difference of chemical action on the rock. Given this, the dynamic solution environment has a certain role in promoting the dispersion of rock porosity, and when the hydro-chemical solution in which the rock mass is located has a higher flow rate, the effect is more obvious.

3.2 Deterioration and Aging Characteristics of Granite Under Flowing Acid Solution

Physical parameters such as the sample mass and the pH value of the immersed solution were determined with 7 days as the time node during the saturation, and measurements were carried out every day during the first 5 days. After the test, the ion chromatography was used to measure and analyze the ion composition and concentration of the chemical solution.

3.2.1 Evolution of Mass Loss

To reduce the random error of test results, the sample was ventilated for 0.5 h to ensure the same test condition. Under the effect of water and various flow rates of acidic aqueous chemical solution, the mass of the sample was reduced inordinately. The mass damage level of granite was described by the mass loss factor D_t:

$$D_t = (m_0 - m_t)/m_0 \times 100\%. \quad (2)$$

In **Eq. 2**, m_0 is the original mass of the sample and m_t is the mass of the sample at time t.

Figure 7 shows the mass loss aging characteristic curves of granite after saturation in four kinds of dynamic aqueous chemical solutions.

As seen in **Figure 7**, the mass loss degree of the sample increased with the decrease in the pH value of the hydro-chemical solution. Under saturation at the same pH value, the mass loss degree of the sample with v = 0 mm·s^{-1} was significantly lower than that of the sample with v =150 mm·s^{-1}. However, the

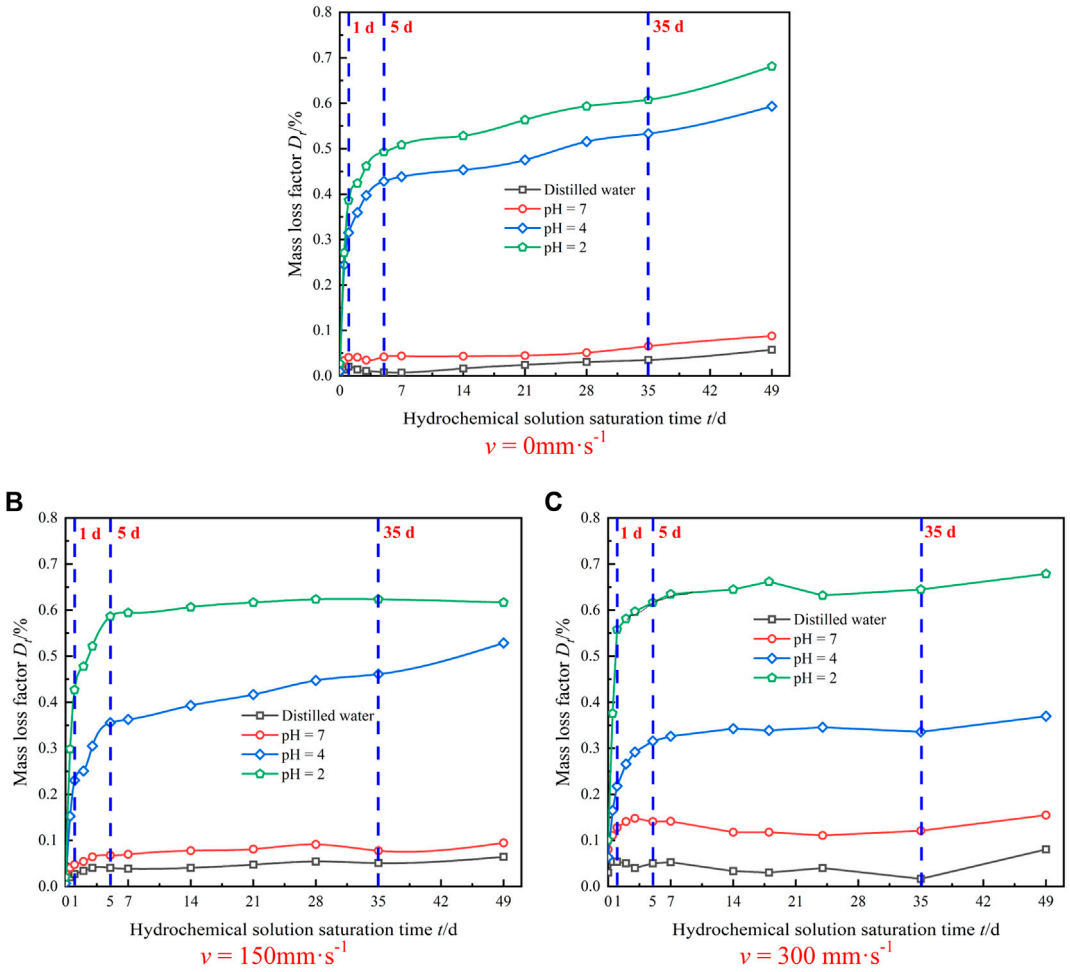

FIGURE 7 | Time-dependent variation curve of rock mass loss during the test process. **(A)** v = 0 mm·s^{-1} . **(B)** v = 150 mm·s^{-1}. **(C)** v = 300 mm·s^{-1}.

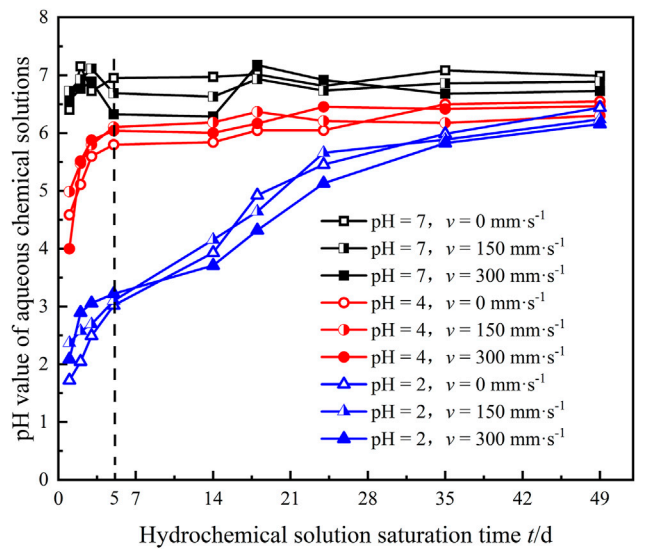

FIGURE 8 | Time-dependent curve of the aqueous chemical solution pH value in the test process.

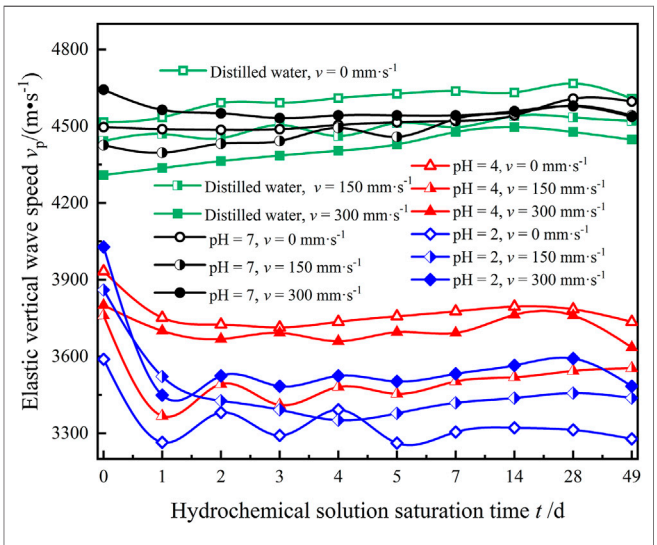

FIGURE 9 | Time-dependent variation curve of the granite elastic vertical wave speed of granite during the test process.

TABLE 2 | Variation in elastic longitudinal wave velocity of granite by different hydro-chemical solutions.

Test environment	Velocity/(mm·s^{-1})	v_{sp}/(m·s^{-1})	v_{fp}/(m·s^{-1})	E_p/%
Distilled water	0	4,516	4,608	−2.04
	150	4,443	4,521	−1.77
	300	4,310	4,448	−3.20
pH = 7	0	4,497	4,597	−2.23
	150	4,426	4,543	−2.63
	300	4,643	4,537	2.27
pH = 4	0	3,934	3,736	5.02
	150	3,760	3,555	5.47
	300	3,801	3,636	4.34
pH = 2	0	3,590	3,279	8.67
	150	3,861	3,438	10.94
	300	4,028	3,484	13.51

mass loss degree of the sample with v = 300 mm·s^{-1} was slightly higher than that of the sample with v = 150 mm·s^{-1}. In the pH = 2 acidic solution, the granite samples reacted strongly in the acidic chemical solution with various flow rates at the initial stage (0 ~ 5 days), and the active minerals dissolved and formed some bubbles. The mass loss rate was the highest (0.487, 0.574, and 0.686%, respectively). As the time went on, the chemical reaction rate gradually slowed down until it became steady.

3.2.2 Law of pH Change With time

As mentioned earlier, the initial pH of the aqueous solution is the key factor to influence the corrosion mechanism of granite. The time, phenomenon, and degree of chemical reaction of the sample during the test can be directly mirrored by the change in solution pH (Miao et al., 2016). **Figure 8** shows the characteristic curve of the pH value with time during the immersion of the sample in acidic solution at various flow rates. In **Figure 8**, the granite sample produced a weak chemical reaction in the NaCl solution immersion with pH = 7, and the measured pH value of the solution ranged from 6.29 to 7.18,

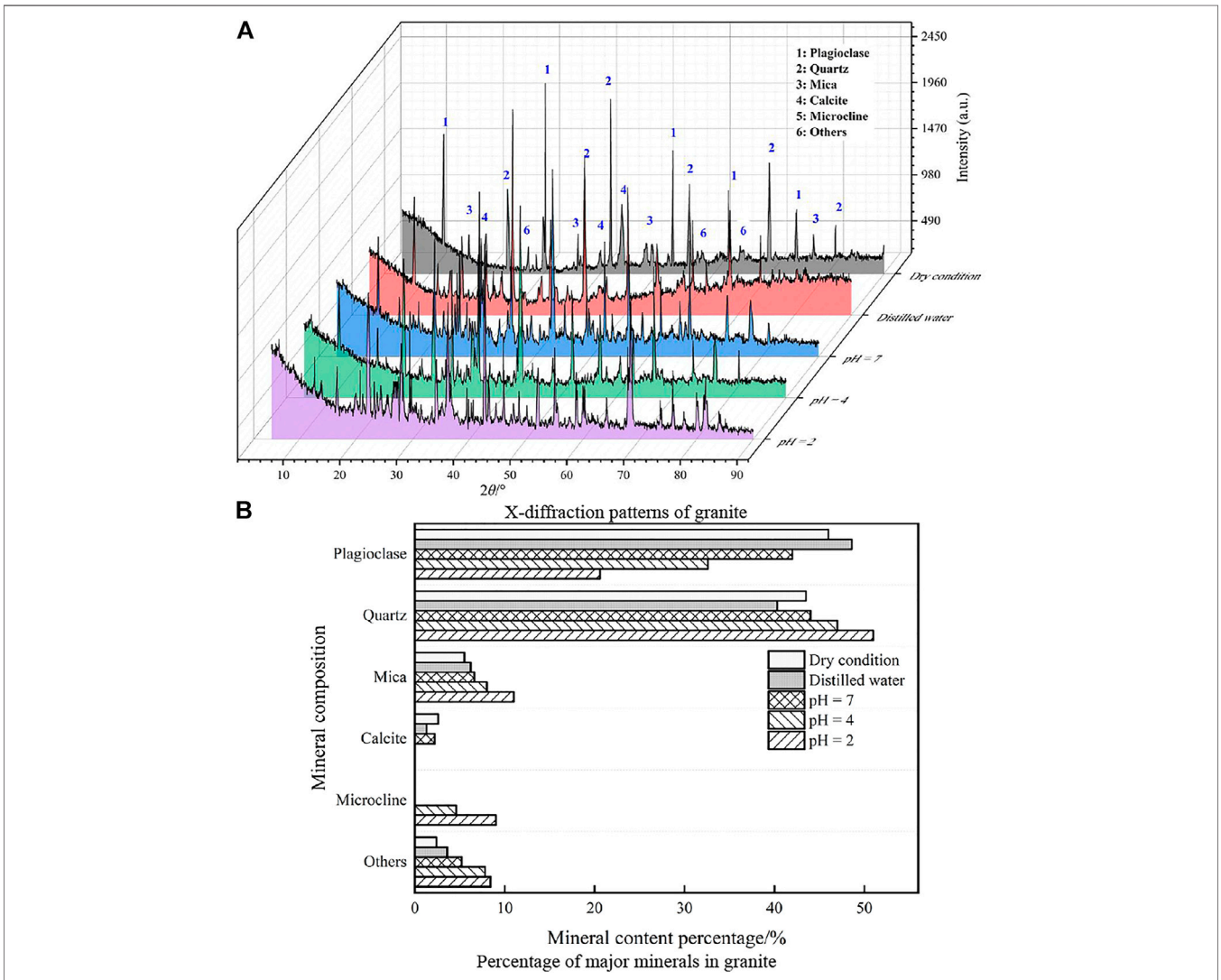

FIGURE 10 | X-ray diffraction results of granite mineral composition before and after different treatment. **(A)** X-diffraction patterns of granite. **(B)** Mineral content percentage/% percentage of major minerals in granite.

TABLE 3 | Content of main mineral components of granite before and after immersion in different aqueous chemical solutions.

Test environment	Mass percentage of mineral content/%					
	Microcline	Calcite	Mica	Quartz	Plagioclase	Others
Dry condition	—	2.6	5.5	43.5	46	2.4
Distilled water	—	1.3	6.2	40.3	48.6	3.6
pH = 7	—	2.2	6.6	44	42	5.2
pH = 4	4.6	—	8	47	32.6	7.8
pH = 2	9	—	11	51	20.6	8.4

TABLE 4 | Contents of the main compounds and chemical elements in granite before and after the action of different hydro-chemical solutions.

Test environment	Mass percentage of the compound and element content/%										
	SiO_2	Al_2O_3	C	CaO	K_2O	Na_2O	Fe_2O_3	Cl	N	TiO_2	MgO
Dry condition	62.10	17.20	9.40	3.49	3.33	2.87	0.91	0.69	0.29	0.27	0.19
Distilled water	64.20	15.00	10.13	1.86	3.16	3.99	0.87	0.10	0.22	0.12	0.9
pH = 7	58.20	14.90	8.02	1.43	3.13	3.37	0.67	0.34	0.46	0.29	0.35
pH = 4	65.90	11.90	10.59	0.92	3.01	2.52	0.62	0.51	0.49	0.20	0.26
pH = 2	73.50	8.80	11.60	0.60	2.50	0.50	0.60	1.00	0.60	0.30	0.10

which reflected a good stability. At the beginning of immersion, the H^+ in the solution and the new active minerals in the sample continually reacted on the granite surface. After corrosion, the active minerals moved with water flow or dissolved in the solution, and the pH value of the solution changed obviously. When v = 300 mm·s^{-1}, the change rates of pH = 7, 4, and 2 after soaking for 5 days were −0.4, 33.8, and 38.9%, respectively. After soaking for 5–6 days, the NaCl solution with pH = 4 was almost stable, but the change rate of the NaCl solution with pH = 2 decreased gradually from 26%/d (0 ~ 5 days) to 5.7%/d (5 ~ 49 days). Upon saturation, the pH values of the three aqueous chemical solutions were basically neutral. "Water–rock Interaction" (WRI) mainly manifests as hydraulic and physical actions, and the chemical corrosion action is nearly inactive.

3.2.3 Time-Dependent Variation in Elastic Vertical Wave Velocity

The physical properties of rock determine the spread rate of ultrasonic waves in the rock to a certain extent (Cherblanc et al., 2016; Weng et al., 2020). The acoustic wave of granite was measured by an acoustic wave tester at each time node of acid solution treatment so as to obtain the aging regularity of granite elastic vertical wave velocity under flowing acidic solution. **Figure 9** shows the measurement result.

From **Figure 9**, it can be seen that there was no obvious fluctuation in the granite elastic vertical wave velocity and the stability was good in the initial stage of the test, when the granite was immersed in water and NaCl solution with pH = 7. The elastic vertical wave velocity (v_p) of granite samples decreased significantly in acidic solution with pH of 4 and 2, and it decreased by 9.1, 8.8, and 14.4% in NaCl solution with pH of 2 with flow rates of v = 0, 150, and 300 mm·s^{-1}, respectively. Then, there were fluctuations, but the fluctuations gradually slowed down over time, and the fluctuation cycle presented an increasing trend over time; v_p hardly changed after 5 ~ 7 days of immersion. As the immersion environment was water and NaCl solution with pH = 7, v_p of a few specimens also fluctuated slightly, but it showed a smooth rise overall.

Based on the large quantity of research and tests (Ha et al., 2015; Hao et al., 2015; Cai et al., 2016; Dong and Luo, 2022), the analysis is as follows: (1) at the initial stage of immersion, the active oxide contained in the sample in the ideal state reacted with H^+ in the acidic solution, resulting in dissolution pores, an increase in porosity, and a decrease in wave velocity; the rate of chemical reaction gradually flattened as the pH value of solution became neutral, and the saturation rate of rock increased gradually due to product precipitation and water absorption. The v_p of the sample witnessed a small increase until it became stable. However, owing to the heterogeneity of granite and its potential micro-fissures, such micro-fractures may continue to develop, expand, or initiate new fissures under the effect of acidic solution. Compared with the environment with v = 0 mm·s^{-1}, the fluctuation of v_p was significantly enhanced due to the water absorption and the WRI brought by low and high speed immersion environment. Meanwhile, under NaCl solution with pH = 7, the pores of rocks gradually reached saturation because of the absorption of water molecules, whereby v_p slowly increased. (2) The saturation of the samples was decreased after extraction and drying for 49 days after immersion. Comparing the saturation of water for 28 days, the measured v_p of all samples decreased. E_P was used to characterize the variation in elastic vertical wave velocity, and its expression is as follows:

$$E_p = \left(v_{sp} - v_{fp}\right)\Big/ v_{sp} \times 100\%. \quad (3)$$

In **Eq. 3**, v_{sp} is the original elastic vertical wave velocity and v_{fp} is the elastic P-wave velocity after the test.

The calculation of E_p of the sample treated with acidic solution is shown in **Table 2**. In **Table 2**, the rock saturation increased

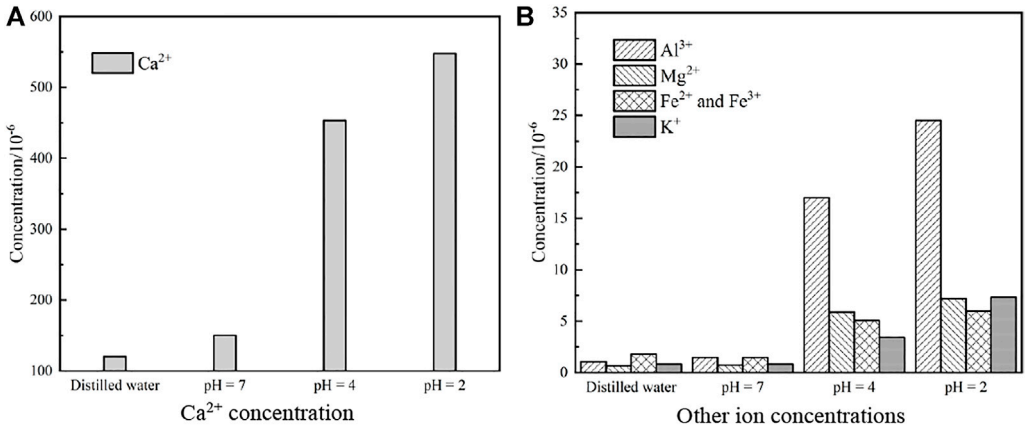

FIGURE 11 | Detection results of ion concentration in aqueous chemical solution after saturation. **(A)** Ca^{2+} concentration. **(B)** Other icon concentration.

after the WRI, but its physical properties deteriorated. The causes are as follows: the reaction of granite active minerals with H^+ in the solution enables the rock to be corroded and dissolved, the whole structure appears fissured, and the porosity increases, which leads to the decrease in v_p.

4 DISCUSSION ON THE MECHANISM OF FLOWING ACIDIC SOLUTION

4.1 Variation in Mineral Composition of Granite

After 49 days of the groundwater velocity (v = 150 mm·s^{-1}) test at the sampling site, the mineral composition profiles of the water and the samples before and after treatment with each acidic solution were obtained by X-ray diffraction phase analysis (see **Figure 10A**). The mineral composition distribution of the sample was obtained using Jade software (see **Figure 10B**) to investigate the mineral composition and physical properties of the granite under the effect of acid solution. The mineral content of the sample is shown in **Table 3**. In order to improve the accuracy of the quantitative analysis of the X-ray diffraction results, the contents of the compounds and elements in all granite samples were determined by a semi-quantitative test (see **Table 4**).

According to **Figure 10** and **Table 3**, calcite and plagioclase increase with acidity, and the contents were reduced to some extent. The calcite was completely dissolved at pH = 4 and 2, but the content of mica and quartz was obviously increased, and new mineral microcline and other impurities were formed in the reaction process.

4.2 Variation in Ion Concentration in Test Solution

When reactive minerals in rocks react with chemical solutions, some elements in rocks enter the solution in the form of ions, and the salinity of the solution changes accordingly. In order to explore the damage mechanism of flowing acidic solution on granite, we analyzed the chemical compounds and mineral components involved in the hydro-chemical reaction of granite, discussed the mode and degree of water–rock interaction, and detected the soaked chemical solution by ion chromatography. The results are shown in **Figure 11**.

Figure 11 shows that H^+ in the immersion solution reacts with mineral components such as calcite and plagioclase in granite to form cations such as Fe^{2+}, Fe^{3+}, Ca^{2+}, Al^{3+}, Mg^{2+}, K^+, and Na^+. Different mineral components had different perceptions of chemical environment, leading to significant differences in the concentration of each ion in the chemical solution. Moreover, the acidic chemical solution contains 0.01 mol·L^{-1} NaCl solution, and the amount of Na^+ precipitated out of granite during the reaction was far less than that of the test solution, so the content variations of Na^+ are not discussed.

In the NaCl solution with pH = 7 and distilled water, there was almost no chemical reaction of granite, and only some silicate and carbonate minerals were hydrolyzed, which led to a slight increase in metal cation concentration. After 49 days of treatment with NaCl solution with pH = 4, the concentration of all metal cations substantially increased, which indicated that the chemical reaction between H^+ in solution and active granite minerals became more and more intense. NaCl solution with pH = 2 for 49 days contained 547.83 × 10^{-6} of Ca^{2+}, 7.19 × 10^{-6} of Mg^{2+}, and 24.52 × 10^{-6} of Al^{3+}, indicating that the precipitated ion concentration was mainly controlled by the initial pH of the chemical solution.

4.3 Chemical Reaction and Mechanism of Granite

4.3.1 Chemical Reaction Process of Acidic Solution With Granite

Tables 3 and **4** show that the mineral composition of granite includes a small amount of mica and calcite and a large amount of plagioclase and quartz. These minerals are easily corroded and hydrolyzed in acidic solutions, and the reaction between calcite and plagioclase and acid solution is more intense, while the reaction between quartz and acid solution is weak. The chemical reactions between acidic solution and the mineral components of the granite are as follows:

1) Reaction between few mica and H^+ ions in solution (Liu et al., 2018):

$$KAl_3Si_3O_{10}(OH)_2 + 10H^+ \rightarrow 3Al^{3+} + 3SiO_2 + 6H_2O + K^+ \quad (4)$$

2) Significant reaction between calcite and H^+ ions in solution (Zhao et al., 2021c):

$$CaCO_3 + 2H^+ \rightarrow Ca^{2+} + H_2O + CO_2 \quad (5)$$

3) Plagioclase, albite, orthoclase, and anorthite as a series of components react with H^+ ions in acidic solution as follows:

$$NaAlSi_3O_8 + 4H^+ \rightarrow Al^{3+} + 3SiO_2 + 2H_2O + Na^+ \quad (6)$$

$$KAlSi_3O_8 + 4H^+ \rightarrow Al^{3+} + 3SiO_2 + 2H_2O + K^+ \quad (7)$$

$$CaAl_2Si_2O_8 + 8H^+ \rightarrow 2Al^{3+} + 2SiO_2 + 4H_2O + Ca^{2+} \quad (8)$$

4) Insignificant hydrolysis reaction occurs after quartz comes into contact with water:

$$SiO_2 + 2H_2O \rightarrow H_4SiO_4 \quad (9)$$

Combined with **Table 3** and **Figure 10A**, we can see that after saturated in NaCl solution with pH = 4 and 2, the calcite in the sample was almost completely hydrolyzed, the content of plagioclase decreased significantly, and microcline was produced. The reaction between acidic solution and mica, quartz, and other mineral reaction was not obvious; hence, the material consumption was less, and the mass percentage of Ca^{2+} precipitated into the solution increased slightly. The micro-mineral composition of granite is easy to change under the effect of acid chemical solution, but the change of mineral composition of the sample is relatively small in the pH = 7 NaCl solution and distilled water.

4.3.2 Chemical Mechanism of Granite in Flowing Acidic Solution

1) Chemical mechanism

Based on the principles of chemical kinetics (Lin et al., 2020), the chemical reactions between the key compounds of granite (see **Table 4**) and the acidic solution are as follows:

$$CaO + 2H^+ == Ca^{2+} + H_2O \quad (10)$$

$$Al_2O_3 + 6H^+ == 2Al^{3+} + 3H_2O \quad (11)$$

$$MgO + 2H^+ == Mg^{2+} + H2O \quad (12)$$

$$Fe_2O_3 + 6H^+ == 2Fe^{3+} + 3H_2O \quad (13)$$

$$K_2O + 2H^+ == 2K^+ + H_2O \quad (14)$$

$$Na_2O + 2H^+ == 2Na^+ + H_2O \quad (15)$$

As can be seen from **Table 4** and **Figure 11**, the content of active compounds such as CaO, MgO, Al_2O_3, Fe_2O_3, Na_2O, K_2O, and so on decreased after the flowing acidic solution, which led to the increase in the concentration of Ca^{2+}, Mg^{2+}, Al^{3+}, Fe^{3+}, K^+, and other metal cations in the solution. Beyond that, in **Table 4** and **Figure 11**, different mineral components in rock samples had different sensitivities in acidic environment: the more acidic the environment, the greater the reaction degree of Al_2O_3 and CaO. In addition, the concentration of plasma such as Al^{3+} and Ca^{2+} increased greatly in the solution after the reaction stopped. The chemical reaction between water and NaCl solution with pH = 7 was weak, and the mineral content in granite was hardly invariant.

Therefore, rock and mineral particles produce various "Ion Exchange (IEX)" under acidic solution, which weakens the compactness of grain skeleton and causes the deterioration of its physical and mechanical properties. Besides, some ions escape with the flowing solution, resulting in the increase of pore size and quantity of granite internal pores, then occurring to the accumulation to form defect morphology, and finally changing the microscopic characterization. The lower the pH value is, the more significant the chemical damage is.

2) Physical effects

The scour and dissolution of the flowing acidic solution reduce the cementation between the granite mineral particles and weaken the friction between the mineral particles. In the meantime, the pore pressure caused by water entering the sample impairs the intergranular compressive stress and then produces a splitting effect on the micropores.

In summary, the chemical disequilibrium between rock minerals and acid solution contributes to an irreversible thermodynamic process, and the physical and chemical reactions between rock and groundwater lead to the deterioration and damage of rock microstructure and mineral composition, which generates hydrolysis and dissolution of primary minerals to form new minerals and components. Moreover, the crystal skeleton and cemented structure of rock particles degenerate, the porosity expands, the rock porosity increases, and the strength decreases. Therefore, the coupling effect between the composition of hydro-chemical solution and the mineral composition, and the overall structure (such as cracks and pores) of rock controls the deterioration mechanism of "water–rock interaction" (WRI), and the microstructure and meso-composition of granite change accordingly.

5 CONCLUSION

In light of the aforementioned work, the main conclusions of this study are as follows:

1) Combined with the SEM and XRD analysis results, the microscopic structure, mineral composition content, and defect morphology of the granite samples change after being treated with various flowing acidic solutions. The initial pH value of solution is the main determinant of chemical corrosion degradation.
2) By observing the test results of damage aging characteristics of granite, granite tends to be stable after acidic solution corrosion for a period of time. At this time, the damage aging curves of sample mass, elastic vertical wave velocity, and chemical solution pH value gradually stabilize. After the granite was soaked in NaCl solution with pH = 2 for 49 days, compared with the low speed (v = 150 mm·s^{-1}, approximate field velocity), the mass damage factor in high speed increased by 8.8% and the elastic vertical wave velocity decreased by 19.3%.

3) The granite secondary porosity increases, the specific surface area increases, the structure tends to be loose, the porosity increases, and the dispersion becomes more obvious after the effect of the flowing acidic solution. The lower the pH value of the solution, the higher the velocity, and the aforementioned variations are more significant.
4) At an approximate in field velocity (v =150 mm·s^{-1}), the chemical reaction process between the rock and the acidic solution and the chemical damage mechanism of the rock are determined by the composition and properties of the aquatic chemical solution, as well as the coupling effect between rock mineral composition and overall structure (such as cracks and pores).

DATA AVAILABILITY STATEMENT

The original contributions presented in the study are included in the article/Supplementary Material, further inquiries can be directed to the corresponding author.

AUTHOR CONTRIBUTIONS

Methodology and funding acquisition: WC, WW, and YZ. Software: QW and SX. Data curation and formal analysis: YZ and XW. Visualization: LW. Supervision: HH. All authors have read and agreed to the published version of the manuscript.

FUNDING

This research was funded by the National Natural Science Foundation of China (51774118, 51774132) and the Natural Science Foundation of Hunan Province (2021JJ30265).

ACKNOWLEDGMENTS

We thank Jie Liu, Min Wang, and Xiaoyu Tang for useful discussions and for early contributions to the project and the reviewers for their very helpful and inspiring comments.

REFERENCES

Bai, B., Long, F., Rao, D., and Xu, T. (2017). The Effect of Temperature on the Seepage Transport of Suspended Particles in a Porous Medium. *Hydrol. Process.* 31 (2), 382–393. doi:10.1002/hyp.11034

Bai, B., Nie, Q., Zhang, Y., Wang, X., and Hu, W. (2021). Cotransport of Heavy Metals and SiO2 Particles at Different Temperatures by Seepage. *J. Hydrology* 597, 125771. doi:10.1016/j.jhydrol.2020.125771

Cai, Y. Y., Yu, J., Fu, G. F., and Li, H. (2016). Experimental Investigation on the Relevance of Mechanical Properties and Porosity of Sandstone after Hydrochemical Erosion. *J. Mt. Sci.* 13 (11), 2053–2068. doi:10.1007/s11629-016-4007-2

Chen, Y., Xiao, P., Du, X., Wang, S., Fernandez-Steeger, T. M., and Azzam, R. (2021). Study on Damage Constitutive Model of Rock under Freeze-Thaw-Confining Pressure-Acid Erosion. *Appl. Sci.* 11 (20), 9431. doi:10.3390/app11209431

Cherblanc, F., Berthonneau, J., Bromblet, P., and Huon, V. (2016). Influence of Water Content on the Mechanical Behaviour of Limestone: Role of the Clay Minerals Content. *Rock Mech. Rock Eng.* 49 (6), 2033–2042. doi:10.1007/s00603-015-0911-y

Dong, L.-j., Zhou, Y., Deng, S.-j., Wang, M., and Sun, D.-y. (2021). Evaluation Methods of Man-Machine-Environment System for Clean and Safe Production in Phosphorus Mines: A Case Study. *J. Cent. South Univ.* 28 (12), 3856–3870. doi:10.1007/s11771-021-4890-8

Dong, L., and Luo, Q. (2022). Investigations and New Insights on Earthquake Mechanics from Fault Slip Experiments. *Earth-Science Rev.* 228, 104019. doi:10.1016/j.earscirev.2022.104019

Dong, L., Sun, D., Shu, W., and Li, X. (2020). Exploration: Safe and Clean Mining on Earth and Asteroids. *J. Clean. Prod.* 257, 120899. doi:10.1016/j.jclepro.2020.120899

Dong, L., Tao, Q., Hu, Q., Deng, S., Chen, Y., Luo, Q., et al. (2022). Acoustic Emission Source Location Method and Experimental Verification for Structures Containing Unknown Empty Areas. *Int. J. Min. Sci. Technol.* 32 (3), 487–497. doi:10.1016/j.ijmst.2022.01.002

Dong, L., Tong, X., Li, X., Zhou, J., Wang, S., and Liu, B. (2019). Some Developments and New Insights of Environmental Problems and Deep Mining Strategy for Cleaner Production in Mines. *J. Clean. Prod.* 210, 1562–1578. doi:10.1016/j.jclepro.2018.10.291

Grgic, D., Al Sahyouni, F., Golfier, F., Moumni, M., and Schoumacker, L. (2022). Evolution of Gas Permeability of Rock Salt under Different Loading Conditions and Implications on the Underground Hydrogen Storage in Salt Caverns. *Rock Mech. Rock Eng.* 55 (2), 691–714. doi:10.1007/s00603-021-02681-y

Ha, Y. D., Lee, J., and Hong, J.-W. (2015). Fracturing Patterns of Rock-like Materials in Compression Captured with Peridynamics. *Eng. Fract. Mech.* 144, 176–193. doi:10.1016/j.engfracmech.2015.06.064

Hao, R.-q., Li, J.-t., Cao, P., Liu, B., and Liao, J. (2015). Test of Subcritical Crack Growth and Fracture Toughness under Water-Rock Interaction in Three Types of Rocks. *J. Cent. South Univ.* 22 (2), 662–668. doi:10.1007/s11771-015-2568-9

Huang, Z., Zeng, W., Gu, Q., Wu, Y., Zhong, W., and Zhao, K. (2021). Investigations of Variations in Physical and Mechanical Properties of Granite, Sandstone, and Marble after Temperature and Acid Solution Treatments. *Constr. Build. Mater.* 307, 124943. doi:10.1016/j.conbuildmat.2021.124943

Huo, R., Li, S., and Ding, Y. (2018). Experimental Study on Physicochemical and Mechanical Properties of Mortar Subjected to Acid Corrosion. *Adv. Mater. Sci. Eng.* 2018, 11. doi:10.1155/2018/3283907

Li, S., Wu, Y., Huo, R., Song, Z., Fujii, Y., and Shen, Y. (2021). Mechanical Properties of Acid-Corroded Sandstone under Uniaxial Compression. *Rock Mech. Rock Eng.* 54 (1), 289–302. doi:10.1007/s00603-020-02262-5

Lin, Y., Zhou, K., Li, J., Ke, B., and Gao, R. (2020). Weakening Laws of Mechanical Properties of Sandstone under the Effect of Chemical Corrosion. *Rock Mech. Rock Eng.* 53 (4), 1857–1877. doi:10.1007/s00603-019-01998-z

Liu, H., Zhu, W., Yu, Y., Xu, T., Li, R., and Liu, X. (2020). Effect of Water Imbibition on Uniaxial Compression Strength of Sandstone. *Int. J. Rock Mech. Min. Sci.* 127, 104200. doi:10.1016/j.ijrmms.2019.104200

Liu, X., Liang, Z., Zhang, Y., Liang, P., and Tian, B. (2018). Experimental Study on the Monitoring of Rockburst in Tunnels under Dry and Saturated Conditions Using AE and Infrared Monitoring. *Tunn. Undergr. Space Technol.* 82, 517–528. doi:10.1016/j.tust.2018.08.011

Liu, X., Wu, L., Zhang, Y., Liang, Z., Yao, X., and Liang, P. (2019). Frequency Properties of Acoustic Emissions from the Dry and Saturated Rock. *Environ. Earth Sci.* 78 (3), 67. doi:10.1007/s12665-019-8058-x

Liu, X., Wu, L., Zhang, Y., and Mao, W. (2021a). Localized Enhancement of Infrared Radiation Temperature of Rock Compressively Sheared to Fracturing Sliding: Features and Significance. *Front. Earth Sci.* 9, 756369. doi:10.3389/feart.2021.756369

Liu, X., Wu, L., Zhang, Y., Wang, S., Yao, X., and Wu, X. (2021b). The Characteristics of Crack Existence and Development during Rock Shear Fracturing Evolution. *Bull. Eng. Geol. Environ.* 80 (2), 1671–1682. doi:10.1007/s10064-020-01997-3

Miao, S., Cai, M., Guo, Q., Wang, P., and Liang, M. (2016). Damage Effects and Mechanisms in Granite Treated with Acidic Chemical Solutions. *Int. J. Rock Mech. Min. Sci.* 88, 77–86. doi:10.1016/j.ijrmms.2016.07.002

Wang, S., Chen, Y., Ni, J., Liu, G., Fernández-Steeger, T. M., and Xu, C. (2021). Mechanical Characteristics and Mechanism of Granite Subjected to Coupling Effect of Acidic Corrosion and Freeze-Thaw Cycles. *J. Earth Sci.* 32 (5), 1202–1211. doi:10.1007/s12583-021-1414-2

Weng, L., Wu, Q.-h., Zhao, Y.-l., and Wang, S.-m. (2020). Dynamic Response and Failure of Rock in Initial Gradient Stress Field under Stress Wave Loading. *J. Cent. South Univ.* 27 (3), 963–972. doi:10.1007/s11771-020-4344-8

Xie, S. Y., Shao, J. F., and Xu, W. Y. (2011). Influences of Chemical Degradation on Mechanical Behaviour of a Limestone. *Int. J. Rock Mech. Min. Sci.* 48 (5), 741–747. doi:10.1016/j.ijrmms.2011.04.015

Zhao, Y., Li, Y., Chang, L., Wang, Y., and Lin, H. (2021a). Shear Behaviors of Clay-Infilled Joint with Different Water Contents: Experiment and Model. *Arab. J. Geosci.* 14 (17), 1724. doi:10.1007/s12517-021-08207-8

Zhao, Y., Liu, Q., Zhang, C., Liao, J., Lin, H., and Wang, Y. (2021b). Coupled Seepage-Damage Effect in Fractured Rock Masses: Model Development and a Case Study. *Int. J. Rock Mech. Min. Sci.* 144, 104822. doi:10.1016/j.ijrmms.2021.104822

Zhao, Y., Wang, Y., and Tang, L. (2019). The Compressive-Shear Fracture Strength of Rock Containing Water Based on Druker-Prager Failure Criterion. *Arab. J. Geosci.* 12 (15), 452. doi:10.1007/s12517-019-4628-1

Zhao, Y., Wang, Y., Wang, W., Wan, W., and Tang, J. (2017a). Modeling of Non-linear Rheological Behavior of Hard Rock Using Triaxial Rheological Experiment. *Int. J. Rock Mech. Min. Sci.* 93, 66–75. doi:10.1016/j.ijrmms.2017.01.004

Zhao, Y., Zhang, C., Wang, Y., and Lin, H. (2021c). Shear-related Roughness Classification and Strength Model of Natural Rock Joint Based on Fuzzy Comprehensive Evaluation. *Int. J. Rock Mech. Min. Sci.* 137, 104550. doi:10.1016/j.ijrmms.2020.104550

Zhao, Y., Zhang, L., Wang, W., Pu, C., Wan, W., and Tang, J. (2016). Cracking and Stress-Strain Behavior of Rock-like Material Containing Two Flaws under Uniaxial Compression. *Rock Mech. Rock Eng.* 49 (7), 2665–2687. doi:10.1007/s00603-016-0932-1

Zhao, Y., Zhang, L., Wang, W., Wan, W., Li, S., Ma, W., et al. (2017b). Creep Behavior of Intact and Cracked Limestone under Multi-Level Loading and Unloading Cycles. *Rock Mech. Rock Eng.* 50 (6), 1409–1424. doi:10.1007/s00603-017-1187-1

Zhou, X.-P., Li, G.-Q., and Ma, H.-C. (2020). Real-time Experiment Investigations on the Coupled Thermomechanical and Cracking Behaviors in Granite Containing Three Pre-existing Fissures. *Eng. Fract. Mech.* 224, 106797. doi:10.1016/j.engfracmech.2019.106797

Zhou, X.-P., Zhang, J.-Z., Qian, Q.-H., and Niu, Y. (2019). Experimental Investigation of Progressive Cracking Processes in Granite under Uniaxial Loading Using Digital Imaging and AE Techniques. *J. Struct. Geol.* 126, 129–145. doi:10.1016/j.jsg.2019.06.003

Conflict of Interest: The authors declare that the research was conducted in the absence of any commercial or financial relationships that could be construed as a potential conflict of interest.

Publisher's Note: All claims expressed in this article are solely those of the authors and do not necessarily represent those of their affiliated organizations, or those of the publisher, the editors, and the reviewers. Any product that may be evaluated in this article, or claim that may be made by its manufacturer, is not guaranteed or endorsed by the publisher.

frontiers | Frontiers in Earth Science

METHODS
published: 22 July 2022
doi: 10.3389/feart.2022.858041

Non-Parametric Simultaneous Reconstruction and Denoising *via* Sparse and Low-Rank Regularization

Lingjun Meng[1], *Zhanzhan Shi*[2,3]*, *Yan Ye*[4] *and Yuanjun Wang*[1,5]

[1]College of Geophysics, Chengdu University of Technology, Chengdu, China, [2]School of Artificial Intelligence, Leshan Normal University, Leshan, China, [3]Key Laboratory of Internet Natural Language Processing of Sichuan Education Department, Leshan Normal University, Leshan, China, [4]Institute of Sedimentary Geology, Chengdu University of Technology, Chengdu, China, [5]School of Education, China West Normal University, Nanchong, China

Spatial irregular sampling and random noise are two important factors that restrict the accuracy of seismic imaging. Seismic wavefield reconstruction and denoising based on sparse representation are two popular antidotes to these two inevitable issues, respectively. This article presents a non-parametric simultaneous reconstruction and denoising via sparse and low-rank regularization that dealt with the prestack gathers efficiently and automatically. The proposed method makes no additional prior assumptions on original data other than that the seismic signal is compressible. The key parameters estimation adopts a data-driven framework without person-dependent intervention. The basic idea of the approach is to combine the two related algorithms. Thus, the sparse decomposition needs to be performed only once. We first extract the solution matrix via Fourier dictionary and then perform the reconstruction and denoising successively in the sparse domain. Obtaining a perfect interpolation result requires that the seismic data satisfy the Shannon–Nyquist sampling theorem. However, data with steep-dip events or gaps, which cannot be adequate for the procedure, are a challenge that must be faced. This work proposes to deal with the common-offset gathers, which is characterized by flat, even approximate horizontal events, to handle the under-sampling obstacle. Another excellent property of the common-offset gathers is the simple and periodic repetitive texture structure, which can be represented sparsely and accurately by the Fourier dictionary. Thus, the computational complexity of the sparse representation is reduced. Both synthetic and practical applications indicate that our algorithm is efficient and effective.

Keywords: wavefield reconstruction, denoising, common offset gather, sparse representation, low-rank regularization

OPEN ACCESS

Edited by:
Wenzhuo Cao,
Imperial College London,
United Kingdom

Reviewed by:
Qiaomu Luo,
Central South University, China
Xueyi Shang,
Chongqing University, China
Fei Wang,
Colorado School of Mines,
United States

***Correspondence:**
Zhanzhan Shi
shizhanzh@163.com

Specialty section:
This article was submitted to Structural Geology and Tectonics, a section of the journal Frontiers in Earth Science

Received: *19 January 2022*
Accepted: *14 June 2022*
Published: *22 July 2022*

Citation:
Meng L, Shi Z, Ye Y and Wang Y (2022) Non-Parametric Simultaneous Reconstruction and Denoising via Sparse and Low-Rank Regularization. Front. Earth Sci. 10:858041. doi: 10.3389/feart.2022.858041

1 INTRODUCTION

Seismic data are inevitably corrupted by missing traces and random noise in field procedures, which often lead to the low signal-noise ratio (SNR), irregular sampling, and even anomalies, such as spatial aliasing and acquisition footprints. Defect data may cause severe consequences in subsequent processing flows, that is, velocity analysis, normal moveout (NMO) correction, migration, amplitude-versus-offset (AVO) analysis, and seismic attributes extraction. Hence, seismic wavefield reconstruction conjugation with denoising play fundamental roles in data analysis.

This article proposes using tools in compressed sensing to solve both interpolation and noise reduction.

However, due to parameter tuning and computational complexity, wavefield reconstruction and denoising are usually regarded as two independent seismic processing flows, even though they share common calculation steps and algorithms, such as sparse decomposition. The target of the seismic wavefield reconstruction is to provide a uniformly sampled data cube. The reconstruction problem has received sufficient study. The previous works addressing this problem can be classified into four categories: wave equation-based interpolation (Ronen 1987), matrix or tensor completion (Kreimer et al., 2013; Chen et al., 2016a; Siahsar et al., 2017; Zhang et al., 2017), deep learning- (Jia and Ma 2017; Oliveira et al., 2018; Wang et al., 2018) and (Cao et al., 2020) compressed sensing-based interpolation. Among them, the compressed sensing-based method has received widespread attention due to its low computational cost. The recorded seismic data can be interpreted as a random sampling of the complete seismic data. Therefore, the problem of seismic data interpolation can be formulated as an inverse problem. Many algorithms have been introduced such as non-equispaced curvelet transform-based method, which processes irregularly sampled data gather by gather (Hennenfent et al., 2010); piecewise random subsampling scheme solved by L_1-norm constrained trust region method (Wang et al., 2011); weighted L_1-norm minimization-based wavefield reconstruction (Mansour et al., 2013), which suggests interpolating 2D partitions of the seismic line instead of the 3D cube to save computer memory (Chen et al., 2019a). reviewed the state-of-the-art interpolation models and their theoretical implications. Curvelet reconstructs the time slices by linearized Bregman method (Zhang et al., 2019); this approach can effectively handle non-uniformly sampled seismic data. The constrained optimization algorithm is an integral part of the reconstruction problem, and algorithms that can solve large-scale sparse representation are desirable. Many different algorithms have been proposed, such as orthogonal matching pursuit (OMP), alternating direction method of multipliers (ADMM) (Lu et al., 2018), Nesterov's algorithm (NESTA) (Becker et al., 2011), spectral projection gradient method (SPGL1) (van den Berg and Friedlander 2008), and linearized Bregman method (Yin 2010). In seismic wavefield reconstruction, the dictionaries for sparse representation are often fast operators. Matrix-free and scale well algorithms, that is, SPGL1 and linearized Bregman, should be required to enable sparse representation for extremely large-scale reconstruction problems.

Random noise suppression attempts to improve the SNR of seismic data with the ultimate aim to improve imaging accuracy (Anvari et al., 2017; Chen et al., 2017) classified the denoising methods into four categories: predictive filtering-based (Chen and Ma 2014), decomposition-based (Gómez et al., 2019), sparse transform-based (Deng et al., 2017; Yuan et al., 2018; Chen et al., 2019b), and rank reduction-based (Chen et al., 2017; Anvari et al., 2019; Wang et al., 2019) seismic denoising. The principles of random noise suppression of all categories are that the statistical characteristics or propagation laws of signal and noise are different in a specific domain. Among them, low rank-based approach is an important category and consistent with the hypothesis that the seismic signal is low-rank in specific domains (Ma 2013; Anvari et al., 2017). Based on this property, noise and the useful signal can be separated by low-rank matrix or tensor decomposition in a specific domain, that is, Hankel (Wang et al., 2019) and synchrosqueezed wavelet (Anvari et al., 2017, 2019) transform. Another appealing low-rank–based denoising is the singular value thresholding (SVT) (Zhou and Zhang 2017) and its variants (Bekara and Van der Baan 2007; Chiu and Howell 2008), which is elegant and flexible and can be used in different steps of seismic signal processing. A vital issue in SVT is how much shrinkage should be imposed. Improper shrinkage may result in large bias or high variance (Candes et al., 2013). Luckily, Candes et al. (2013) proposed an unbiased risk estimate for SVT based on Stein's unbiased risk estimate (SURE).

Simultaneous reconstruction and denoising of multichannel seismic data is not a new topic. A lot of published literature targeting solving the two problems at the same time have been published. The clean prestack cube is inherently low-rank in the *f-x* domain and other transform domains. When missing-traces are encountered and corrupted by random noise, the defective seismic data's rank is inevitably increasing. Rank reduction and low-rank decomposition have been developed to overcome these two problems. Typical studies include: Oropeza and Sacchi (2011) proposed a rank reduction algorithm based on multichannel singular spectrum analysis (MSSA) and can be easily implemented by singular value decomposition (SVD). Instead of organizing spatial data into block Hankel matrixes (Kreimer and Sacchi 2012), rank-reduction to the fourth-order seismic tensor via higher-order singular value decomposition (HOSVD) was applied (Ely et al., 2015), and a 5D completion and denoising based on a complexity-penalized algorithm and tensor singular value decomposition (tSVD) was proposed. The method needs to tune only one regularization parameter. Sternfels et al. (2015) show that the method of joint low-rank and sparse inversion is suitable for random and erratic noise. To deal with the extremely noisy cube, Chen et al. (2016b) introduced a damped rank-reduction method to formulate the Cadzow rank-reduction and proposed a 5-D reconstruction and denoising method.

In this article, a practical implementation of simultaneous reconstruction and denoising was presented, which is parameter-free and can be solved via sparse and low-rank regularization efficiently. The contributions of this article are four-fold. First, the classic simultaneous denoising and interpolation algorithm map the seismic data to a high-dimensional (4D or 5D) tensor and are computationally intensive. The new method only involves matrix operations instead of handling tensor and extracting the coefficient matrix only once. Second, the parameters are adaptively obtained and do not need to be tuned manually. Third, the work demonstrated by experiments that compare to common mid-point (CMP), common-shot gathers, and common-offset gathers strategy enjoys its anti-aliasing ability and is bright to handle the under-sampling obstacle. Fourth, the

sparse representation of common-offset gather via the Fourier dictionary is accurately enough and computationally inexpensive compared to the curvelet dictionary.

2 METHODOLOGY

2.1 Problem Formulation

Seismic data have two dimensions of time and space. The seismic traces are usually uniformly sampled in the temporal domain, and the Nyquist–Shannon sampling theorem is satisfied. However, due to existing obstacles and economic restrictions, there is always missing traces in seismic data, resulting in non-uniformly sampled, even aliased in the spatial domain. Moreover, seismic data are inevitably polluted by random noise. Complete and clean seismic data need to be reconstructed from recorded noisy and incomplete seismic data.

The relationship between the recorded seismic data and the complete data can be formalized as:

$$\mathbf{y} = \mathbf{L}\mathbf{x}, \tag{1}$$

where $\mathbf{y}$ and $\mathbf{x}$ are the recorded (incomplete) seismic data and complete data, respectively. Both $\mathbf{y}$ and $\mathbf{x}$ are constructed by arranging all the traces of the recorded ($\mathbf{Y}$) and complete ($\mathbf{X}$) data matrix into vectors. $\mathbf{L}$ represents the measurement matrix, which is a block diagonal matrix and is defined as $\mathbf{L} = \begin{bmatrix} \mathbf{I} & & & & & \\ & \mathbf{I} & & & & \\ & & \mathbf{0} & & & \\ & & & \mathbf{I} & & \\ & & & & \ddots & \\ & & & & & \mathbf{I} \end{bmatrix}$ (each $\mathbf{0}$ represents a missing trace, and each $\mathbf{I}$ represents a recorded seismic trace).

It should note that both $\mathbf{y}$ and $\mathbf{x}$ are infected by random noise. The purpose of the proposed method is to reconstruct the expected clean and complete data $\mathbf{x}^*$ from $\mathbf{y}$. Solving **Eq. 1** can only give rise to complete noisy data. However, worse still, seismic wavefield reconstruction aims to recover a high-dimensional signal cube from a smaller number of measurements. **formula (1)** is underdetermined and has infinitely many solutions. The proposed countermeasure to address these two bottlenecks will be described in detail in the following subsections.

2.2 Simultaneous Reconstruction and Denoising in the Sparse Domain

It is possible to reconstruct sparse signals from highly incomplete sets, which can be done by sparse representation. The seismic data are compressible and sparse in the curvelet and Fourier domains. The sparsity adds effective constraints to the underdetermined inverse problem, thereby reducing the distress of the multiplicity. So, an effective strategy for the underdetermined problem **(1)** is that we can transform $\mathbf{x}$ into the Fourier or curvelet domain (as shown in **Eq. 2**) and then formulate the reconstruction problem as an L_1-norm regularization (as shown in **Eq. 3**) (Mansour et al., 2013).

$$\mathbf{y} = \mathbf{A}\mathbf{m}, \mathbf{A} = \mathbf{L}\mathbf{F}^H, \tag{2}$$

where $\mathbf{F}$ is a sparsifying operator; that is, Fourier or curvelet transform, $\mathbf{m}$ is the Fourier or curvelet coefficient, and superscript H represents the conjugate transpose.

$$\arg\min_{\mathbf{m}} \|\mathbf{m}\|_1 \; s.t. \; \left\|\mathbf{y} - \mathbf{A}\mathbf{m}\right\|_2^2 \le \varepsilon, \tag{3}$$

where $\|\cdot\|_1$ and $\|\cdot\|_2$ denote L_1- and L_2-norms, respectively; ε is a fitting error. We have learned that **Eq. 3** is a basis pursuit denoise (BPDN) problem; it can be optimized by the spectral projection gradient method. However, L_1-norm is non-differentiable and the augmented model for **Eq. 2** is adopted (Yin 2010):

$$\mathbf{m}^* = \arg\min_{\mathbf{m}} \|\mathbf{m}\|_1 + \frac{1}{2\alpha}\|\mathbf{m}\|_2 \; s.t. \; \left\|\mathbf{y} - \mathbf{A}\mathbf{m}\right\|_2^2 \le \varepsilon, \tag{4}$$

where typically $\alpha = 1$.

Solving **Eq. 4** can only get complete noisy data, that is, $\mathbf{m}^*$ is corrupted by noise. Consequently, the next step is to denoise the reconstruction $\mathbf{m}^*$. We first rearrange $\mathbf{m}^*$ into a 2D matrix $\mathbf{M}$.

Due to the repetitive texture structure, the prestack seismic gathers are low-rank matrixes (Ma 2013). In a transformed domain, that is, Fourier and curvelet domains, the coefficient matrix $\mathbf{M}$ is also characterized by the low-rank feature (Nazari Siahsar et al., 2016). Suppose $\mathbf{M}$ is sullied by Gaussian noise, we have the noisy coefficient matrix $\mathbf{M}$ about a clean low-rank matrix $\mathbf{M}_{\text{den}}$ of interest. A natural approach to this problem is singular value thresholding (SVT), which formalizes noise suppression as:

$$\mathbf{M}_{\text{den}} = \text{SVT}_\lambda(\mathbf{M}) = \arg\min_{\mathbf{M}_{\text{den}}} \lambda \text{rank}(\mathbf{M}_{\text{den}}) + \frac{1}{2}\|\mathbf{M} - \mathbf{M}_{\text{den}}\|_F^2, \tag{5}$$

where $\|\cdot\|_F$ is the Frobenius norm and $\mathbf{M} = \mathbf{U}\mathbf{\Sigma}\mathbf{V}^H$ ($\mathbf{U} = [\mathbf{u}_1, \mathbf{u}_2, \cdots \mathbf{u}_n]$ and $\mathbf{V} = [\mathbf{v}_1, \mathbf{v}_2, \cdots \mathbf{v}_n]$ are left and right singular vectors, respectively; $\mathbf{\Sigma} = diag(\sigma_1, \sigma_2, \cdots, \sigma_n)$ is a diagonal matrix with singular values of $\mathbf{M}$ on its diagonal) is the singular value decomposition (SVD) of $\mathbf{M}$. The solution of **(5)** is given by retaining only the part of the expansion with singular values exceeding λ (Candes et al., 2013):

$$\mathbf{M}_{\text{den}} = \sum (\sigma_i - \lambda)_+ \mathbf{u}_i \mathbf{v}_i^H, \tag{6}$$

where $x_+ = \max(x, 0)$ and λ is the threshold value which can be estimated by Stein's unbiased risk estimate (SURE).

The clean and complete seismic section is reconstructed from the denoised coefficient matrix $\mathbf{M}_{\text{den}}$ just via matrix-vector multiplication, which can be formulated as

$$\mathbf{y}_{\text{den}} = \mathbf{F}\mathbf{m}_{\text{den}}, \tag{7}$$

where $\mathbf{m}_{\text{den}}$ is the vectorization of $\mathbf{M}_{\text{den}}$.

Now we recall the simultaneous reconstruction and denoising methods as follows:

1. Noise level estimation: estimating the parameter ε for (4) (discussed in **Subsection 2.5**).

2. Estimating a complete sparse and low-rank coefficient vector $\mathbf{m}^*$ by solving **Eq. 4** via linearized Bregman method (discussed in **Subsection 2.3**).
3. Denoising coefficient matrix $\mathbf{M}$ by SVT (discussed in **Subsection 2.4**).
4. Reconstructing the clean and complete seismic section by **(6)**.

2.3 Linearized Bregman Method

The original Bregman method was proposed to restore noisy and blurry images via total variation (TV) regularization (Osher et al., 2005), and then be formulized to solving the basis pursuit (BP) problem (Yin et al., 2008), where the author had proved that Bregman iterative method was equivalent to the augmented Lagrangian method.

The Bregman distance with respect to a convex function J between two points u and v is defined as

$$D_J^p(u,v):\ = J(u) - J(v) - \geq \langle p, u - v\rangle, \tag{8}$$

where $p \in \partial J(v)$ ($\partial J(v)$ denotes the subdifferential of J at v), and symbol $\langle\cdot,\cdot\rangle$ denotes the inner product. The original Bregman method is an iterative regularization procedure which focuses on the problem $\arg\min_{\mathbf{x}} J(\mathbf{x}) s.t.\ \mathbf{Ax} = \mathbf{b}$, that solves a sequence of convex problems, which can be formulated as

$$\mathbf{x}^{k+1} = \min_{\mathbf{x}} D_J^{p^k}\left(\mathbf{x}, \mathbf{x}^k\right) + \frac{1}{2}\|\mathbf{Ax} - \mathbf{b}\|_2^2. \tag{9}$$

As a variant of the original Bregman method, the linearized Bregman algorithm imposes two modifications to the original method: (1) substitute the last quadratic penalty term $\|\mathbf{Ax} - \mathbf{b}\|_2^2$ with its linearization $\langle \mathbf{A}^T(\mathbf{Ax}^k - \mathbf{b}), \mathbf{x}\rangle$ (superscript T denotes the transposition), (2) add a new quadratic penalty term $\frac{1}{2\alpha}\|\mathbf{x} - \mathbf{x}^k\|_2^2$. Then, we get the following updates for the linearized Bregman algorithm (Yin, 2010):

$$\begin{cases} \mathbf{x}^{k+1} = \min_{\mathbf{x}} D_J^{p^k}\left(\mathbf{x}, \mathbf{x}^k\right) + \langle \mathbf{A}^T\left(\mathbf{Ax}^k - \mathbf{b}\right), \mathbf{x}\rangle + \frac{1}{2\alpha}\left\|\mathbf{x} - \mathbf{x}^k\right\|_2^2 \\ p^{k+1} = p^k - \mathbf{A}^T\left(\mathbf{Ax}^k - \mathbf{b}\right) - \frac{1}{\alpha}\left(\mathbf{x}^{k+1} - \mathbf{x}^k\right) \end{cases}, \tag{10}$$

Based on the equivalence between the linearized Bregman algorithm and the gradient descent, Yin (2010) generalized the linearized Bregman by integrating the gradient-based optimization techniques to make the method more accurate and much faster.

To address **Eq. 4**, we take $J(\mathbf{x}) = \|\mathbf{x}\|_1$, and the problem can be solved with the linearized Bregman algorithm by the following iterative scheme:

$$\begin{cases} \mathbf{v}^{k+1} = \mathbf{v}^k + \delta^k\left(\mathbf{b} - \alpha\mathbf{A}Shrink\left(\mathbf{A}^T\mathbf{x}^k\right)\right) \\ \mathbf{x}^{k+1} = \alpha Shrink\left(\mathbf{A}^T\mathbf{v}^{k+1}\right) \end{cases}, \tag{11}$$

where δ^k is the step size at iteration k.

2.4 Optimal Threshold Value Estimation by SURE

In this subsection, we focus on the vital issue of threshold parameter selection because the unreasonable threshold inevitably limits the denoising ability even to generate artifacts. Specifically, excessive shrinkage results in a large bias, while excessively low threshold value results in a high variance. Common methods of parameter selection include discrepancy principle, cross-validation (Li et al., 2019), L-curve (Hansen 1992), and estimation of the mean-squared error (MSE) (Batu and Cetin 2011), and so on. Ramani et al. (2012) summarized the advantages and disadvantages of these methods and recommended using MSE to optimize the regularization parameter quantitatively. A classical unbiased estimator of the MSE is SURE (Stein 1981), which was reported to be used in quantitative parameter optimization (Ramani et al., 2012; Candes et al., 2013; Rasti et al., 2015).

MSE-estimation-based methods tune the regularization parameter λ to minimize the MSE or risk:

$$R_\lambda = E\|\mathbf{M}_{\text{den}} - \mathbf{M}_0\|_F^2, \tag{12}$$

where $\mathbf{M}_0$ is the ground truth.

When the seismic data are corrupted by additive random noise, it is possible to obtain an unbiased estimate of the risk via SURE (Candes et al., 2013):

$$R_\lambda = -ab\tau + \sum_{i=1}^{\min(a,b)} \min\left(\lambda^2, \sigma_i^2\right) + 2\tau^2 \text{div}\left(\text{SVT}_\lambda(\mathbf{M})\right), \tag{13}$$

where τ is the standard variance of the additive random noise; a and b are the numbers of rows and columns, respectively; symbol "div" denotes the divergence operator. From Candes et al. (2013), it is clear that

$$\text{div}\left(\text{SVT}_\lambda(\mathbf{M}^*)\right) = (2|a-b|+1)\sum_{i=1}^{\min(a,b)}\left(1 - \frac{\lambda}{\sigma_i}\right) + \sum_{i=1}^{\min(a,b)} I(\sigma_i > \lambda) + \sum_{i\neq j, i,j=1}^{\min(a,b)} \frac{\sigma_i(\sigma_i - \lambda)_+}{\sigma_i^2 - \sigma_j^2}, \tag{14}$$

where I is the indicator function.

2.5 Noise Level Estimation

Noise level is an extremely important parameter to achieve a guaranteed performance of both sparse representation and SVT. Specifically, in **Eqs 3**, **4**, parameter ε prescribes the desired fit in $\mathbf{Am} \approx \mathbf{y}$, which can be substituted by noise variance τ^2 in the random noise scenario. Meanwhile, a reliable estimate of the noise level is needed for SURE to get the proper threshold value. In this work, we choose the multiple regression theory-based approach (Roger and Arnold 1996; Chein-I and Qian 2004; Bioucas-Dias and Nascimento 2008) for noise level estimation. The seismic gather, especially common-offset gather, exhibits high spatial coherence between neighboring traces in both the time and frequency domains, which guarantees the successful application of the multiple regression theory-based approach.

Let $Y = [\mathbf{y}_1, \mathbf{y}_2, \cdots, \mathbf{y}_M]$ denote a $M \times N$ matrix holding the seismic gather, with each column $\mathbf{y}_i$ accommodating a single trace. Let $\mathbf{Y}_{\partial i} = [\mathbf{y}_1, \mathbf{y}_2, \cdots, \mathbf{y}_{i-1}, \mathbf{y}_{i+1}, \cdots, \mathbf{y}_M]$ be the explanatory data matrix of $\mathbf{y}_i$. Let us assume that $\mathbf{y}_i$ can be linearly represented by other seismic traces in the gather. Therefore, we can express $\mathbf{y}_i$ as

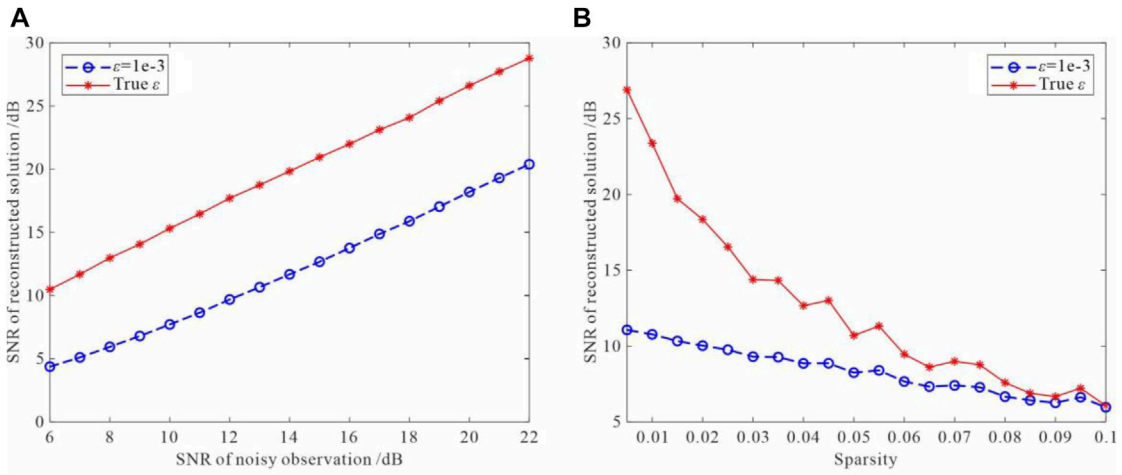

FIGURE 1 | Comparison of the performance of different fitting errors. Blue: $\varepsilon = 1e^{-3}$. Red: ε is the L_2-norm of the noise. **(A)** SNRs of reconstructed solutions for different ε with a fixed sparsity (sparsity = 2 %), while varying the observations' SNRs. **(B)** Plots of SNRs of reconstructed solutions versus sparsity with the observations' SNRs are fixed at 10 dB.

$$\mathbf{y}_i = \mathbf{Y}_{\partial i}\boldsymbol{\beta}_i + \boldsymbol{\xi}_i, \tag{15}$$

where $\boldsymbol{\beta}_i$ denotes the regression vector of length $M-1$, $\boldsymbol{\xi}_i$ denotes the modeling error of length N. The noise for each trace can be derived from the following formula:

$$\hat{\boldsymbol{\xi}}_i = \mathbf{y}_i - \mathbf{Y}_{\partial i}\boldsymbol{\beta}_i. \tag{16}$$

Then, it is easy to calculate the noise variance using the standard formula.

3 Performance Evaluation With Simulated Data

In this section, we validate the effectiveness of the proposed method by simulated data. We first consider a classic problem of sparse solution recovery to emphasize the importance of ε in **(3)** and **4**. We then provide a layered model and perform wavefield modeling, followed by randomly decimated data with 25% missing traces. A set of experiments, that is, noise level estimation and simultaneous reconstruction and denoising, are conducted. All experiments deal with common-shot gathers and common-offset gathers separately, and the purpose is to compare different method combinations.

3.1 Fitting Error Versus Optimality

In **(3)** and **4**, parameter ε prescribes the fitting error. However, the importance of parameter ε is often ignored in literature or software packages. $\varepsilon = 1e^{-3}$ is usually recommended. The parameter ε is essentially an estimate of the noise level of the seismic signal and can be quantified by an upper bound on its norm. In this subsection, we make a digression to emphasize the importance of ε, with a compressive sensing problem based on random Gaussian matrices. The size of the matrices is 2000×4000. We compare SNRs of reconstructed solutions on two sets of values for the parameter ε: $1e^{-3}$ and L_2-norm of deterministic noise. We first fix the sparse signal with 5% non-zero entries. The results of the model (4) with noisy observations of different SNRs are plotted in **Figure 1A**. On the contrary, SNRs of the observations are fixed and equal to 10 dB, we change the sparsity of the sparse solutions, and plot the calculation results of **Eq. 4** in **Figure 1B**. Both **Figure 1A,B** indicate that the proper parameter value of ε is a sufficient condition for recovering the sparse solution to high accuracy. Taking L_2-norm of deterministic noise can be potentially much better than the default. We fix sparsity = 2 % and SNR of the observation is 10 dB and plot the computed coefficients (red) on top of the ground truth (blue) in **Figure 2**. Model (4) finds better solutions when ε takes the L_2-norm of noise.

3.2 Simulating the Randomly Decimated Data

We first use a five-layer model (**Figure 3A**) to perform wavefield modeling. The synthetic line has 48 shot gathers, and 48 traces per each shot gather and CMP gather. Source-station and receiver-station spacings are both 50 m. The data are recorded for 1.000 s, with a sample interval of 0.002 s. **Figure 3B,C** show the reflectivity and seismogram gathers of the first CMP gather. **Figure 3D** presents the 24th common-offset gather (offset is 50 m). CMP gather is characterized by hyperbolic events, while the common-offset gather consists of flat events, which share approximately equal two-way times. Compared with CMP gather, each trace in common-offset gather shows better similarity and simpler texture structure. This makes it easier to deal with common-offset gather in both the time-space domain and Fourier domain.

The field-recorded seismic data are inevitably perturbed by random noise. Therefore, we add random noise at various levels to the synthetic data to make the SNR of each noisy trace vary within a range of 1–10 dB. The first noisy CMP and the 24th noisy

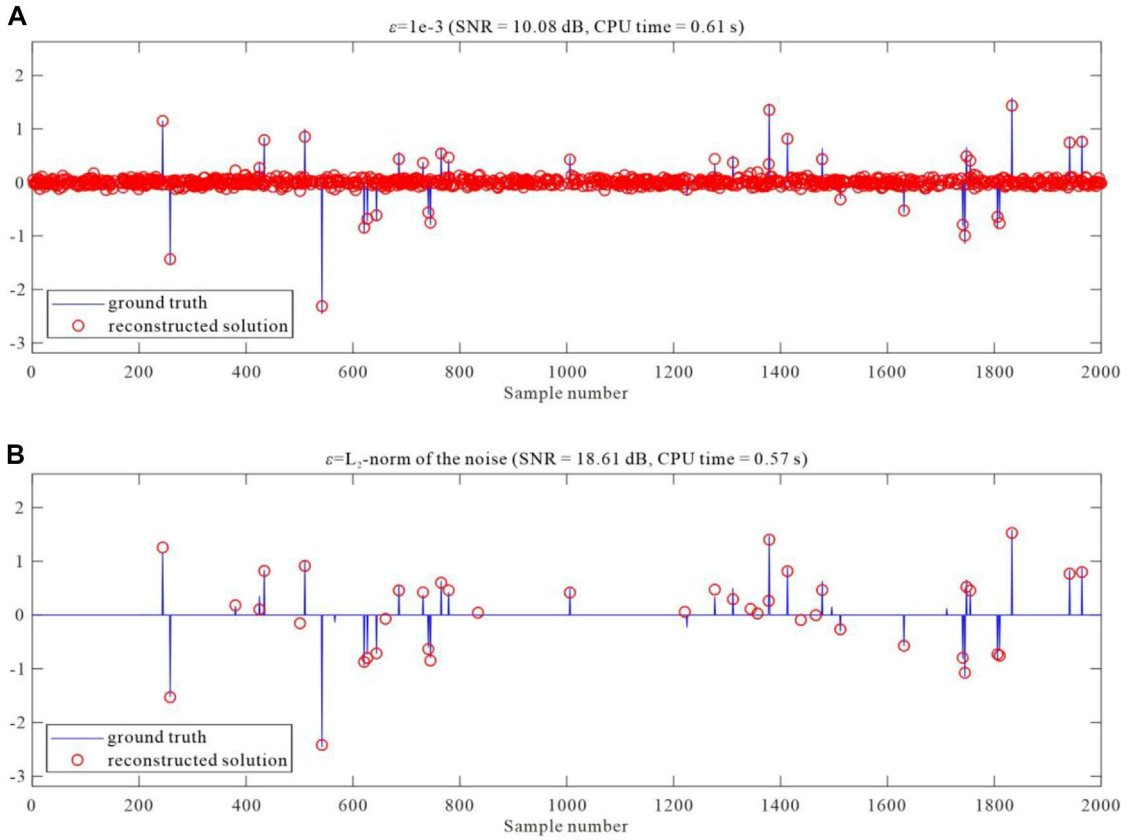

FIGURE 2 | Plots of reconstructed solutions for $\varepsilon = 1e^{-3}$ and ε are the L_2-norm of the noise. Reconstructed solutions (red) are plotted on top of the ground truth (blue). **(A)** $\varepsilon = 1e^{-3}$. **(B)** ε is the L_2-norm of the noise.

common-offset gathers are shown in **Figure 4A,B**, respectively. To simulate the irregularly sampled seismic data, we randomly zero out 25% of the receivers and artificially create some gaps to increase the difficulty of the experiments. The incomplete noisy CMP and common-offset gathers are shown in **Figure 4C,D**, respectively.

To inspect the amplitudes of the seismic data at different frequencies and wave-numbers, we perform 2-D Fourier transform on both complete noisy CMP and common-offset gathers to transform them into frequency-wavenumber (*f-k*) domain, as indicated in **Figure 5A,B**, respectively. Note that obvious spatial aliasing exists in the *f-k* spectra for the CMP gather that indicates insufficient sampling of the data along the space axis. However, COG is free from aliasing.

3.3 Curvelet Transform Operator Tests

Most relevant literature (Zhang et al., 2019; Cao et al., 2020) characterizes the sparse representation of seismic data based on curvelet transform. We use the approved algorithm (curvelet domain approach) to deal with the common-offset and the CMP gathers, separately. The experiment served two purposes: (1) Spatial aliasing has severe effects on the performance of curvelet domain approach in the time-offset domain (common-shot and CMP gathers); (2) Noise estimation and wavefield reconstruction can be done better in the time-midpoint domain (common-offset gather).

Determining an optimal threshold value is an essential first step for sparse representation and the implicit reconstruction and denoising. We first apply the multiple regression theory-based approach to evaluate the noise level both in time-midpoint and time-offset domain, respectively. In implementing this step, we get poor result with CMP gather, as demonstrated in **Figure 6A**. The estimated L_2-norm of the noise aliasing in each trace is much lower than the actual noise level. This is basically because the multiple regression theory-based method assumes that each trace can be linearly represented by other seismic traces in the gather. CMP gather is characterized by hyperbolic events that have disparate TWT. They share a low correlation between neighboring traces that dissatisfy the multiple regression theory-based method. The procedure is also applied to common-offset gather, and the obtained result is plotted in **Figure 6B** that indicates that the estimated value is approximately correct.

To fill in the gaps and denoise the incomplete noisy data using sparse representation, we use the curvelet transform as "sparse basis" to create matrices **A** in **Eq. 2**. The linear relation between the **y** and **m** inspires us to consider estimating complete sparse and low-rank coefficient vector $\mathbf{m}^*$ by solving **Eq. 4** via the

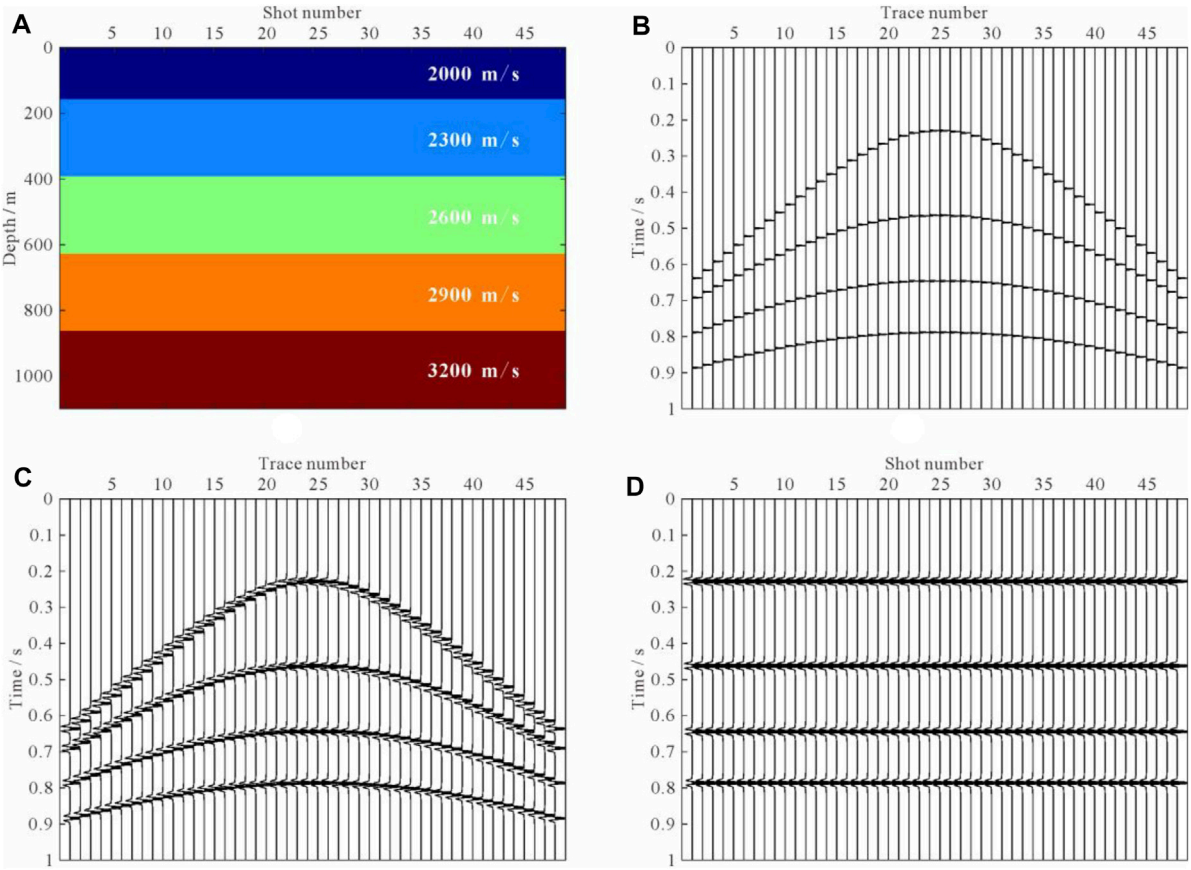

FIGURE 3 | Geologic model and seismic wavefield modeling. **(A)** Geologic model. **(B)** first reflectivity CMP gather. **(C)** first seismogram CMP gather, which is characterized by hyperbolic events. **(D)** 24th common-offset gather (offset is 50 m), which is characterized by flat events.

linearized Bregman method. We take ε as the Frobenius norm of noise to balance the fidelity and sparsity. **Figure 7A,B** are based upon the processing of the CMP gather, and they illustrate reconstructed data (first CMP gather) using the curvelet dictionary and corresponding residual section. It does not seem plausible that the curvelet dictionary is to blame for false artifacts, because the curvelet transform has only a weak ability to anti-aliasing, even though it has proven to have an outstanding ability that enables a nearly optimal representation of seismic data. However, such spatial aliasing can be maximumly remitted in the time-midpoint domain because the common-offset gather is characterized by flat, even approximate horizontal events. The reconstructed results of the first CMP and the 24th common-offset gathers using the time-midpoint domain approach are shown in **Figure 7C,E**, respectively. **Figure 7D,F** show the corresponding residuals of the CMP and common-offset gathers, respectively. As expected, the curvelet reconstruction performs much better in the time-midpoint domain than in the time-offset domain. All missing seismic traces are perfectly reconstructed. The defect is that random noise is not well suppressed.

3.4 Fourier Transform Operator Tests

We next examine whether Fourier transform operator does it as good as the curvelet transform operator. The results from the Fourier transform operator associated with both the time-offset and the time-midpoint domains approaches are plotted in **Figure 8A,C**, respectively. The corresponding residual images are shown in **Figure 8B,D**, respectively. There are no apparent differences between curvelet and Fourier transform operators. However, to our surprise, the Fourier transform operator does slightly better than the curvelet transform operator both in the time-offset domain and the time-midpoint domain. The possible reason is that the simulation data used in this experiment are spatially under-sampled. The curvelet transform operator tended to express the local tectonics of the seismic section, and its anti-aliasing ability is weak. The opposite effect is observed for the Fourier transform operator, which points to the ability of the Fourier transform operator to address issues that arose in the field of aliased data. There is no doubt that the computational complexity of the Fourier transform is much lower than the curvelet transform. Therefore, the Fourier transform operator is the best option.

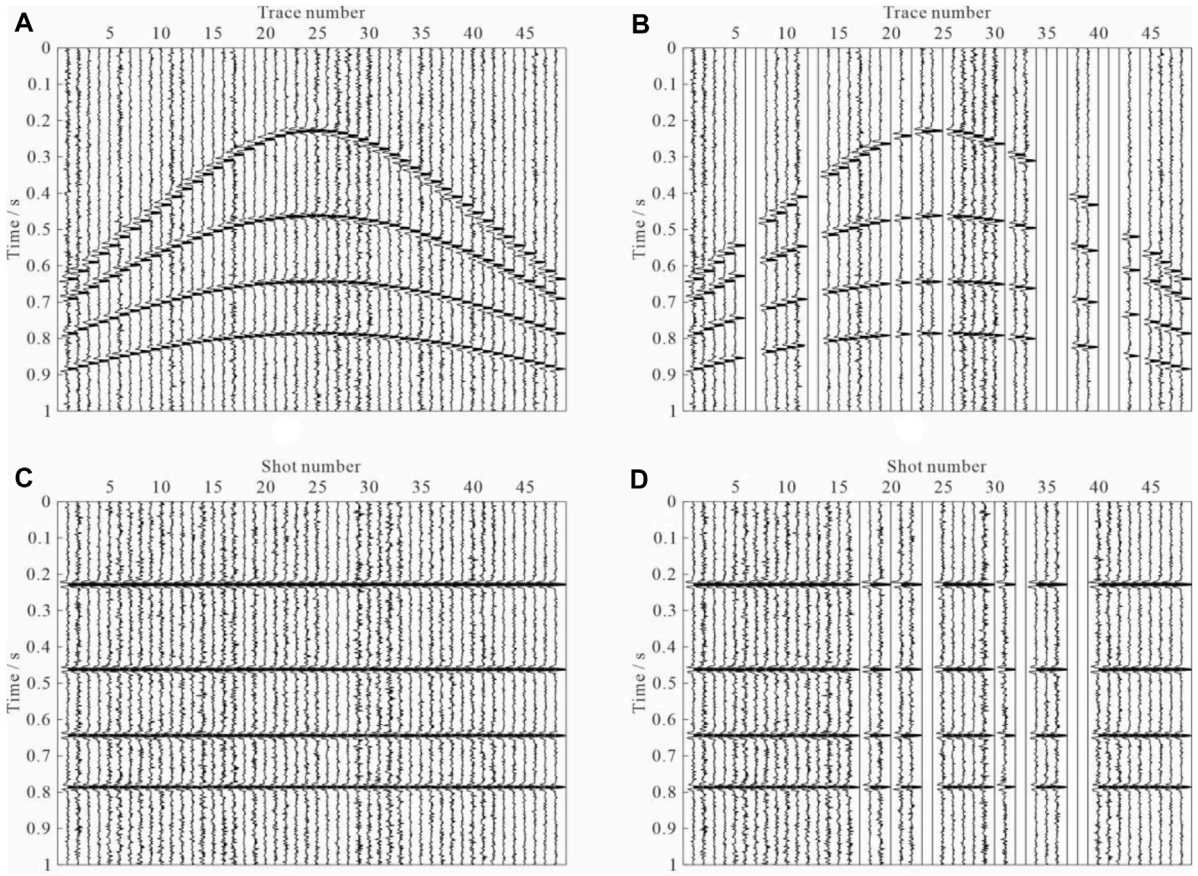

FIGURE 4 | Incomplete noisy seismic data. **(A)** and **(B)** are complete and incomplete noisy CMP gathers, respectively. **(C)** and **(D)** are complete and incomplete noisy common-offset gathers, respectively. 25% of the traces are missing based on the under-sampling strategy.

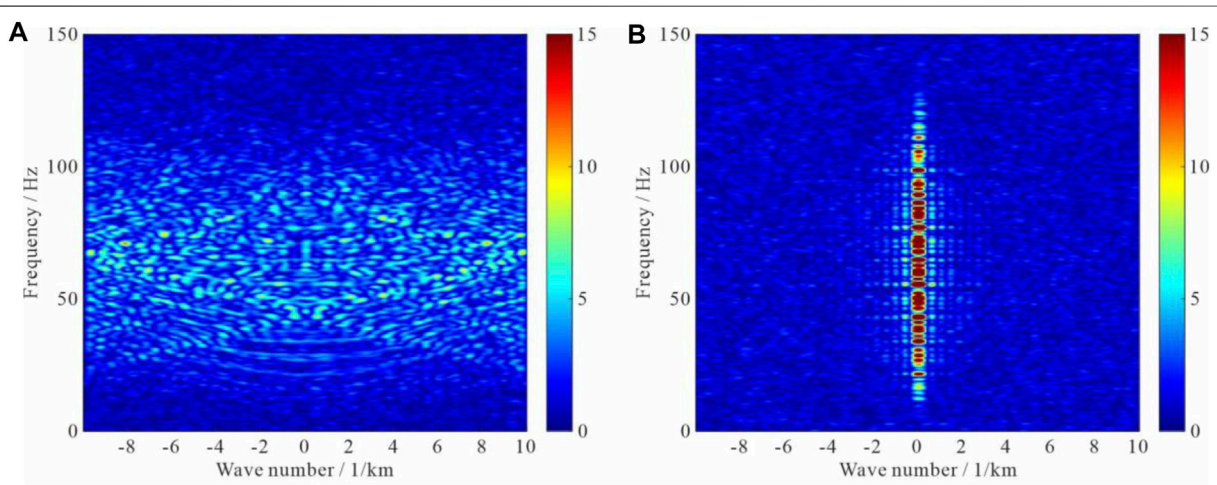

FIGURE 5 | *f-k* spectra for **(A)** the complete noisy CMP gather and **(B)** the common-offset gather. Note that apparent spatial aliasing exists in the *f-k* spectra for the CMP gather. However, COG is free from aliasing.

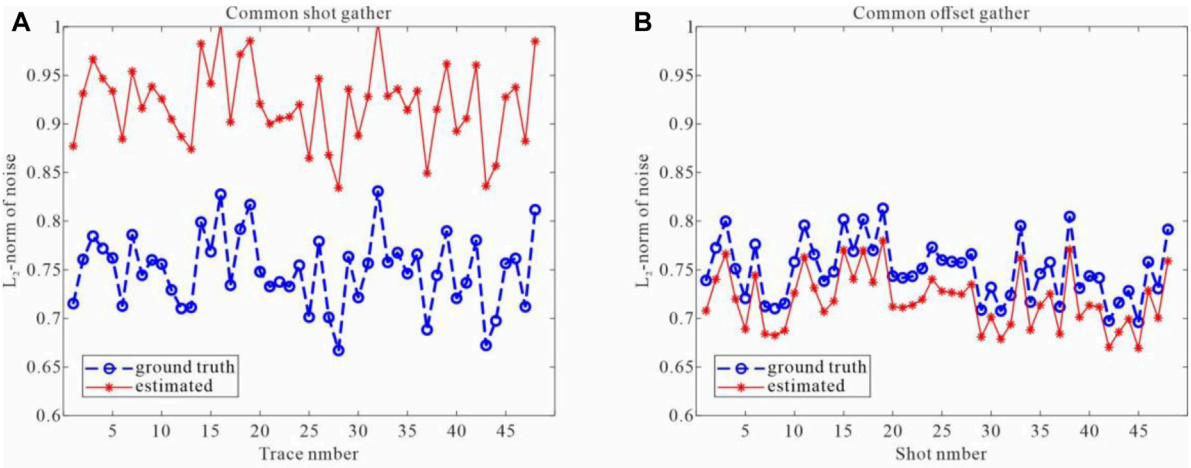

FIGURE 6 | Noise estimation by the multiple regression theory-based approach in both **(A)** the time-offset domain (CMP gather) and **(B)** the time-midpoint domain (common-offset gather). In all plots, the *y*-axes represent the L_2-norm of the noise; the *x*-axes represent the trace number **(A)** and shot number **(B)**, respectively. Estimated values (red) are plotted on top of the ground truth (blue).

3.5 Evaluation of the Proposed Sparse and Low-Rank Regularization Approach

We have experimentally verified the superiority of the time-midpoint domain approach and Fourier transform operator in the previous subsection. Naturally, a combination of the two is also appreciated. The assay is performed as described in **Subsection 2.1**. **Figure 9A** shows the recovered common-offset gather in the time-midpoint domain, and **Figure 9B** is the corresponding residual image. Both two objectives of reconstruction and denoising have been achieved. Next, we sort the data into common-shot gathers to obtain the final result shown in **Figure 9C**, which is very close to the clean synthetic seismogram (**Figure 3C**). **Figure 9D** is the corresponding residual image. The proposed approach improves the SNR of seismic data as compared with the previous two experiments.

To quantitatively compare the reconstruction performance in detail, we plot the noise-free single trace which is a missing trace deleted in the preceding step and the reconstructions with different methods in **Figure 10**. **Figure 10A,E** plot the clean and noisy signal (SNR = 4.421 dB), respectively. Results of three independent experiments are all obtained by time-midpoint domain approach, as plotted in **Figure 10B–D**. Full recovery of the missing trace is perfectly achieved in each of the three experiments. Fourier and curvelet transform operators suppress the random noise and improve the SNR of data to some extent, as plotted in **Figure 10B,C**. The SNRs of reconstructed traces of the two methods are 6.994 and 7.812 dB, respectively. Comparing the two methods, we can see that the superiority of the proposed method is clear (**Figure 10D**). SNR of the proposed method is equal to 18.243 dB.

4 Application to Field Seismic Data

In this section, we apply the proposed simultaneous reconstruction and denoising method to a prestack data set. The original raw data consist of 1,001 shot records with 120 channels per shot record. The minimum and maximum offsets are 262 and 3237 m, respectively. Both the source station interval and receiver station interval are 25 m. This study extracts 48 shot gathers from the raw data to ensure that the source station interval is 50 m, exactly twice the original source station interval. Then, each shot gather is down-sampled to reduce the number of channels to 60; that is, the receiver station interval is increased to 50 m. **Figure 11A,B** show the observed shot gather and common-offset gather, respectively. Intuitively, the shot gather consisted of hyperbolic reflected events and gradient direct and seabed reflection waves. However, the common-offset gather is characterized by much flatter events, which is very well adapted to reconstruction and denoising. Such down-sampling may give rise to spatial aliasing. **Figure 12A** shows the *f-k* spectra for the shot record with strong spatial aliasing, as indicated by the solid arrows. As mentioned previously, processing seismic data in the time-shotpoint domain is a simple and efficient strategy. **Figure 12B** demonstrates the *f-k* spectra for the common-offset gather shown in **Figure 11B**, and spatial aliasing is not visible as of the common-shot gather. To simulate the observed incomplete field data, we just take out the columns with missing receivers. 25% of the receivers are deleted randomly in this study. **Figure 11C,D** show the incomplete shot and common-offset gathers, respectively.

We perform three shortened versions of the simultaneous reconstruction and denoising experiments on the truncated seismic data, that is, curvelet transform operator, Fourier transform operator, and the proposed sparse and low-rank regularization approach. The complete workflow of each experiment consisted of three flows: (1) transforms the seismic data to the time-shotpoint (common-offset) domain, (2) noise level estimation, and (3) reconstructs the clean and complete seismic section by different methods. The reconstructed common-offset gathers of three different methods are

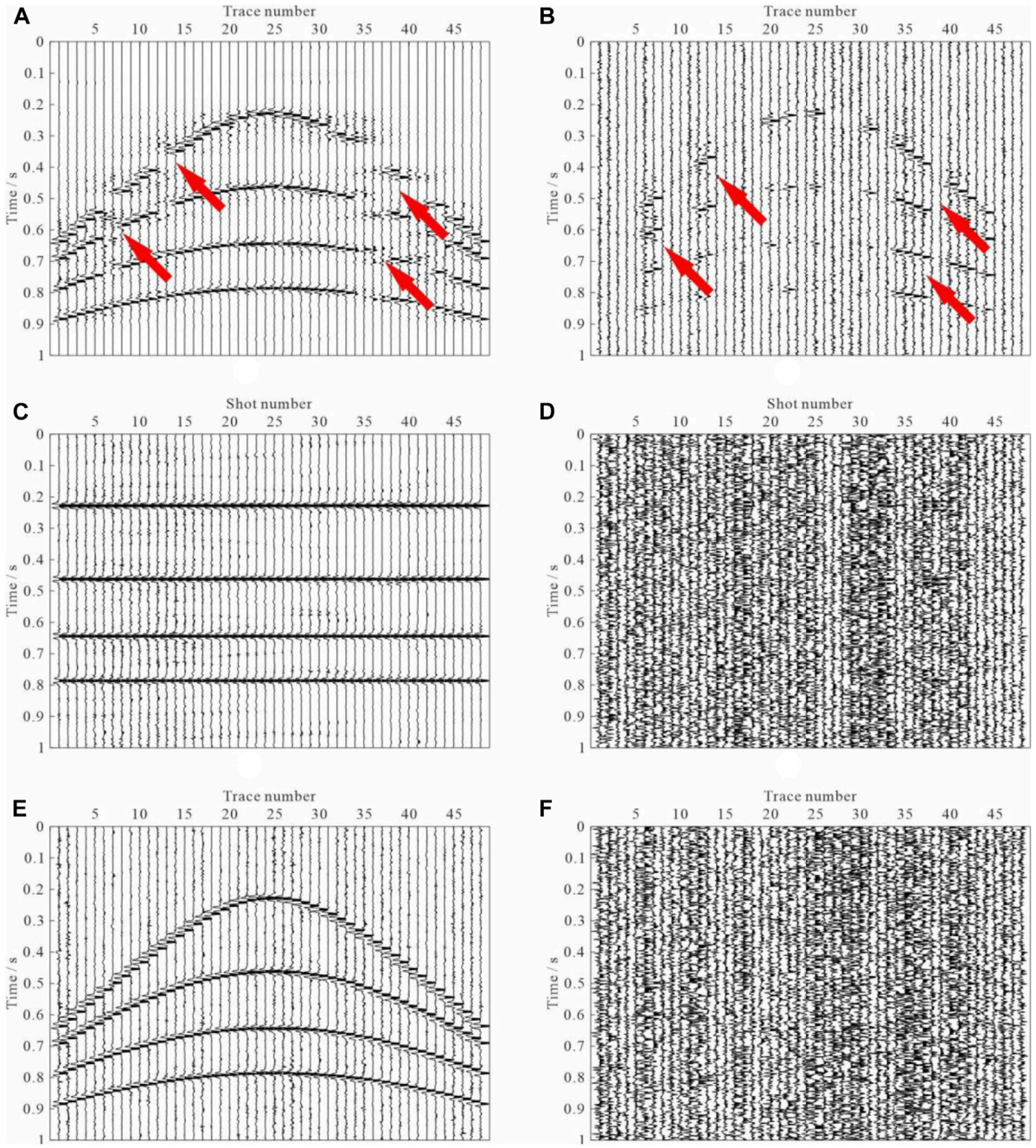

FIGURE 7 | Reconstruction results of subsampled data using curvelet interpolation. **(A)** Recovered CMP gather using linearized Bregman method across CMP gathers in the time-offset domain, and **(B)** the corresponding residual section. **(C)** Recovered common-offset gather across offset gathers in the time-midpoint domain, and **(D)** the corresponding residual image. **(E)** Recovered CMP gather in the time-midpoint domain, which is the same as in **(B)**. **(F)** The residual section corresponding to **(E)**.

contrasted in **Figure 13**. The reconstructed result using the curvelet transform operator and the associated difference section are shown in **Figure 13A,B**, respectively. The narrow gaps are well recovered, while the reconstructed results of the big gaps are not as good as it would be expected (indicated by the arrows in **Figure 13A,B**). Recovered common-offset gather using Fourier transform operator and the associated difference section are shown in **Figure 13C,D**, respectively. The missing traces were well recovered, in particular at the big gaps. However, reconstructed data seem to have significant residual noise in the big gap at 0–0.5s. **Figure 13E,F** demonstrate the interpolated result and the corresponding residuals of the proposed strategy. As can be seen, the recovery is comparable to the Fourier transform operator. A further advantage is that we can obtain

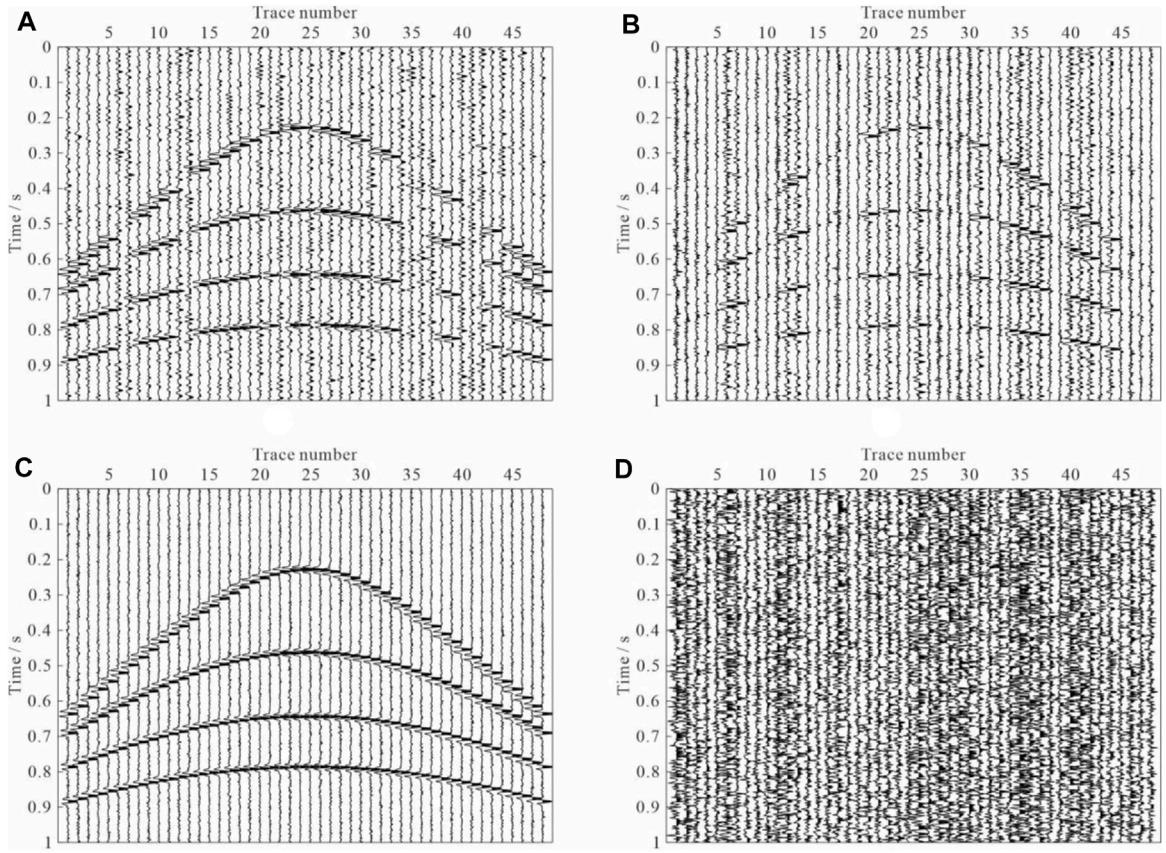

FIGURE 8 | Reconstruction results of subsampled data using Fourier interpolation. **(A)** Recovered CMP gather using linearized Bregman method across CMP gathers in the time-offset domain, and **(B)** the corresponding residual section. **(C)** Recovered CMP gather across offset gathers in the time-midpoint domain, and **(D)** the corresponding residual image.

much cleaner data that does not contain the artifacts before the first arrivals.

The reconstructed and denoised common-offset gathers are transformed into the common-shot gathers. **Figure 14** compares the recovered shot gathers of all the three methods. **Figure 14A,C,E** indicate the recovered shot gathers of the three different approaches, respectively. **Figure 14B,D,F** show the corresponding residuals. Similar conclusions can also be obtained based on the comparison of reconstructed results and corresponding residuals of the three methods. The proposed method is more effective in seismic wavefield reconstruction and denoising than the curvelet and Fourier transforms operators. To better compare the details of reconstructed results by the above three methods, we compare the recoveries of a single trace, as plotted in **Figure 15**. **Figure 15A** plots the real noisy trace (Trace No. 39 from the noisy shot shown in **Figure 11A**). **Figure 15B–D** plot the recovered traces of the three different approaches, respectively. **Figure 15E–G** correspond to the removed noise associate to each method. These results can be explained as follows. The result of the curvelet transform operator is not very good. The result of the Fourier transform operator is close to the exact solution. However, we should note that the presence of noise before the first arrival (at 0–1.5 s, as indicated by the arrows in **Figure 15C,F**) is caused by not very good localization of Fourier transform. The proposed method compensates for the defect exactly, and the recovered signal does not contain the evident artifacts and noise. Therefore, the proposed sparse and low-rank regularization approach should be the best choice owing to its effectiveness and fidelity.

5 DISCUSSION

In this work, we present a novel technique for simultaneous reconstruction and denoising of prestack seismic data. To fully exploit the sparse and low-rank nature, we first interpolate the common-offset gather in the 2D Fourier domain, that approach is capable of attenuating random noise to some extent, but new random noise may be introduced. The SVT is then adopted to handle the Fourier coefficient matrix by utilizing the low-rank property, and the residual and generated random noise is washed out. The results shown above demonstrate that it offers a flexible and effective way for both interpolation and denoising.

Curvelet and Fourier transforms are two tools to transform seismic sections into a domain where it has a sparse

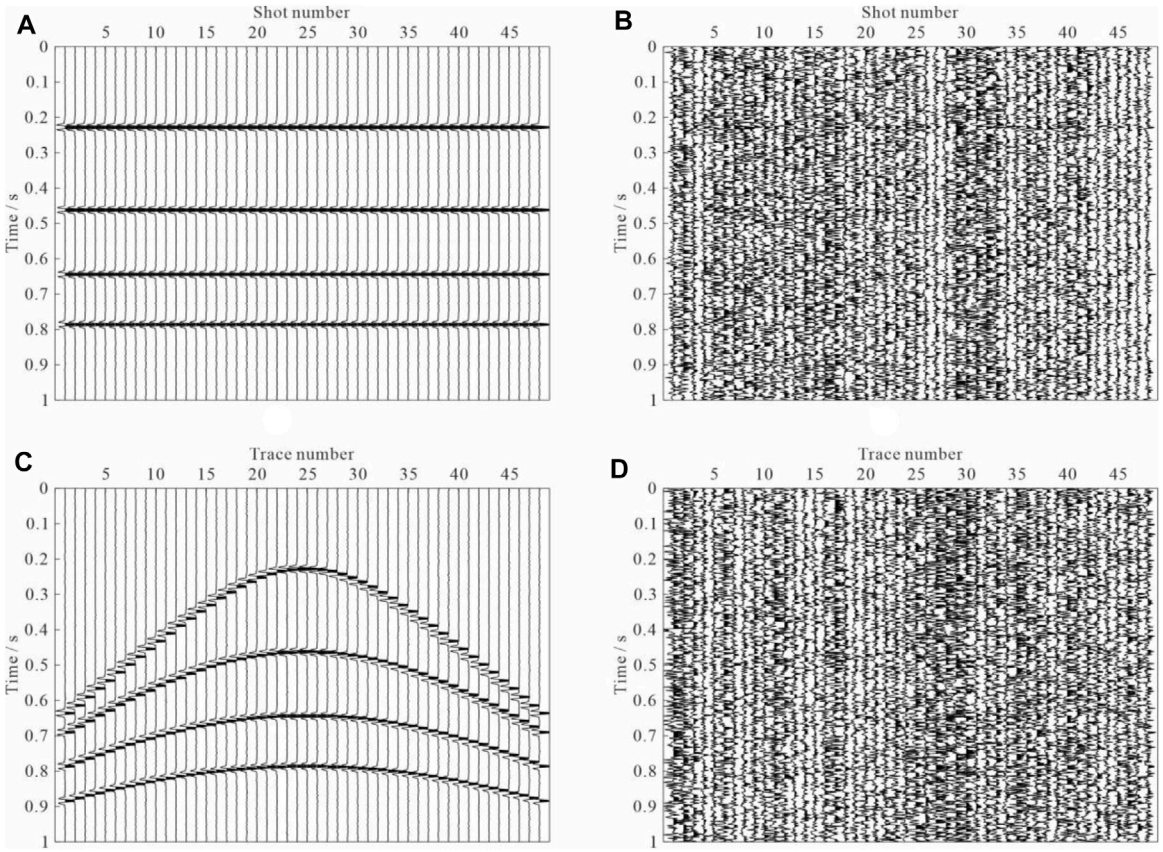

FIGURE 9 | Reconstruction results of subsampled data using the proposed method. **(A)** Recovered common-offset gather across offset gathers in the time-midpoint domain, and **(B)** the corresponding residual image. We then transform the reconstruction results into CMP gathers to generate **(C)** and **(D)**. **(C)** recovered CMP gather. **(D)** The residual section corresponding to **Figure 7C**.

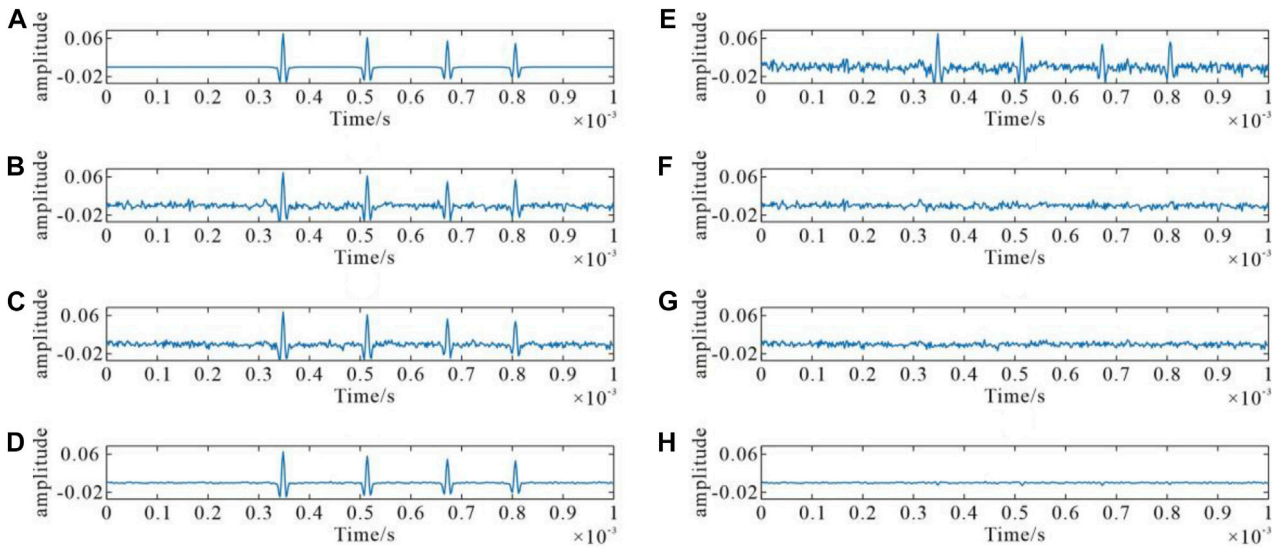

FIGURE 10 | Single trace comparisons of original data and reconstructed results using the three methods. **(A)** is the clean 35th trace, which is a missing trace deleted in the preceding step. **(B)**, **(C)**, and **(D)** Denoised and reconstructed data using curvelet interpolation, Fourier interpolation, and the proposed method, respectively. **(E)** Noisy synthetic trace with SNR = 4.421 dB. **(F)**, **(G)**, and **(H)** corresponding differences between **(B)**, **(C)**, and **(D)** and clean trace **(A)**.

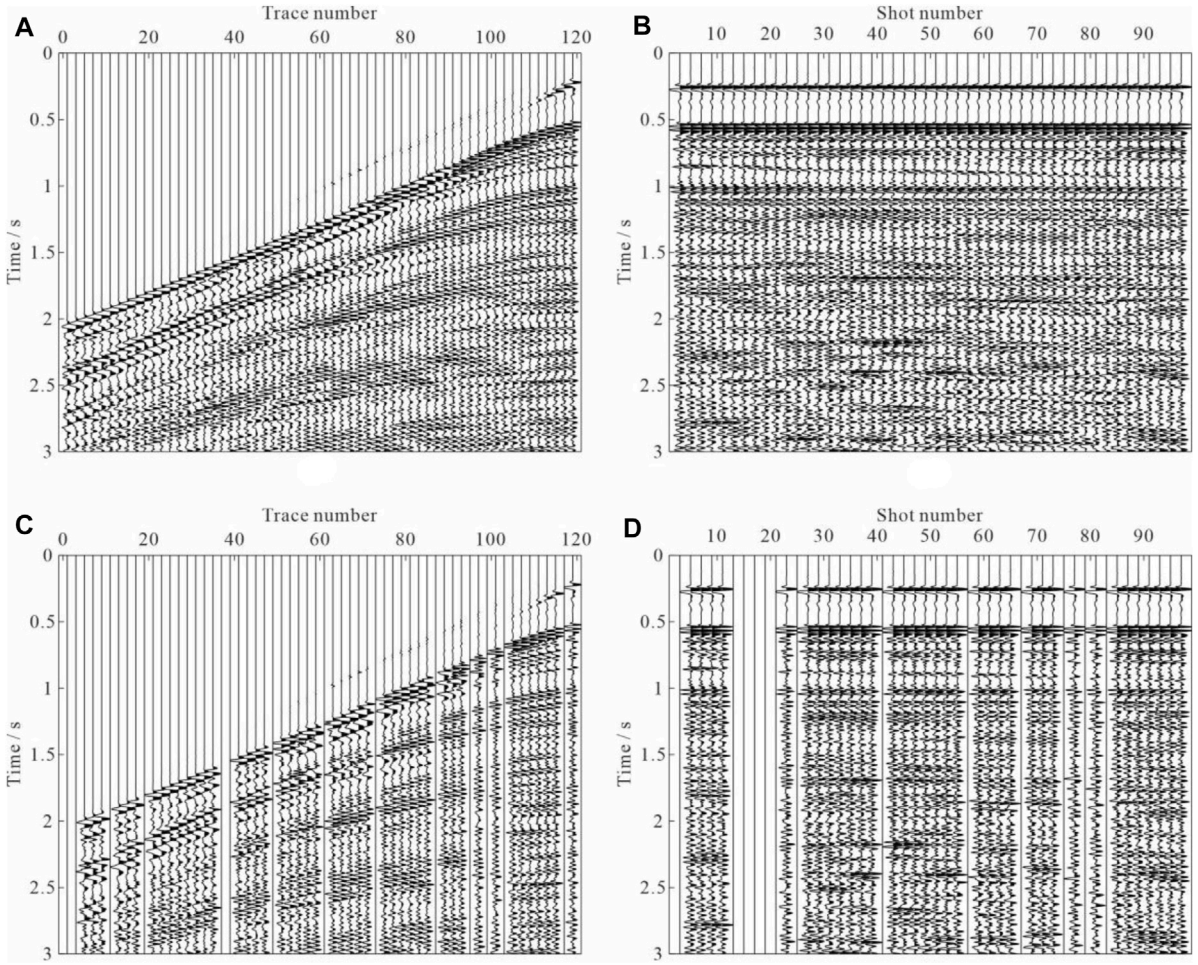

FIGURE 11 | Field seismic data. **(A)** Observed complete common-shot gather, and **(B)** common-offset gather. Incomplete **(C)** common-shot gather and **(D)** common-offset gather, with 30% random missing data.

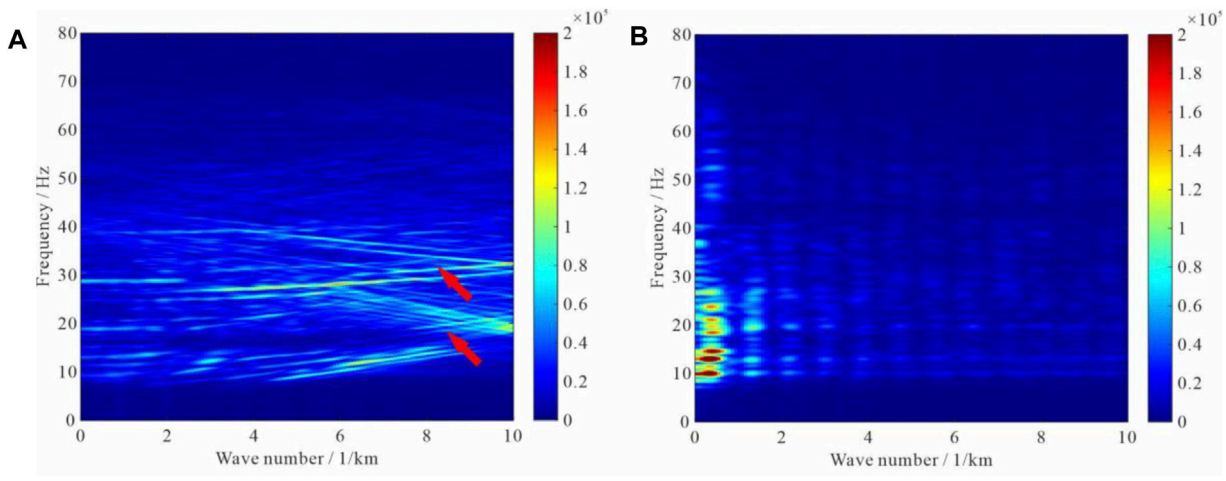

FIGURE 12 | *f-k* spectral analysis for **(A)** the common-shot gather and **(B)** the common-offset gather shown in **Figure 11A,B**.

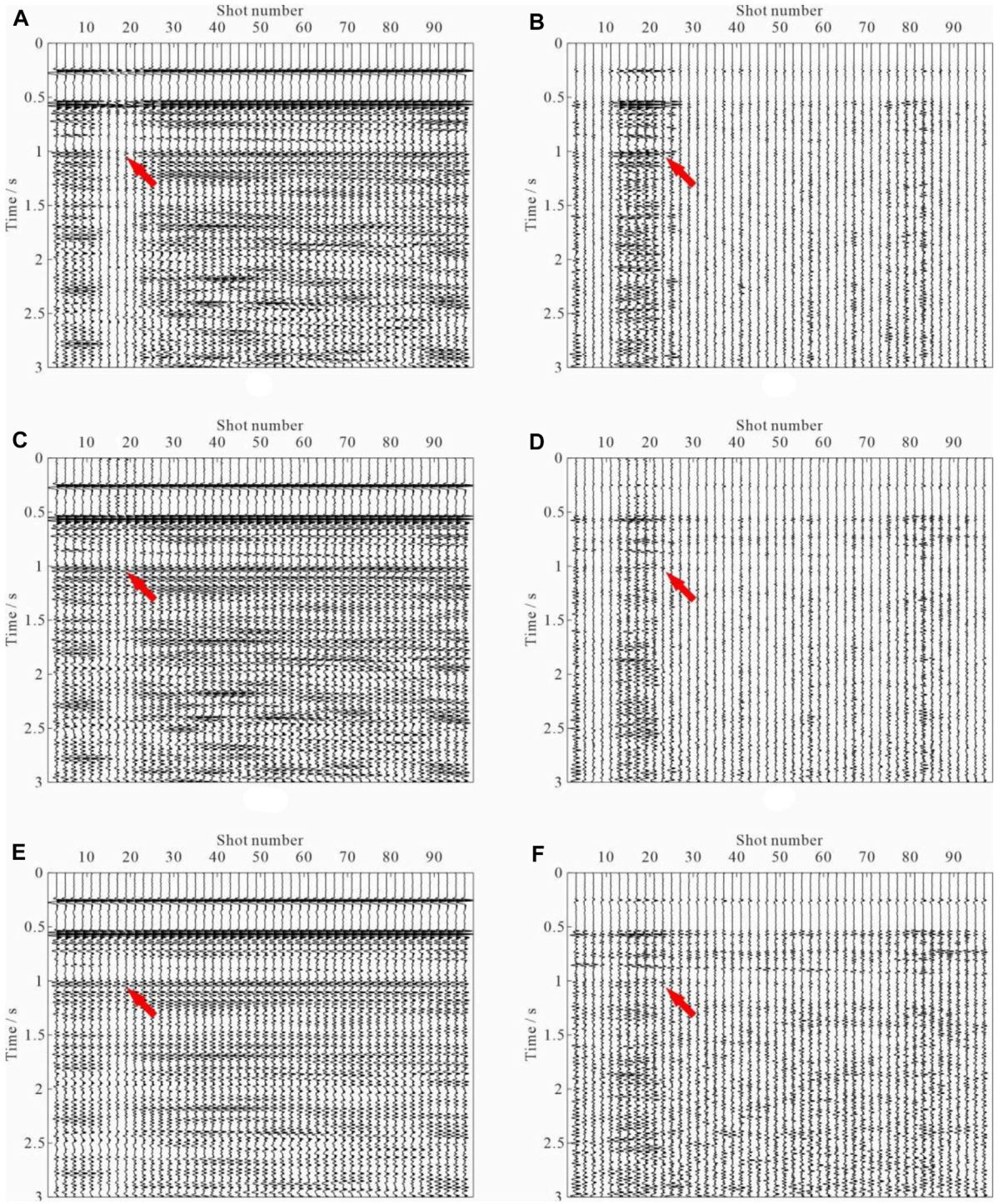

FIGURE 13 | Reconstructed common-offset gather. The reconstructed result using **(A)** the curvelet transform operator and **(B)** the associated difference section. Result of **(C)** Fourier transform operator and associated **(D)** difference section. Result of **(E)** the proposed sparse and low-rank regularization approach and **(F)** the associated difference section.

representation. The computational complexity of the second generation curvelet transform is $O(n^2 \log n)$ for n by n Cartesian arrays, while the complexity of 2D Fourier is $O(n^2)$ (Candès et al., 2006). had compared the ratio between the running time of the fast discrete curvelet transform (FDCT) and that of the fast Fourier transform (FFT). The ratios of wrapping-based FDCT varied from 6.0793 to 11.2383, and the USFFT-based is 18.2202–28.9579. To compute the curvelet

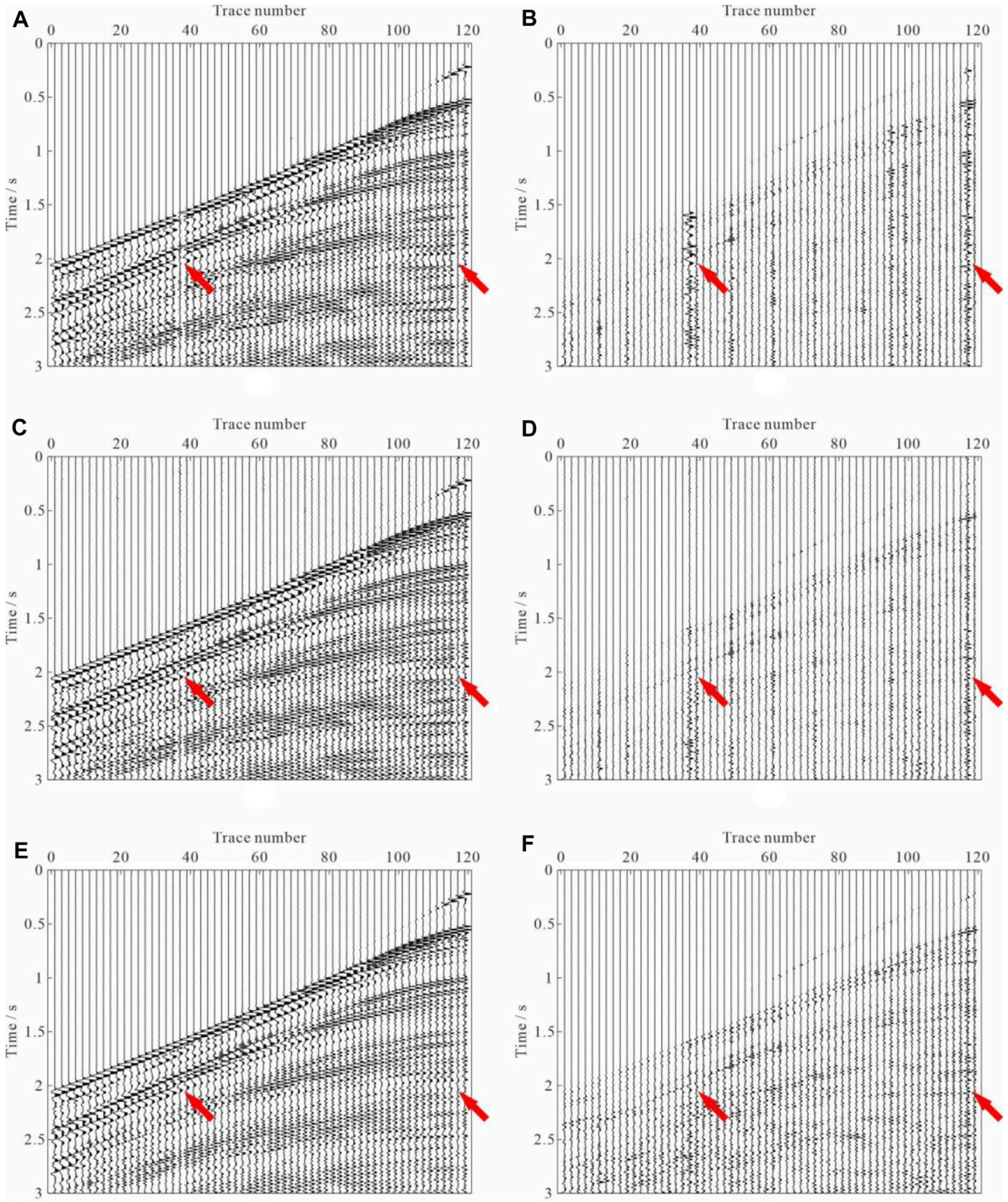

FIGURE 14 | Comparison of the reconstructed results of common-offset gathers. The reconstructed result using **(A)** the curvelet transform operator and **(B)** associated difference section. Result of **(C)** the Fourier transform operator and **(D)** the associated difference section. Result of **(E)** the proposed sparse and low-rank regularization approach and **(F)** the associated difference section.

coefficients, we must take on the heavy computational burden. The curvelet transform has only a weak ability to anti-aliasing, even though it has proven to have an outstanding ability in obtaining an essentially optimal representation of seismic data. In **Figures 7**, **13**, and **14**, we find that the curvelet transform operator reconstructs single missing-traces accurately. Conversely, the curvelet operator cannot obtain satisfactory results where gaps are existing. In both cases, the Fourier

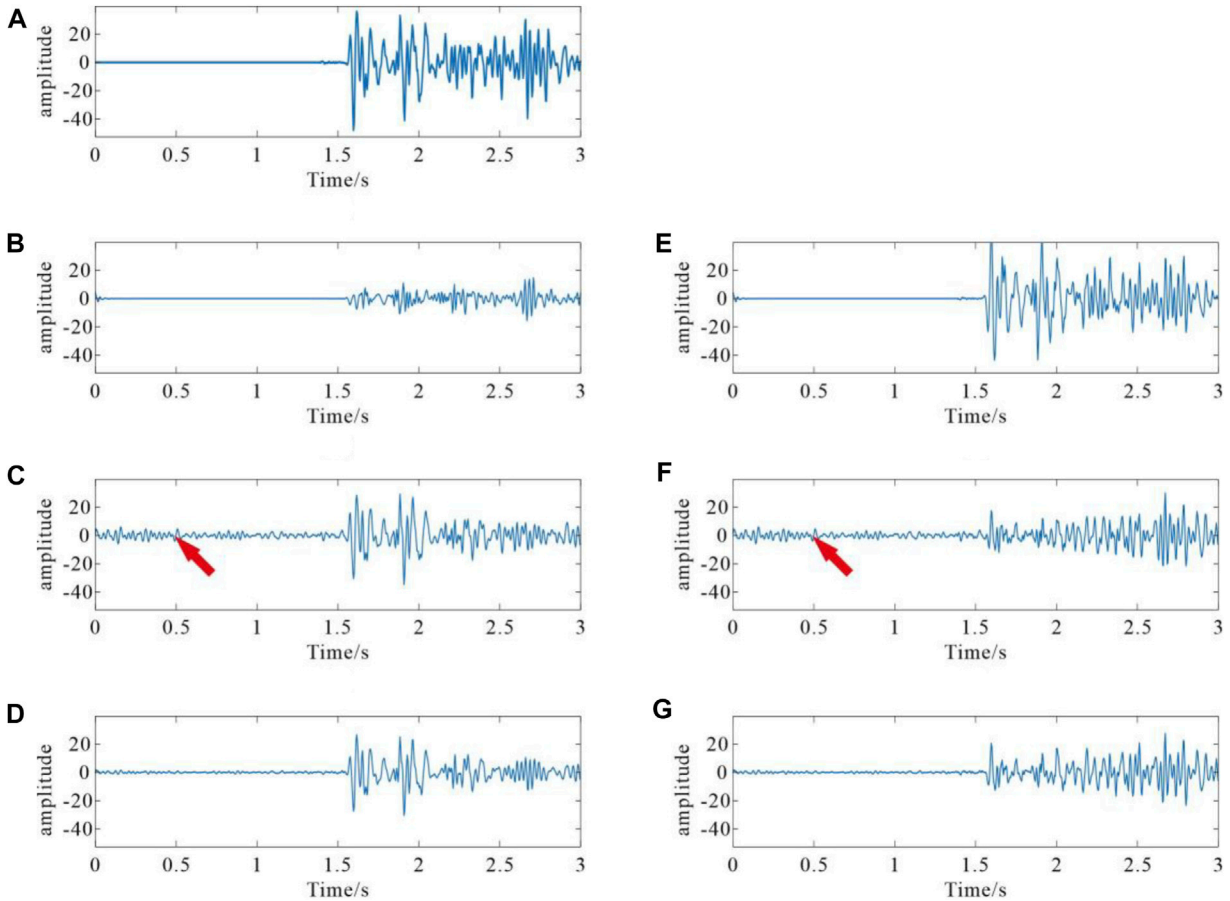

FIGURE 15 | Single trace comparisons of original trace and reconstructed traces. **(A)** Noisy real trace (Trace No. 39 from the noisy shot shown in **Figure 11A**). Reconstructed results using **(B)** the curvelet transform operator, **(C)** the Fourier transform operator, and **(D)** the proposed sparse and low-rank regularization approach. **(E)**–**(G)** Removed noise corresponding to **(B)**–**(D)**.

transform operator performs well and reconstructs data accurately.

The proposed method operates in the time-shotpoint domain, characterized by flat, even approximate horizontal events that benefit noise level estimation and seismic wavefield reconstruction. In this work, we choose the multiple regression theory-based approach for noise level estimation. The method assumes that each trace can be linearly represented by other seismic traces in the gather. The common-offset gather rather than the shot gather and CMP gather met the key assumption of the linear mixing scenario. **Figure 6** compares the noise estimation results by the multiple regression theory-based approach in both the time-midpoint domain and time-offset domain. The L_2-norm of the estimated noise associated with common-offset gather is much more accurate than that of the CMP. The classical wavefield reconstructions are designed for the case of no spatial aliasing. However, this is an ideal case for both the shot and CMP gathers. Spatial aliasing is encountered frequently in the fieldwork. We find that the steeper the dip, the lower the frequency at which spatial aliasing occurs. Compared to the two gathers, the proposed common-offset gather strategy enjoys its anti-aliasing ability and is bright to handle the under-sampling obstacle. **Figures 7–10, 13–15** validate the advantage of the common-offset gather and support our method's validity.

There are two parameters (regularization parameter α and fitting error ε) in the augmented model (4) that need to be appropriately chosen to ensure that the algorithm converges to the global minimum. L_1-norm regularization is non-differentiable, which is particularly troublesome in numerical optimization. One strategy is to introduce an extra L_2-norm regularization to ensure the objective function is strictly convex. A unique solution could be guaranteed, however, of introducing additional regularization parameter. Fortunately, the relative error is insensitive to α, which only affects the computational efficiency (Yin 2010; Kang et al., 2013). Taking $\alpha = 1$ is a logical choice. The fitting error ε denotes the constraint ensures fidelity to the models (1) and (2). However, the importance of parameter ε is often ignored in literature or software packages. $\varepsilon = 1e^{-3}$ is usually recommended. The parameter ε is essentially an estimate of the noise level of the seismic signal and can be quantified by an upper bound on its

norm. To clarify the impacts of the fitting error ε on the augmented model (4), we compare the performance of different fitting errors, that is, $\varepsilon = 1e^{-3}$ and ε is equal to the L_2-norm of the noise. Output SNRs of reconstructed solutions in terms of SNR and sparsity of noisy observations are plotted in **Figure 1A,B**, respectively. In **Figure 2**, reconstructed solutions (red) are plotted on top of the ground truth (blue). It is straightforward to see that output SNR is sensitive to ε, and an appropriate ε consistently increases the precision and accuracy of the solution.

SVT can be achieved in two ways. The first type can be achieved by retaining only the part of the singular values and refers to hard-thresholding. Comparatively, the soft-thresholding is more usually used, which shrinks all the singular values towards zero by a threshold value λ. The difficulty is how to select the proper threshold. A simple and intuitive strategy is an intuitive comparison of the calculated results of various parameters λ. In this article, unbiased risk estimation for the trade-off is obtained with the help of SURE, which is already being applied in MRI and hyperspectral images. The non-parametric simultaneous reconstruction and denoising method is achieved with the automatic estimation of the parameters.

The reconstruction problem (as shown in **Eq. 2**) involves finding the solution **m** with the smallest number of non-zero entries that can represent the useful data sparsely and accurately. The accurate identification of the Fourier or curvelet coefficient is crucial for the sparse recovery problem. The discrimination method may help to increase the accuracy of the solutions further. The idea is appealing, as stated in Lindenbaum et al. (2020) and Dong et al. (2020).

6 CONCLUSION

This article considered the problem of simultaneous interpolation of missing-traces and random noise attenuation. In the approach, we transform the common-offset gather into the 2D Fourier domain and recover the gaps via the linearized Bregman method. SVT attenuates the residual and generated random noise and artifacts. The tandem approach essentially imposes two effective constraints: sparsity and low-rank. In the proposed methodology, we do not assume a single set of hyperparameters but estimate the noise level and the optimal threshold value of SVT by the multiple regression theory and SURE, respectively. These tools allow us to obtain a non-parametric method without person-dependent intervention in the seismic data conditioning. The proposed method handles the common-offset gathers rather than the shot gathers or CMP gathers. Therefore, our approach can provide accurate estimates of the noise level and offers more flexible control on the model, which enjoys its anti-aliasing ability and is bright to handle the highly insufficient seismic gathers. To better handle the spatially aliased data, we use Fourier transform to solve the corresponding sparse representation problem in the time-shotpoint (or time-midpoint) domain. Both synthetic and real seismic data examples confirm the effectiveness of the proposed method for simultaneous wavefield reconstruction and random noise suppression.

DATA AVAILABILITY STATEMENT

The raw data supporting the conclusions of this article will be made available by the authors, without undue reservation.

AUTHOR CONTRIBUTIONS

LM, ZS, YY, and YW contributed to conception of the study. LM and ZS wrote the first draft of the manuscript. LM, ZS, and YY wrote sections of the manuscript. All authors contributed to manuscript revision, read, and approved the submitted version.

FUNDING

The financial support from the Key Research and Development Program (Grant No. 21ZDYF2939) of the Science and Technology Department of Sichuan Province, Sichuan Tourism Development Research Center (Grant No. LY22-20), Sichuan Provincial University Key Laboratory of Detection and Application of Space Effect in Southwest Sichuan (Grant No. YBXM202102001), and Leshan Normal University (Grant No. RC2021010).

REFERENCES

Anvari, R., Kahoo, A. R., Mohammadi, M., Khan, N. A., and Chen, Y. (2019). Seismic Random Noise Attenuation Using Sparse Low-Rank Estimation of the Signal in the Time-Frequency Domain. *IEEE J. Sel. Top. Appl. Earth Obs. Remote Sens.* 12, 1612–1618. doi:10.1109/JSTARS.2019.2906360

Anvari, R., Nazari Siahsar, M. A., Gholtashi, S., Roshandel Kahoo, A., and Mohammadi, M. (2017). Seismic Random Noise Attenuation Using Synchrosqueezed Wavelet Transform and Low-Rank Signal Matrix Approximation. *IEEE Trans. Geosci. Remote Sens.* 55, 6574–6581. doi:10.1109/TGRS.2017.2730228

Batu, O., and Cetin, M. (2011). Parameter Selection in Sparsity-Driven SAR Imaging. *IEEE Trans. Aerosp. Electron. Syst.* 47, 3040–3050. doi:10.1109/TAES.2011.6034687

Becker, S., Bobin, J., and Candès, E. J., (2011). NESTA: A Fast and Accurate First-Order Method for Sparse Recovery. *SIAM J. Imaging Sci.* 4, 1–39. doi:10.1137/090756855

Bekara, M., and Van der Baan, M. (2007). Local Singular Value Decomposition for Signal Enhancement of Seismic Data. *Geophysics* 72, V59–V65. doi:10.1190/1.2435967

Bioucas-Dias, J. M., and Nascimento, J. M. P. (2008). Hyperspectral Subspace Identification. *IEEE Trans. Geosci. Remote Sens.* 46, 2435–2445. doi:10.1109/TGRS.2008.918089

Candès, E., Demanet, L., Donoho, D., and Ying, L. (2006). Fast Discrete Curvelet Transforms. *Multiscale Model. Simul.* 5, 861–899. doi:10.1137/05064182X

Candes, E. J., Sing-Long, C. A., and Trzasko, J. D. (2013). Unbiased Risk Estimates for Singular Value Thresholding and Spectral Estimators. *IEEE Trans. Signal Process.* 61, 4643–4657. doi:10.1109/TSP.2013.2270464

Cao, J., Cai, Z., and Liang, W. (2020). A Novel Thresholding Method for Simultaneous Seismic Data Reconstruction and Denoising. *J. Appl. Geophys.* 177, 104027. doi:10.1016/j.jappgeo.2020.104027

Chang, C.-I., and Du, Q. (2004). Estimation of Number of Spectrally Distinct Signal Sources in Hyperspectral Imagery. *IEEE Trans. Geosci. Remote Sens.* 42, 608–619. doi:10.1109/TGRS.2003.819189

Chen, Y., Chen, X., Wang, Y., and Zu, S. (2019a). The Interpolation of Sparse Geophysical Data. *Surv. Geophys.* 40, 73–105. doi:10.1007/s10712-018-9501-3

Chen, Y., Huang, W., Zhang, D., and Chen, W. (2016a). An Open-Source Matlab Code Package for Improved Rank-Reduction 3D Seismic Data Denoising and Reconstruction. *Comput. Geosciences* 95, 59–66. doi:10.1016/j.cageo.2016.06.017

Chen, Y., and Ma, J. (2014). Random Noise Attenuation Byf-Xempirical-Mode Decomposition Predictive Filtering. *Geophysics* 79, V81–V91. doi:10.1190/geo2013-0080.1

Chen, Y., Peng, Z., Li, M., Yu, F., and Lin, F. (2019b). Seismic Signal Denoising Using Total Generalized Variation with Overlapping Group Sparsity in the Accelerated ADMM Framework. *J. Geophys. Eng.* 16, 30–51. doi:10.1093/jge/gxy003

Chen, Y., Zhang, D., Jin, Z., Chen, X., Zu, S., Huang, W., et al. (2016b). Simultaneous Denoising and Reconstruction of 5-D Seismic Data via Damped Rank-Reduction Method. *Geophys. J. Int.* 206, 1695–1717. doi:10.1093/gji/ggw230

Chen, Y., Zhou, Y., Chen, W., Zu, S., Huang, W., and Zhang, D. (2017). Empirical Low-Rank Approximation for Seismic Noise Attenuation. *IEEE Trans. Geosci. Remote Sens.* 55, 4696–4711. doi:10.1109/TGRS.2017.2698342

Chiu, S. K., and Howell, J. E. (2008). "Attenuation of Coherent Noise Using Localized-adaptive Eigenimage Filter," in *SEG Technical Program Expanded Abstracts 2008* (Las Vegas: Society of Exploration Geophysicists), 2541–2545. doi:10.1190/1.3063871

Deng, L., Yuan, S., and Wang, S. (2017). Sparse Bayesian Learning-Based Seismic Denoise by Using Physical Wavelet as Basis Functions. *IEEE Geosci. Remote Sens. Lett.* 14, 1993–1997. doi:10.1109/LGRS.2017.2745564

Dong, L.-j., Tang, Z., Li, X.-b., Chen, Y.-c., and Xue, J.-c. (2020). Discrimination of Mining Microseismic Events and Blasts Using Convolutional Neural Networks and Original Waveform. *J. Cent. South Univ.* 27, 3078–3089. doi:10.1007/s11771-020-4530-8

Ely, G., Aeron, S., Hao, N., and Kilmer, M. E. (2015). 5D Seismic Data Completion and Denoising Using a Novel Class of Tensor Decompositions. *Geophysics* 80, V83–V95. doi:10.1190/geo2014-0467.1

Gómez, J. L., Velis, D. R., and Sabbione, J. I. (2020). Noise Suppression in 2D and 3D Seismic Data with Data-Driven Sifting Algorithms. *Geophysics* 85, V1–V10. doi:10.1190/geo2019-0099.1

Hansen, P. C. (1992). Analysis of Discrete Ill-Posed Problems by Means of the L-Curve. *SIAM Rev.* 34, 561–580. doi:10.1137/1034115

Hennenfent, G., Fenelon, L., and Herrmann, F. J. (2010). Nonequispaced Curvelet Transform for Seismic Data Reconstruction: A Sparsity-Promoting Approach. *Geophysics* 75, WB203–WB210. doi:10.1190/1.3494032

Jia, Y., and Ma, J. (2017). What Can Machine Learning Do for Seismic Data Processing? an Interpolation Application. *Geophysics* 82, V163–V177. doi:10.1190/geo2016-0300.1

Kang, M., Yun, S., Woo, H., and Kang, M. (2013). Accelerated Bregman Method for Linearly Constrained $$\ell _1$$ - $$\ell _2$$ Minimization. *J. Sci. Comput.* 56, 515–534. doi:10.1007/s10915-013-9686-z

Kreimer, N., and Sacchi, M. D. (2012). A Tensor Higher-Order Singular Value Decomposition for Prestack Seismic Data Noise Reduction and Interpolation. *Geophysics* 77, V113–V122. doi:10.1190/geo2011-0399.1

Kreimer, N., Stanton, A., and Sacchi, M. D. (2013). Tensor Completion Based on Nuclear Norm Minimization for 5D Seismic Data Reconstruction. *Geophysics* 78, V273–V284. doi:10.1190/geo2013-0022.1

Li, F., Xie, R., Song, W.-Z., and Chen, H. (2019). Optimal Seismic Reflectivity Inversion: Data-Driven ℓ_p -Loss-ℓ_q -Regularization Sparse Regression. *IEEE Geosci. Remote Sens. Lett.* 16, 806–810. doi:10.1109/LGRS.2018.2881102

Lindenbaum, O., Rabin, N., Bregman, Y., and Averbuch, A. (2020). Seismic Event Discrimination Using Deep CCA. *IEEE Geosci. Remote Sens. Lett.* 17, 1856–1860. doi:10.1109/LGRS.2019.2959554

Lu, C., Feng, J., Yan, S., and Lin, Z. (2018). A Unified Alternating Direction Method of Multipliers by Majorization Minimization. *IEEE Trans. Pattern Anal. Mach. Intell.* 40, 527–541. doi:10.1109/TPAMI.2017.2689021

Ma, J. (2013). Three-dimensional Irregular Seismic Data Reconstruction via Low-Rank Matrix Completion. *Geophysics* 78, V181–V192. doi:10.1190/geo2012-0465.1

Mansour, H., Herrmann, F. J., and Yılmaz, Ö. (2013). Improved Wavefield Reconstruction from Randomized Sampling via Weighted One-Norm Minimization. *Geophysics* 78, V193–V206. doi:10.1190/geo2012-0383.1

Nazari Siahsar, M. A., Gholtashi, S., Kahoo, A. R., Marvi, H., and Ahmadifard, A. (2016). Sparse Time-Frequency Representation for Seismic Noise Reduction Using Low-Rank and Sparse Decomposition. *Geophysics* 81, V117–V124. doi:10.1190/geo2015-0341.1

Nazari Siahsar, M. A., Gholtashi, S., Olyaei Torshizi, E., Chen, W., and Chen, Y. (2017). Simultaneous Denoising and Interpolation of 3-D Seismic Data via Damped Data-Driven Optimal Singular Value Shrinkage. *IEEE Geosci. Remote Sens. Lett.* 14, 1086–1090. doi:10.1109/LGRS.2017.2697942

Oliveira, D. A. B., Ferreira, R. S., Silva, R., and Vital Brazil, E. (2018). Interpolating Seismic Data with Conditional Generative Adversarial Networks. *IEEE Geosci. Remote Sens. Lett.* 15, 1952–1956. doi:10.1109/LGRS.2018.2866199

Oropeza, V., and Sacchi, M. (2011). Simultaneous Seismic Data Denoising and Reconstruction via Multichannel Singular Spectrum Analysis. *Geophysics* 76, V25–V32. doi:10.1190/1.3552706

Osher, S., Burger, M., Goldfarb, D., Xu, J., and Yin, W. (2005). An Iterative Regularization Method for Total Variation-Based Image Restoration. *Multiscale Model. Simul.* 4, 460–489. doi:10.1137/040605412

Ramani, S., Zhihao Liu, Z., Rosen, J., Nielsen, J., and Fessler, J. A. (2012). Regularization Parameter Selection for Nonlinear Iterative Image Restoration and MRI Reconstruction Using GCV and SURE-Based Methods. *IEEE Trans. Image Process.* 21, 3659–3672. doi:10.1109/TIP.2012.2195015

Rasti, B., Ulfarsson, M. O., and Sveinsson, J. R. (2015). Hyperspectral Subspace Identification Using SURE. *IEEE Geosci. Remote Sens. Lett.* 12, 2481–2485. doi:10.1109/LGRS.2015.2485999

Roger, R. E., and Arnold, J. F. (1996). Reliably Estimating the Noise in AVIRIS Hyperspectral Images. *Int. J. Remote Sens.* 17, 1951–1962. doi:10.1080/01431169608948750

Ronen, J. (1987). Wave-equation Trace Interpolation. *Geophysics* 52, 973–984. doi:10.1190/1.1442366

Stein, C. M. (1981). Estimation of the Mean of a Multivariate Normal Distribution. *Ann. Stat.* 9, 1135–1151. doi:10.1214/aos/1176345632

Sternfels, R., Viguier, G., Gondoin, R., and Le Meur, D. (2015). Multidimensional Simultaneous Random Plus Erratic Noise Attenuation and Interpolation for Seismic Data by Joint Low-Rank and Sparse Inversion. *Geophysics* 80, WD129–WD141. doi:10.1190/geo2015-0066.1

van den Berg, E., and Friedlander, M. P. (2009). Probing the Pareto Frontier for Basis Pursuit Solutions. *SIAM J. Sci. Comput.* 31, 890–912. doi:10.1137/080714488

Wang, B., Zhang, N., Lu, W., and Wang, J. (2019). Deep-learning-based Seismic Data Interpolation: A Preliminary Result. *Geophysics* 84, V11–V20. doi:10.1190/geo2017-0495.1

Wang, C., Zhu, Z., Gu, H., Wu, X., and Liu, S. (2019). Hankel Low-Rank Approximation for Seismic Noise Attenuation. *IEEE Trans. Geosci. Remote Sens.* 57, 561–573. doi:10.1109/TGRS.2018.2858545

Wang, Y., Cao, J., and Yang, C. (2011). Recovery of Seismic Wavefields Based on Compressive Sensing by an L1-Norm Constrained Trust Region Method and the Piecewise Random Subsampling. *Geophys. J. Int.* 187, 199–213. doi:10.1111/j.1365-246X.2011.05130.x

Yin, W. (2010). Analysis and Generalizations of the Linearized Bregman Method. *SIAM J. Imaging Sci.* 3, 856–877. doi:10.1137/090760350

Yin, W., Osher, S., Goldfarb, D., and Darbon, J. (2008). Bregman Iterative Algorithms for ℓ_1-Minimization with Applications to Compressed Sensing. *SIAM J. Imaging Sci.* 1, 143–168. doi:10.1137/070703983

Yuan, S., Wang, S., Luo, C., and Wang, T. (2018). Inversion-based 3-D Seismic Denoising for Exploring Spatial Edges and Spatio-Temporal Signal Redundancy. *IEEE Geosci. Remote Sens. Lett.* 15, 1682–1686. doi:10.1109/LGRS.2018.2854929

Zhang, D., Zhou, Y., Chen, H., Chen, W., Zu, S., and Chen, Y. (2017). Hybrid Rank-Sparsity Constraint Model for Simultaneous Reconstruction and Denoising of 3D Seismic Data. *Geophysics* 82, V351–V367. doi:10.1190/geo2016-0557.1

Zhang, H., Diao, S., Chen, W., Huang, G., Li, H., and Bai, M. (2019). Curvelet Reconstruction of Non-uniformly Sampled Seismic Data Using the Linearized Bregman Method. *Geophys. Prospect.* 67, 1201–1218. doi:10.1111/1365-2478.12762

Zhou, Y., and Zhang, S. (2017). Robust Noise Attenuation Based on Nuclear Norm Minimization and a Trace Prediction Strategy. *J. Appl. Geophys.* 147, 52–67. doi:10.1016/j.jappgeo.2017.09.005

Conflict of Interest: The authors declare that the research was conducted in the absence of any commercial or financial relationships that could be construed as a potential conflict of interest.

Publisher's Note: All claims expressed in this article are solely those of the authors and do not necessarily represent those of their affiliated organizations, or those of the publisher, the editors and the reviewers. Any product that may be evaluated in this article, or claim that may be made by its manufacturer, is not guaranteed or endorsed by the publisher.

frontiers | Frontiers in Earth Science

TYPE Original Research
PUBLISHED 17 August 2022
DOI 10.3389/feart.2022.924124

OPEN ACCESS

EDITED BY
Longjun Dong,
Central South University, China

REVIEWED BY
Geng Jiabo,
Jiangxi University of Science and Technology, China
Erol Yilmaz,
Recep Tayyip Erdoğan University, Turkey
Bing Bai,
Beijing Jiaotong University, China
Xueyi Shang,
Chongqing University, China
Fuqiong Huang,
China Earthquake Networks Center, China

*CORRESPONDENCE
Jianjun Dong,
dongjianjun@lntu.edu.cn

SPECIALTY SECTION
This article was submitted to Structural Geology and Tectonics, a section of the journal Frontiers in Earth Science

RECEIVED 20 April 2022
ACCEPTED 11 July 2022
PUBLISHED 17 August 2022

CITATION
Dong J, Zhang Y, Xie Z and Gao K (2022), Heterogeneous rock mass detection in the Goaf underlying the Yingbin substation.
Front. Earth Sci. 10:924124.
doi: 10.3389/feart.2022.924124

Heterogeneous rock mass detection in the Goaf underlying the Yingbin substation

Jianjun Dong[1,2]*, Ying Zhang[1,2], Zhengquan Xie[1,2] and Ke Gao[1,2]

[1]College of Safety Science and Engineering, Liaoning Technical University, Huludao, China, [2]Laboratory of Mine Thermodynamic Disasters and Control of Ministry of Education, Liaoning Technical University, Huludao, China

The existence of heterogeneous rock mass in the goaf easily causes surface deformation, subsidence, and even collapse, which restricts the development of urbanization of the buildings above the goaf. Because of the saturation of the city and the shortage of power supply, the idea of building the Yingbin substation was proposed on the old coal mine goaf in Xinhua District, Pingdingshan City, Henan Province, China. To ensure the safety and stability of the foundation of the proposed substation, the comprehensive detection method was proposed, which is mainly based on transient electromagnetic detection and supplemented via drilling detection. It was used to determine the spatial position and location of heterogeneous rock mass in the goaf underlying the proposed substation. The results show that 1) after eliminating the interference to the transient electromagnetic detection, it is found that there are low-resistance anomalies near the depth of −160 m at points 1 to 2 and point 8 of the X_2 line and at points 1 to 3 of the Y_3 line, which are preliminarily presumed to be the influence of the heterogeneous rock mass. 2) The apparent resistivity anomalous areas of −160 and −200 m depth are highly consistent, and the location and scope of the heterogeneous rock mass were basically determined. 3) The abnormal depth range of core rate obtained by drilling is in good agreement with the abnormal range of apparent resistivity at the same location obtained by transient electromagnetic, which indicates the reliability of the detection results. 4) Combining the detection results of the two methods, the location and scope of the heterogeneous rock mass were basically determined, which is located in the western part of the proposed area. The detection results can provide a basis for the safety and stability of the proposed substation foundation. To ensure the safe and stable operation of the proposed substation foundation, effective governance measures for the heterogeneous rock mass of the goaf should be taken.

KEYWORDS

goaf, heterogeneous, rock mass, transient electromagnetic detection, drilling detection

1 Introduction

The old goaf has been compacted for a long time, there is still heterogeneous rock mass in some areas. Under construction and other external environments, ground subsidence, cracks (Xie et al., 2022), and even collapse (Dong L. J. et al., 2021) can occur, causing severe damage to the buildings above it. The characteristics of the heterogeneous rock mass in the old mine goaf have become a difficult problem restricting the urbanization above it. The extreme saturation of the city and the shortage of power resource supply also make the construction of substations imminent. To solve this problem, it was proposed for the first time to build the Yingbin substation in the old coal mine goaf of Xinhua District, Pingdingshan City, Henan Province, China. However, the detection of anomalous regions with complex structures is very challenging (Dong et al., 2020). Thus, the key is to ensure the safety and stability of the foundation of the proposed substation to clarify the spatial location and distribution range of the heterogeneous rock mass in the goaf underlying the proposed substation.

The drilling method is widely used in geological exploration because of the advantages of intuitive detection results, accurate depth positioning, and small site restrictions (Ji and Ma, 2009). Xiong et al. (2010) comprehensively used drilling and residual settlement to detect the iron tower site in the goaf and analyzed the feasibility of iron tower construction. Hu et al. (2019) conducted drilling detection in the Pingshuo mining area according to the layout principle of "multiple use of one hole, and combination of sparse and dense" and revealed the coal quality in the mining and stripping area, which provided geological data for the mining and stripping planning of the mine. Li and Tian, (2013) used drilling technology and electrical conductivity imaging system to detect and analyze the structure and stability of the goaf and verified the reliability of the drilling method to detect the goaf through actual engineering cases. Ye et al. (2012) used the method of combining drilling and laser detector to obtain fine spatial data of goaf. Although drilling detection is widely used in geological exploration, it has disadvantages such as high cost and low efficiency, and because this technology is to use points to analyze the foundation structure, it cannot form coherent image data (Lin and Qiu, 2021). In addition, extensive drilling will cause damage to the detection object, so it is not suitable for large-scale applications.

During the last 50 years, geological detection has developed rapidly (Dong L. et al., 2021). The transient electromagnetic method plays an important role in geological detection because of its high sensitivity (Cheng et al., 2021), low investment, and accurate exploration. Chen et al. (2019) used the finite element method to simulate the transient electromagnetic response law of surrounding rock mass and abnormal body under different electrical properties and geometric parameters, which improved the interpretation effect of transient electromagnetic method detection. Relying on a goaf in the Ordos mining area, Mou (2018) confirmed that the transient electromagnetic method can effectively detect the shallow buried deep goaf through interference tests, parameter optimization tests, and analysis of typical goaf response characteristics. Xu (2019) combined the known data in the minefield with transient electromagnetic detection to find out the scope of the goaf and the water accumulation area, which proved the feasibility of the method. Si et al. (2020) used the least squares method to constrain the inversion of the transient electromagnetic method, which improved the speed and effectiveness of data interpretation and made the inversion of geological information more accurate. Lu et al. (2021) used the multiground source transient electromagnetic method to detect and analyze a goaf in Gansu Province, China, and the results show that this method can effectively increase the detection depth and improve the ability to distinguish geological anomalies.

The focus of the above-mentioned transient electromagnetic method research is mainly on the accuracy verification and accuracy improvement of the goaf detection, and there are very few foundation investigation studies for buildings on goaf. In view of the respective characteristics of the two detection methods, the goaf underlying the substation was comprehensively detected using the transient electromagnetic method as main and the drilling method as auxiliary based on the principle of complementary advantages, and the spatial location and distribution range of the heterogeneous rock mass in the goaf underlying the proposed substation was finally determined.

2 Comprehensive detection of the goaf

2.1 Hydrogeological situation

The substation is intended to be built on the old coal mine goaf in Xinhua District, Pingdingshan City, Henan Province, China, with poor geological properties and a complex environment. It is located in the Cenozoic overlying area, and the strata in the area are Quaternary, Permian, Carboniferous, and Cambrian from new to old. The lithology and apparent resistivity of each layer are summarized in Table 1.

2.2 Situation of coal mining

The proposed area is located at the southeastern edge of the mining area of the No. 7 mine of Pingmei Group, which is within the coal mining subsidence area. The surface elevation of this area is approximately +85 m. The mining engineering of the nearby coal seam is shown in Figure 1. The mining depth is 160 m, and the mining time was from 1987 to 1993. The longwall

TABLE 1 Stratigraphic electrical properties in the underlying goaf of the substation.

Strata	Thickness/m	Apparent resistivity/Ω.m
Neozoic, Quaternary (N + Q)	<60 m	10–100
Permian (P)	60–85 m, average = 68.7 m	60–150
Carboniferous (C)	average = 66 m	>150
Cambrian(Є)	>50 m	>200

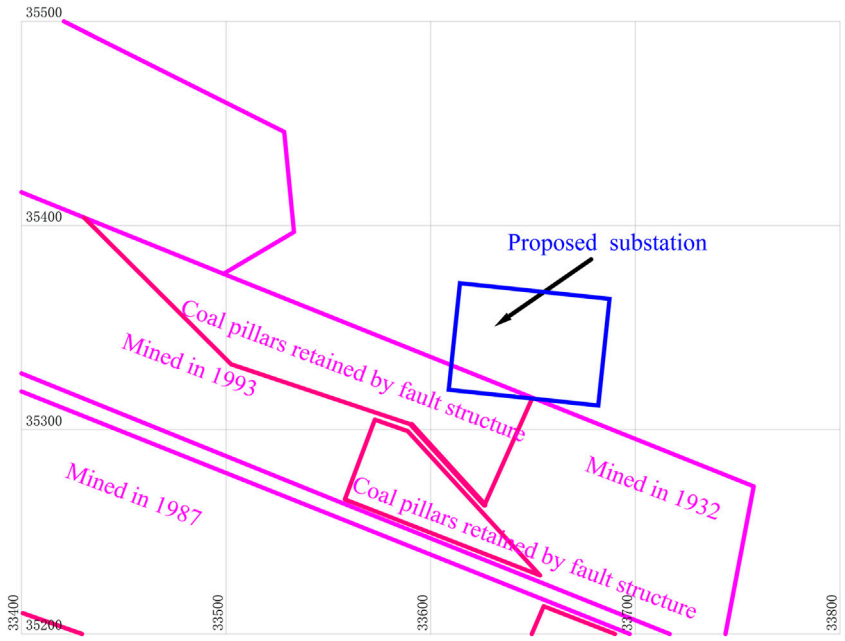

FIGURE 1
The distribution of coal mining projects underlying and near the site.

working face is shot mining, general mining, or fully mechanized mining, and the roof is managed using the full subsidence method. Since underground coal mining caused large-scale ground subsidence in the western section of Jianshe Road and Yingcheng Cultural Square from 1992 to 1993, the ground subsidence pits and ground fissures were extremely developed, which had a significant impact on the local surface morphology. At present, the goaf is in the residual state subsidence deformation period. It can be seen from Figure 1 that the lower left part of the proposed area is located in the old coal mine goaf. To clarify the spatial location and distribution range of the heterogeneous rock mass in the goaf underlying the proposed substation, the lower left part of the figure was selected as the detection area.

After clarifying the primary geological conditions and mining conditions of the goaf underlying the proposed substation, the comprehensive detection of goaf with ground transient electromagnetic method as the main detection and drilling as the auxiliary detection was conducted to detect the spatial location and distribution range of the heterogeneous rock mass in the goaf underlying the proposed substation.

2.3 Detection using the transient electromagnetic method

The transient electromagnetic method is an artificial source electromagnetic detection method based on the principle of electromagnetic induction (Zhang et al., 2022). The transient electromagnetic method measurement device consists of two parts: the transmitting loop and the receiving loop. The working process of the transient electromagnetic method can be divided into three parts: emission, electromagnetic induction, and reception. When the stable current in the transmitting loop is suddenly cut off, according to the theory of electromagnetic induction, the sudden change of the current in the transmitting loop will inevitably generate

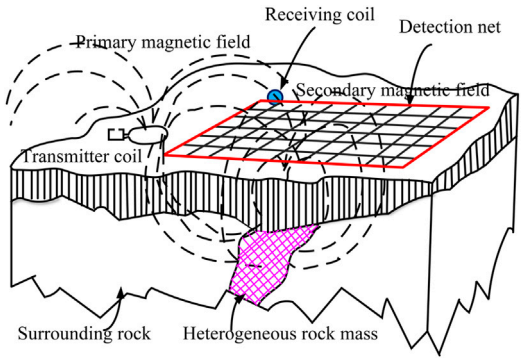

FIGURE 2
The working principle of transient electromagnetic method.

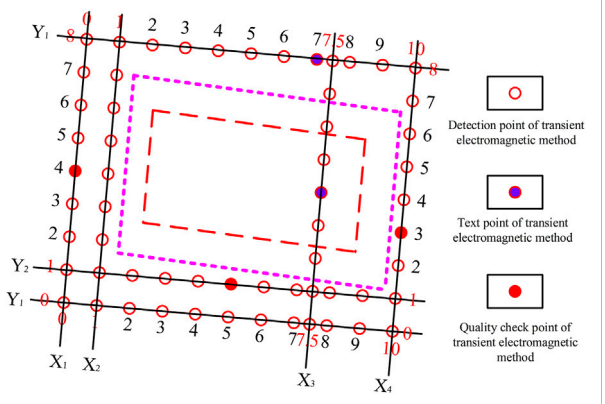

FIGURE 3
Layout of the detection.

a magnetic field around it, which is called the primary magnetic field. During the propagation of the primary magnetic field around, if it encounters a well-conducted underground geological body, induced current, also known as secondary current, will be excited inside the geological body. Since the secondary current changes with time, a new magnetic field is generated around it, which is called the secondary magnetic field. The secondary magnetic field is observed through the receiver coil. Its working principle is shown in Figure 2.

Because the measured value of the transient electromagnetic method in the field is not the true resistivity but the time-varying value of the induced electromotive force (generated by the secondary magnetic field in the receiving coil caused by the eddy current), the change value cannot directly reflect the structure of the geoelectric section. This is not conducive to the inference and interpretation of the underground geological body. Therefore, it is necessary to implement resistivity and time and depth conversion processes and convert the measured induced electromotive force into the apparent resistivity value of the formation that changes with depth before it can be used for geological inference and interpretation.

Under the assumption of a one-dimensional geoelectrical section in a uniform half-space, the calculation formula for the depth and the apparent resistivity can be obtained by theoretical derivation as follows (Hai et al., 2018):

$$\rho_t = \frac{\mu_0}{4\pi t}\left(\frac{2\mu_0 S_t S_r}{5t(V(t)/I)}\right)^{2/3} \tag{1}$$

$$h_t = \left(\frac{3S_t S_r}{16\pi(V(t)/I)\sigma_t}\right)^{1/4} - \frac{t}{\mu_0\sigma_t} \tag{2}$$

$$\sigma_t = \frac{16}{\mu_0}\left(\frac{\pi}{3S_t S_r}\right)^{1/3}\frac{(V(t)/I)^{5/3}}{(d(V(t)/I/dt))^{4/3}} \tag{3}$$

where ρ_t is the apparent resistivity, Ω; μ_0 is the permeability of the formation medium, H/m; t is the recording time, s; S_t is the area of the transmitting coil, m^2; S_r is the area of the receiving coil, m^2; $V(t)$ is the induced electromotive force of a window at a specific time, V; I is the power supply current of the transmitting coil, A; h_t is the depth, m; σ_t is the longitudinal conductance, S; and $V(t)/I$ is the normalized induced electromotive force, V.

Although the apparent resistivity is not the actual formation resistivity, its spatial variation characteristics are consistent with the real site cross-sections, which can objectively show the spatial distribution characteristics of underground geological bodies.

2.3.1 Field detection

The choice of transient electromagnetic working parameters and working devices will directly affect the quality and results of field data collection and affect the processing and interpretation of data. There are various working devices for transient electromagnetic exploration. According to the analysis of the ground features and geological conditions in the detection area, as well as the analysis of the buried data of the target layer, the 1.5 m × 1.5 m small wire frame overlapping loop working device was selected.

To ensure reasonable construction parameters, the tests of the transmission frequency and the number of superimpositions were mainly conducted to meet the required exploration depth and accuracy. Combined with the geological characteristics of the detection area and previous detection experience, the emission frequency is 6.25 Hz, the emission wire frame is 1.5 m × 1.5 m, and the stacking times were selected from 256 to 1,024 times, and a total of two test points have been completed. In addition, the collected data are less affected by interference factors, so it is inferred that this set of parameters is suitable for this detection area. After the test, the number of stacking in this detection area is not less than 512 times to ensure effective suppression of random interference.

2.3.2 Detection scheme layout

After several field tests on the goaf underlying the proposed substation, it was found that the transmission frequency that

meets the detection requirements is 6.25 Hz, the transmission wireframe is 1.5 m × 1.5 m, and the superposition is more than 512 times. Seven survey lines were set up according to the above construction parameters. The distance between each line of detection differed according to the ground object conditions. The distance between each point on the detection line was 10 m; There are 60 physical points (including two test points) and three quality check points on the line. A total of 63 transient electromagnetic physical points were obtained. The total length of the section was 620 m, and the specific layout is shown in Figure 3.

A total of 63 production records were obtained in this transient electromagnetic detection. Among them, 52 are grade A records, with a grade A rate of 82.5%; 11 are grade B records, with a grade B rate of 17.5%. There are a total of 63 qualified records, with a pass rate of 100%.

After analyzing the three quality checkpoints in the entire area (5% of the physical points on the line), the maximum relative error was 9.21%, the minimum error was 0.11%, and the total average relative error of the entire detection area was 4.79%. The pass rate of the original data was 100%, which meets the standard of "Coal Electricity Exploration Specification" (MT/T898-2000).

2.3.3 Analysis of detection results

The changes in soil deformation and water content are mutually influential (Bai et al., 2021). The water content (Bai et al., 2022) and temperature of the soil (Bai et al., 2021) have an influence on the conductivity of the soil. Because of the small detection depth range, the formation temperature changes very little, so the effect of temperature on the formation resistivity can be ignored. According to the known data, most of the goaf is filled with water, so the influence of water content on soil conductivity cannot be ignored. Under normal circumstances, the precise resistivity profile contour of the formation is consistent with its trend. When the geological structure is developed, or when there are other low-resistance anomalies, the apparent resistivity contours are distorted, or the gradient changes in the horizontal and vertical directions. When there is no water in the goaf, it exhibits a high resistance relative to the surrounding rock. On the contrary, the goaf offers low resistance relative to the surrounding rock when it contains water (Chang et al., 2020). In this proposed area, the coal seams of Ji_{16-17} were mainly mined, and the water came from limestone aquifers and Quaternary surface water. After a comprehensive analysis of the known data, it was inferred that most of the goaf was filled with water, resulting in low resistance reflection.

The transient electromagnetic method observation data induced electromotive force of each time window of each measuring point, which needs to be converted into parameters such as apparent resistivity and apparent depth to interpret the data. According to formulas (1)~(3), the apparent resistivity of each point at each depth can be obtained. By arranging the seven survey lines, the vertical and horizontal apparent resistivity detection of the entire complex goaf can be obtained. The induced electromotive force measured by the device is transmitted to the microcomputer, and the measured data are calculated and checked. Then, a $V(t)/I$ multimeasurement channel cross-section curve was drawn. According to the curve change characteristics, the distortion point data are removed, and the off-time correction is further implemented to eliminate the distortion of the transient electromagnetic response curve caused by the off-effect, so as to achieve the purpose of reflecting the true underground resistivity response. On this basis, the apparent resistivity (ρ_t) is calculated, and the apparent resistivity and the existing geological data are used to invert each measuring point to transform the "apparent resistivity-time" relationship into the "apparent resistivity-depth" model, and then, the detection results of the vertical and horizontal apparent resistivity were drawn. The detection results and analysis results of the seven survey lines are as follows.

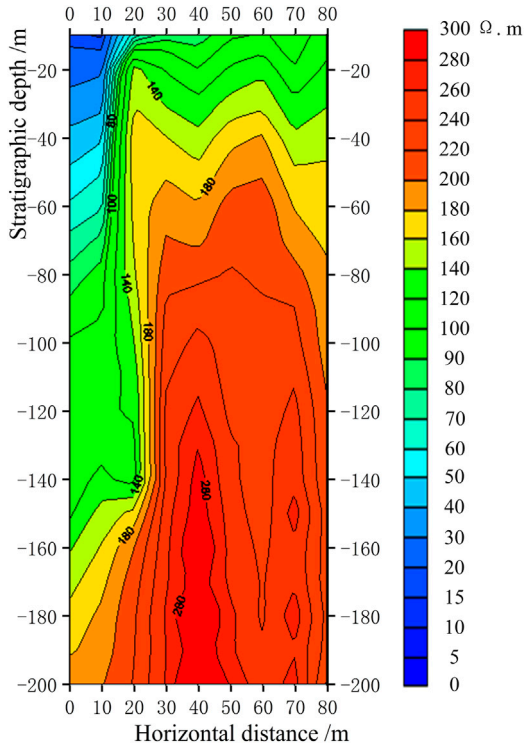

FIGURE 4
Longitudinal section view of resistivity of X_1 line.

The detection points of the detection line X_1 are from 0 to 8. From the longitudinal section of the apparent resistivity (Figure 4), it can be seen that between the lateral distances of 0 and 20 m (points 0–2), when the depth is greater than −160 m, the apparent resistivity contour is bent down, showing a low-resistance anomaly. This anomaly is because of the influence of

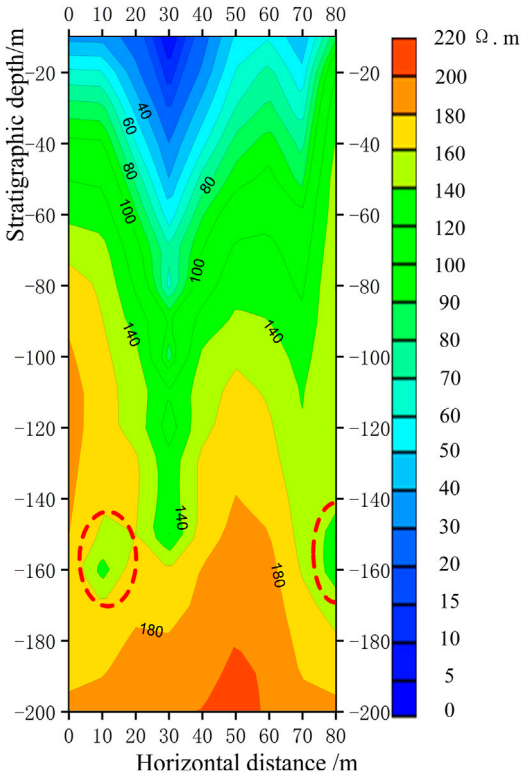

FIGURE 5
Longitudinal section view of resistivity of X_2 line.

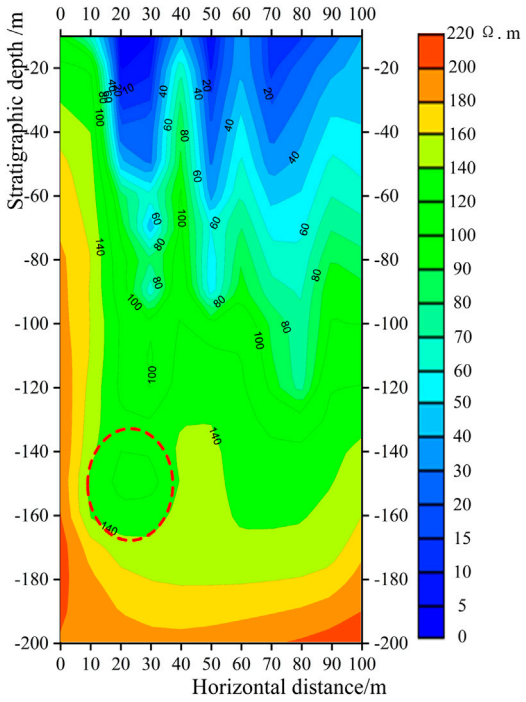

FIGURE 6
Longitudinal section view of resistivity of Y_3 line.

the iron fence on the side of the Eagle City Square table tennis court between points 0 and 2. There is no obvious low-resistance anomaly near the depth of −160 m in other parts, so there is no abnormal goaf.

The detection points of the detection line X_2 are from points 0 to 8. From the longitudinal section of the apparent resistivity (Figure 5), it can be found that the contour line at a depth of −160 m is a low-resistance depression at a lateral distance of 30 m (point 3). It is predicted that this abnormality is because of the influence of the coal mine goaf, but it is located in the color board room of the badminton court in Yingcheng Square, so it can be inferred that this abnormality is because of the color board house. At lateral distances of 10, 20, and 80 m (points 1, 2, and 8), the contour line at a depth of −160 m has a low-resistance-closed and semiclosed circle, which is inferred to be an abnormal goaf, as shown by the red dashed line in Figure 5.

The detection points of the detection line Y_3 are from points 0 to 10. From the longitudinal section of the apparent resistivity (Figure 6), it can be seen that there is a low-resistance depression at a depth of −160 m between the lateral distances of 10 and 30 m (points 1–3), which is inferred to be an abnormal goaf, as shown by the red dashed line in Figure 6.

The apparent resistivity sections of the detection line X_3, the detection line X_4, the detection line Y_1, and the detection line Y_2 are respectively shown in Figures 7A–D. It can be seen from these four profiles of apparent resistivity that there is no downward distortion of apparent resistivity contours or other obvious low-resistance depressions in the vicinity of the depth of −160 m. Therefore, it is speculated that there is no low-resistance abnormal area in those areas.

After completing the data processing and analysis of the seven survey lines, they were combined with the collected geology of the survey area and coal seam mining conditions, and horizontal profiles of the apparent resistivity were obtained at depths of −160 and −200 m in the detection area. The electrical characteristics of the detection area were further studied to analyze the distribution of the abnormal goaf in the detection area.

The horizontal profile of the apparent resistivity at a depth of −160 m is shown in Figure 8. The color in Figure 8 changes from red to green, representing a gradual decrease in the apparent resistivity. Figure 8 shows the electrical distribution at a depth of −160 m in the detection area, which exhibits high left, low right, and high and low electrical characteristics. The low-resistance area is indicated by the red dashed line in Figure 8. The distribution range is relatively uniform. In addition, the scope of the low-resistance area is large, and it is speculated to be an abnormal goaf.

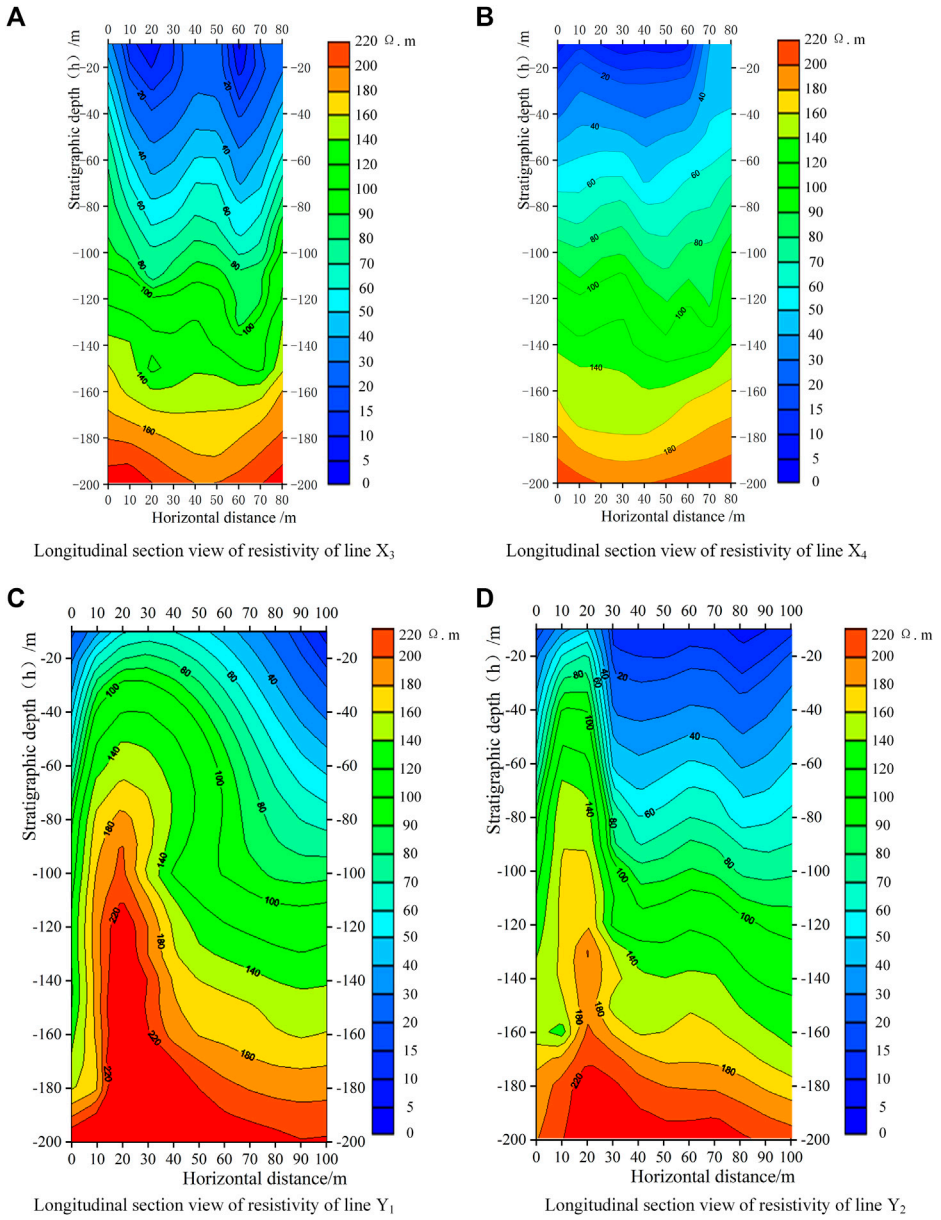

FIGURE 7
Longitudinal section view of resistivity of X_3, X_4, Y_1, and Y_2 line.

The horizontal profile of the apparent resistivity at a depth of −200 m is shown in Figure 9. The color in Figure 9 changes from red to blue, representing a gradual decrease in the apparent resistivity. Figure 9 shows the electrical distribution at a depth of −200 m in the detection area, where the electrical characteristics are high on the left, bottom, and right sides and relatively low on the upper side. The low-resistance area is circled by the red dashed line in Figure 9, and it is speculated to be an abnormal goaf. This abnormal area coincides with the abnormal position in the horizontal profile of the apparent resistivity at a depth of −160 m.

To further analyze the relationship between the stratigraphic depth and the apparent resistivity, the relationship curve between the stratigraphic depth and the apparent resistivity at point 3 of the Y_3 line is drawn, as shown in Figure 10. The apparent resistivity at point 3 of the Y_3 line exhibits an increasing trend as the depth of the stratigraphic increases. However, the apparent resistivity decreases at

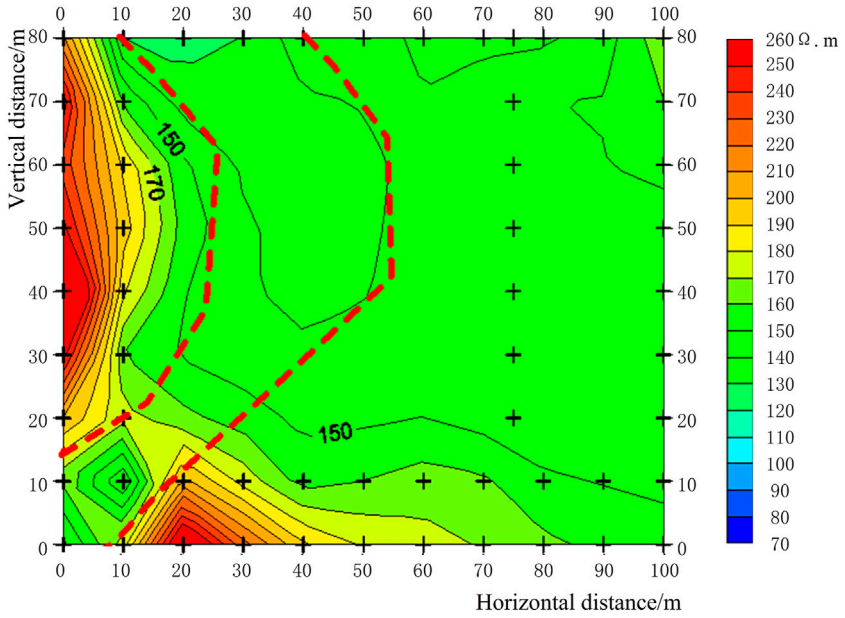

FIGURE 8
Horizontal profile of apparent resistivity at a depth of -160 m.

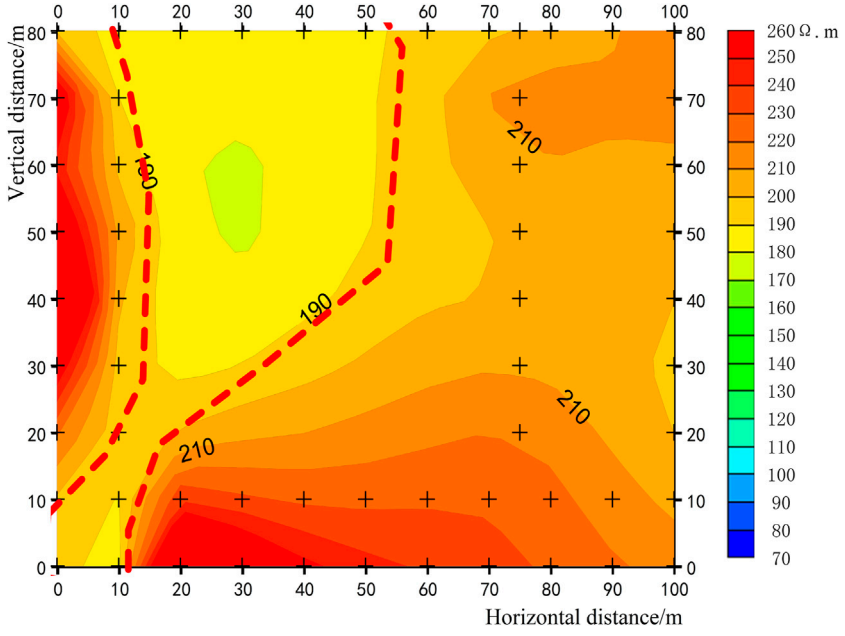

FIGURE 9
Horizontal profile of apparent resistivity at a depth of -200 m.

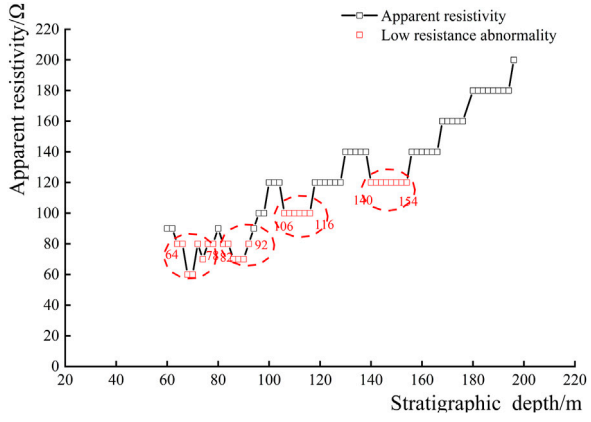

FIGURE 10
Relationship between formation depth and apparent resistivity at point 3 of the Y_3 line.

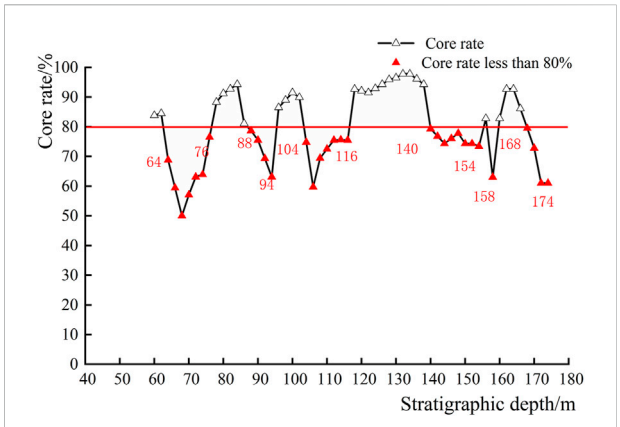

FIGURE 12
Relationship between the drilling depth and the core ratio at point 3 of the Y_3 line.

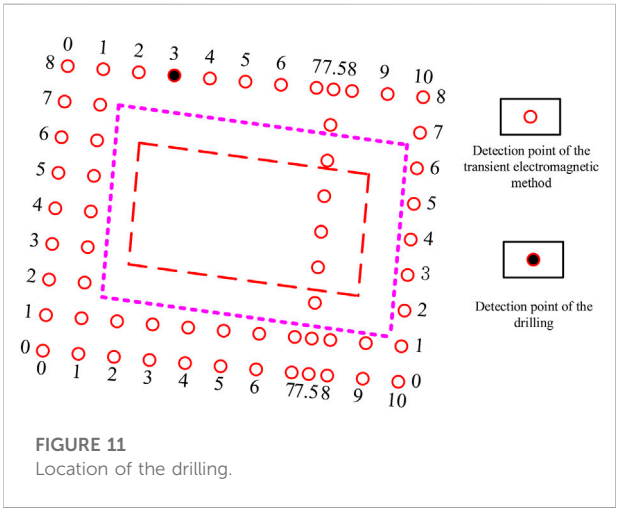

FIGURE 11
Location of the drilling.

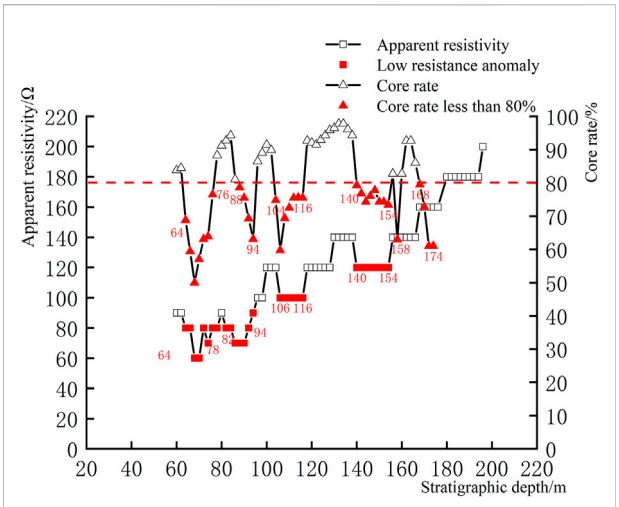

FIGURE 13
Core rate and the apparent resistivity at point 3 of the Y_3 line.

depths of −64 to −78 m, −82 to −92 m, −106 to −116 m, and −140 to −154 m.

2.4 Detection of drilling

To further provide the stratum data for foundation stability and disaster assessment, drilling detection was used to reveal the primary conditions of the detection area. The drilling is located in the speculated goaf in the northwest corner of the site and is the transient electromagnetic detection point 3 of the Y_3 line. The drilling depth is −170 m, and the position is shown in Figure 11.

The high-speed drilling rig used for drilling detection was an XY-4-type mechanical drive, a hydraulic-feed high-speed drilling rig. A mud-protected wall and a core tube with an outer diameter of 108 mm were used for drilling at a depth of 0 to −60 m. A 60 m casing with mud to protect the wall was used, and a core tube with an outer diameter of 75 mm was drilled at depths of −60 to −150 m. A 150 m casing with mud to protect the wall was also used, and a core tube with an outer diameter of 60 mm was drilled at depths of −150 to −170 m.

During the drilling process, the joints and fissures in the shale rock at the depths of −64 to −76 m, −88 to −94 m, −104 to −116 m, and −140 to −154 m are relatively developed, and there is a small amount of water leakage. The drill is buried at approximately −105 m (determined based on the situation in the core tube of 75 m after the drilling was finished). The results of drilling detection indicate that there is fragmentation in the lower part of the rock mass (shale rock layer), and the cracks are relatively developed. However, the original rock mass structure was retained, and the skeleton particles were in contact with each other. However, at depths of −164 to −170 m, the rock was relatively broken, and the fracture zone was filled with some

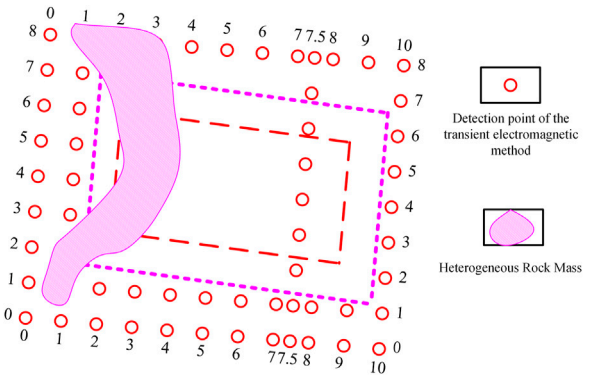

FIGURE 14
Heterogeneous rock mass in the goaf underlying the proposed substation.

fluid substances, such as mud and water. It can be seen from the above that although the rock stratum is developed in many depths, the original rock mass structure is still retained. Only at the depths of −164 to −170 m, there is a fault zone in the rock mass, so only the depths of −164 to −170 m are considered to be the heterogeneous rock mass in the goaf.

Figure 12 is the relationship between the drilling depth and the core rate at point 3 of the Y_3 line. In general, the core rate is not less than 80% for general rocks and not less than 65% for soft and broken rocks. The rocks in the proposed are of the general type. It can be seen that from Figure 12, the core collection rate is less than 80% when the drilling depths are −64 to −76 m, −88 to −94 m, −104 to −116 m, −140 to −154 m, −158 m, and −168 to −174 m. There is a 1.6 m coal seam around the depth of −158 m.

3 Safety and stability evaluation of the proposed substation

The results of apparent resistivity at point 3 of the Y_3 line and the results of drilling detection at this point are shown in Figure 13 at the same time. It can be seen from Figure 13 that the results of transient electromagnetic detection and drilling detection are highly consistent, indicating the reliability of the detection results. In addition, from the results of the drilling detection, it can be known that the abnormal goaf inferred by the transient electromagnetic method is the heterogeneous rock mass in the goaf.

The heterogeneous rock mass in the goaf underlying the proposed substation can be determined finally through a comprehensive analysis of the horizontal profile of the apparent resistivity at depths of −160 and −200 m, the relationship curve between the stratum depth and the apparent resistivity, and the relationship curve between the drilling depth and the core rate. The heterogeneous rock mass in the goaf underlying the detection area is the pink-shaded area in Figure 14. This indicates that there are uncertain factors in the safety and stability of the proposed area. Therefore, it is necessary to adopt effective governance measures to ensure the safety and stability of its operations.

4 Conclusion

According to the geological conditions of the proposed area and the characteristics of transient electromagnetic detection and drilling detection, the transient electromagnetic method was selected as the main detection method, and the most subjective and effective detection method—drilling detection—was used as auxiliary detection. The research results show the following:

1) After eliminating the interference, in the longitudinal section of apparent resistivity of the seven detection lines of the transient electromagnetic method, points 1 to 2 and point 8 of the X_2 detection line, and points 1 to 3 of the Y_3 detection line, there is a low-resistance anomaly near the depth of -160 m, which is presumed to be an abnormal goaf; the other five detection lines have no obvious low-resistance anomaly, indicating that there is no abnormal goaf at these locations.
2) The apparent resistivity at depths of −160 and −200 m was sliced, and the abnormal regions in the two apparent resistivity slice maps are highly consistent. It is basically determined that the abnormal goaf underlying the proposed substation is located on the west side of the proposed area.
3) Drilling was conducted at point 3 of the Y_3 line, and the relationship between the drilling depth and the core rate was drawn. The depth range where the core rate is lower than 80% is in good agreement with the depth range of the low-resistance anomaly of the transient electromagnetic method, indicating the reliability of the detection results. In addition, it can be known that the abnormal goaf inferred by the transient electromagnetic method is the heterogeneous rock mass in the goaf from the results of the drilling detection.
4) The comprehensive analysis of the detection results of the two methods can determine the spatial location and distribution range of the heterogeneous rock mass in the goaf underlying the proposed substation accurately, which is located on the west side of the detection area. There are uncertain factors in the safety and stability of the proposed area, and effective governance measures should be taken for the heterogeneous rock mass of the goaf to ensure the safe and stable operation of the proposed substation.

Data availability statement

The original contributions presented in the study are included in the article/supplementary material; further inquiries can be directed to the corresponding author.

Author contributions

Conceptualization, JD, YZ, ZX, and KG; methodology, JD; validation, JD, YZ, and KG; formal analysis, JD; investigation, JD and YZ; resources, JD; writing—original draft preparation, JD; writing—review and editing, JD, YZ, ZX, and KG; visualization, JD, YZ, and KG.

Funding

This study was financially supported by the National Natural Science Foundation of China (Grant No. 52074148) and the Educational Department of Liaoning Province (Grant No. LJ2020JCL019).

Conflict of interest

The authors declare that the research was conducted in the absence of any commercial or financial relationships that could be construed as a potential conflict of interest.

Publisher's note

References

Bai, B., Zhou, R., Cai, G. Q., Hu, W., and Yang, G. C. (2021). Coupled thermo-hydro-mechanical mechanism in view of the soil particle rearrangement of granular thermodynamics. *Comput. Geotechnics* 137 (8), 104272. doi:10.1016/j.compgeo.2021.104272

Bai, B., Wang, Y., Rao, D., and Bai, F. (2022). The effective thermal conductivity of unsaturated porous media deduced by pore-scale SPH simulation. *Front. Earth Sci.* 10, 943853. doi:10.3389/feart.2022.943853

Chang, J. H., Su, B. Y., Malekian, R., and Xing, X. J. (2020). Detection of water-filled mining goaf using mining transient electromagnetic method. *IEEE Trans. Ind. Inf.* 16 (05), 2977–2984. doi:10.1109/TII.2019.2901856

Chen, Q. J., Zhang, Y. C., Qiu, H., Lian, W. G., and Fan, L. L. (2019). Transient electromagnetic response characteristics of mine water-rich area. *Saf. Coal Mines* 50 (10), 185–189. doi:10.13347/j.cnki.mkaq.2019.10.043

Cheng, H., Yu, C. T., Han, Y. L., Wang, H. M., Yang, X. C., and Yang, Y. (2021). Detection accuracy of various goafs by transient electromagnetic method. *Sci. Technol. Eng.* 21 (6), 2262–2268. doi:10.3969/j.issn.1671-1815.2021.06.019

Dong, L., Chen, Y., Sun, D., and Zhang, Y. (2021a). Implications for rock instability precursors and principal stress direction from rock acoustic experiments. *Int. J. Min. Sci. Technol.* 31 (5), 789–798. doi:10.1016/j.ijmst.2021.06.006

Dong, L. J., Tong, X. J., Hu, Q. C., and Tao, Q. (2021b). Empty region identification method and experimental verification for the two-dimensional complex structure. *Int. J. Rock Mech. Min. Sci.* 147, 104885. doi:10.1016/j.ijrmms.2021.104885

Dong, L., Tong, X., and Ma, J. (2020). Quantitative investigation of tomographic effects in abnormal regions of complex structures. *Engineering* 7 (7), 1011–1022. doi:10.1016/j.eng.2020.06.021

Hai, S. Y., Yun, M. H., and Zhao, Q. F. (2018). Application and interpretation method of TEM data based on drilling constraint. *Coal Geol. Explor.* 46 (4), 174–180. doi:10.3969/j.issn.1001-1986.2018.04.028

Hu, G. X., Li, W. H., Li, J. T., Li, P. T., and Li, G. (2019). Borehole layout for production geological exploration in Pingshuo open-pit mine. *Opencast Min. Technol.* 34 (6), 85–87. doi:10.13235/j.cnki.ltcm.2019.06.023

Ji, S. H., and Ma, Z. H. (2009). Analysis of drilling technology in engineering geology prospecting. *Coal Technol.* 28 (9), 152–153.

Li, X. L., and Tian, Y. B. (2013). Analyses and application of detection technique for old coal mining area. *J. Henan Polytech. Univ. Sci.* 32 (3), 277–280. doi:10.3969/j.issn.1673-9787.2013.03.006

Lin, X. Y., and Qiu, Z. H. (2021). Application practice of detecting shallow goaf based on down-the-hole drilling. *Min. Technol.* 21 (1), 101–103. doi:10.13828/j.cnki.ckjs.2021.01.029

Lu, K. L., Li, X., Fan, Y. N., Zhou, J. M., Qi, Z. P., Li, W., et al. (2021). The application of multi-grounded source transient electromagnetic method in the detections of coal seam goafs in Gansu Province, China. *J. Geophys. Eng.* 18 (04), 515–528. doi:10.1093/jge/gxab031

Mou, Y. (2018). Experimental study on response characteristics of transient electromagnetic method in shallow gob. *Coal Sci. Technol.* 46 (10), 203–208. doi:10.13199/j.cnki.cst.2018.10.032

Si, Y. L., Li, M. F., Liu, Y. N., and Guo, W. H. (2020). One-dimensional constrained inversion study of TEM and application in coal goafs' detection,open. *Geosciences* 12 (01), 1533–1540. doi:10.1515/geo-2020-0148

Xie, X., Hou, E., Long, T., Feng, D., Hou, P., Wei, Q., et al. (2022). Study on evaluation and prediction of the degree of surface damage caused by coal mining. *Front. Earth Sci.* 9, 805248. doi:10.3389/feart.2021.805248

Xiong, C. X., Liang, H. C., Ma, J. R., and Zhang, E. F. (2010). Stability analysis of the building foundation over goal area. *J. Min. Saf. Eng.* 27 (1), 100–105. doi:10.3969/j.issn.1673-3363.2010.01.019

Xu, X. P. (2019). Application of the transient electromagnetic method to flooding survey in a coal. *Min. Area Shanxi Prov.* 55 (2), 579–584. doi:10.12134/j.dzykt.2019.02.012

Ye, T. Q., Chen, J. J., and Wang, T. (2012). Risk detecting and analysis of complex gob in the opencast mining. *China Min. Mag.* 21 (1), 87–89. doi:10.3969/j.issn.1004-4051.2012.01.022

Zhang, J. C., Wu, B. C., Wang, F., Shi, S. Z., Liu, J. J., Wang, M. X., et al. (2022). Experimental research of compound monitoring on multiple temporary blocking refracturing for long-section horizontal wells. *Front. Earth Sci.* 9, 760390. doi:10.3389/feart.2021.760390

frontiers | Frontiers in Earth Science

TYPE Original Research
PUBLISHED 08 September 2022
DOI 10.3389/feart.2022.961277

OPEN ACCESS

EDITED BY
Wenzhuo Cao,
Imperial College London,
United Kingdom

REVIEWED BY
Holger Steeb,
University of Stuttgart, Germany
Xiangxin Liu,
North China University of Science and Technology, China
Xueyi Shang,
Chongqing University, China
Fuqiong Huang,
China Earthquake Networks Center, China

*CORRESPONDENCE
Yonghwan Joo,
jooyh@kigam.re.kr

SPECIALTY SECTION
This article was submitted to Structural Geology and Tectonics, a section of the journal Frontiers in Earth Science

RECEIVED 04 June 2022
ACCEPTED 19 August 2022
PUBLISHED 08 September 2022

CITATION
Yu J, Joo Y and Kim B-Y (2022), A multi-model fitting algorithm for extracting a fracture network from microseismic data.
Front. Earth Sci. 10:961277.
doi: 10.3389/feart.2022.961277

A multi-model fitting algorithm for extracting a fracture network from microseismic data

Jeongmin Yu, Yonghwan Joo* and Byoung-Yeop Kim

Petroleum & Marine Research Division, Korea Institute of Geoscience and Mineral Resources, Daejeon, South Korea

Fractures are increasingly employed in tectonic movement and earthquake risk analyses. Because fracture connectivity influences fluid flow pathways and flow rates, fractures are studied to evaluate sites for CO_2 sequestration, radioactive waste storage and disposal, petroleum production, and geothermal energy applications. Discrete fracture networks are an effective method for imaging fractures in three-dimensional geometric models and for analyzing the fluid behavior that cause movements in fracture zones. Microseismic event monitoring data can be used to analyze the event source mechanisms and the geometry, distribution, and orientation of the fractures generated during the event. This study proposes a method for simultaneously imaging multi-fracture networks using microseismic monitoring data. The random sample consensus and propose, expand, and re-estimate labels algorithms commonly used in multi-model fitting were integrated to produce an upgraded method that accommodates geophysical data for faster and more accurate simultaneous multi-fracture model imaging within a point cloud. The accuracy of the method was improved using circular calculation and density-based spatial clustering of applications with noise, such that the estimated fracture orientations correspond well to those at the actual locations. The proposed algorithm was applied to synthetic data to assess the impact of considering orientation and outlier data on the model results. The errors in the results when considering orientation were 1.32% and 0.83% for the strike and dip angles, respectively, and those without considering were 20.23% and 24.63% respectively. In addition, the errors in the results obtained from data containing many outliers were 1.89% and 1.64% for the strike and dip angles, respectively. Field microseismic data were also used to depict fractures representing the dominant orientation, and the errors of the strike and dip angle estimates were 2.89% and 2.83%, respectively. These results demonstrate the suitability of the algorithm for fast and accurate field data modeling.

KEYWORDS

microseismic data monitoring, borehole geophysics, image processing, fracture network, enhanced geothermal system, CO2 sequestration

1 Introduction

Fractures form when the stress exceeds the rock strength, causing the rock to split into separate pieces. A fracture can be classified as a fault if the relative rock displacement is parallel to the fracture direction or as a joint if there is no relative displacement (Mitcham, 1963; Gudmundsson, 2011). Fault planes represent structurally vulnerable subsurface areas that require earthquake risk analysis and the determination of large-scale structure safety. Joints are useful for tectonic movement analysis because they can be used to estimate changes caused by stress after rock formation. Therefore, fracture analysis studies have been widely conducted in many disciplines to identify subsurface structures.

Understanding subsurface fracture connectivity is vital for analyzing fluid flow pathways. Numerous studies have conducted core analysis and numerical modeling of groundwater flow through natural fractures (Raven and Gale, 1985; Kwicklis and Healy, 1993; Mayer and Sharp, 1998). In the petroleum industry, hydraulic fracturing is used to improve oil and gas recovery and geothermal energy production, as well as to create artificial fractures for improving subsurface connectivity (Valko and Economides, 2001; Montgomery and Smith, 2010; Zhang et al., 2010).

Microseismic events are very weak earthquakes with a negative moment magnitude that occur on very small spatial scales, and are generated by anthropogenic changes to the natural stress-strain state of formations, such as by hydraulic fracturing, or by natural forces, such as tectonic motions. Microseismic events associated with hydraulic fracturing generally occur in three areas: parent hydraulic fracture side-wall because of the leakage of the pressurized fluid, critically stressed natural fracture, and close to the hydraulic fracturing tip (Busetti et al., 2014). Microseismic monitoring is an important tool for identifying, positioning, and characterizing these events, which can provide information on the growth patterns of fractures induced by high-pressure fluid injection and overall dimensions (Economides and Nolte, 2000; Warpinski et al., 2013). Thus, uncertainties can be analyzed for individual events and leakage events that are not associated with major fracture networks by estimating the extent of microseismic event clouds.

Discrete fracture networks (DFNs) are widely used to analyze fracture connectivity. DFNs can be used to image and model individual three-dimensional (3D) fractures to evaluate the changes in their geometry and behaviors of associated fluids (Dershowitz and Fidelibus, 1999; Li and Lee, 2008; Hyman et al., 2015). They can be constructed in many ways, such as by linking fracture imaging to seismic activity based on microseismic monitoring data (Fadakar Alghalandis et al., 2013) or the source mechanism (Yu et al., 2016; Yu et al., 2020). They are useful because they can identify and display fracture locations solely based on microseismic data. However, fracture orientations determined solely from microseismic event locations often exhibit poor accuracy. Therefore, it is necessary to enhance the reliability of fracture orientation data by incorporating the strike and dip angles at the event location. However, no method for extracting multiple fracture network models has been developed so far.

A method for extracting points associated with each fracture is required to image a DFN in a 3D point cloud, such as the location of a microseismic event. Complementary computer vision techniques have been developed for this purpose, including the widely used Random Sample Consensus (RANSAC) (Fischler and Bolles, 1981) and Hough transform (Duda and Hart, 1972) algorithms. Although these techniques are appropriate for locating a point within the cloud that easily meets specific threshold conditions, the input variables, computation time, and sequential model estimation remain problematic. Isack and Boykov developed the Propose, Expand, and Re-estimate Labels (PEARL) energy-based multi-model optimization algorithm to resolve these issues (Isack and Boykov, 2011). This algorithm iteratively estimates inliers and model parameters based on a global regularization function. As PEARL lowers the variable dependency, it effectively reduces the computation time, and allows simultaneous multi-fracture imaging; however, as only the distance energy between feature points in the image is utilized, it is difficult to consider the direction in three dimensions.

This study proposes a method for imaging fractures using microseismic data based on the multi-fitting algorithm, and represents an improvement over the existing PEARL algorithm for geophysical data systems. This approach integrates microseismic event locations and fracture orientations to enhance the reliability and accuracy of fracture imaging. To confirm the effectiveness of proposed method, a synthetic model simulating microseismic event locations was created and the resulting fracture images were compared, taking into account the influence of orientation and outlier data. The applicability of the proposed method was also tested using field data provided by a geothermal data repository (http://gdr.openei.org/submitssi-ons/1091) operated by the Department of Energy (DOE) Geothermal Technology Office (Gritto et al., 2018).

2 Methodology

2.1 RANSAC algorithm

The RANSAC algorithm (Fischler and Bolles, 1981) was developed to detect simple shapes such as lines, circles, and planes within a point cloud through the iterative estimation of model parameters by randomly sampling data points for consensus. A simple RANSAC algorithm for a microseismic event involves the following steps.

1) A plane model is generated by randomly selecting three points from the event location data.

2) The distances between the generated fracture planes and all other points are calculated.

3) Inlier points are selected from among the threshold distance (t_d) parameter values.

4) If the number of inlier points is greater than the number of threshold points (t_p), or the minimum number of points required extracting the plane model, then only these points are used to refit the generated plane.

5) The objective function is updated,

$$O = \sum_{p=1}^{n_p} (distance) \Big/ n_p \tag{1}$$

where n_p is the number of inliers, and the record is the most effective if $O_k < O_{k-1}$, where k is the iteration counter.

6) The process is then restarted from Step 2) until the desired iteration is attained.

The number of iterations (n_k) for optimal results in RANSAC must be chosen sufficiently to ensure the probability that at least one of the point datasets contains only inliers, and is generally determined as follows

$$n_k = \frac{\log(1-a)}{\log(1-(1-b)^r)} \tag{2}$$

where, b is the probability of success, a represents the probability that any selected data point is an outlier, and r is the number of points used to generate the model (2 and 3 for a line and plane, respectively).

Although RANSAC has mainly been applied in image processing and computer vision, its capability to extract a model from a point cloud can be exploited to image fractures based on seismic event location data. Thus, RANSAC can robustly estimate the model parameters with good accuracy, even if there are many outliers. However, the algorithm involves a high computational load because it utilizes random models, which can require a large number of iterations, and the values of several input parameters are set by the user, which significantly influences the results. RANSAC selects only one optimal model from the iterative random sampling models in a sequential estimation process. Therefore, the dataset used to estimate a model is disregarded before a new model is obtained in the next iteration. Therefore, simultaneous estimation of multiple models using RANSAC remains challenging.

2.2 PEARL and energy minimization

PEARL (Isack and Boykov, 2011) involves an iterative method similar to RANSAC to extract models from a point cloud. However, unlike the RANSAC model extraction, which of the PEARL algorithm does not rely solely on the threshold distance or number of points within the point cloud. PEARL

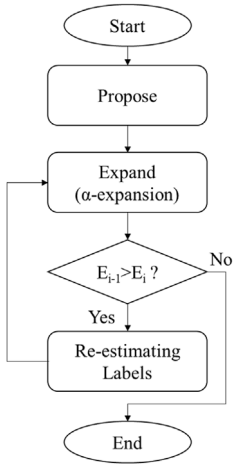

FIGURE 1
Schematic diagram of the original Propose, Expand, and Re-estimate Labels (PEARL) algorithm.

method aims to minimize the function of energy and is generally possible through fewer iterations. PEARL is suitable for obtaining multiple models without disregarding the previously used data in subsequent iterations.

Geometric multi-model fitting using PEARL can be formalized through an optimal labeling problem, where each data point p belongs to a separate label, L_p. The PEARL algorithm was designed for multi-model extraction that minimizes the energy function $E(\mathcal{L})$ by labeling $\mathcal{L}$ as $\{L_p \mid p \in P\}$, as follows (Isack and Boykov, 2011; Delong et al., 2012).

$$E(\mathcal{L}) = \sum_p \|p - L_p\| + \lambda \cdot \sum_{(p,q)\in\mathcal{N}} \omega_{pq} \cdot \delta(L_p \neq L_q) \tag{3}$$

The first term on the right side of Eq. 3 represents a geometric measurement of the data, which is calculated using the distance errors between points assigned to the label and the associated model; p is a point belonging to dataset P, L_p is the label associated with point p, including the model parameter, and $\|p - L_p\|$ represents the Euclidean distance between a point and its associated label. As this distance decreases, the probability of extracting the model by using L_p to which point $p$is assigned, increases. By contrast, as the distance increases, the probability decreases, and the label associated with point p may also change.

The second term of Eq. 3 is used for smoothing, where $\mathcal{N}$ represents a set of neighboring points, $(p, q) \in \mathcal{N}$ indicates that points p and $q$are neighboring points, and L_p and $L_q$are the labels associated with p and q, respectively. The value of $\delta(L_p \neq L_q)$ is 0 when L_p and $L_q$are assigned to the same label, and 1 when they are assigned to different labels. Thus, a discontinuity penalty is applied when neighboring points are assigned to different labels, and assigning neighboring points to the same label is encouraged.

The weight of the discontinuity penalty, $\omega_{pq}$is expressed as follows.

$$\omega_{pq} = exp - \frac{\|p-q\|^2}{\xi^2} \tag{4}$$

where ξ and λ are empirical constants and $\|p-q\|$represents the Euclidean distance between points p and q.

The original PEARL algorithm comprises three steps: propose, expand, and re-estimate. A simplified flowchart of the algorithm is shown in Figure 1. The operations in each step can be summarized as follows.

1) In the propose step, the data are randomly sampled as in RANSAC to generate the initial label set (L_o) for a predefined number of models.

2) In the expand step, α-expansion (Boykov et al., 2001) is performed using an arbitrary label, α, assigned to a generated L_i for energy minimization using Eq. 3. In this step, the spatially consistent label containing the largest number of inliers is obtained through expansion between labels.

3) During the operation of the iterative algorithm, if energy minimization is not achieved during the expand step, then the output of the final label is required, followed by the termination of the algorithm.

4) In contrast, if energy minimization is achieved, the points assigned to each label are used for re-estimation. The existing label set and model parameters are then replaced by a new label set that satisfied the following equation.

$$\hat{L}_i = \underset{l}{\operatorname{argmin}} \sum_{p \in P(L_i)} \|p - l\| \tag{5}$$

where $P(L_i) = \{p \mid L(p) = L_i\}$represents the set of points $p$assigned to label L_i,followed by a return to the expand step using the re-estimated labels in the next iterative step: $i = (i+1)$.

Although the conventional PEARL algorithm is suitable for extracting multi-models from a point cloud, extraction in a full 3D domain using image processing has received limited attention to date. Considering that event location data acquired from the surface include complex and sporadically generated point clouds with many outliers, optimal model extraction is challenging, particularly in terms of increased computation time.

2.3 GARNET algorithm

In this study, the efficiency and accuracy of the original PEARL algorithm were improved for fracture imaging using only the seismic event location and fracture orientation data. The developed algorithm is named as geometric model-fitting algorithm for fracture network (GARNET). In contrast to the original PEARL estimation model, which relies solely on the distances between points and labels, the fracture estimation approach is expected to enhance the model accuracy and reduce the computation time by incorporating fracture orientation data, which can be obtained by analyzing the moment tensor of seismic data recorded by a receiver. This tensor is a mathematical expression of the seismic source, where the displacement at an arbitrary point $\mathbf{x}$ at time t, $u_j(\mathbf{x}, t)$ is represented as the convolution of the second-order moment tensor M_{nk} and the Green's function $G_{jn,k}$(Aki and Richards, 2009), which is expressed as follows.

$$u_j(\mathbf{x}, t) = M_{nk} * G_{jn,k} \tag{6}$$

The moment tensor is symmetrical and comprises six elements characteristic of its source. It is a valuable tool for monitoring earthquakes and microseismic activity because the source mechanism and fault orientations (strike, dip, and rake) can be obtained through its inversion.

Fracture models are created using orientation data acquired from the moment tensor as additional input, employing an algorithm capable of processing such data. Therefore, the orientations associated with a microseismic event and those estimated using the fracture model can be compared to evaluate the accuracy and reliability of the orientation data. The use of orientations that are representative of the event associated with the fracture model represents a faster and more reliable method for comparing the orientations estimated using a model and those of a seismic event. Therefore, methods for calculating the statistical parameters (e.g., mean and variance) of the orientations of multiple events are required. However, circular measurements, such as strike and dip, exhibit fundamentally different characteristics from those of linear measurements. The angles of 0° and 360° represent the same strike orientation, although at opposite locations on a linear scale; therefore, circular measurements require specific analytical methods. In this study, statistical methods (Fisher, 2005; Mardia and Jupp, 2009) were applied to calculate orientations using the following equations.

$$C = \sum_{p=1}^{m} \cos\theta_p,\ S = \sum_{p=1}^{m} \sin\theta_p,\ R^2 = C^2 + S^2\ (R \geq 0) \tag{7}$$

where m is the number of orientations in a group and θ is the strike/dip angle associated with the event. The mean orientation $\bar{\theta}$ is the average of all orientations, and is calculated as follows.

$$\cos\bar{\theta} = \frac{C}{R},\ \sin\bar{\theta} = \frac{S}{R} \tag{8}$$

$$\bar{\theta} = \begin{cases} \tan^{-1}\left(\frac{S}{C}\right) & S>0,\ C>0 \\ \tan^{-1}\left(\frac{S}{C}\right) + \pi & C>0 \\ \tan^{-1}\left(\frac{S}{C}\right) + 2\pi & S<0,\ C<0 \end{cases} \tag{9}$$

The quantity R is the length of the resultant vector, and the mean resultant length associated with the mean direction is expressed as follows.

$$\bar{R} = \frac{R}{m} \tag{10}$$

These equations can be used to compare the strike/dip angles of multiple events with the estimated fracture orientations.

2.3.1 Initial model and label

In RANSAC, a model satisfying the given constraints is ultimately selected from among randomly extracted models, whereas in GARNET, all randomly generated fracture models are utilized as initial model and associated points are assigned as initial labels. Generally, a higher number of initial random models produce better results. However, rather than increasing the number of models infinitely, predetermining which models involve similar fracture orientations can enhance the accuracy of the results and reduce computation time. Accordingly, the initial label sets were randomly generated within the point cloud by applying a loose distance threshold to the original RANSAC method. The angular difference between the normal vector of the generated plane and mean angle of the events belonging to the plane is calculated as follows.

$$\theta_t = \cos^{-1}\left(\frac{\mathbf{v}_m \cdot \mathbf{v}_f}{\|\mathbf{v}_m\|\|\mathbf{v}_f\|}\right) \tag{11}$$

where $\mathbf{v}_f$ is the normal vector of the plane, $\mathbf{v}_m$ is the normal vector of the points in the plane, and θ_t is the angle between the normal vectors.

The minimum angle between the normal vectors was calculated as follows.

$$\theta_m = \min\{\theta_t, \pi - \theta_t\} \tag{12}$$

Planes exceeding the threshold were eliminated before reconstructing an initial label set with enhanced reliability to determine fracture orientations.

2.3.2 Moment tensor clustering and model elimination

Using the original PEARL algorithm, the energy calculated using Eq. 3 following α-expansion was based on the distance between each label and the microseismic event locations assigned to each label; thus, the fracture orientations at event locations were neglected. Many event points were associated with a label based on distance, but exhibited significantly different strike or dip angles relative to the other points. To resolve this issue, a clustering method is applied to the point orientations assigned to each label.

Clustering is a widely used unsupervised learning method that produces data clusters by considering the characteristics of the data, yielding specific points or variables that are representative of the data. Thus, a cluster contains data with similar characteristics, whereas data with different characteristics are classified as different clusters or noise. In this study, the density-based spatial clustering of applications with noise (DBSCAN) method (Ester et al., 1996) was applied to orientation clustering. Unlike other clustering methods that rely on the K-means or similar distance algorithms, DBSCAN is advantageous because it does not require the user to designate the number of clusters. Because of these advantages, it is a clustering algorithm used in various fields such as radar data (Guo et al., 2020), fault diagnosis (Liu et al., 2020), and visual analysis (Chebi et al., 2016).

The DBSCAN algorithm expands the cluster by finding close data that meet the conditions in the initial data, where the input parameters are the number of neighbors needed to define the dense region (MinPts) and the distance representing the neighborhood (ε). Using these parameters, the data were classified into three types: if the number of points within a neighborhood with distance εexceeded the minimum, then such a point was designated as a core point. After a core point was located, data within its neighborhood were defined as connected points or other core points. If a data point was not connected to a neighbor, it was designated as a border point. Finally, the data in clusters that were neither core nor border points were designated as noise.

The DBSCAN method was applied to the strike and dip angles of points assigned to labels before the re-estimation step. While extracting the cluster with the most points, the consistency of the direction was improved by excluding other clusters or outliers that deviated from trends, such as noise. However, clustering cannot determine whether the orientation value at a location is consistent with that estimated using the model. Therefore, the method of selecting the initial model by comparing the orientation of the points belonging to labels and those of the plane models described above was applied to exclude models with large orientation errors. This process significantly improves the accuracy of the orientations of the fracture model.

Labels with a number of location points higher than the threshold number were retained, and those with lower points were excluded. Although such a constraint is not mandatory, it lowers the computation time during the iterative algorithm operation, thereby promoting faster energy convergence.

2.3.3 Model merging

After the re-estimation step, the usability of the algorithm was enhanced via appropriate post-treatment. If two plane models are separated from other labels owing to the inadequate spatial distribution of location points despite high connectivity, these planes cannot be merged using Eq. 3. Therefore, a process for connecting models with similar parameters is required. The algorithm was set to merge planes if the distance between the two plane models and the differences between the normal vector angles of each plane satisfied these conditions. Thus, fracture plane models with enhanced connectivity between the points were extracted.

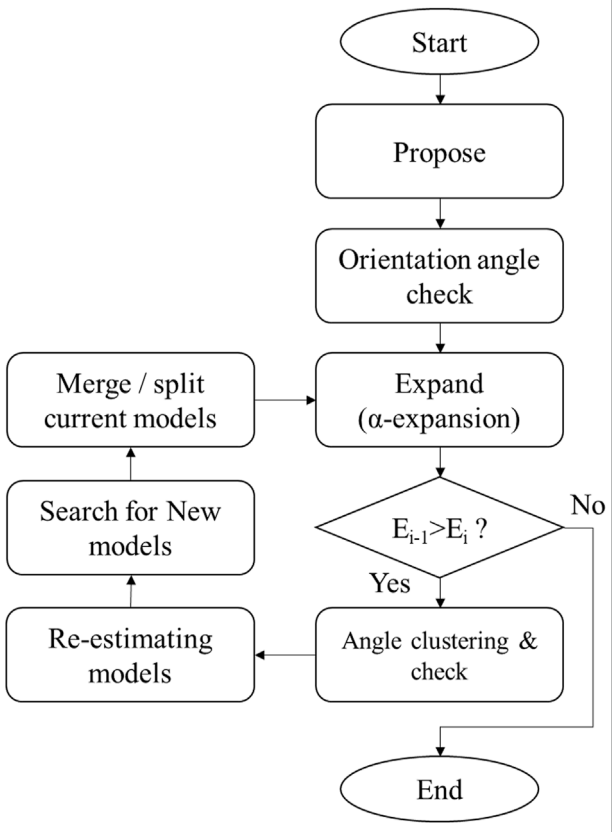

FIGURE 2
Schematic diagram of the GARNET algorithm.

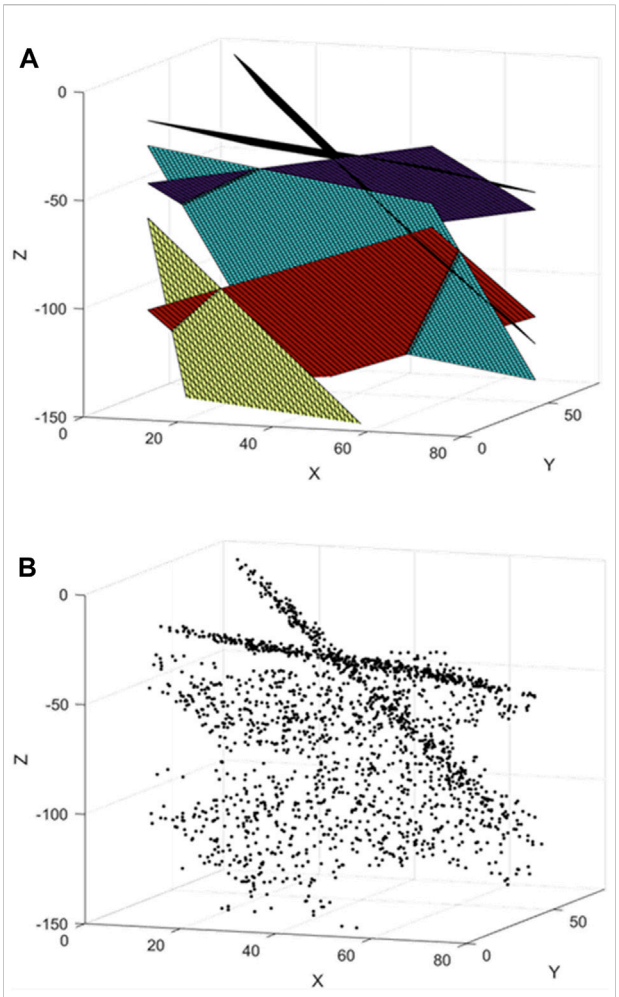

FIGURE 3
Synthetic experiments to verify the effect of orientation on fracture plane extraction. **(A)** True model consisting of six fracture planes and **(B)** 200 randomly distributed points from each fracture plane with low ratios of location errors.

2.3.4 Outlier labels

It is generally difficult to utilize all the data from seismic monitoring during fracture model generation. The acquired data can contain insignificant signals such as noise caused by mechanical problems and uncertainties during data processing. In addition, not all accurately recorded seismic activities are associated with fractures. These points were defined as outliers during the fracture imaging process and were assigned to a specific label, ϕ. Accordingly, the energy function $E(\mathcal{L})$ in equation (3) is redefined as follows

$$E(\mathcal{L}) = \sum_p \|p - L_p\| + \lambda \cdot \sum_{(p,q)\in\mathcal{N}} \omega_{pq} \cdot \delta(L_p \neq L_q) + \varphi \|p_\phi - L_\phi\| \quad (13)$$

where φ is an empirical constant reflecting the weight of the outlier energy, whereas for $\|p_\phi - L_\phi\|$, all outliers are associated with the constant, unlike the geometric terms. Thus, the outlier term is a uniform label.

The outlier label also included points assigned to label that were excluded because they failed to satisfy the criteria of the initial model selection process and those that were removed from the labels because they were outside the selected cluster during orientation clustering. However, these points may include significant data that can demonstrate fracture connectivity, but are excluded because they were not assigned to a suitable label during the algorithm operation. Therefore, new fracture models were searched for outlier label after the re-estimation step to allow reassignment of some outlying points to labels rather than outliers.

2.3.5 Flowchart of algorithm

A flowchart of the developed algorithm, GARNET, is shown in Figure 2. The main steps are summarized as follows.

1) Initial label sets (L_0) are generated from the given data by random sampling, using the maximum number of predefined models possible. The initial model generation should incorporate the maximum number of possible

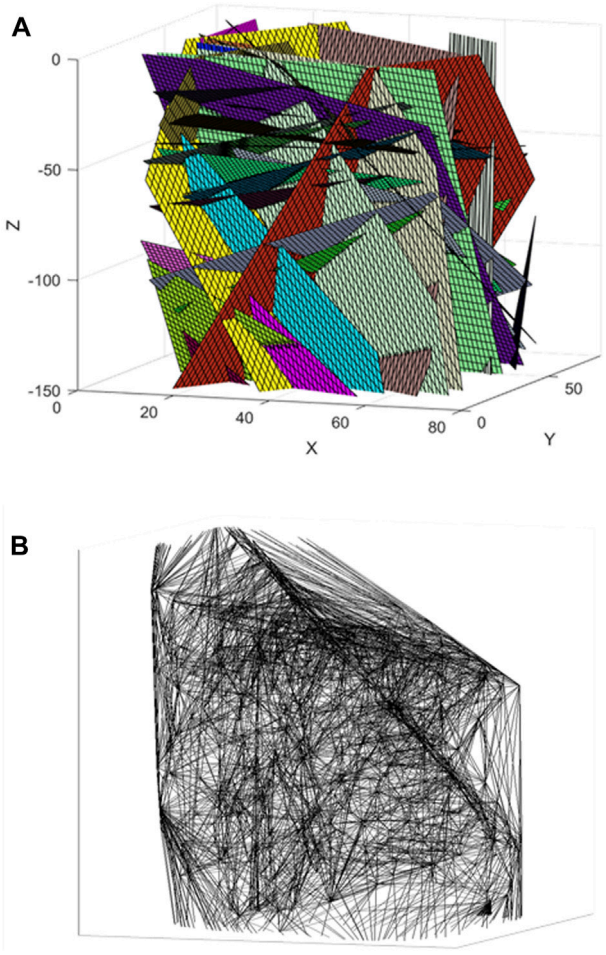

FIGURE 4
(A) Initial model created using the Random Sample Consensus (RANSAC) method with 100 randomly generated planes. **(B)** Results of Delaunay triangulation application to the synthetic data shown in Figure 3B.

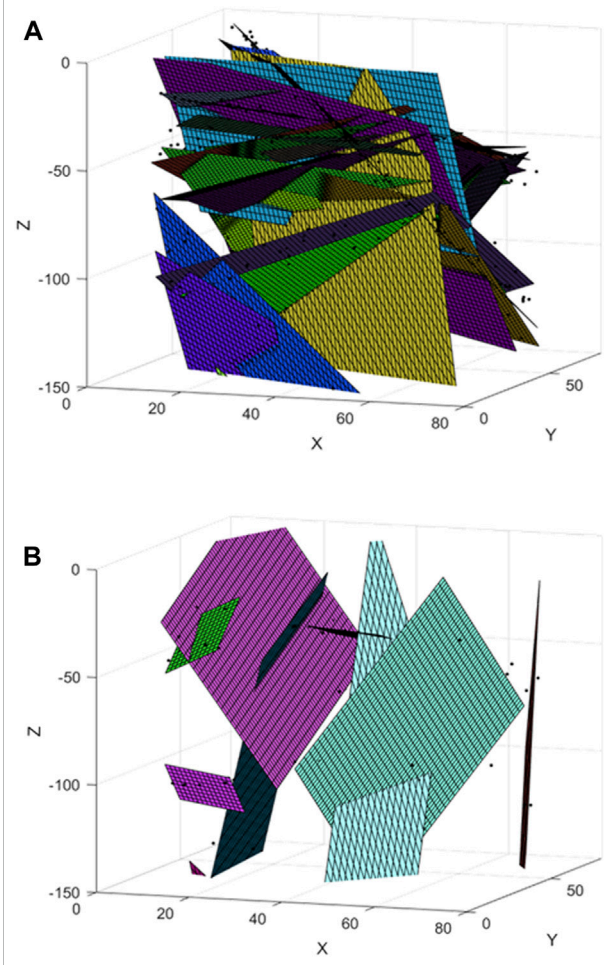

FIGURE 5
(A) Result of the re-estimated model in the first iteration without using orientation data. **(B)** New plane models for the outlier label after the re-estimation step.

points. In this study, the RANSAC algorithm was used to rapidly generate the initial models and assign points to initial labels.

2) The orientations of the generated fracture model from label and those of the points assigned to the label are compared to eliminate insignificant data showing large angle-value differences. In this study, the angle was calculated using the difference between the normal vectors.

3) For energy minimization, α-expansion is performed using Eq. 3. In this step, the spatially consistent label that includes the highest number of inliers is obtained through expansion between labels.

4) If energy minimization is not achieved in step 3), the final labels are output and calculate the errors between their normal vector angles of plane and point. Conversely, the iterative algorithm operation was continued.

5) When the energy decreases, DBSCAN is used to cluster the orientations of the points assigned to each label for classification. The cluster with the maximum number of points is extracted and then compared the orientations from the fracture model and the location points used in step 2) to eliminate data with large angle differences from the label.

6) The remaining labels are re-estimated and the existing label set is replaced with a new set satisfying Eq. 5.

7) New points associated with the fracture models are extracted from the points assigned to the outlier label.

8) If planes with similar model parameters are present, the difference between their normal vector angles and distances are calculated, and the fracture planes satisfying the conditions are merged. Then we return to Step 3) to restart from the α-expansion for energy minimization.

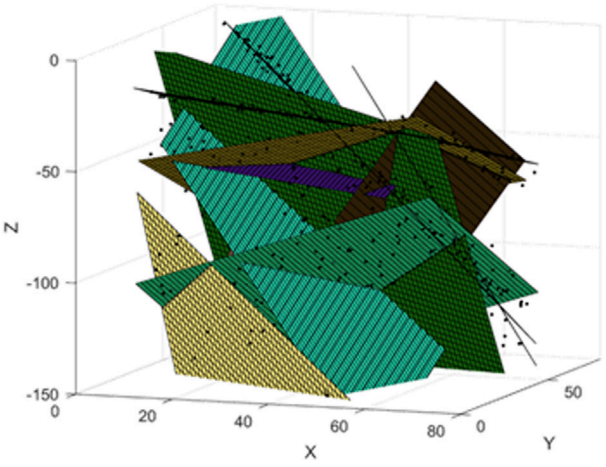

FIGURE 6
Result of fracture modeling without orientation data. The extracted planes were overestimated compared to the true model shown in Figure 3A.

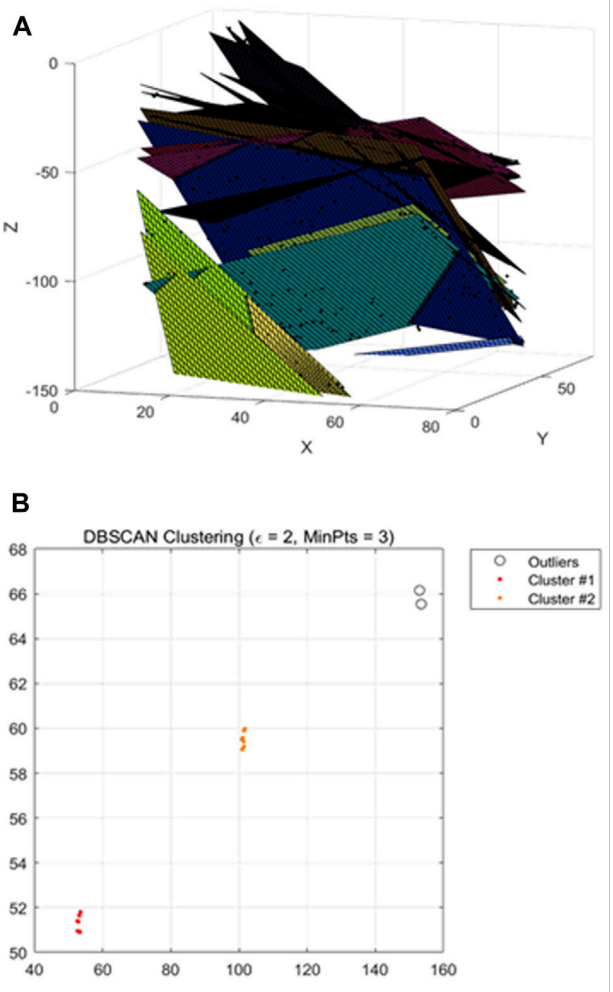

FIGURE 7
(A) Initial model removing planes with large angular differences between planes and locations. **(B)** Results of orientation clustering after energy reduction.

3 Numerical experiments

A synthetic seismic dataset was applied to the fracture network imaging using the GARNET algorithm.

3.1 Orientation angle usability

The principal difference between the GARNET algorithm and the original PEARL algorithm is the incorporation of orientation data for accurate model imaging. Therefore, the effect of orientation on fracture imaging was examined using an identical point cloud. The synthetic data model was constructed to include six fracture planes in 80 m × 80 m × 150 m cubes and approximately 200 randomly distributed locations per plane, as shown in Figure 3. To reproduce the measurements and errors during data processing, a standard deviation (SD) of 2 was applied to the actual points to randomly alter their locations.

First, the fractures were estimated using only points without orientations as the synthetic data. The initial model created using these points, with approximately 100 randomly generated planes, is shown in Figure 4A. Instead of using three points to generate numerous initial models, the RANSAC algorithm was used to promote the rapid assignment of points to labels. The value of threshold distance was 2 and each plane was generated using at least four points.

To calculate the energy, the smoothing term in Eq. 1 requires clear information about the neighborhood from which the data are collected. In this study, the Delaunay triangulation method was used to reproduce the neighborhood system of the data, and the results are shown in Figure 4B. The first iteration of the re-estimated model is shown in Figure 5A. Compared with the initial model, the number of insignificant planes decreased significantly after the expansion and re-estimation steps, indicating that the points switched labels. Images of the fracture model created after the re-estimation step incorporating outlier labels are shown in Figure 5B. New models were also investigated using points that were excluded from the existing label during the algorithm operation, thereby producing several models that were added to the existing labels.

The result of fracture modeling without orientation data are shown in Figure 6. Although convergence was achieved after only four iterations, 10 planes were estimated, demonstrating an overestimation compared to the actual fracture planes shown in Figure 3A. The estimated fracture orientations of many planes

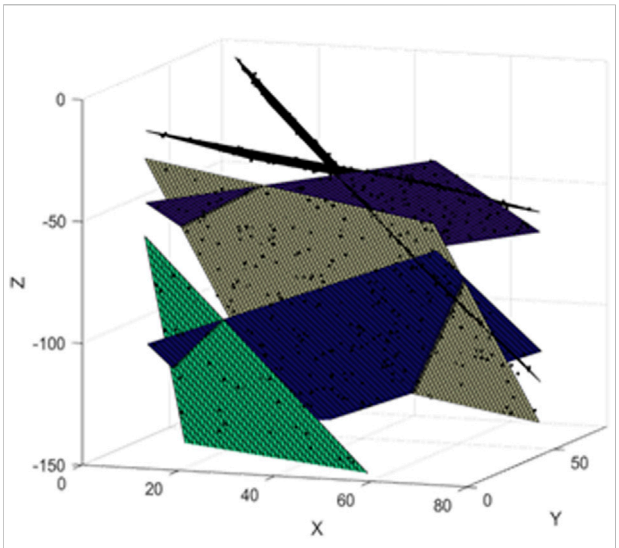

FIGURE 8
Result of fracture modeling using orientation data. The number and orientation of the planes were almost identical to those of the true model shown in Figure 3A.

differ from the actual orientations. The errors associated with the strike and dip angle of plane estimates were 20.23% and 24.63%, respectively. If the actual fracture pattern is partially known, then it is safe to assume that statistical estimation is possible after multiple iterations, as long as the input parameters are adequately controlled. However, the accuracy of the orientations of the modeled fractures cannot be guaranteed.

Next, the fractures were modeled by integrating the orientation data with the location points as input data in the GARNET algorithm and applying these data to the synthetic model shown in Figure 3. After the initial model selection and energy calculation, the orientation clustering step was added to the estimation method, using only the location points. The results of eliminating models using orientation data with differences ≥30° between the plane orientation and the mean angle of the location points after the initial model was generated are shown in Figure 7A, confirming that the randomly generated initial model exhibited sorting consistent with the actual fracture pattern based solely on the selection process.

During subsequent energy calculations, orientation clustering was performed for each label if the energy decreased; the result confirmed the presence of clusters with different orientations within the same label (Figure 7B). This indicates that the application of energy optimization for distance can produce inaccurate fracture models. Therefore, the cluster with the most points was extracted and retained after clustering, whereas all other points were excluded from the label.

The result of fracture modeling using orientation data are presented in Figure 8. Convergence was achieved after only three iterations, and the number and orientation of the modeled

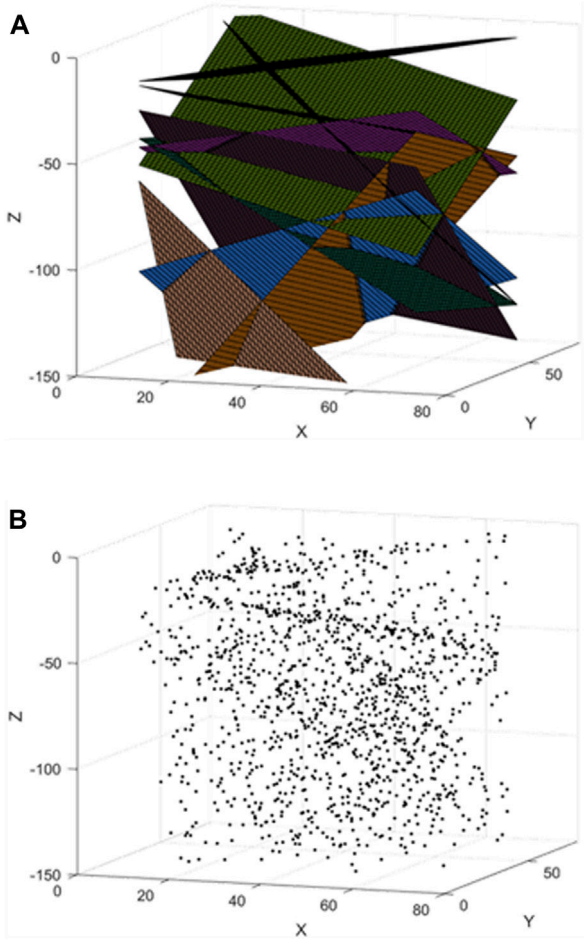

FIGURE 9
Synthetic experiments to verify the suitability of the GARNET algorithm for location data including outliers. **(A)** True model consisting of 10 fracture planes, **(B)** 100 randomly distributed points from each fracture plane with high ratios of location errors and 500 outlier points independent of the microseismic event.

fracture planes were consistent with those of the actual fracture model (Figure 3A). The errors of the plane shown in the result were 1.32% and 0.83% for the strike and dip, respectively. When the orientation data were missing, the number of iterations was lower and the computation time was reduced. These results confirm that fractures were modeled more rapidly and reliably using the GARNET algorithm involving the orientation data.

3.2 Application to synthetic data including noise and outliers

The applicability of the GARNET algorithm was verified using a fracture model. In this subsection, we examine the

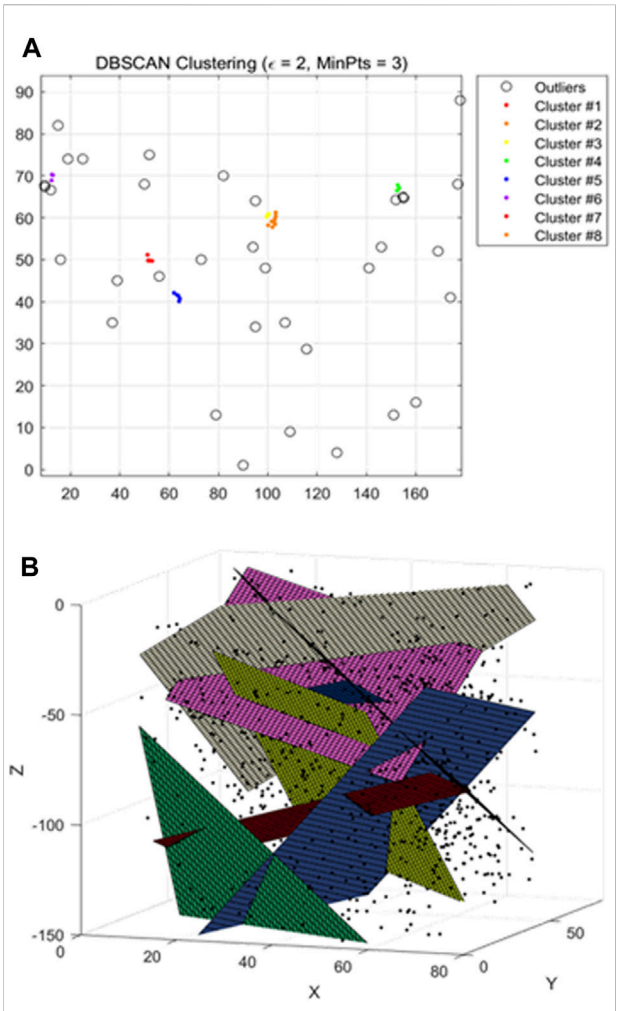

FIGURE 10
(A) Result of orientation clustering using the density-based spatial clustering of applications with noise (DBSCAN) method in the first iteration. Events associated with labels were classified as orientation clusters and outliers. **(B)** Result of the re-estimated model in the first iteration. Extracted planes were similar to those of the true model from among data with many outliers.

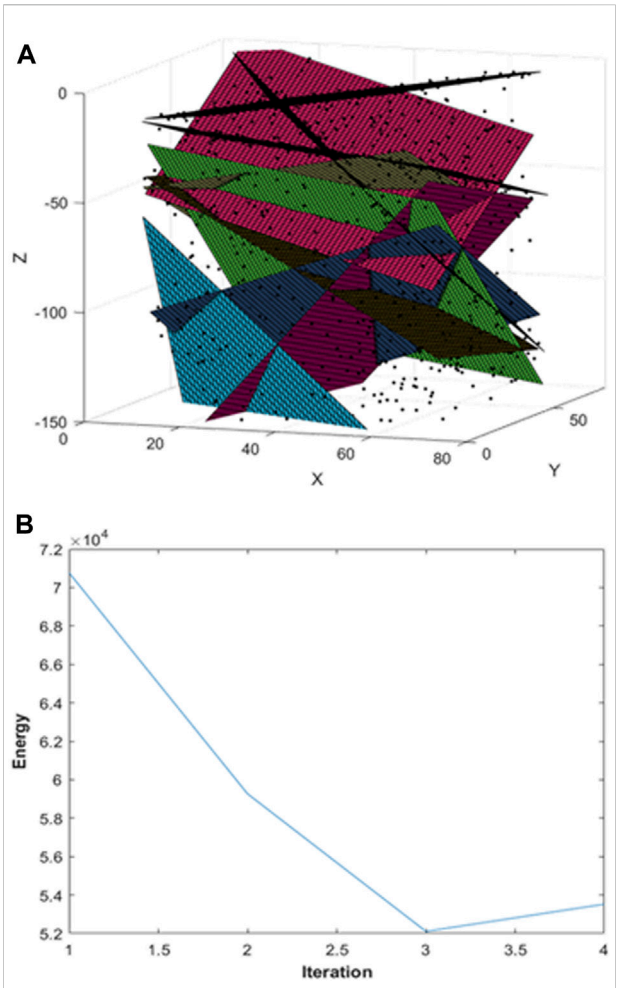

FIGURE 11
(A) Result of fracture modeling using the GARNET algorithm for data containing high noise levels and many outliers. **(B)** Energy values obtained after each iteration were minimized in the third iteration.

suitability of the algorithm for modeling fractures when the locations cannot be accurately expressed owing to the presence of many errors and outliers unrelated to fractures in the acquired data. The synthetic data model comprises 10 fracture planes (Figure 9A), with each plane containing approximately 100 randomly distributed points. To reproduce data with many errors, SD values of 6 and ≥12 were applied to the location and orientation data, respectively, to randomly alter both parameters. In addition, 500 outlier points that were unrelated to the microseismic event were randomly generated (Figure 9B).

The results of the DBSCAN analysis performed on the orientation of the points assigned to the labels during the first iteration (Figure 10A) indicate that for fractures associated with a complex formation process, the probability of points assigned to the labels belonging to multiple clusters with diverse orientations and many outliers is high. The results of the model re-estimation performed after orientation clustering for the same number of iterations are shown in Figure 10B. Although not all fracture planes were identified, a pattern similar to that of the actual planes emerged, despite many outliers. The results of the fracture modeling using data, including noise and outliers, are presented in Figure 11A. The number and orientation of the modeled fracture planes were not significantly different from those of the actual fracture model (Figure 9A). The errors of the strike and dip angle estimates were 1.89% and 1.64%, respectively.

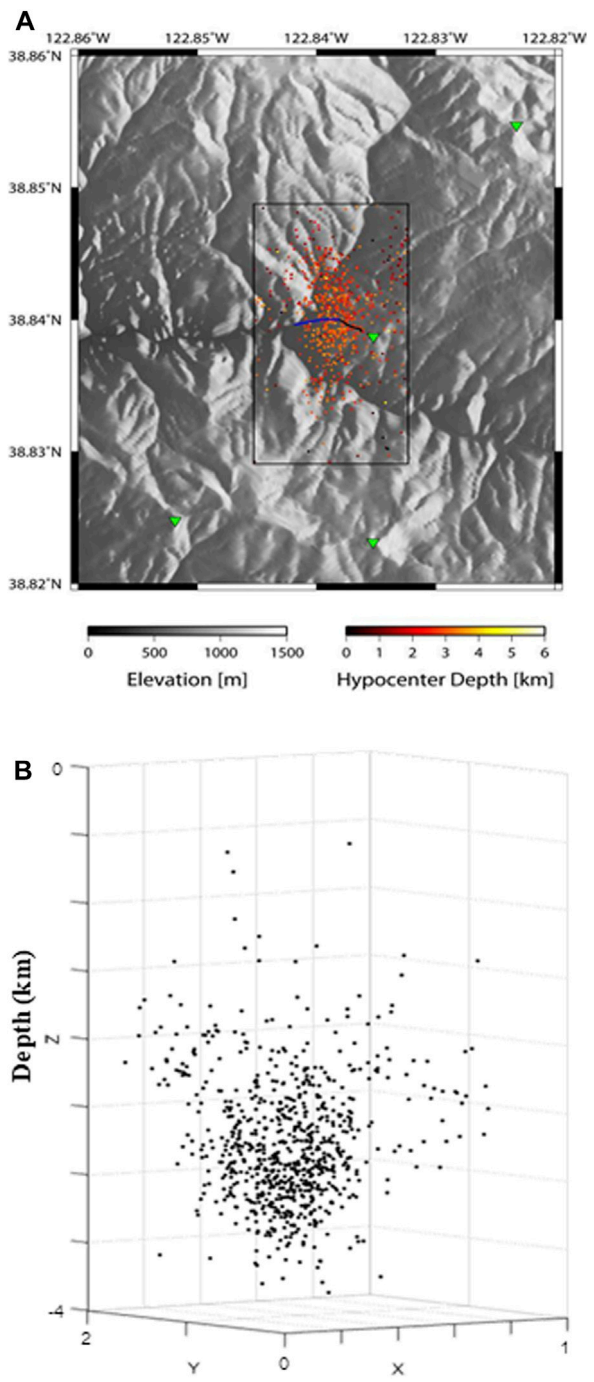

FIGURE 12
(A) Microseismic events detected by The Geysers broadband and geophone network in the vicinity near the injection site, adapted from Gritto et al. (2018). **(B)** Microseismic data were monitored by 34 permanent and 33 temporary geophones; 752 microseismic events were evaluated.

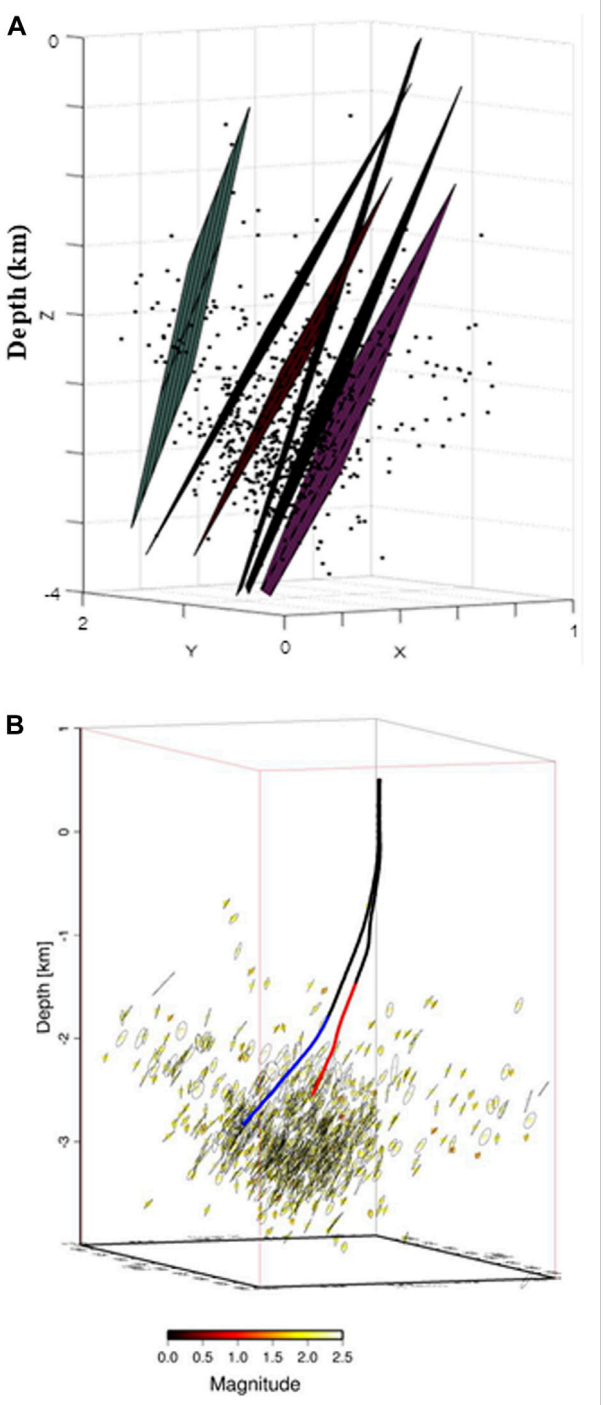

FIGURE 13
(A) Fracture network imaging results obtained using the GARNET algorithm with microseismic location and orientation data. **(B)** Statistical representation of the generated fracture network below production well (red) and injection well (blue), adapted from Gritto et al. (2018).

The energy decreased rapidly during the iteration, and the optimal fracture model planes were estimated through energy minimization within three iterations (Figure 11B). These synthesis model results confirmed that the fracture models were robustly estimated using the proposed GARNET algorithm, despite the inclusion of many location measurement errors or outliers in the data.

4 Application to field microseismic data

To investigate the applicability of the developed algorithm to field microseismic data, it was utilized data acquired during the Geysers Enhanced Geothermal System (EGS) resource development project in California, USA as shown in Figure 12A. This project was conducted to enhance the technology for assessing the temporal changes and volumetric distribution of fluids introduced during resource development, as well as field stress magnitudes, fracture sizes, and orientations. Using a network comprising 34 permanent geophones, high-frequency seismic data were acquired as broadband data using a temporary network containing 33 geophones. The analysis of the acquired data revealed 752 microseismic events (Gritto et al., 2018), as shown in Figure 12B.

During the fracture network modeling, orientation clustering was performed for each label by applying the GARNET algorithm to the field data. The ε and MinPts values were 2 and 3, respectively, and the result of fracture network produced is shown in Figure 13A. The angle of the normal vector for convergence was set to 15°, and the fracture planes were obtained via energy convergence after only three iterations. The estimated number of fracture planes was 6, and the errors associated with the strike and dip angle estimates were 2.89% and 2.83%, respectively. All fracture planes produced strike values of N10°E-N30°E and a dip of 75°–85°, with no overlapping orientation. The statistical representation result of the fracture network using the same microseismic event data are presented in Figure 13B (Gritto et al., 2018). The rupture area is shown by the size of the circle; the colored points at the hypocenters represent the moment magnitude of the event. The estimated orientation of the rupture area is almost similar to the orientation estimated by GARNET with a strike of N10°E±10° and a dip of 80°±10°.

These results demonstrate that the fractures progressed along a particular orientation owing to hydraulic fracturing in the boreholes. Because data with inconsistent orientations or insufficient points are eliminated by orientation clustering, network modeling is simpler. These results confirm the suitability of the algorithm for orientation and location data in the rapid and accurate modeling of field data involving major fracture plane networks.

5 Conclusion

The GARNET algorithm was developed as an improved version of the PEARL algorithm, and then used for fracture network imaging. The GARNET algorithm exploits the location data acquired during microseismic events or earthquakes, and orientation data obtained from the moment tensors of associated events. The function of this algorithm improves the location accuracy of the estimated fracture plane by generating and reproducing labels based on the energy differences between locations. In addition, clustering using DBSCAN was applied to the orientation angle to improve the reliability of the extracted fracture direction.

Synthetic data suitable for simulating microseismic events were used to assess the performance of the algorithm. A synthetic fracture model relying solely on location data exhibited poor accuracy in estimating the number and orientation of the fracture planes. Conversely, the number and orientation of the fracture planes obtained using the proposed algorithm incorporating orientation data matched those in the actual data. In the second synthetic model, fractures were modeled by applying the algorithm to data with high noise levels and many outliers. The results demonstrated robust fracture plane estimation with a negligible impact of errors and outliers, despite few iterations. The proposed algorithm was also applied to field data acquired during an EGS resource development project to assess its utility. The resulting fracture network modeling process produced strike orientations of N10°E–N30°E and a dip angle of 75°–85°, with six representative fracture planes. The errors associated with the strike and dip angle estimates were 2.89% and 2.83%, respectively. These results are similar to statistical representation results, and we validated the suitability of the algorithm for accurately simulating fracture locations and orientations in real fracture networks.

Data availability statement

The datasets presented in this study can be found in online repositories. The names of the repository/repositories and accession number(s) can be found below: The field data were obtained through work supported by the Department of Energy's Office of Energy Efficiency and Renewable Energy (EERE) in association with the Geothermal Technologies Office (GTO) and can be found in the Geothermal Data Repository (https://gdr.openei.org/).

Author contributions

JY wrote the article and developed the code. YJ conceptualized the modeling methods and analyzed the

applied techniques. BK provided field data information and data processing expertise.

Funding

This work was supported by a basic research project of the Korea Institute of Geoscience and Mineral Resources (GP 2020–023) funded by the Ministry of Science and ICT of Korea.

Acknowledgments

The authors would like to thank the reviewers for their valuable and careful comments.

Conflict of interest

The authors declare that the research was conducted in the absence of any commercial or financial relationships that could be construed as a potential conflict of interest.

Publisher's note

References

Aki, K., and Richards, P. G. (2009). *Quantitative seismology*. Sausalito: University Science Books, Cop.

Boykov, Y., Veksler, O., and Zabih, R. (2001). Fast approximate energy minimization via graph cuts. *IEEE Trans. Pattern Anal. Mach. Intell.* 23 (11), 1222–1239. doi:10.1109/34.969114

Busetti, S., Jiao, W., and Reches, Z. (2014). Geomechanics of hydrolic fracturing microseismicity: Part 2. Stress state determination. *Am. Assoc. Pet. Geol. Bull.* 98, 2459–2476. doi:10.1306/05141413124

Chebi, H., Acheli, D., and Kesraoui, M. (2016). Dynamic detection of abnormalities in video analysis of crowd behavior with DBSCAN and neural networks. *Adv. Sci. Technol. Eng. Syst. J.* 1, 56–63. doi:10.25046/aj010510

Delong, A., Osokin, A., Isack, H., and Boykov, Y. (2012). Fast approximate energy minimization with label costs. *Int. J. Comput. Vis.* 96 (1), 1–27. doi:10.1007/s11263-011-0437-z

Dershowitz, W. S., and Fidelibus, C. (1999). Derivation of equivalent pipe network analogues for three-dimensional discrete fracture networks by the boundary element method. *Water Resour. Res.* 35 (9), 2685–2691. doi:10.1029/1999wr900118

Duda, R. O., and Hart, P. E. (1972). Use of the Hough transformation to detect lines and curves in pictures. *Commun. ACM* 15 (1), 11–15. doi:10.1145/361237.361242

Economides, M. J., and Nolte, K. G. (2000). *Reservoir stimulation*. Chichester: Wiley.

Ester, M., Kriegel, H.-P., Sander, J., and Xu, X. (1996). A density-based algorithm for discovering clusters in large spatial databases with noise. *Kdd* 96, 226–231.

Fadakar Alghalandis, Y., Dowd, P. A., and Xu, C. (2013). The RANSAC method for generating fracture networks from micro-seismic event data. *Math. Geosci.* 45 (2), 207–224. doi:10.1007/s11004-012-9439-9

Fischler, M. A., and Bolles, R. C. (1981). Random sample consensus: A paradigm for model fitting with applications to image analysis and automated cartography. *Commun. ACM* 24 (6), 381–395. doi:10.1145/358669.358692

Fisher, N. I. (2005). *Statistical analysis of circular data*. Cambridge: Cambridge University.

Gritto, R., Boyd, O. S., and Dreger, D. S. (2018). *Seismic analysis of spatio-temporal fracture generation during EGS resource development-deviatoric MT, fracture network, and final report*. United States: USDOE Geothermal Data Repository. doi:10.15121/1494306

Gudmundsson, A. (2011). *Rock fractures in geological processes*. Cambridge: Cambridge University Press.

Guo, Z., Liu, H., Pang, L., Fang, L., and Dou, W. (2020). DBSCAN-based point cloud extraction for Tomographic synthetic aperture radar (TomoSAR) three-dimensional (3D) building reconstruction. *Int. J. Remote Sens.* 42 (6), 2327–2349. doi:10.1080/01431161.2020.1851062

Hyman, J. D., Karra, S., Makedonska, N., Gable, C. W., Painter, S. L., and Viswanathan, H. S. (2015). dfnWorks: A discrete fracture network framework for modeling subsurface flow and transport. *Comput. Geosci.* 84, 10–19. doi:10.1016/j.cageo.2015.08.001

Isack, H., and Boykov, Y. (2011). Energy-based geometric multi-model fitting. *Int. J. Comput. Vis.* 97 (2), 123–147. doi:10.1007/s11263-011-0474-7

Kwicklis, E. M., and Healy, R. W. (1993). Numerical investigation of steady liquid water flow in a variably saturated fracture network. *Water Resour. Res.* 29 (12), 4091–4102. doi:10.1029/93wr02348

Li, L., and Lee, S. H. (2008). Efficient field-scale simulation of black oil in a naturally fractured reservoir through discrete fracture networks and homogenized media. *SPE Reserv. Eval. Eng.* 11, 750–758. doi:10.2118/103901-pa

Liu, Y., Song, B., Wang, L., Gao, J., and Xu, R. (2020). Power transformer fault diagnosis based on dissolved gas analysis by correlation coefficient-DBSCAN. *Appl. Sci. (Basel).* 10 (13), 4440. doi:10.3390/app10134440

Mardia, K. V., and Jupp, P. E. (2009). *Directional statistics*. Chichester: John Wiley & Sons.

Mayer, J. R., and Sharp, J. M. (1998). Fracture control of regional ground-water flow in a carbonate aquifer in a semi-arid region. *Geol. Soc. Am. Bull.* 110 (2), 269–283. doi:10.1130/0016-7606(1998)110<0269:fcorgw>2.3.co;2

Mitcham, T. W. (1963). Fractures, joints, faults, and fissures. *Econ. Geol.* 58 (7), 1157–1158. doi:10.2113/gsecongeo.58.7.1157

Montgomery, C. T., and Smith, M. B. (2010). Hydraulic fracturing: History of an enduring technology. *J. Petroleum Technol.* 62 (12), 26–40. doi:10.2118/1210-0026-JPT

Raven, K. G., and Gale, J. E. (1985). Water flow in a natural rock fracture as a function of stress and sample size. *Int. J. Rock Mech. Min. Sci. Geomechanics Abstr.* 22 (4), 251–261. doi:10.1016/0148-9062(85)92952-3

Valko, P., and Economides, M. J. (2001). *Hydraulic fracture mechanics*. Chichester: John Wiley & Sons.

Warpinski, N. R., Mayerhofer, M., Agarwal, K., and Du, J. (2013). Hydraulic-fracture geomechanics and microseismic-source mechanisms. *SPE J.* 18, 766–780. doi:10.2118/158935-pa

Yu, J., Byun, J., and Seol, S. J. (2020). Imaging discrete fracture networks using the location and moment tensors of microseismic events. *Explor. Geophys.* 52 (1), 42–53. doi:10.1080/08123985.2020.1761760

Yu, X., Rutledge, J., Leaney, S., and Maxwell, S. (2016). Discrete-fracture-network generation from microseismic data by use of moment-tensor- and event-location-constrained Hough transforms. *SPE J.* 21 (1), 221–232. doi:10.2118/168582-pa

Zhang, H., Nadeau, R. M., and Toksoz, M. N. (2010). Locating nonvolcanic tremors beneath the San Andreas Fault using a station-pair double-difference location method. *Geophys. Res. Lett.* 37 (13), L13304. doi:10.1029/2010gl043577

frontiers | Frontiers in Earth Science

TYPE Original Research
PUBLISHED 12 September 2022
DOI 10.3389/feart.2022.952314

OPEN ACCESS

EDITED BY
Wenzhuo Cao,
Imperial College London,
United Kingdom

REVIEWED BY
Bing Bai,
Beijing Jiaotong University, China
Fuqiong Huang,
China Earthquake Networks Center, China
Xueyi Shang,
Chongqing University, China
Xiangxin Liu,
North China University of Science and Technology, China

*CORRESPONDENCE
Haijiang Zhang,
zhang11@ustc.edu.cn

†These authors have contributed equally to this work

SPECIALTY SECTION
This article was submitted to Structural Geology and Tectonics, a section of the journal Frontiers in Earth Science

RECEIVED 24 May 2022
ACCEPTED 25 August 2022
PUBLISHED 12 September 2022

CITATION
Qian J, Wang K, Zhang H, Tan Y, Xu C, Wang Q, Xiong Q and Malinowski M (2022), First observation of paired microseismic signals during solution salt mining.
Front. Earth Sci. 10:952314.
doi: 10.3389/feart.2022.952314

First observation of paired microseismic signals during solution salt mining

Jiawei Qian[1,2†], Kangdong Wang[2,3†], Haijiang Zhang[2*], Yuyang Tan[4], Chuanjian Xu[3], Qingsong Wang[3], Qiangqing Xiong[3] and Michal Malinowski[5]

[1]College of Oceanography, Hohai University, Nanjing, China, [2]Laboratory of Seismology and Physics of Earth's Interior, School of Earth and Space Sciences, University of Science and Technology of China, Hefei, China, [3]Geological Exploration Technology Institute of Anhui Province, Hefei, China, [4]Frontiers Science Center for Deep Ocean Multispheres and Earth System, Key Lab of Submarine Geosciences and Prospecting Techniques MOE, College of Marine Geosciences, Ocean University of China, Qingdao, China, [5]Institute of Geophysics, Warsaw, Poland

To monitor the status of cavern roof instability induced by solution salt mining, we deployed a surface microseismic monitoring system for Dongxing salt mine, Dingyuan county, China. The microseismic monitoring system consists of 11 three-component geophones installed in shallow holes of 5 m deep. From 7-month continuous monitoring data, we have detected a novel type of signal that consists of two events. The first event has a long duration (>15 s) and generally has higher frequencies at the beginning. The 2nd event has a shorter duration of ~3 s with lower frequencies. The two events are separated by ~30–90 s in time. From May 2017 to November 2017, there are a total of 88 distinct paired signals with two events in sequence. We propose the first event corresponds to a series of fracturing processes on the cavern roof, and microseismic signals associated with different fractures are mixed and overlapped to produce a mixed signal with a longer duration. Due to a series of fracturing processes, some zones of cavern roof become instable and some rock debris may fall from the roof and collide on the cavern floor. This collision can produce a short duration signal, which corresponds to the 2nd event of the paired signal. The further analysis of polarities of the first arrivals for the 2nd event further proves its collision origin. The time interval between two events is related to the time for the falling rock debris through the brine, which is controlled by the cavern height and various physical properties of the rock debris and brine. Through the detailed analysis of paired signals, we can have a better understanding of the cavity development status for solution salt mining.

KEYWORDS

induced seismicity, paired signals, solution salt mining, cavern roof stability, fracturing

Introduction

Salt is not only an indispensable necessity for human life, but also one of the main raw materials for the basic chemical industry. As a special mining method, solution mining has been widely used in salt mines to effectively extract subsurface salt reservoirs, where fresh water is injected into the salt layer through wells (Berest et al., 2008; Schléder et al., 2008; Liu et al., 2019; Xing et al., 2021). However, when solution mining continues, it can create cavities beneath injection wells and between injection and extraction wells. As a result, geological disasters such as surface subsidence and sinkholes may be induced by solution mining, which could result in large damages for human life and property (Ege, 1984; Waltham et al., 2005; Ellsworth et al., 2012; Gutiérrez et al., 2014; Kinscher et al., 2014).

The commonly used methods for monitoring the potential collapse of solution salt mines include seismic method, settlement monitoring, hydrophone monitoring, and cavity scanning (Liu et al., 2020). Seismic method includes two-dimensional and three-dimensional seismic imaging using active sources, ambient noise tomography, and microseismic monitoring. Two-dimensional or three-dimensional seismic exploration method has been widely used in salt mining, which can be used to image the dissolution cavities (Xiong et al., 2019), but it is generally expensive to conduct the survey and cannot dynamically monitor the development of dissolution cavities. Surface subsidence monitoring cannot be used to image cavities and may not provide sufficient information about the cavity development. Although the InSAR (Synthetic Aperture Radar Interferometry) technology has a good spatial coverage (Valentino, 2016), due to the lack of good scatterers in the salt mine field it may not be sensitive to the actual surface subsidence.

Compared with other seismic methods, microseismic monitoring provides an effective way to monitor the solution mining process dynamically. It was first applied in the early sixties (Cook, 1963) and has grown to be a routine tool in daily mining hazard assessment (Ge, 2005). As solution mining continues, the cavity roof may become instable and can produce some fractures. As a result, the fracturing process will produce some microseismic signals that can be detected by the microseismic monitoring system (Guarascio, 1987; Trifu and Shumila, 2010; Nayak and Dreger, 2014; Kinscher et al., 2016). For example, a local seismic network installed over an underground salt cavern in the Lorraine basin recorded microseismic events possibly related to fluid-filled cracking process and rock-debris falling into the cavern from delamination of clay marls in the immediate roof (Mercerat et al., 2010).

Earthquake waveforms are highly complex due to multiple effects including source mechanism, stress drop, scattering, site-effects, phase conversions and interference from a multitude of noise sources (Das and Zoback, 2011; Eaton et al., 2013; Zhu and Beroza, 2019). In general, the signals generated by the brittle failure of rock are easily identified. Hydroacoustic monitoring of the controlled collapse of the Cerville-Buissoncourt salt cavity has identified two types of events, termed "X" events and "seismic" events, which could serve as precursory events of the collapse (Lebert et al., 2011). The "X" events may be related to the damaging and breaking process in the roof that involves microcracks appearing and then coalescing. In comparison, the "seismic" events that occur after the period of "X" events are likely related to the postrupture rock movements related to the intense deformation of the cavity roof (Lebert et al., 2011). Some microseismicity observed in the vicinity of an underground salt cavern was triggered by a remote M ~ 7.2 earthquake that is ~12,000 km away (Jousset and Rohmer, 2012). They documented three types of earthquakes (brittle-like micro-earthquakes, Long Period events and Very Long Period earthquakes), similar to those recorded in volcanic or hydrothermal systems (Jousset and Rohmer, 2012). In addition to microseismic events, roof failure could also produce ground shaking events (Dahm et al., 2011).

In this study, we report the characteristic paired signals that are first observed from solution salt mining from the 7-month continuous surface microseismic monitoring of the Dingyuan salt mine in China. For the first time we have observed paired signals that are induced by cavern roof instability. No previous research has found this pairing phenomenon in solution salt mining, and no research has explained the second event of paired signal associated with the collision between the fallen debris and the cavern floor. This paired signal may be related to the detachment process of roof debris and its impact on the cavity floor. We give a detailed analysis of the mechanism for forming the observed paired signals and show their potential applications on assessing the stability of the cavity roof.

Surface microseismic monitoring system

The Dingyuan salt mine with dozens of wells lies in Dongxing Town, Dingyuan County of China (Figure 1A). Millions of tons of salt have been exploited by solution mining since 1988, which produced many caverns full of brine in the underground (Xiong et al., 2019). There have been three surface collapses in the area which seriously affected the normal production and exacerbated the public panic on salt mining (Zhang et al., 2018, 2019).

Eleven three-component geophones (VHL5) of Weihai Sunfull Geophysical Exploration Equipment Co., Ltd. were installed in shallow holes of 5 m deep covering the area of 1,400 m by 1,000 m (Figure 1B) to monitor solution mining. The geophones have the response frequency of 5 Hz and have

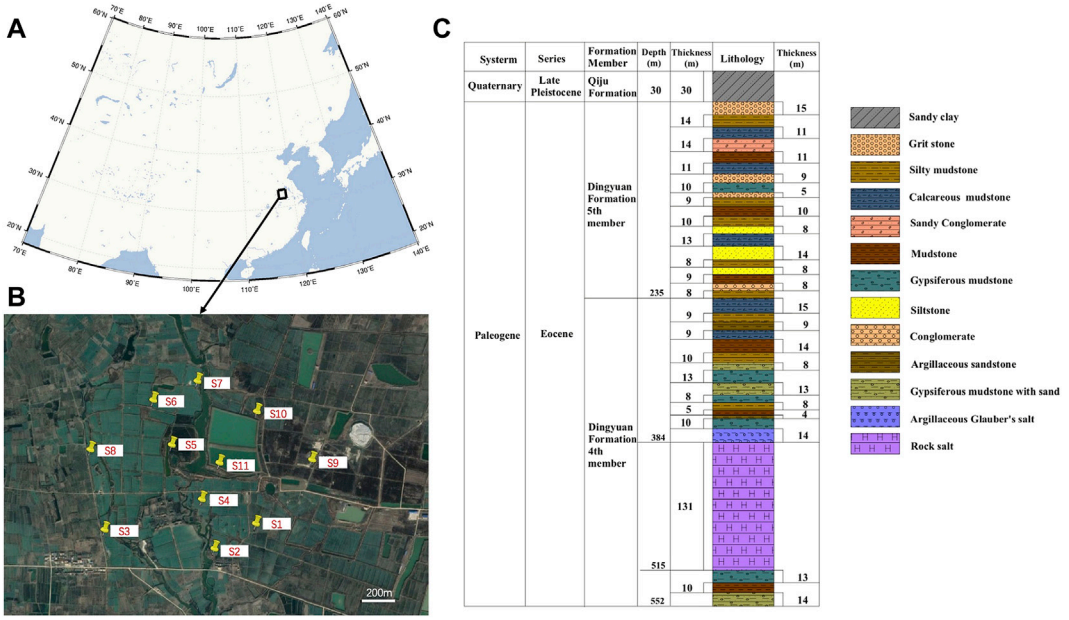

FIGURE 1
(A) The geographic location of the Dongxing salt mine in eastern China. **(B)** The distribution of surface geophones of the microseismic monitoring system. **(C)** Stratigraphic column of the Dongxing salt mine (modified after Zhang et al., 2018).

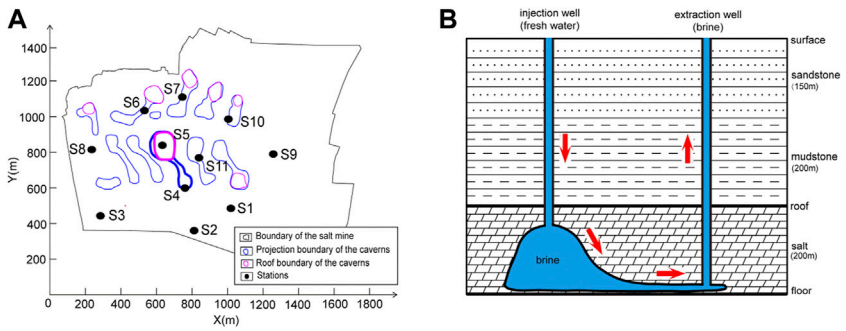

FIGURE 2
(A) Map showing the distribution of 11 seismic stations (black dots) and solution caverns (enclosed areas). The red and blue lines represent the roof and floor boundaries of the caverns, respectively, which are derived from the 3D active seismic imaging. The cavity with thickened lines is the cavern C1. **(B)** Layout diagram illustrating the dual-well solution mining. The cavern is full of the brine.

the sensitivity of 200 v/m/s. Its temperature sensitivity ranges from minus 40°C to 100°C, and its coil resistance is 3,600 Ω. The sampling frequency is set to be 500 Hz. We use the 7-month continuous monitoring data from May 2017 to November 2017. The roof boundary of cavern C1 (Figure 2A) has been imaged from the 3D seismic exploration (Xiong et al., 2019). It is full of brine and beneath seismic stations S5 and S4. The thickness of the sediment deposit ranges from 8 to 36 m in this area. The underlying bedrocks are sandstone, mudstone, gypsum mudstone and salt, respectively (Figure 1C). The salt formations in the basin are buried continuously at depths of ~300–600 m. Solution mining is the process of extracting soluble minerals. Fresh water is injected from the injection well and the brine is extracted from the extraction well which is called the dual-well convection. As a result, the caverns continuously grow as the salt is dissolved (Figure 2B). When the soluble minerals are mined, salt cavities will be formed and become larger, which may induce surface collapse hazards.

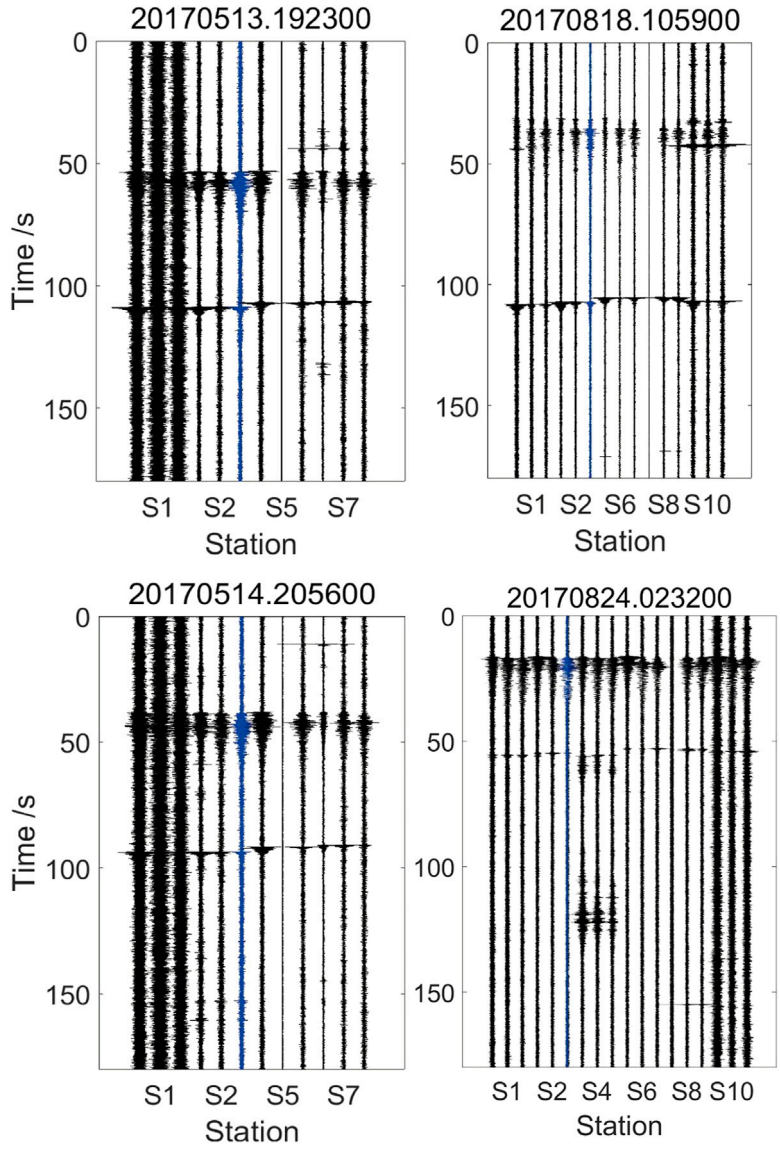

FIGURE 3
Four examples of paired signals having the window length of 180 s. The title of each waveform is the UTC time for the beginning time of the record. The horizontal coordinate is the station number and three channels for each station are shown.

Accompanied by mining, many physical processes like fracturing in the roof and debris hitting the floor may produce microseismic signals which can be received by our surface microseismic monitoring system.

The paired microseismic signals

With 7 months of observation, we have detected many signals including natural earthquake signals and microseismic signals in the salt mine with the standard STA/LTA algorithm (Allen, 1978). In these waveforms, we detected a new kind of microseismic signal consisting of two parts, which is for the first time observed for solution salt mining. The first part of the paired signal is a long-duration signal of about 15 s. The second part is a short duration signal. The separation between two signals ranges from 30 to 90 s (Figure 3). The durations of the two parts are different and the first one is longer than the second one. From May 2017 to November 2017, there are a total of 88 distinct paired signals with these characteristics and they are randomly distributed at any time of the day.

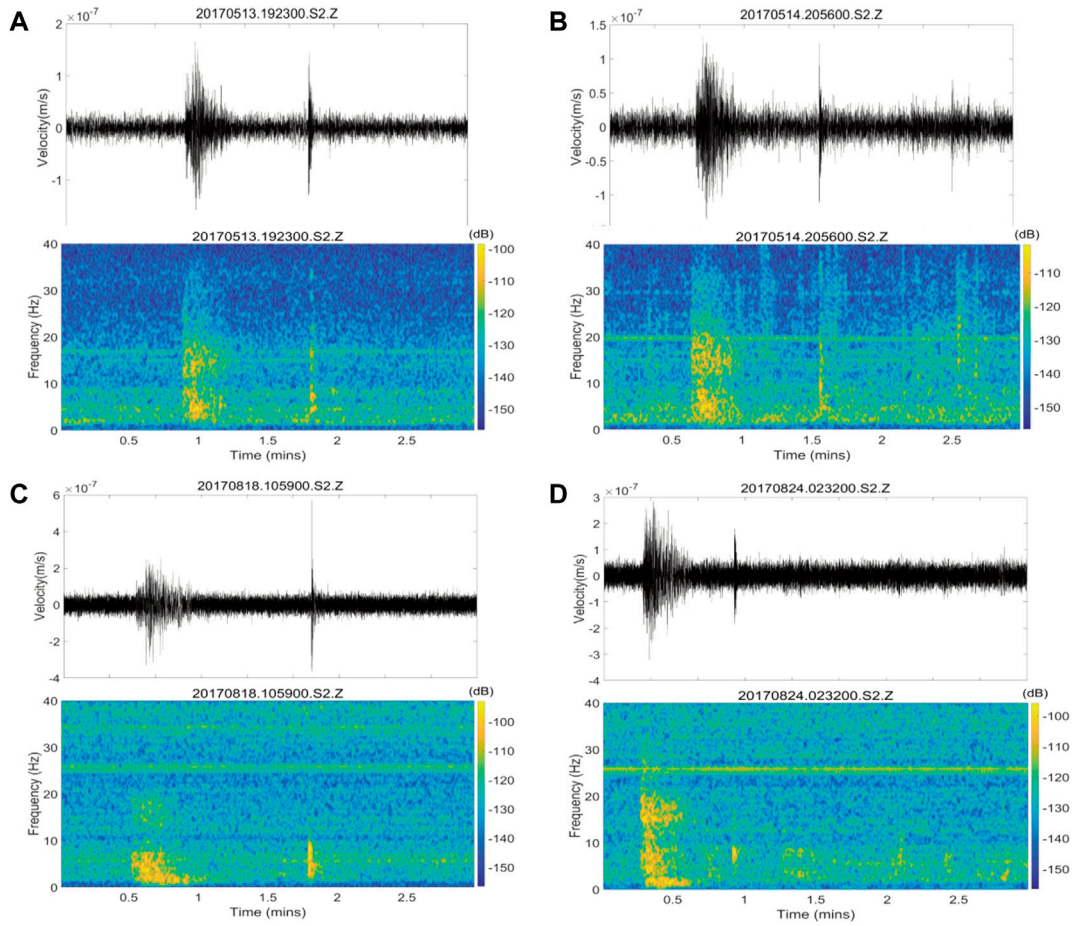

FIGURE 4
Time frequency analysis of the Z-component of the four paired signals at station S2. The top one is the waveform and the bottom one is the time frequency spectrogram of the corresponding waveform. **(A)** The paired signal on 13 May 2017, 19:23:00 UTC. **(B)** The paired signal on 14 May 2017, 20:56:00 UTC. **(C)** The paired signal on 18 August 2017, 10:59:00 UTC. **(D)** The paired signal on 24 August 2017, 02:32:00 UTC.

To further compare these two parts of the paired signals, we analyze their time-frequency properties and initial motions. From the time frequency analysis of the vertical (Z) component of the seismic data, we can find that the frequency content of the first part of the paired signal is below 40 Hz, and it decreases gradually. In comparison, the frequency of the second part of the signal concentrates below 10 Hz (Figure 4). The initial motions of the first signal are random but the initial motions of the second signal are moving downward in the vertical direction (Figure 5). Usually, the second signal waveform has a narrow frequency band (Figure 6). These characteristics are ubiquitous in our 88 paired signals.

Besides, there is a significant difference between these two parts. The travel time differences on different stations for the first signals are almost all less than one second, but the travel time differences on different stations for the second signals can be up to about 3 s (Figure 5). Usually the stations S6, S8, and S10 received the second signal earlier, and the stations S1 and S2 recorded the latest.

Double-pair double-difference location

Event-pair double-difference earthquake location method, as incorporated in hypoDD (Waldhauser and Ellsworth, 2000), has been widely used in improving relative earthquake locations. One advantage of the double-difference location method is that the relative locations are less affected by velocity uncertainties because some common path anomalies outside the source region can be cancelled out due to similar ray paths. Similarly, station-pair differential arrival times from one event to pairs of stations can also be used to improve earthquake locations by cancelling out the event origin time and some path anomalies inside the source region (Zhang et al., 2010). To utilize advantages of both double-difference location methods, Guo and Zhang (2017) developed a double-pair double-difference location method using differential times constructed from pairs of events to pairs of stations.

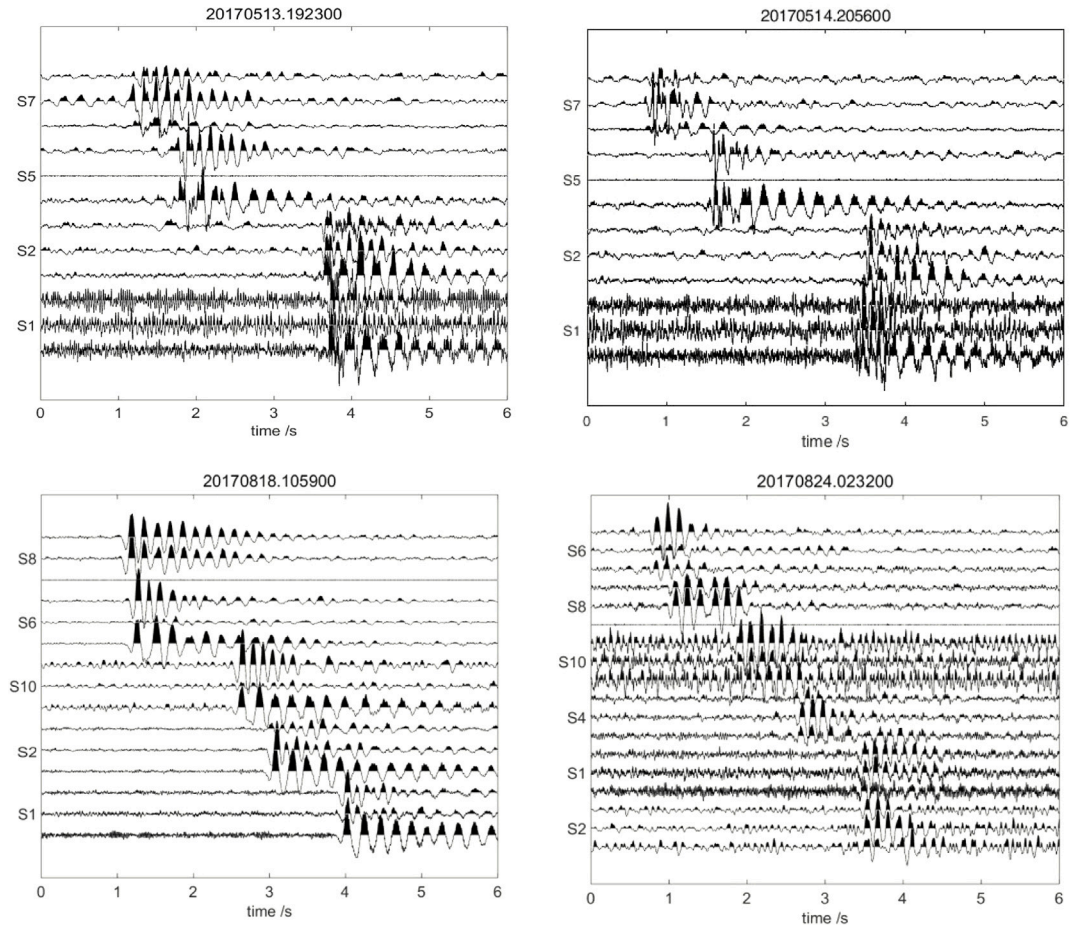

FIGURE 5
The second event waveforms for four paired signals in Figure 3.

We have relocated the first signals with the double-pair double-difference earthquake location algorithm (Guo and Zhang, 2017). We set the velocity model according to the lithology of the overburden (Figure 7A). The initial locations are constructed by grid search location method. After double-pair double-difference location, root mean square values for differential time residuals decrease from 64.59 to 30.26 ms (Figure 7B). Overall. The first microseismic signals are located around station S5 (Figure 8) where it is under mining.

Discussion

The first event of the paired signal has a longer duration of ~15 s and has a mixed frequency band of 5–30 Hz (Figure 4). It can be related to multiple fracturing processes on the cavern roof before the falling of a rock debris. Individual fracturing process on the roof can emit different microseismic signals and these signals can be mixed together. In addition, smaller fractures can coalesce to form larger fractures. As a result, the corresponding microseismic signals would have lower frequencies (Martínez-Martínez et al., 2016; Du et al., 2020). This crack generation and propagation process on the roof is consistent with the time-frequency characteristics of the first event with higher frequencies at the beginning and lower frequencies in the later part. The cotransport of heavy metals and particles by seepage on the roof will affect the generation of the first event (Bai et al., 2021). This type of microseismic signal corresponding to a series of fracturing processes before the detachment of a debris from the roof has also been found in other solution salt mining (e.g., Kinscher et al., 2014).

When the rock debris is detached from the roof, it can collide with the bottom or the floor of the cavern, which could also produce seismic signals. The second part of the paired signal is consistent with this collision process. First, the signal resulting from collision is expected to be short and actually the duration of the second part of the paired signal is only

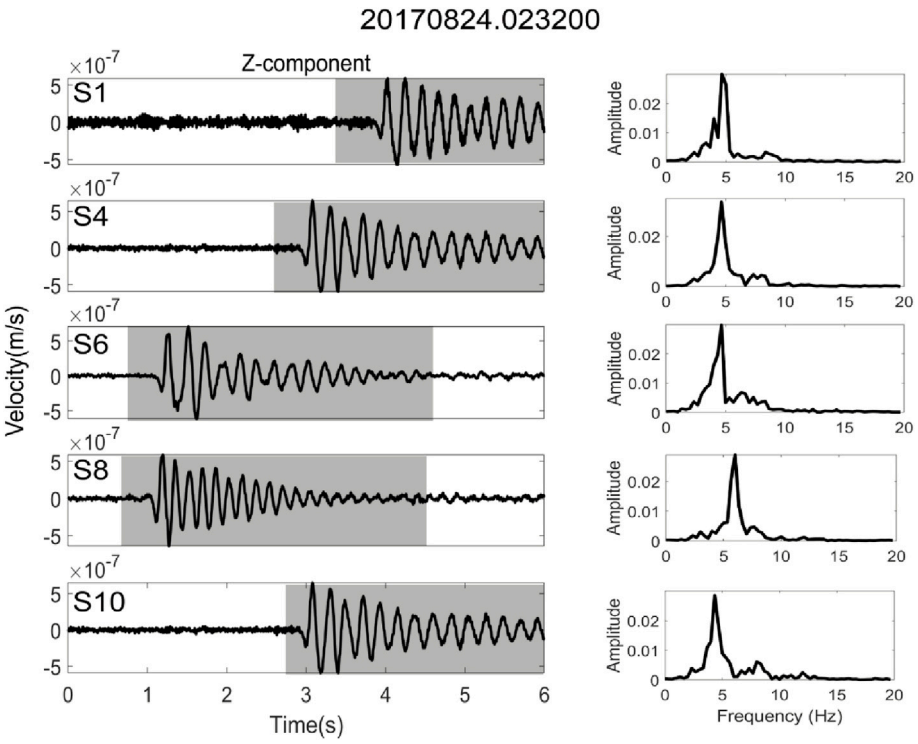

FIGURE 6
Zoom-in waveforms of the second event (left) and the corresponding frequency spectra (right) at five stations for the paired signal observed on 24 August 2017, 02:32:00 UTC. The frequency spectra are computed using the waveforms in the time windows marked by the grey rectangles.

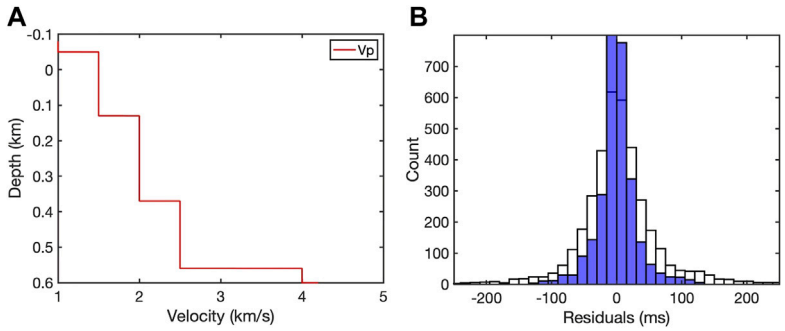

FIGURE 7
(A) P-wave velocity model used for location. **(B)** Histograms of travel time residuals before (white) and after (white) event relocation.

~3 s. Second, for the signal produced by the collision, its initial motion polarity should be negative in the vertical component because the equivalent force vector due to collision points upwards. When we check the polarities of the first arrivals of second events, most of them are clearly negative (Figure 5), consistent with this process. Based on the above analysis, we think the first event of the paired signal represents the fracture development and the detachment process for rock debris from the cavern roof, and the second event represents the collision between the debris and the cavern floor.

Kinscher et al. (2014) proposed that the process of fracturing development that could lead to the debris detachment on the cavity roof in the overlying Marl layer and the overburden can generate acoustic emissions. The microseismic signals may be isolated or tremor-like. However, he claimed that due to low

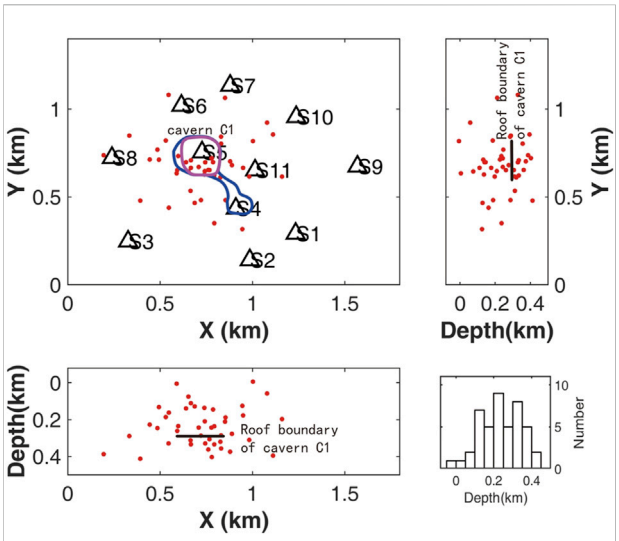

FIGURE 8
Distribution of event locations for the first events of the paired signals detected during the 7-month period, The events are located by the method of double-pair double-difference earthquake location algorithm (Guo and Zhang, 2017). The black triangles represent the seismic stations and the red dots represent the first events of paired signals.

energy released by the impacts of falling blocks on the cavity floor, the related signals may not be detectable by the seismic instruments. If the floor is covered by the heavy mud layer, most energy of the collision will be attenuated and absorbed. In our case, we clearly detect the collision signals, indicating the floor is not covered by the heavy mud layer that could act as a cushion for the falling debris.

For the paired signal, the separation time between two events ranges from ~30 to ~90 s (Figure 3), which should correspond to the travel time for the debris through the brine. The delay times between two signals should be controlled by the shape and density of debris and viscosity of the brine. By assuming the debris has a circular shape, we can roughly estimate the falling-velocity of the rock debris (w) in the brine as follows (Ahrens, 2000),

$$w = C1\Delta g d^2 \Big/ \nu + Ct\sqrt{(\Delta g d)} \tag{1}$$

where $\Delta = (\rho s - \rho)/\rho$, $Cl = 0.055\tanh[12A^{-0.59}\exp(-0.0004A)]$, $Ct = 1.06\tanh[0.016A^{0.50}\exp(-120/A)]$, $A = \Delta g d^3/\nu^2$ is the Archimedes buoyancy index, d is the characteristic diameter of the debris which means the diameter of the circle, ν is the kinematic viscosity of brine, ρ_s is the density of the debris, ρ is the density of the brine, and g is the acceleration of gravity.

The falling velocity of the rock debris in the brine varies from a few meters per 10 s to a few meters per second which depends on the shape and size of the debris, the density of the rock and the temperature of the brine (Figure 9C). The solution is saturated brine which determines the density of the brine and the kinematic viscosity of brine. These two values play an important role in determining the falling velocity of the rock debris. The ambient temperature and the hydraulic and thermal conductivity of geotechnical media also play a role in

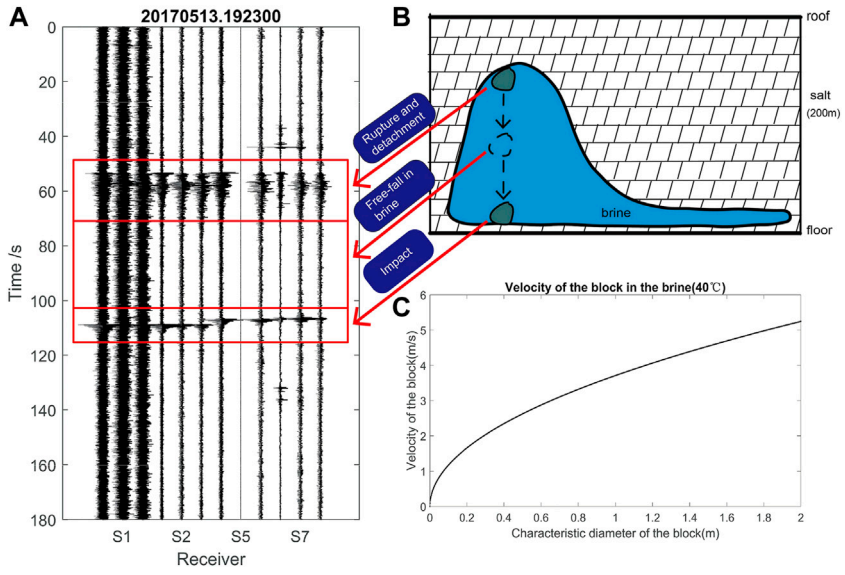

FIGURE 9
Cartoon showing the mechanism of the observed paired signals for solution salt mining. **(A)** The paired signals observed at different stations. **(B)** The cartoon showing the physical process producing paired signals. **(C)** The velocity of the falling bock from the roof through the brine estimated using Eq. 1.

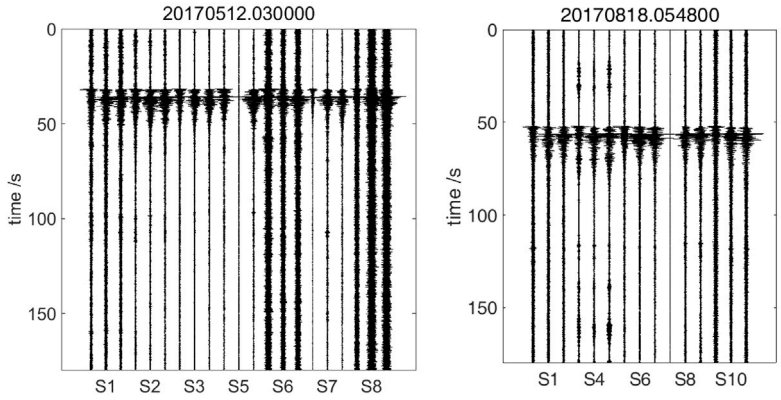

FIGURE 10
Two examples of signals similar to the first part of the paired signals but without the second part having the window length of 180 s. The title of each waveform is the UTC time for the beginning time of the record. The horizontal coordinate is the station number and three channels for each station are shown.

determining the falling velocity (Bai et al., 2022). Here we set the brine temperature as 40°C, density ρ as 1,200 kg/m^3, kinematic viscosity of brine ν = 1.9858e-6 m^2/s, and the block density ρ_s = 2,700 kg/m^3.

In our case, the cavern has the height of about 200 m. Based on the estimated falling velocity, the rock debris will spend dozens of seconds to fall onto the cavern floor, which is consistent with our observations. Therefore, in theory, the time interval between two events of paired signal could be used to characterize the height of the cavern.

It is noted that the first event of the paired signal has travel time differences within 1 s at different seismic stations. In comparison, the travel time differences for the second event of the paired signal are much larger. This is mainly because the first event of the paired signal travels through the media above the cavern roof and its shallower layers and seismic velocities may not change greatly. In comparison, for the second event of the paired signal, they need to travel through some cavities filled with brine and seismic velocities may vary greatly in space. As a result, the travel times to different stations will differ at a larger degree. This also makes it difficult to locate the second event of the paired signal because the velocity heterogeneity is very large and accurate velocity model is difficult to obtain. In comparison, we can more accurately locate the first events with the double-pair double-difference earthquake location algorithm (Guo and Zhang, 2017), which is less sensitive to velocity heterogeneities. It can be seen that these events are mostly located around cavern C1 below station S5 (Figure 8). These events extend a relatively large depth range of ~200 m. On one hand, this may reflect the fact that cavern roof has varying heights. On the other hand, this could be due to location uncertainties due to inaccurate arrival time picks and velocity models used for location.

In addition to paired signals, we also observed signals similar to the first event of the paired signal but without the second part (Figure 10). This could be because the corresponding rock debris is too small so that the collision cannot produce enough energy to be detected by geophones. Or it could be because the cavern floor is covered by heavy mud materials so that the collision energy is absorbed and attenuated. It could also be due to the fact that there are some fractures created in the roof due to the roof instability but without debris falling. Observing the distinct second part depends on the size of the fallen blocks and the lithological characters of the fallen blocks and the cavern floor. Only relatively huge and hard blocks and relatively hard floor of the cavern can produce obvious collision signals.

Conclusion

By using a surface microseimic monitoring system for the Dongxing salt mine located in Dongxing county, China, for the first time we have observed paired signals that are induced by cavern roof instability. The first event of the paired signal has a longer duration, which is caused by a series of crack generation and propagation on the cavern roof before the debris detachment from the roof. The second event of paired signal is associated with the collision between the fallen debris and the cavern floor. The time delay between two events of paired signal corresponds to the falling time of the debris through brine. Therefore, by using the paired signal we can better understand the whole process of fracturing development on the cavern roof before the rock debris starts to fall, the time for the debris falling through the brine, and the collision of the debris on the cavern floor.

By using paired signals, it is helpful for better understanding the cavern roof instability status and thus assessing the cavern

collapse hazard. By locating the first event of paired signals, we can delineate the spatial distribution of cavern roof. The delay time between two events of paired signals can be used to qualitatively estimate the height of the cavern. The observation of collision signal could be used to derive the size of the rock debris through some further analysis. The derived information could be combined to assess the cavern collapse hazard through some rock mechanics analysis.

Data availability statement

The original contributions presented in the study are included in the article/supplementary material, further inquiries can be directed to the corresponding author.

Author contributions

JQ and KW: methodology, software, data curation, writing—original draft. HZ: supervision, writing-review and editing, funding acquisition. YT: data curation. CX, QW, and QX: funding acquisition, project administration. MM: writing-review and editing. All authors contributed to the article and approved the submitted version.

Funding

This work is a part of the joint Polish-Chinese FULLIMAGE project, which received funding in the SHENG call from National Natural Science Foundation of China (NSFC) under grant no. 41961134001 and the Polish National Science Centre (NCN) under grant no. UMO-2018/30/Q/ST10/00680 the National Natural Science Foundation of China under grants U2139204 and the Fundamental Research Funds for the Central Universities under grant WK2080000153.

Conflict of interest

The authors declare that the research was conducted in the absence of any commercial or financial relationships that could be construed as a potential conflict of interest.

Publisher's note

All claims expressed in this article are solely those of the authors and do not necessarily represent those of their affiliated organizations, or those of the publisher, the editors and the reviewers. Any product that may be evaluated in this article, or claim that may be made by its manufacturer, is not guaranteed or endorsed by the publisher.

References

Ahrens, J. P. (2000). A fall-velocity equation. *J. Waterw. Port. Coast. Ocean. Eng.* 126 (2), 99–102. doi:10.1061/(asce)0733-950x(2000)126:2(99)

Allen, R. V. (1978). Automatic earthquake recognition and timing from single traces. *Bull. Seismol. Soc. Am.* 68 (5), 1521–1532. doi:10.1785/bssa0680051521

Bai, B., Nie, Q., Zhang, Y., Wang, X., and Hu, W. (2021). Cotransport of heavy metals and SiO2 particles at different temperatures by seepage. *J. Hydrology* 597, 125771. doi:10.1016/j.jhydrol.2020.125771

Bai, B., Wang, Y., Rao, D., and Bai, F. (2022). The effective thermal conductivity of unsaturated porous media deduced by pore-scale SPH simulation. *Front. Earth Sci. (Lausanne).* 1057. doi:10.3389/feart.2022.943853

Berest, P., Brouard, B., Feuga, B., and Karimi-Jafari, M. (2008). The 1873 collapse of the Saint-Maximilien panel at the Varangeville salt mine. *Int. J. Rock Mech. Min. Sci.* 45 (7), 1025–1043. doi:10.1016/j.ijrmms.2007.10.007

Cook, N. (1963). "The seismic location of rockbursts," in *Proceedings of the fifth rock mechanics symposium* (Pergamon Press), 463, 516.

Dahm, T., Heimann, S., and Bialowons, W. (2011). A seismological study of shallow weak micro-earthquakes in the urban area of Hamburg city, Germany, and its possible relation to salt dissolution. *Nat. Hazards (Dordr).* 58 (3), 1111–1134. doi:10.1007/s11069-011-9716-9

Das, I., and Zoback, M. D. (2011). Long-period, long-duration seismic events during hydraulic fracture stimulation of a shale gas reservoir. *Lead. Edge* 30 (7), 778–786. doi:10.1190/1.3609093

Du, K., Li, X., Tao, M., and Wang, S. (2020). Experimental study on acoustic emission (AE) characteristics and crack classification during rock fracture in several basic lab tests. *Int. J. Rock Mech. Min. Sci.* 133, 104411. doi:10.1016/j.ijrmms.2020.104411

Eaton, D., van der Baan, M., Tary, J. B., Birkelo, B., Spriggs, N., Cutten, S., et al. (2013). Broadband microseismic observations from a Montney hydraulic fracture treatment, northeastern BC, Canada. *Ele* 1150 (1200), 1250.

Ege, J. R. (1984). Mechanisms of surface subsidence resulting from solution extraction of salt. Man-induced land subsidence. *Geol. Soc. Am. Rev. Eng. Geol.* 6, 203–221.

Ellsworth, W. L., Horton, S., Benz, H., Hickman, S., Leeds, A., Leith, W. S., and Herrmann, R. B. (2012). *Tremors in the bayou: The events on the napoleonville salt dome, Louisiana*. San Francis, CA: AGUFM, S51E–S2453.

Ge, M. (2005). Efficient mine microseismic monitoring. *Int. J. Coal Geol.* 64 (1-2), 44–56. doi:10.1016/j.coal.2005.03.004

Guarascio, M. (1987). Microseismic monitoring of solution mining cavities. *APCOMMining* 871, 49.

Guo, H., and Zhang, H. (2017). Development of double-pair double difference earthquake location algorithm for improving earthquake locations. *Geophys. J. Int.* 208, 333–348. doi:10.1093/gji/ggw397

Gutiérrez, F., Parise, M., De Waele, J., and Jourde, H. (2014). A review on natural and human-induced geohazards and impacts in karst. *Earth-Science Rev.* 138, 61–88. doi:10.1016/j.earscirev.2014.08.002

Jousset, P., and Rohmer, J. (2012). Evidence for remotely triggered microearthquakes during salt cavern collapse. *Geophys. J. Int.* 191 (1), 207–223. doi:10.1111/j.1365-246x.2012.05598.x

Kinscher, J., Bernard, P., Contrucci, I., Mangeney, A., Piguet, J. P., and Bigarre, P. (2014). Location of microseismic swarms induced by salt solution mining. *Geophys. J. Int.* 200 (1), 337–362. doi:10.1093/gji/ggu396

Kinscher, J., Cesca, S., Bernard, P., Contrucci, I., Mangeney, A., Piguet, J. P., et al. (2016). Resolving source mechanisms of microseismic swarms induced by solution mining. *Geophys. J. Int.* 206 (1), 696–715. doi:10.1093/gji/ggw163

Lebert, F., Bernardie, S., and Mainsant, G. (2011). Hydroacoustic monitoring of a salt cavity: An analysis of precursory events of the collapse. *Nat. Hazards Earth Syst. Sci.* 11 (9), 2663–2675. doi:10.5194/nhess-11-2663-2011

Liu, W., Zhang, Z., Chen, J., Jiang, D., Wu, F., Fan, J., et al. (2020). Feasibility evaluation of large-scale underground hydrogen storage in bedded salt rocks of China: A case study in jiangsu province. *Energy* 198, 117348. doi:10.1016/j.energy.2020.117348

Liu, X., Xing, X., Wen, D., Chen, L., Yuan, Z., Liu, B., et al. (2019). Mining-induced time-series deformation investigation based on SBAS-InSAR technique: A case study of drilling water solution rock salt mine. *Sensors* 19 (24), 5511. doi:10.3390/s19245511

Martínez-Martínez, J., Fusi, N., Galiana-Merino, J. J., Benavente, D., and Crosta, G. B. (2016). Ultrasonic and X-ray computed tomography characterization of progressive fracture damage in low-porous carbonate rocks. *Eng. Geol.* 200, 47–57. doi:10.1016/j.enggeo.2015.11.009

Mercerat, E. D., Driad-Lebeau, L., and Bernard, P. (2010). Induced seismicity monitoring of an underground salt cavern prone to collapse. *Pure Appl. Geophys.* 167 (1-2), 5–25. doi:10.1007/s00024-009-0008-1

Nayak, A., and Dreger, D. S. (2014). Moment tensor inversion of seismic events associated with the sinkhole at Napoleonville salt dome, Louisiana. *Bull. Seismol. Soc. Am.* 104 (4), 1763–1776. doi:10.1785/0120130260

Schléder, Z., Urai, J. L., Nollet, S., and Hilgers, C. (2008). Solution-precipitation creep and fluid flow in halite: A case study of zechstein (Z1) rocksalt from neuhof salt mine (Germany). *Int. J. Earth Sci.* 97 (5), 1045–1056. doi:10.1007/s00531-007-0275-y

Trifu, C. I., and Shumila, V. (2010). Microseismic monitoring of a controlled collapse in field II at ocnele mari, Romania. *Pure Appl. Geophys.* 167 (1-2), 27–42. doi:10.1007/s00024-009-0013-4

Valentino, B. (2016). *Application of InSAR to salt mine subsidence.*

Waldhauser, F., and Ellsworth, W. L. (2000). A double-difference earthquake location algorithm: Method and application to the northern Hayward fault, California. *Bull. Seismol. Soc. Am.* 90 (6), 1353–1368. doi:10.1785/0120000006

Waltham, T., Bell, F. G., Culshaw, M. G., Knez, M., and Slabe, T. (2005). *Sinkholes and subsidence: Karst and cavernous rocks in engineering and construction*. Berlin: Springer.

Xing, X., Zhu, Y., Yuan, Z., Xiao, L., Liu, X., Chen, L., et al. (2021). Predicting mining-induced dynamic deformations for drilling solution rock salt mine based on probability integral method and weibull temporal function. *Int. J. Remote Sens.* 42 (2), 639–671. doi:10.1080/01431161.2020.1813345

Xiong, Q., Yuan, X., and Gu, H. (2019). Application of 3D seismic exploration on the detection of shape of salt cavity and the integrity of overlying strata. *Chin. J. Eng. Geophys.* 16 (3), 266–272.

Zhang, G., Wang, Z., Wang, L., Chen, Y., Wu, Y., Ma, D., et al. (2019). Mechanism of collapse sinkholes induced by solution mining of salt formations and measures for prediction and prevention. *Bull. Eng. Geol. Environ.* 78 (3), 1401–1415. doi:10.1007/s10064-017-1173-6

Zhang, G., Wang, Z., Zhang, K., Li, Y., Wu, Y., Chen, Y., et al. (2018). Collapse mechanism of the overlying strata above a salt cavern by solution mining with double-well convection. *Environ. Earth Sci.* 77 (16), 588. doi:10.1007/s12665-018-7739-1

Zhang, H., Nadeau, R. M., and Toksoz, M. N. (2010). Locating nonvolcanic tremors beneath the San Andreas fault using a station-pair double-difference location method. *Geophys. Res. Lett.* 37 (13). doi:10.1029/2010gl043577

Zhu, W., and Beroza, G. C. (2019). PhaseNet: A deep-neural-network-based seismic arrival-time picking method. *Geophys. J. Int.* 216 (1), 261–273.

frontiers | Frontiers in Earth Science

TYPE Original Research
PUBLISHED 06 January 2023
DOI 10.3389/feart.2022.1022719

OPEN ACCESS

EDITED BY
Wenzhuo Cao,
Imperial College London,
United Kingdom

REVIEWED BY
Lu Jun,
Shenzhen University, China
Quan Jiang,
Institute of Rock and Soil Mechanics (CAS), China

*CORRESPONDENCE
Erchao Li,
bqt1800604029@student.cumtb.edu.cn

SPECIALTY SECTION
This article was submitted to Structural Geology and Tectonics, a section of the journal Frontiers in Earth Science

RECEIVED 18 August 2022
ACCEPTED 22 November 2022
PUBLISHED 06 January 2023

CITATION
Li E, Gao Q, Li X, Mao T and Zheng B (2023), Displacement response characteristics of different sand tunnel excavation faces under true triaxial loading.
Front. Earth Sci. 10:1022719.
doi: 10.3389/feart.2022.1022719

Displacement response characteristics of different sand tunnel excavation faces under true triaxial loading

Erchao Li[1]*, Quanchen Gao[1], Xiao Li[2,3], Tianqiao Mao[2,3] and Bo Zheng[2,3]

[1]School of Mechanics and Civil Engineering, China University of Mining and Technology (Beijing), Beijing, China, [2]Key Laboratory of Shale Gas and Geoengineering, Institute of Geology and Geophysics, Chinese Academy of Sciences, Beijing, China, [3]College of Earth and Planetary Sciences, University of Chinese Academy of Sciences, Beijing, China

During the construction of subway tunnels, the geotechnical body is affected by excavation to produce three-dimensional spatial deformation. The deformation of geotechnical bodies is an important safety hazard for project advancement, so it is important to understand the excavation disturbance range and deformation mechanism. The current related research is mainly about the theory of land subsidence and the two-dimensional plane displacement of the stratum, and there are few studies on the specific three-dimensional disturbance mode and its mechanism. In order to better understand the three-dimensional displacement characteristics of the tunnel excavation soil, a tunnel excavation model test was established based on a true triaxial stress loading system combined with three-dimensional scanning technology for a superimposed sandy soil. Based on the established model, the vector displacement response range and three-dimensional deformation characteristics of the excavation face were studied in the main displacement affected area around the excavation face. Meanwhile, the deformation characteristics, such as vertical settlement and horizontal displacement of the stratum in the main influence area were analyzed. The results show that the main influence area of tunnel excavation is elliptical and distributed within a range of twice the diameter of the tunnel axis. The main influence range is bell-shaped in the vertical direction and inverted wedge-shaped in the horizontal direction. The three-dimensional space presents a "W" deformation distribution. The three-dimensional deformation theoretical model of the excavation face established in this paper can provide some references for the excavation engineering of superimposed sand-soil tunnels.

KEYWORDS

full-section tunnel, true triaxial loading, model test, stratum deformation, displacement vector, excavation face displacement model

1 Introduction

With the continuous advancement of the urbanization process, more and more underground tunnel excavation projects are being carried out. In tunnel construction, controlling strata movement to ensure effective excavation is the main problem that must be considered (Mair, 2008; Zhu, 2014). The analysis of the characteristics of stratum disturbance caused by tunnel construction generally believes that the stratum movement presents regional differences around the tunnel, and the interface between the disturbance areas changes with the different working face soil (Yuan et al., 2018). Strata movement is inevitable during tunnel excavation and different geological conditions show different displacement characteristics (Pinto et al., 2014). Taking the typical sandy soil in the Beijing area as an example, the excavation displacement of the tunnel in the sandy soil layer is particularly obvious (Li and Ma, 2011; Cheng et al., 2019). The existing research on face subsidence and stratum displacement is relatively complete, but the research on the three-dimensional displacement of the excavation face at a certain excavation position after excavation is limited, and the research on the influence of the superimposed stratum displacement of different soils is even less. Therefore, this paper proposes a specific study on the displacement of the excavation face caused by the full-section tunnel excavation of the superimposed sand layer.

The displacement of soil mass on the face and in the stratum can be predicted through theoretical calculation (Yoshikoshi et al., 1978; Mair et al., 1993; Verruijt, 1998; Park, 2005; Pinto and Whittle, 2014). Peck (1969) integrated a large number of tunnel excavation face settlement monitoring data and found that the shape of the settlement tank per unit length can be estimated by a normal (Gaussian) distribution curve. On the basis of a series of *in situ* observations and a theory of face loss, an empirical solution for estimating face subsidence caused by tunnel excavation is systematically proposed for the first time (Peck, 1969). In addition, the mirror image method (Sagaseta, 1987; Loganathan and Poulos, 1998) and the random medium theory system (Litwiniszyn, 1957; Yang and Wang, 2011) are also widely used in the study of soil deformation caused by tunnel construction. However, the theoretical analysis of relevant scholars is more about face subsidence, and the impact of excavation on the face built environment is understood through the description of the face subsidence tank (Hagiwara et al., 1999; Mollon et al., 2012; Cao et al., 2020; Yang et al., 2021). The stratum movement is three-dimensional during the tunneling process, and Attewell et al. (1986) extended the Peck formula to establish a three-dimensional empirical solution (Attewell et al., 1986). Pinto and Whittle simplified soil plasticity and derived a relatively innovative analytical solution (Pinto et al., 2014). The three-dimensional solution is mostly based on the time-history curves of land subsidence and overall formation subsidence from the two-dimensional solutions. The three-dimensional displacement is shown by combining the two-dimensional displacements.

In the last 3 decades, laboratory physical models have played an increasingly important role in tunnelling research (Meguid et al., 2008; Marshall et al., 2012). In order to study the response of tunnel excavation to strata, more and more modeling techniques have been developed and applied. From the point of view of gravity mechanics, the model tests mainly include centrifugal model tests and conventional model tests (Nomoto et al., 1999; Berthoz et al., 2012; Berthoz et al., 2018; Chen et al., 2018; Song and Marshall, 2020). N. Loganathan accelerated the centrifuge to 100 g, used a scale model of 1:100, and evaluated the soil deformation caused by tunnel excavation through three centrifugal model tests and measured the vertical and lateral ground motions induced by the excavation (Loganathan et al., 2000). Mahmoud Ahmed uses transparent soil to simulate sand, and studies the movement characteristics of the ground and nearby soil caused by shield tunnel construction through the analysis of full-field displacement vector, ground deformation profile, and internal strain (Ahmed and Iskander, 2011). Even though the effect of gravitational acceleration can be taken into account in the centrifugal test to simulate the natural gravity state of the soil as well as possible, the tunneling process is usually simulated as a two-dimensional response process.

At present, there are many methods for predicting the face subsidence disturbed by tunnel excavation, but there are few studies on the three-dimensional subsidence deformation of the tunnel. Based on the elastic analysis method proposed by Verruijt and Booker and the principle of conservation of ground loss (Verruijt and Booker, 1998), Haiqing Yang studied the influence of tunnel burial depth on face settlement and the influence of different excavation length and burial depth on three-dimensional settlement grooves through the tunnel radial shrinkage model test (Yang et al., 2019). Hongliang Tu used a numerical simulation method to study the deformation of surrounding rock and the mechanical properties of supporting structures under different excavation methods. Different soils will lead to differences in stratum movement. During excavation, it is necessary to monitor the internal displacement of surrounding rock, understand the mechanism of stratum movement, and determine the sliding failure face and stratum subsidence curve. It is also necessary to establish a specific kinematic model of the excavation face.

2 Experiments and methods

2.1 Sample preparation

In order to simulate the typical sandy soil in the Beijing area and compare the deformation characteristics of different soils, several sections of the soil at the construction site were selected for laboratory physical property measurement and reshaping

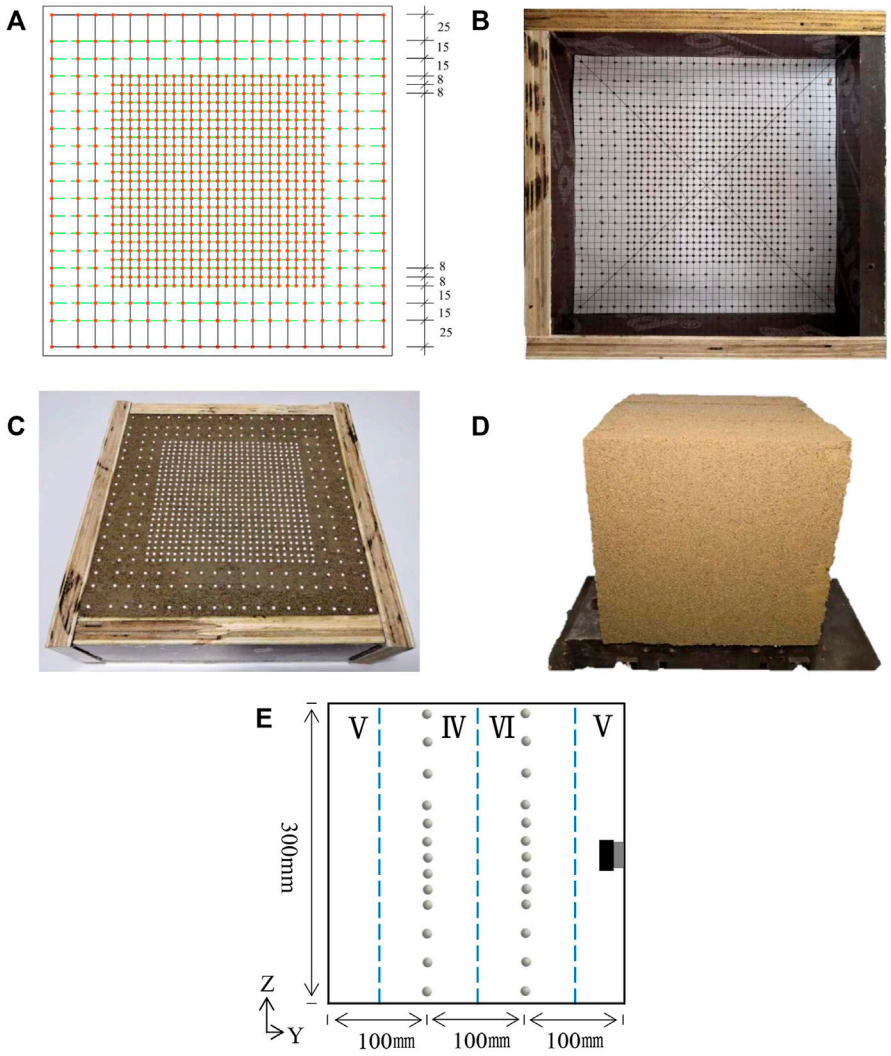

FIGURE 1
Sample preparation: **(A)** Marker layout plan, **(B)** Marker localization, **(C)** Marker placement effectmonitoring surface, **(D)** Overall cube specimen, **(E)** Marker monitoring surface position.

applications. Ten soil screening tests showed that the soil was sandy soil. According to the soil sample preparation standard (Geotechnical test method standard GBT50123-2019), the material is mixed evenly with a mixer, and the model space is filled layer by layer with an appropriate compaction method by hammering, and the model density is adjusted by controlling the material quality and filling height. The experimental simulation in this paper refers to Beijing Metro Line 17. The outer diameter of the shield tunnel is 6.4 m and the inner diameter is 5.8 m. The thickness of the segment is 0.3 m. As shown in Figure 1, according to the theoretical ratio of similar models of 160:1, the diameter of the excavated tunnel in the experiment is 55 mm, and the length, width and height of the model sample are 300 mm each. In order to avoid the influence of the boundary effect, this size meets the basic requirement that the boundary range of the model is greater than 5 times the diameter of the tunneling work face. The physical and mechanical parameters of the sandy soil are shown in Table 1.

Since this study focuses on the deformation on the excavation face of the tunnel, in order to focus on considering the influence range of the hole after excavation, the grid density of the marking points buried around the tunnel is higher than that of the marking points in the external area, so as to achieve the effect of establishing an accurate model. The specimens were compacted in six layers, which are silty clay, 60% sandy soil, 40% sandy soil, and silty clay in sequence. Figure 1 shows two monitoring sections arranged perpendicular to the excavation direction, located at 1/3 and 2/3 along the excavation direction.

TABLE 1 Mechanical properties of sandy soil.

	Moisture content (%)	Cohesion (kPa)	Internal friction angle (°)	Elastic Modulus (MPa)	Poisson's ratio	Density (g/cm^{-3})
Excavation face one	12.5	28.711	34.04	0.022	0.25	2
Excavation face two	12.5	54.436	20.87	0.026	0.27	2

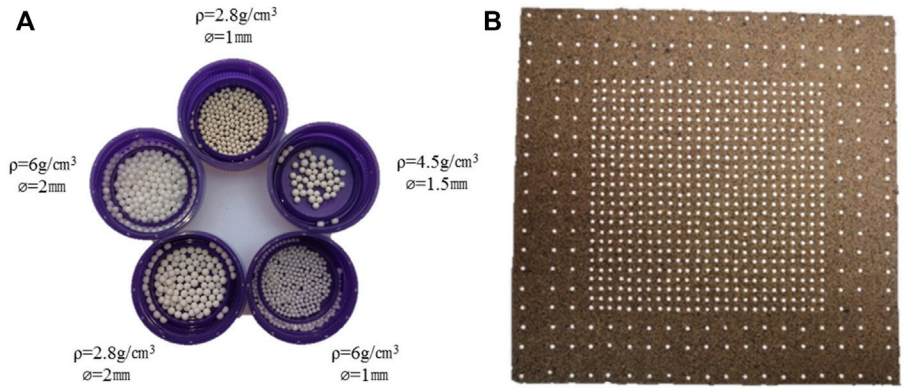

FIGURE 2
Marker selection effect: **(A)** Marker comparison, **(B)** Marker placement effect.

The first monitoring section is in the 60% sandy soil layer, and the second is in the 40% sandy soil layer. This is so that the overall movement of the excavation face in the different sandy soil layers can be tracked in three dimensions. (Figure 1). The specific placement process for the markers is as follows:

- Prepare the sandy soil into the model box with multiple sieves to 200 mm from the excavation direction;
- Set the initial position of the marker on this plane using cardboard (a positioning device);
- Embedding the marker into the monitoring plane by means of a positioned coordinate point and sprinkling a small amount of 5,000 mesh ultra-fine mica powder on the surface (to facilitate the splitting of the specimen);
- Continue to sieve the sandy soil to the position of 100 mm in the excavation direction, after installing the marker at the 100 mm position, prepare the sand until the initial position of excavation.

2.2 Marker selection

In the past, researchers often arranged markers outside the model monitoring surface and took moving pictures of the simulated tunnel construction monitoring surface (Grant and Taylor, 2000) to measure the displacement and deformation of the soil. Such a displacement observation method is not only limited by dimensions (two-direction displacement in two dimensions and limited in the third direction), but also affected by the friction of the model frame itself. Trends and displacements have an effect.

The minimum display size of the 3D scanner is 0.04 mm. In order to reduce the influence of marker density on the experimental effect, Ga_2O with a diameter of 1 mm and a specific gravity of 2.8 g/cm^3 was selected as the displacement tracking marker after scanning as shown in Figure 2. In addition, the face of the marker is sanded to increase friction in order to diminish the effects of the contact face between the materials.

2.3 Experimental facilities

The test system was developed by the Institute of Geology and Geophysics, Chinese Academy of Sciences. The stress loading system is composed of a high-stiffness true triaxial servo control loading unit, an excavation bit, and a 3D scanner measuring system, as shown in Figure 3. Three independent hydraulic piston cylinders apply confining pressure, and the effective force measuring range is 10N-3000 kN . The resolution of force measurement is 15 N, the accuracy of force measurement is within ±1%, the fluctuation of

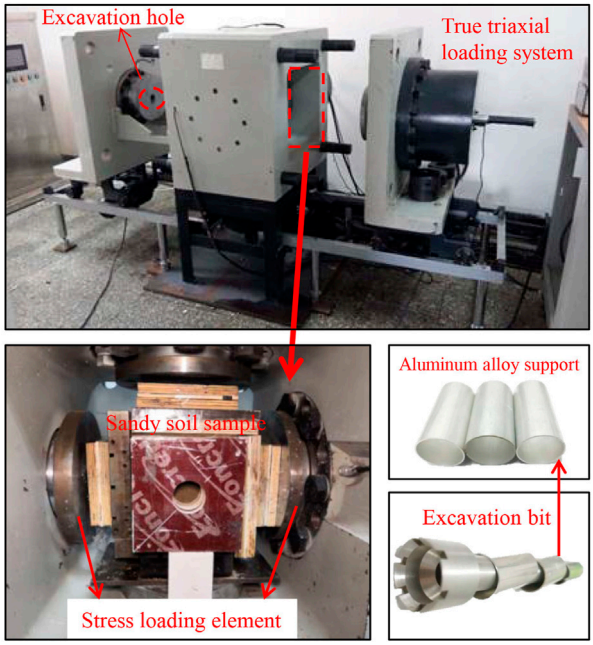

FIGURE 3
Schematic diagram of true triaxial stress loading system.

force control is less than 0.1%, and the loading rate in each direction is 10 N-10 kN/s. The computer carries out servo control of test force, stress, deformation, strain and displacement for the whole test process and can be maintained. In the triaxial loading shown in the figure, the interlocking staggered placement of wooden spacers wraps the specimen, so that both the stress can be applied effectively and the pads can be pushed relative to each other to form a perfect closure. The wooden spacers are dried and then sprayed with a reinforcing agent of a modified polyurethane nature. In this case, the hardness of the wooden spacers is up to 2.5–3H on the Brinell scale, and the modulus of elasticity is up to 100 MPa. A film with lubricant is attached between the bearing plate and the sample surface. The lubricant is high-quality Vaseline, which reduces the friction between the sample and the bearing plate. The applied stress has no effect on the deformation of the wooden spacers or the specimen.

Traditional land subsidence monitoring methods generally use micrometers, and most of them are two-dimensional point measurements. Here we use laser scanning to locate the marking beads embedded in the sample and develop a three-dimensional laser scanning displacement comparison technology of the excavation face to reconstruct the three-dimensional point cloud model of the vertical tangent plane before and after the tunnel excavation. The model after foundation displacement changes is compared with the model in the initial stage, so as to observe the three-dimensional deformation of the rock mass around the excavation face and give the three-dimensional deformation and displacement model of the excavation face under the condition of true three-dimensional *in-situ* stress.

In this study, a three-dimensional (3D) laser scanner with a resolution of 0.04 mm (the distance between the midpoints of two parallel scan lines) was used to measure the three-dimensional morphology of the test face before and after excavation. Measure and obtain face features under the establishment of a three-dimensional world coordinate system. After scanning, the images were analyzed using the Geomagic Studio software. Three stereoscopic machine heads can cover a maximum scanning area of about 500 mm * 500 mm. From the 300 mm * 300 mm square pattern window generated by scanning, 817 embedded marker beads are read to characterize the specific position coordinates of each point on its face. An "Isometric View" of the selected digital copy is shown in Figure 4.

During progressive or intermittent excavation of underground tunnels, unloading excavation will inevitably lead to obvious spatial adjustment and transfer of the internal stress of the rock mass. The soil redistribution stress makes the stress concentrated in specific areas of the cavern chamber and leads to the gradual transfer of soil displacement to the deep part after driving soil displacement around the cavern (Jiang et al., 2017). In the experiment, three sections of rigid aluminum alloy casing of 120 mm in length, 50 mm in outer diameter, and 1 mm in wall thickness are used to simulate the support and effectively control the continuous deformation displacement of the surrounding rock in the stress concentration area. Taking the deformation-inhibiting design for the stability of full-section excavation surrounding rock under full ground stress as the guideline (Jiang et al., 2019):

$$\text{Min}\ (D, RFD) = f\,(S, P, T) \tag{1}$$

Where: S is the excavation scheme, P is the support parameter, T is the support timing, D is the destroyed depth, and RFD is the fracture evaluation index of the surrounding sandy soil.

The entire project uses the method of simulating support after the excavation bit with an aluminum alloy casing. The applied force is based on the maximum deformation range, and the further deformation of the surrounding rock is suppressed by the support. Rigid support is used to fully use the surrounding rock's own bearing performance to keep and rebuild the soil-bearing arch and reach the goal of supporting to control deformation.

2.4 Experimental procedure

Before and after full stress loading, the 3D scanning marker position change and surrounding rock deformation observation steps are as follows: initial monitoring surface 3D scanning—true triaxial full stress loading—sand sample unloading dismantling

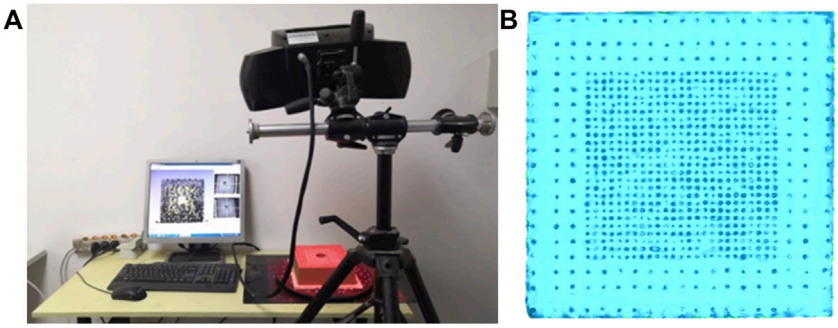

FIGURE 4
3D scanning system: **(A)** Operation mode of 3D scanner, **(B)** 3D scanning effect.

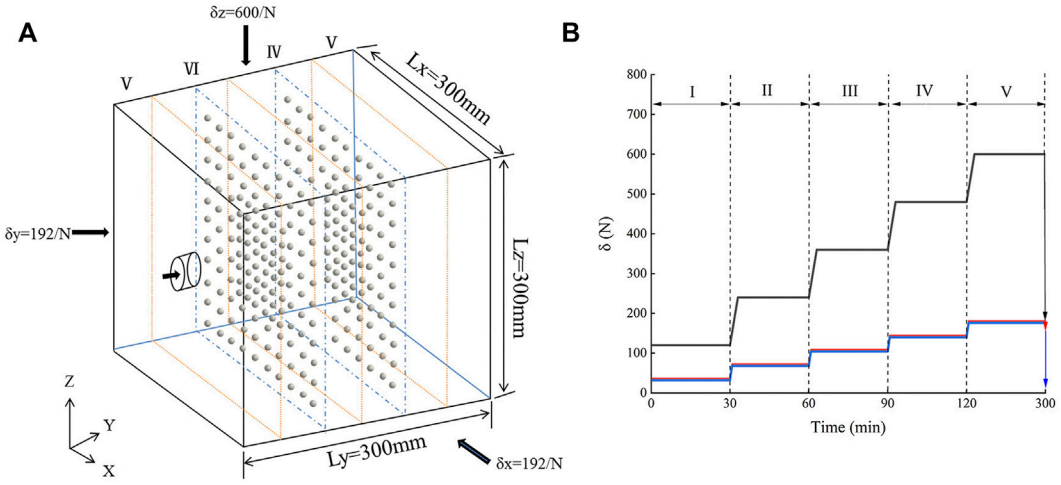

FIGURE 5
Isotropic stress applied to cube specimen during five loading stages: **(A)** Schematic diagram of model excavation, **(B)** Stress loading time-history curve.

monitoring surface 3D scanning—reloading sample stress loading and excavating the tunnel—end of excavation secondary unloading to dismantle the specimen and carry out 3D scanning of the monitoring surface. By excavating under full ground stress loading and then observing the 3D scan without loading, the 3D coordinate changes of the markers are derived, and the plastic deformation range of the two superimposed sand enclosures is obtained.

The stress is applied successively in the form of graded loading. The initial *in-situ* stress field is determined by the soil bulk density γ and the lateral pressure coefficient K_0. That is, vertically, the self-weight stress of the overlying soil layer on the foundation is loaded to σ_{cz} in the Z direction, while the X and Y directions are applied horizontally by multiplying the self-weight load by the soil lateral pressure coefficient K_0. Stress σ_{cx} and σ_{cy}, and then achieve three-dimensional *in-situ* stress loading of real soil. The hierarchical loading is divided into five stages and a three-way simultaneous stress application. The first stage is applied to 1/5 of the stress, followed by 2/5, 3/5, and 4/5 until the final full stress is applied. After each loading time step was completed, the pressure was stabilized for 30 min to achieve the overall stress balance of the sample. The stress loading path is shown in Figure 5.

(1) Vertical self-weight stress:

$$\sigma_{cz} = \gamma \cdot H \tag{2}$$

γ-weight density of soil (γ_1 =18 kN/m^3、 γ_2 =20 kN/m^3、 $\frac{\gamma_1+\gamma_2}{2}$ =19 kN/m^3).

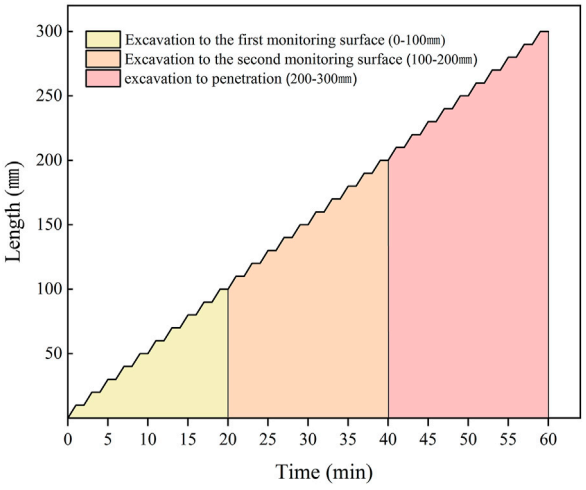

FIGURE 6
Excavation time step.

(2) Horizontal self-weight stress:

$$\sigma_{cx} = \sigma_{cy} = K_0\sigma_{cz} = K_0\gamma H \quad (3)$$

$$K_0 = \frac{\nu}{1-\nu} \quad (4)$$

K_0-Lateral pressure coefficient of soil

ν-Poisson's ratio of soil (ν_1 =0.39、 ν_2 =0.24、 $\frac{\nu_1+\nu_2}{2}$ =0.32).

According to the dimensional analysis method of the similarity principle in the model test, combined with factors such as the simulation range and the loading conditions of the testing machine, the geometric similarity constant Cl = 160, the stress similarity ratio Cσ = 160, and the severe similarity coefficient Cγ = 1. Figure four depicts the calculated principal stress loading of 600 N and lateral stress of 192 N.

In order to fully simulate the impact of open full-section excavation on the surrounding rock and working face of the tunnel, the total length of the tunnel is excavated in stages. According to the similarity theory, in the experiment, the excavation was 10 mm per minute and then the drilling was stopped for 1 min (one excavation step) to simulate the excavation and downtime in the project, respectivelyand the excavation was divided into 30 steps and took 60 min to complete. As shown in Figure 6, the entire excavation process is divided into three major sections based on the location of the monitoring surface in the sample in three equal parts and the method of hard aluminum alloy support in three sections. Excavation to the first monitoring section, digging to the position of 100 mm of the sample, total excavation time of 10 steps is 20 min; excavation to the second monitoring sample of 200 mm, total excavation time of 20 steps is 40 min; and finally, excavation to the sample penetration, total excavation time of 30 steps is 60 min Monitoring surfacemonitoring surface.

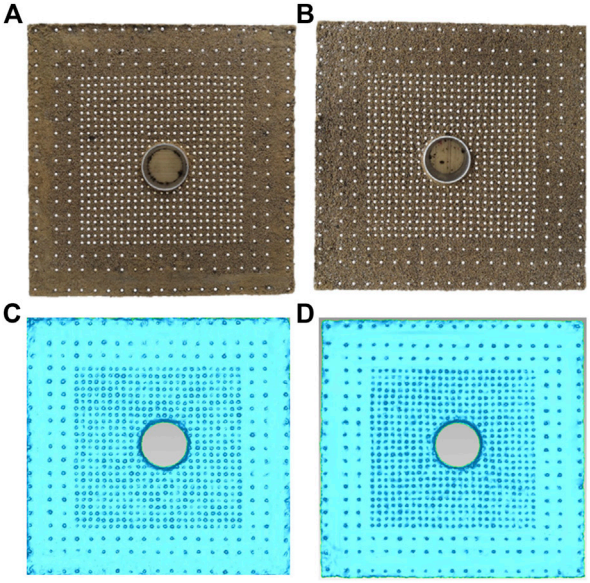

FIGURE 7
Monitoring section after excavation: **(A)** Experimental results of excavation face 1, **(B)** Experimental results of excavation face 2, **(C)** 3D scanning image of excavation face 3, **(D)** 3D scanning image of excavation face 2.

3 Experimental results and discussion

3.1 Influence range of hole excavation plane

At present, there is not much accumulation of measured data of stratum displacement caused by tunnel construction in rock and soil mass, especially the continuous stratum displacement data below the face, which is rare. In this paper, the deformation of surrounding rock and the subsidence of a foundation are analyzed in detail through laboratory tests. The displacement markers embedded in the model show that the original equilibrium state of the surrounding rock was destroyed by the tunnel excavation, and the stress redistribution occurred inside the rock mass, resulting in the deformation of the surrounding rock. Through Geomagic Studio's point cloud reconstruction, the deformation of the monitored section perpendicular to the excavation direction is constructed. The displacement of surrounding rock X and Y under different excavation steps is shown in Figure 7. These displacements come from the measuring points on sections I and II, and it can be seen from the Figure that the marked points around the holes have obvious displacements. Since the experiment mainly studies the displacement and deformation of the surrounding rock and the excavation face during the excavation process, the effects of grouting on the project are not considered. The displacement of the mark points is mainly concentrated

around the hole, and all of them move towards the tunnel axis. On the whole, the displacement of the excavation face 2 is larger than that of the excavation face 1.

The damage caused by displacement is mainly influenced by plastic deformation, and the deformation-inhibiting design applied above mainly targets the control of plastic deformation as well. In this paper, the focus is on the effect of plastic deformation on the tunnel's surrounding rock; the related elastic deformation is less studied than plastic deformation. On the other hand, it is also because this part of elastic deformation is basically recoverable and will not directly lead to settlement damage, so this paper will consider less elastic deformation compared to plastic deformation.

3.1.1 Vertical influence range of holes

The displacements of the markers in the sand layer are represented by vector arrows, which represent the main deformations of the surrounding soil under different soils of the tunnel. The initial coordinates are obtained by scanning the radiograph before excavation in Figure 6 (the initial settlement is 0), and the vector within the range of 1.5 times the diameter of the hole outside the hole is used to characterize the orientation trend of the displacement vector on the excavation face. It presents the stratum reaction characteristics and deformation characteristics before and after tunnel excavation and reflects the change of rock mass stiffness in a certain area.

Z values at three-dimensional coordinate points of markers are extracted centeredly in order to observe vertical settlement. The X value after loading and excavation and the X value before excavation are regarded as the same fixed value, and then the Z value of the two is compared so as to intuitively give the specific vertical settlement of the marked points around the hole.

It can be seen from Figure 8 that the vertical displacements of both strata are distributed in a "bell shape." The vertical displacement on the excavation face increases sequentially from the distal end to the proximal end of the tunnel axis, and the maximum settlement occurs at the top and bottom of the hole. On the one hand, due to the influence of the settlement tank, with the change of the depth, the soil layer above the tunnel produces soil arches when the stratum is lost, and the soil arches limit the development of stratum settlement. On the other hand, due to the redistribution of the surrounding rock stress during the excavation of the hole, the linear shape of the three-dimensional stress disturbance at the near-axis end increases, resulting in a significant displacement along the hole direction. Under the vault and parallel to the axis, the vertical settlement trend is opposite to that outside the vault or arch bottom. Because under the vertical load of self-weight stress, the vertical stress and reaction force at the tunnel axis position are almost superimposed, the interference of the two forces cancels out, and the vertical displacement decreases significantly toward the axis position.

It is not difficult to see from the Figure ure that the main influence range of excavation face 1 is obviously smaller than that of excavation face 2, which accounts for about 2/3 of that of excavation face 2. Among them, the influence range of the excavation face 1 is mainly concentrated on the sixth floor above the top of the tunnel, which is about 45 mm away from the top of the tunnel, which is 0.75 times the diameter of the tunnel. The main influence area below the bottom of the cave is within the range of 0.5 times the diameter of the cave on the fourth floor. The influence range of the excavation face 2 is 9 floors above the top of the tunnel, which is 68 mm from the top, which is 1.2 times the diameter of the tunnel. The main influence area below the bottom of the cave is within 0.75 times the diameter of the cave on the sixth floor. The upper compression is a little bit bigger than the lower compression. This is because the acting force is the main stress, and the tunnel vault is more likely to fail in a tensile way when the ground load is acting on it. As a result, there is more deformation and movement along the diameter of the tunnel.

3.1.2 Hole horizontal influence range

The horizontal displacement trend on both sides of the tunnel axis is mainly manifested as the indented displacement towards the central axis of the tunnel. Due to the constraints outside the tunnel excavation boundary, the horizontal intrusion displacement mainly occurs within the range of 1 * the hole diameter of the tunnel face. The horizontal intrusion displacement outside the main influence area of the tunnel perimeter is only 20%–30% of the maximum horizontal intrusion displacement in the central area, and the intrusion displacement gradually becomes negligible outside the area where the radial distance from the tunnel axis is greater than 1.5D.

For horizontal displacement, first the Z value of each marker after loading excavation and the Z value before excavation are treated as the same constant value. Then, the X values of both are compared to find the marker point's horizontal displacement vector.

Figure 9 shows that the horizontal displacement mainly occurs on the left and right sides of the tunnel, and that the two sides are basically symmetrically distributed. The main influence range of the horizontal displacement is in an "inverted wedge" distribution as a whole, and the horizontal movement of excavation face o1 and excavation face 2 decreases from the two sides of the tunnel axis, from the proximal end to the distal end. Affected by the coincidence of the horizontal stress on both sides of the axis, the horizontal stress on both sides of the axis gradually increases along the outside of the axis and reaches a state of equilibrium near the axis.

Similarly, the influence range of excavation face 2 is obviously larger than that of excavation face 1, and the influence range is about 1.5 times that of excavation face 2. The influence area of the

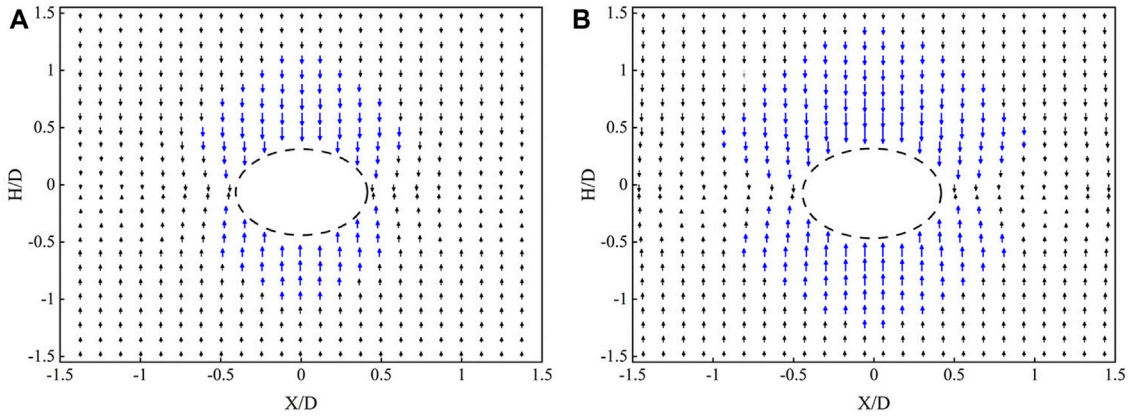

FIGURE 8
Displacement vector comparison of vertical influence range (In order to express clearly, it is not drawn according to the actual scale, and the effect is enlarged at a scale of 1.5 times): **(A)** Vertical displacement vector diagram of plane 1, **(B)** Vertical displacement vector diagram of plane 2.

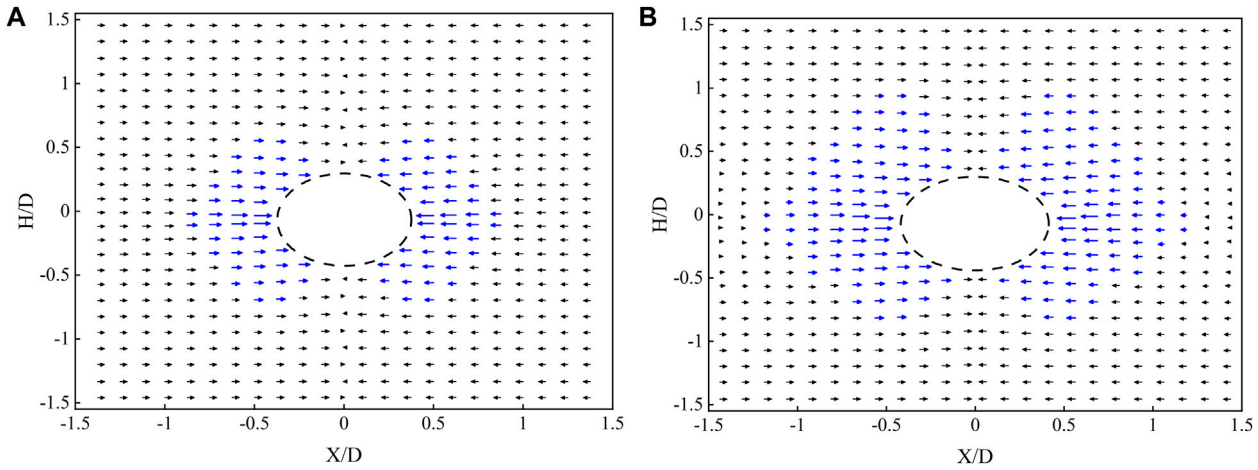

FIGURE 9
Displacement vector comparison of horizontal influence range: **(A)** Horizontal displacement vector diagram of face 1. **(B)** Horizontal displacement vector diagram of face 2.

excavation face is mainly concentrated in the four floors outside the side of the tunnel, which is about 30 mm from the side of the tunnel, or 0.5 times the diameter of the tunnel, and the main influence area below the bottom of the tunnel accounts for about 4/5 of the area above the top of the tunnel. The influence range of the excavation face 2 is 6 floors outside the side of the tunnel, 45 mm away from the side of the tunnel, or 0.75 times the diameter of the tunnel. The main influence range above the top of the tunnel is about 1.67 times that below the bottom of the tunnel. Under the impact of horizontal load, the vertical settlement of soil at the tunnel's waistline becomes horizontal displacement.

3.1.3 The influence range of holes on the plane

The excavation faces are located at 1/3 and 2/3 to obtain the X+Y overall shear strain vector distribution. The X and Z values in the 3D coordinates of the markers were extracted by scanning. The X and Z value coordinate points after loading excavation were compared with the X and Z value coordinate points before excavation in terms of position, and the 2D displacement vector and the main disturbance zone were depicted on the cross section. The main influence areas of both are shown in Figure 10. The main influence range of displacement and settlement of excavation face 1 and excavation face 2 is elliptical distribution, and the settlement range on the top of

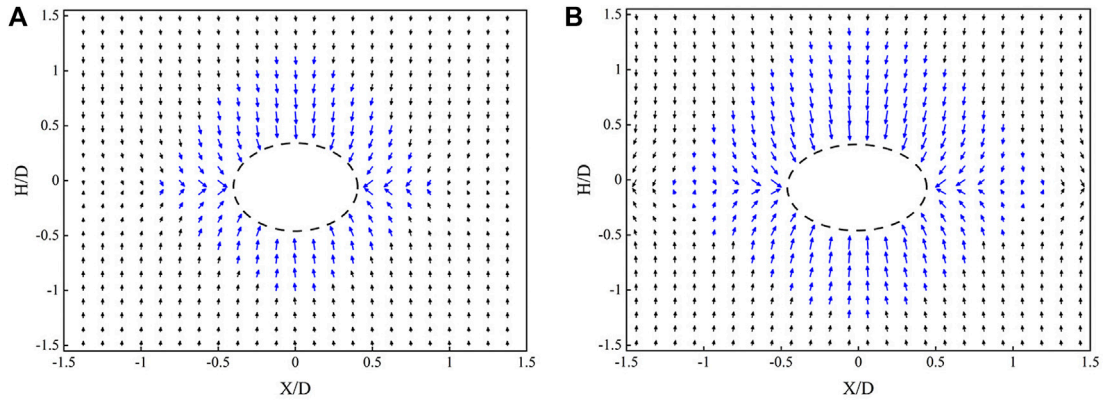

FIGURE 10
Displacement vector comparison of two-dimensional influence range in plane: **(A)** Displacement vector diagram of plane 1 X+Z, **(B)** Displacement vector diagram of plane 2 X+Z.

the cave is slightly larger than the displacement at the bottom of the cave. In Figure 10A., the deformation around the hole on the first excavation face occurs within one to two radii around the tunnel, and in Figure 10B., the deformation on the second excavation face occurs within two to three radii around the tunnel. The specific numerical value of the displacement influence range in each direction is basically the same as the vertical settlement and horizontal displacement data described above. The specific range value will not be repeated.

The range of tunnel settlement and uplift is much larger than the displacement range of the sidewall convergence, and the horizontal movement is relatively smaller than the vertical movement. Tunnel excavation is the main cause of stratum subsidence. After the excavation is completed, the overall tunnel is in the form of upper part sinking、 lower part uplifting, and both sides shrinking. Due to the different stress states of the soil around the cutter head, the spatial displacements of soil elements are different under the same nodal stress. Affected by the stress difference of overexcavation effect, the displacement moves to the direction of the hole with large stress difference. Under the action of different uniform loads, the tunnel's overall deformation shows a non-uniform convergence elliptical non-equivalent radial movement deformation trend.

3.2 Vertical horizontal displacement of the stratum

3.2.1 Comparative analysis of stratum subsidence and uplift curves

Figure 11 shows the vertical displacement response curves of the marked points in the soil layer at different buried depths on the excavation face 1 and the excavation face 2. The results show that the vertical displacement and settlement curves of soil bodies with different buried depths up and down the central axis of the tunnel under the principal stress load show a normal distribution (Gaussian function curve) along the horizontal direction of the stratum, which can be expressed by Eq. 5 (Wei et al., 2006). The vertical strata subsidence data in the Figure match the "modified Loganathan" formula; the measured data agrees well with the modified Loganathan formula calculation results; the analytical solution is smaller than the width of the ground subsidence trough monitored in this paper; and the maximum calculated displacement of the soil is greater than the monitoring mark deformation.

Under both geological conditions, the maximum displacement of surrounding rock occurs at the top and bottom of the tunnel. The vertical displacement of a hole roof on the excavation face is 0.6–1.3 d, decreasing successively from the maximum 1.5 mm–0.8 mm and 0.3 mm; the hole bottom 0.7–1.1 d vertical displacement of 1, 0.6, and 0.3 mm. When the X value between the top and bottom of the tunnel is equal, the maximum displacement values from top to bottom are 0.7, 0.4, and 0.5 mm, respectively. The vertical displacement decreases linearly as the top and bottom of the tunnel approach the axis.

The excavation face 2 and the excavation face 1 show the same trend of change, but the response range and response value are larger than the overall response range. Among them, the 0.6, 1.1, and 1.6D settlements above the top of the cave are 2, 1.2, and 0.5 mm; the 0.7, 1, and 1.3D displacements below the bottom of the cave are 1.7, 0.9, and 0.3 mm, respectively; and the maximum vertical direction of the monitoring point between the top and bottom of the cave is 1, 0.6, and 0.8 mm, respectively. The smallest amount of movement is up and down the axis, which is centered on the change from horizontal to maximum movement.

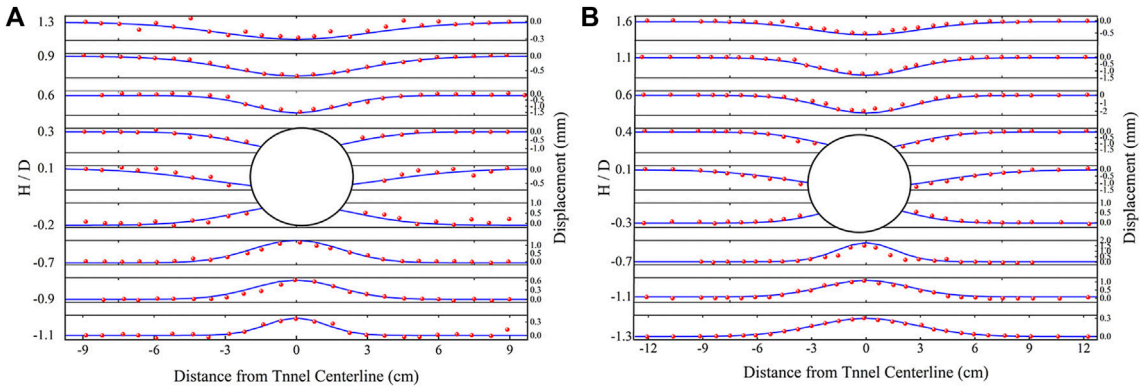

FIGURE 11
Vertical monitoring displacement curve of formation: **(A)** Vertical displacement curve of face 1, **(B)** Vertical displacement curve of face 2.

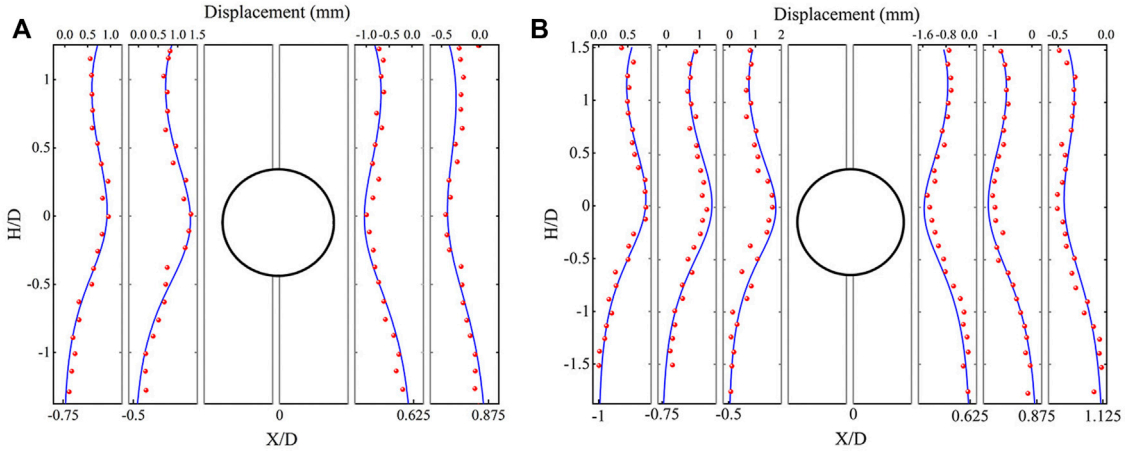

FIGURE 12
Horizontal monitoring displacement curve of formation: **(A)** Horizontal displacement curve of plane 1, **(B)** Horizontal displacement curve of plane 2.

(1) Soil vertical displacement calculation formula

$$U_z(x,z) = \frac{R^2}{2} * \left\{ \frac{h-z}{x^2+(h-z)^2} + \frac{h+z}{x^2+(h+z)^2} - \frac{2z\left[x^2-(h+z)^2\right]}{\left[x^2+(h+z)^2\right]^2} \right\} * \frac{4Rg-g^2}{4R^2} \mathrm{Bexp}\left[\frac{x^2 \ln\lambda}{(h+R)^2} + \frac{z^2(\ln\lambda - \ln\delta)}{(h+d)^2} \right] \tag{5}$$

$$\mathrm{B} = \frac{4\mathrm{h}\left[\mathrm{h}+\mathrm{d}-\sqrt{(\mathrm{h}+\mathrm{d})^2-\eta(\mathrm{R}+\mathrm{d})^2}\right]}{\mathrm{R}\eta(\mathrm{R}+\mathrm{d})} \tag{6}$$

$$\lambda = \frac{1}{4} - \frac{g}{\pi R\eta}\left[\arcsin\left(\frac{d}{R-g/2}\right) + \sqrt{1-\left(\frac{d}{R-g/2}\right)^2} - 1 \right] \tag{7}$$

$$\delta = \frac{1}{2} - \frac{g}{\pi R^2 \eta}(R - \mathrm{g}/4)\arcsin\left(\frac{d}{R-g/4}\right) \tag{8}$$

Where η is the soil loss percentage (%), h is the buried depth of the tunnel axis, R is the outer radius of the tunnel, d is the distance from the moving focus of the soil to the center of the tunnel, g is the equivalent soil loss parameter. In actual construction, the g value is small, usually within 0.35 m, μ is Poisson's ratio. The soil is non-drainage, so the Poisson's ratio of the soil is assumed to be $\mu = 0.5$.

(2) Soil horizontal displacement calculation formula:

$$U_x(x,z) = -\frac{R^2 x}{2} \frac{h}{h+d} \left\{ \frac{1}{x^2+(h-z)^2} \frac{1}{x^2+(h+z)^2} \frac{4z(h+z)}{\left[x^2+(h+z)^2\right]^2} \right\} \cdot \frac{4Rg-g^2}{4R^2} B \exp\left[\frac{x^2 \ln \lambda}{(h+R)^2} + \frac{z^2(\ln \lambda - \ln \delta)}{(h+d)^2} \right] \quad (9)$$

3.2.2 Comparative analysis of horizontal displacement curves

Figure 12 shows the horizontal movement curve of soil. The displacements on both sides of the tunnel are symmetrically distributed, and the measured data are in good agreement with the modified Loganathan formula as a whole. The horizontal displacement measured in the upper section of the axis is smaller than the calculated horizontal displacement, and the difference between the calculated value and the measured value in the section below the axis is small. This is because the modified Loganathan formula is based on the idea of an ideal elastic-plastic homogeneous soil layer. However, the laboratory soil will always have stress concentrations under rigid construction loading, and the real stress distribution in the soil layer is fairly complicated, so there may be errors in the calculation results and experimental data.

Figure 12A shows the horizontal displacement of a tunnel from 0.5D to 0.875D on the excavation face 1. The horizontal displacement gradually decreases with the increase of the axial extension of the tunnel, until the value beyond the minimum displacement tends to be stable, with a maximum horizontal displacement of 1.5 mm and a minimum of 0.5 mm. Figure 12B shows the data and fitting curve of the horizontal displacement monitoring points at 0.5D to 1.125D around the second hole on the excavation face. The maximum horizontal displacement at the edge of the hole is 2 mm, and the minimum horizontal displacement at 1.125D at the outer edge is 0.5 mm. The overall horizontal displacement of excavation face 1 is smaller than that of excavation face 2. The influence range of horizontal displacement of excavation face 1 is extended by about 1/3D, and the extension of excavation face 2 is about 1/2D.

3.3 Three-dimensional displacement characteristics of the excavation face

3.3.1 Three-dimensional displacement face model

When calculating the displacement of soil due to loading or unloading, it is mainly assumed that the soil is an ideal linear elastic body. This assumption is often not in line with the soil properties, especially for soft soils, and even results in erroneous calculations. Some scholars have derived a two-dimensional analytical model considering the influence of soil viscoelasticity. However, tunnel excavation is a three-dimensional dynamic evolution process, which exhibits soil disturbance caused by excavation and soil displacement caused by additional force with time. Therefore, the study of the three-dimensional displacement model of the excavation face is of great significance to accurately understanding and predicting the disturbance and displacement trend of surrounding rock caused by construction.

The specific 3D coordinate X, Y, and Z values of the marker are extracted by scanning, and the 3D coordinate values of the marker after loading excavation are compared with the coordinate values before excavation to construct a 3D deformation trajectory of the excavation surface.

Figure 13 shows the excavation faces 1 and 2 and the integrated displacement characteristic faces of the first and second faces, respectively. It is not difficult to imagine that due to the excavation of the soil body, the surrounding soil body is in a state of active Earth pressure and stratum loss occurs on both sides and in the upper and lower areas, resulting in soil movement. In the early stage of tunnel excavation, the excavation disturbance has little effect on the markers buried in the model, and the displacement is in a relatively stable state. As the excavation advances, the cutter head gradually approaches the measuring point, which has an obvious disturbance effect on the surrounding rock, and the displacement value increases significantly.

When the cutter head is excavated to the front of the excavation face measurement point, due to the thrust of the cutter head, the excavation face is displaced along the tunnel excavation direction, which appears as a bulge state on the ground face. When the cutting section of the cutter head approaches the measuring point, the displacement tends to increase due to the circumferential support of the cutter head. The tool head is close to the section of the measuring point, and the stagnation of the tool head causes the emergence of intermittent voids. Under the action of three-way stress, the displacement of surrounding soil in the air direction (*X*, *Y* and *Z* directions) increases sharply, and the face changes from uplift to settlement. Then, as the cutter head keeps moving forward, it finally stops moving and stays stable within a certain range of values.

3.3.2 Comparative analysis of excavation direction displacement curve

As shown in Figure 14, the three vertical sections perpendicular to the *X*-axis direction, that is, the displacement components in the *Y*-direction, are symmetrically distributed along the *X*-axis. The displacement deformation mode of excavation face 1 is the same as that of excavation face 2, but the influence range and displacement value are different. The excavation face 1 is at X=0 of the tunnel axis, as shown in Figure 14A, and the top of the tunnel is gradually sunk from 1D to 1.5D. The maximum sag is −0.7 mm; close to the edge of the hole within 0.5D, the maximum protrude to 0 mm. The up and down displacements of the tunnel axis are symmetrically distributed, with a small difference in value.

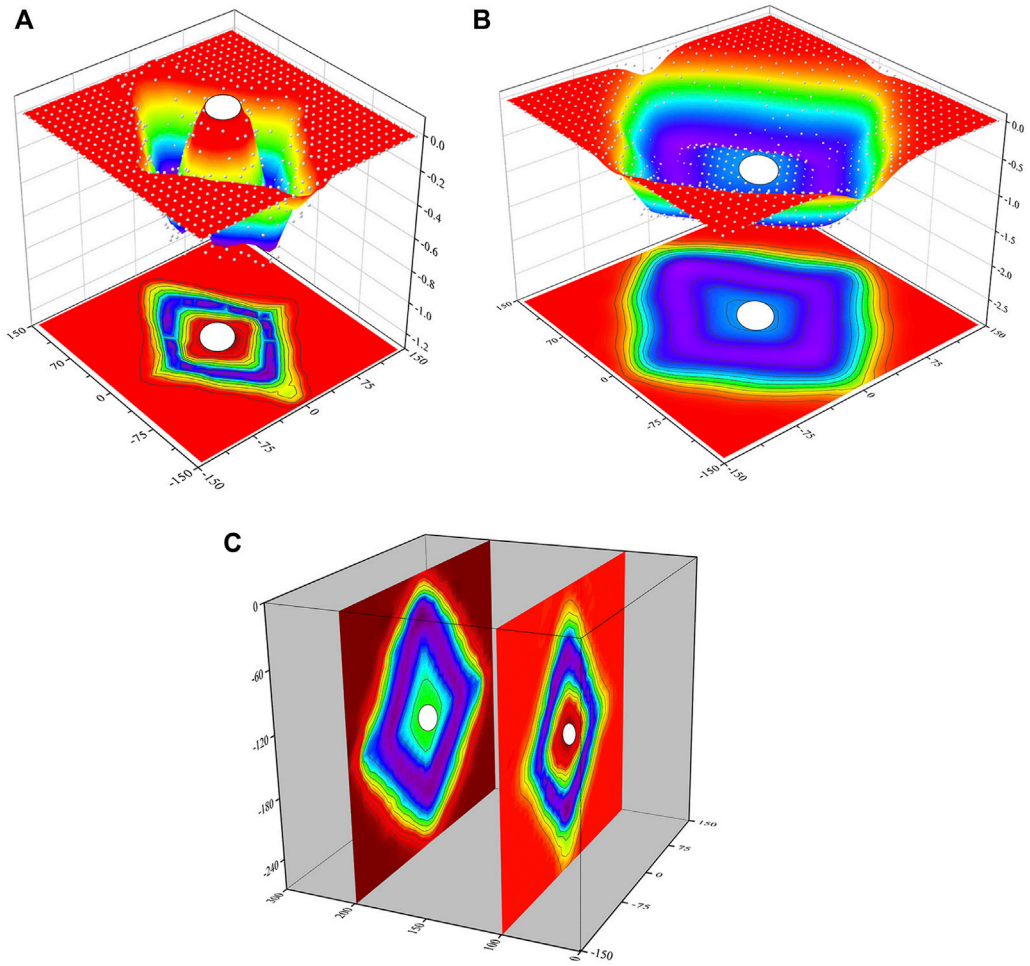

FIGURE 13
Displacement deformation model of excavation face: **(A)** Displacement deformation model of excavation face 1, **(B)** Displacement deformation model of excavation face 2, **(C)** superimposed displacement deformation model.

X = 1D, 0.5D to 1.25D within the largest sag range of −0.4 mm; axis at 0.5D within the maximum raised to −0.2 mm. At X = 2D, the whole thing barely deforms.

Figure 14B The excavation face is gradually concave in a quadratic function form between 1D and 2D, and the maximum sag value is −1.1 mm. The largest sag to the hole edge position is deformation gradually reverse protruding, the largest protruding to −0.6 mm. At X=1D, between 0.5D and 1.5D near the axis, the maximum concave value of gradual concave deformation is −0.7 mm; within the range of 0.5D above and below the axis, it gradually protrudes and deforms, and the maximum convexity value is displaced by −0.3 mm. The upward displacement of the tunnel axis is slightly larger than the downward displacement, and the shapes are almost the same. At X = 2D, the overall deformation is concave, and the maximum displacement value is 0.4 mm at the axis.

3.4 Evolution of the plastic zone of soil excavation and stress action

Due to the disturbance of excavation and unloading, the soil near the excavation face will produce dynamic elastic-plastic deformation along the forward and reverse directions of the excavation face. The deformation of the plastic zone of tunnel excavation is mainly divided into three stages: the depression deformation stage of the working face affected by the propulsion force, the rapid outward convex deformation stage of the tunnel facing the void, and the stable deformation stage. In the early stage of excavation, with the advancement of the cutter head, the soil body is subjected to the continuous thrust and disturbance of the cutter head, and a certain three-dimensional disturbance zone is formed within the range of 0.5 times the diameter in front of the cutter head. Before reaching the monitoring surface, under the thrust of the cutter head, the monitoring surface is mainly

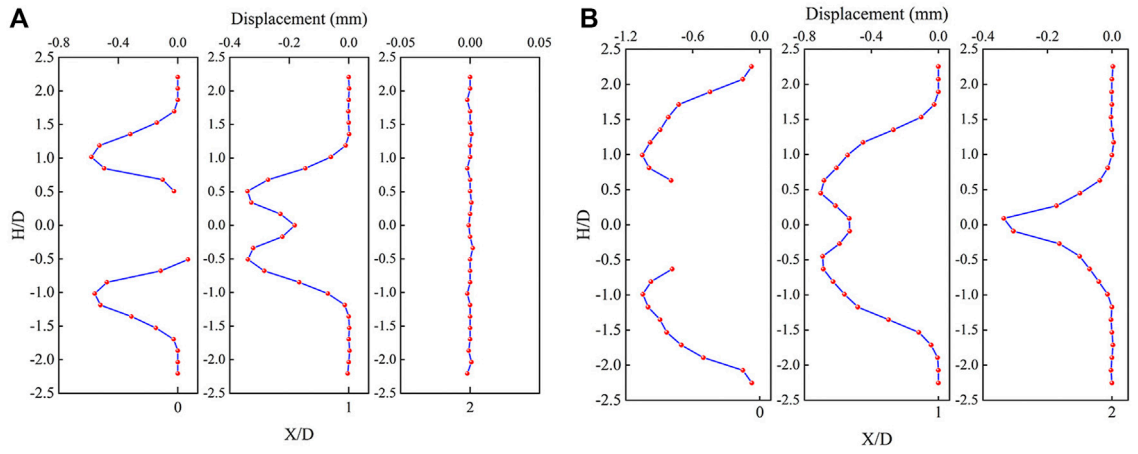

FIGURE 14
Displacement curve of excavation section: **(A)** Displacement curve of section 1, **(B)** Displacement curve of section 2.

deformed along the excavation direction, and the deformation gradually increases to the maximum as the cutter head approaches; During the simulation support period, the surrounding rock with a diameter of about 1 times the diameter around the tunnel rapidly moved plastically toward the reverse excavation direction. After the excavation continued to exceed the monitoring surface, due to the rigid support, the plastic deformation of the surrounding rock of the tunnel gradually tended to be stable, with gradual deformation smoothing to a certain value. Finally, the plastic deformation characteristics of the sag outside the tunnel and the surrounding bulge were observed. The specific deformation is caused by many geological factors, like the kind of soil and where it is.

The internal reason for the deformation of the surrounding rock mass caused by full-face excavation is that the initial stress state of the soil has changed, making the undisturbed soil experience complex stress paths such as extrusion, shearing, and twisting. The disturbance of the surrounding soil is mainly manifested as a change in stress and strain states. When the total thrust of the drill bit is greater than the initial equilibrium stress of the sample, the soil in front of the drill bit is in a state of compression loading, and elastic-plastic deformation occurs. The range of soil affected by extrusion is indicated by the cone in the dotted line in Figure 15. Under the action of thrust, the stress of soil extrusion loading is concentrated, and the soil bodies in ② and ④ areas are subjected to large extrusion deformation. The horizontal and vertical stresses in ② area both increase, and the effect of shear stress is obvious; ④ area concentratedly reflects the extrusion stress. Effect; ③The soil in the area is affected by the cutting friction of the cutter head, and is in a very complex stress state. When the cutter head is in a static state, the total thrust of the drill bit is less than the total

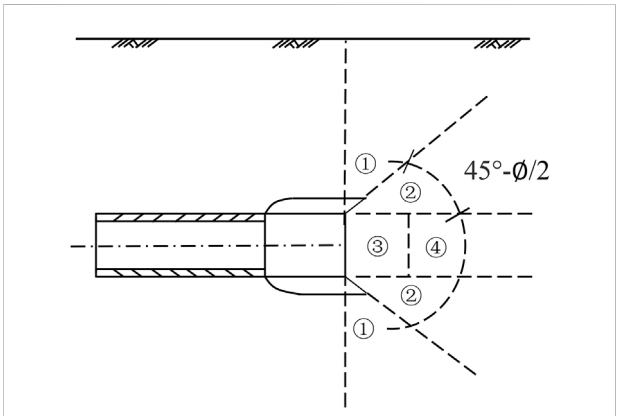

FIGURE 15
Excavation disturbance—stress zoning.

equilibrium stress of the sample. At this time, it corresponds to the state of severe over-excavation of the soil, and the stress relaxation of the excavation surface is obvious if the support is not timely. Because the soil in front of the excavation did not apply support in time, the stress of the soil was released, and it slipped to the free surface. Excessive ground stress release on the excavation surface will cause large plastic deformation of the surrounding rock, which will transform from a stable state to an unstable state. After a certain expansion process at the boundary of the plastic zone, the maximum shear stress can gradually decrease due to the confining pressure due to the existence of the plastic zone. After the rigid support is added, the deformation of the surrounding rock is effectively controlled, the sandy soil is in sub-consolidation and creep deformation, and the total stress gradually returns to a

TABLE 2 Relationship between surrounding rock deformation and stress state.

Deformation type	Cause of deformation	Stress disturbance	Deformation mechanism
Deformation before the cutter head arrives at the monitor	The soil is deformed by thrust extrusion	Effective stress and total stress increase	Void ratio change
Deformation of the cutter head to the monitoring surface stopping the drilling support	The air surface is generated, and the balance pressure at the working face is too large	Soil stress release	Elastic-plastic deformation
Cutterhead continues excavation beyond the monitoring surface	Soil construction disturbance, shear between cutter head and soil	Soil stress release	Elastic-plastic deformation
Soil secondary consolidation deformation	Subsequent aging deformation of soil	Soil stress relaxation	Creep compression

relatively balanced state. The specific relationship between surrounding rock deformation and stress state is shown in Table 2.

4 Conclusion

In this study, a new experimental model of tunnel excavation confining pressure disturbance was used to study the displacement response characteristics of the excavation face in different soils. The real *in-situ* stress is simulated by the true triaxial loading method, and the three-dimensional displacement and deformation of the excavation face are obtained by using a full-section three-dimensional scanning device. Based on the reconstructed spatial displacement patterns, the impact degree of specific excavation disturbance of different soil masses was evaluated. The following conclusions are drawn:

1 The excavation of the full-section tunnel will cause displacement and deformation of the surrounding strata, and these displacements are mainly vertical and horizontal. The displacement vector is concentrated at the top, bottom, shoulder, waist, and other positions of the tunnel, and the main influence range is within 2 times the diameter of the tunnel extension, which is elliptically distributed on the two-dimensional plane.

2 The tunnel deformation caused by excavation is the combined effect of three basic modes: radial shrinkage, non-uniform elliptical shrinkage, and three-dimensional face deformation. The displacement of the surrounding soil increases with proximity to the tunnel, and the vertical and horizontal displacement curves conform to the modified Loganathan formula.

3 The change process of the excavation face is a deformation pattern that is concave first and then convex. The specific protruding and concave displacements are closely related to the mechanical properties and location of the soil itself. Under the influence of overlapping and crossing strata, the movement characteristics of the face before and after are the same and the displacement amount is different.

4 In the sand model test, the method of arranging measurement markers to establish a grid description, combined with 3D digital image scanning and image analysis methods, is a simple and effective non-contact deformation field measurement method within a certain deformation range. It gives a good way to analyze the local deformation and three-dimensional displacement of the excavation model in a more quantitative way.

Data availability statement

The original contributions presented in the study are included in the article/Supplementary Material, further inquiries can be directed to the corresponding author.

Author contributions

EL: conceptualization, investigation, methodology, writing—original draft, writing–review and editing; QG: supervision, funding acquisition; XL: conceptualization, resources, investigation. TM: resources; BZ: investigation.

Funding

This work was supported by the National Natural Science Foundation of China (51734009).

Conflict of interest

The authors declare that the research was conducted in the absence of any commercial or financial relationships that could be construed as a potential conflict of interest.

Publisher's note

References

Ahmed, M., and Iskander, M. (2011). Analysis of tunneling-induced ground movements using transparent soil models. *J. Geotech. Geoenviron. Eng.* 137 (5), 525–535. doi:10.1061/(asce)gt.1943-5606.0000456

Attewell, P. B., Yeates, J., and Selby, A. R. (1986). *Soil movements induced by tunnelling and their effects on pipelines and structures*. London: Blackie and Son Ltd, 10–50.

Berthoz, N., Branque, D., Subrin, D., Wong, H., and Humbert, E. (2012). Face failure in homogeneous and stratified soft ground: Theoretical and experimental approaches on 1g EPBS reduced scale model. *Tunn. Undergr. Space Technol.* 30, 25–37. doi:10.1016/j.tust.2012.01.005

Berthoz, N., Branque, D., Wong, H., and Subrin, D. (2018). TBM soft ground interaction: Experimental study on a 1 g reduced-scale EPBS model. *Tunn. Undergr. Space Technol.* 72, 189–209. doi:10.1016/j.tust.2017.11.022

Cao, L., Zhang, D., and Fang, Q. (2020). Semi-analytical prediction for tunnelling-induced ground movements in multi-layered clayey soils. *Tunn. Undergr. Space Technol.* 102, 103446. doi:10.1016/j.tust.2020.103446

Chen, R., Yin, X., Tang, L., and Chen, Y. (2018). Centrifugal model tests on face failure of Earth pressure balance shield induced by steady state seepage in saturated sandy silt ground. *Tunn. Undergr. Space Technol.* 81, 315–325. doi:10.1016/j.tust.2018.06.031

Cheng, H., Chen, J., and Chen, G. (2019). Analysis of ground surface settlement induced by a large EPB shield tunnelling: A case study in beijing, China. *Environ. Earth Sci.* 78 (20), 605. doi:10.1007/s12665-019-8620-6

Grant, R. J., and Taylor, R. N. (2000). "Tunnelling-induced ground movements in clay," in *Proceedings of the institution of civil engineers - geotechnical engineering*.

Hagiwara, T., Grant, R. J., Calvello, M., and Taylor, R. N. (1999). The effect of overlying strata on the distribution of ground movements induced by tunnelling in clay. *Soils Found.* 39 (3), 63–73. doi:10.3208/sandf.39.3_63

Jiang, Q., Fan, Y., Feng, X., Li, Y., Pei, S., and Liu, G. (2017). Unloading break of hard rock under high geo-stress condition:inner cracking observation for the basalt in the Baihetan¢s underground powerhouse. *Chin. J. Rock Mech. Eng.* 36 (05), 1076–1087. doi:10.13722/j.cnki.jrme.2016.1112

Jiang, Q., Feng, X., Li, S., Su, G., and Xiao, Y. (2019). Cracking-restraint design method for large underground caverns with hard rock under high geostress condition and its practical application. *Chin. J. Rock Mech. Eng.* 38 (06), 1081–1101. doi:10.13722/j.cnki.jrme.2018.1147

Li, H., and Ma, X. (2011). "Analysis of settlement caused by TBM construction in sand formations in Beijing," in *Icptt 2011: Sustainable solutions for water, sewer, gas, and oil pipelines*, 1884–1896.

Litwiniszyn, J. (1957). "The theories and model research of movements of ground masses," in *Proceedings of the European congress on ground movement* (Leeds, United Kingdom: University of leeds), 203–209.

Loganathan, N., and Poulos, H. G. (1998). Analytical prediction for tunneling-induced ground movements in clays. *J. Geotech. Geoenviron. Eng.* 124 (9), 846–856. doi:10.1061/(asce)1090-0241(1998)124:9(846)

Loganathan, N., Poulos, H. G., and Stewart, D. P. (2000). Centrifuge model testing of tunnelling-induced ground and pile deformations. *Géotechnique* 50 (3), 283–294. doi:10.1680/geot.2000.50.3.283

Mair, R. J. (2008). Tunnelling and geotechnics: New horizons. *Geotechnique* 58 (9), 695–736. doi:10.1680/geot.2008.58.9.695

Mair, R., Taylor, R., and Bracegirdle, A. J. G. (1993). Subsurface settlement profiles above tunnels in clays. *Geotechnique* 43 (2), 315–320. doi:10.1680/geot.1993.43.2.315

Marshall, A. M., Farrell, R., Klar, A., and Mair, R. (2012). Tunnels in sands: The effect of size, depth and volume loss on greenfield displacements. *Géotechnique* 62 (5), 385–399. doi:10.1680/geot.10.P.047

Meguid, M. A., Saada, O., Nunes, M. A., and Mattar, J. (2008). Physical modeling of tunnels in soft ground: A review. *Tunn. Undergr. Space Technol.* 23 (2), 185–198. doi:10.1016/j.tust.2007.02.003

Mollon, G., Dias, D., and Soubra, A.-H. (2012). Probabilistic analyses of tunneling-induced ground movements. *Acta Geotech.* 8 (2), 181–199. doi:10.1007/s11440-012-0182-7

Nomoto, T., Imamura, S., Hagiwara, T., Kusakabe, O., and Fujii, N. (1999). Shield tunnel construction in centrifuge. *J. Geotech. Geoenviron. Eng.* 125 (4), 289–300. doi:10.1061/(asce)1090-0241(1999)125:4(289)

Park, K.-H. (2005). Analytical solution for tunnelling-induced ground movement in clays. *Tunn. Undergr. Space Technol.* 20 (3), 249–261. doi:10.1016/j.tust.2004.08.009

Peck, R. B. (1969). *Deep excavations and tunneling in soft ground*, 7th Int. Conf. on SMFE, Mexico City: State of the Art Volume, 225–290.

Pinto, F., and Whittle, A. J. (2014). Ground movements due to shallow tunnels in soft ground. I: Analytical solutions. *J. Geotech. Geoenviron. Eng.* 140 (4). doi:10.1061/(asce)gt.1943-5606.0000948

Pinto, F., Zymnis, D. M., and Whittle, A. J. (2014). Ground movements due to shallow tunnels in soft ground. II: Analytical interpretation and prediction. *J. Geotech. Geoenviron. Eng.* 140 (4). doi:10.1061/(asce)gt.1943-5606.0000947

Sagaseta, C. (1987). Analysis of undrained soil deformation due to ground loss. *Géotechnique* 37 (3), 301–320. doi:10.1680/geot.1987.37.3.301

Song, G., and Marshall, A. M. (2020). Centrifuge modelling of tunnelling induced ground displacements: Pressure and displacement control tunnels. *Tunn. Undergr. Space Technol.* 103, 103461. doi:10.1016/j.tust.2020.103461

Verruijt, A., and Booker, J. R. (1998). Surface settlements due to deformation of a tunnel in an elastic half plane. *Géotechnique* 48 (5), 709–713. doi:10.1680/geot.1998.48.5.709

Verruijt, A. (1998). Deformations of an elastic half plane with a circular cavity. *Int. J. Solids Struct.* 35 (21), 2795–2804. doi:10.1016/s0020-7683(97)00194-7

Wei, G., Wei, X., Gong, C., and Ding, Z. (2006). Study on calculation for shield tunneling-induced ground movements in clays. *Rock Soil Mech.* (06), 995–999. doi:10.16285/j.rsm.2006.06.030

Yang, G., Zhang, C., Min, B., and Chen, W. (2021). Complex variable solution for tunneling-induced ground deformation considering the gravity effect and a cavern in the strata. *Comput. Geotech.* 135, 104154. doi:10.1016/j.compgeo.2021.104154

Yang, H., Liu, F., and Lin, S. (2019). Investigation on the 3D ground settlement induced by shallow tunneling considering the effects of buildings. *KSCE J. Civ. Eng.* 24 (2), 365–376. doi:10.1007/s12205-019-2201-9

Yang, X. L., and Wang, J. M. (2011). Ground movement prediction for tunnels using simplified procedure. *Tunn. Undergr. Space Technol.* 26 (3), 462–471. doi:10.1016/j.tust.2011.01.002

Yoshikoshi, W., Watanabe, O., and Takagi, N. (1978). Prediction of ground settlements associated with shield tunnelling. *Soils Found.* 18 (4), 47–59. doi:10.3208/sandf1972.18.4_47

Yuan, W., Fu, H., Zhang, J., and Huang, Z. (2018). Analytical prediction for tunneling-induced ground movements with modified deformation pattern. *Int. J. Geomech.* 18 (6). doi:10.1061/(asce)gm.1943-5622.0001156

Zhu, X. G. (2014). The research reviewed of subway construction impact on stratum deformation law. *Appl. Mech. Mater.* 670-671, 474–478. doi:10.4028/www.scientific.net/amm.670-671.474

Frontiers in Earth Science

Investigates the processes operating within the major spheres of our planet

Advances our understanding across the earth sciences, providing a theoretical background for better use of our planet's resources and equipping us to face major environmental challenges.

Discover the latest Research Topics

See more →

Frontiers

Avenue du Tribunal-Fédéral 34
1005 Lausanne, Switzerland
frontiersin.org

Contact us

+41 (0)21 510 17 00
frontiersin.org/about/contact